International Journal of Antennas and Propagation

Advances in Statistical Channel Modeling for Wireless Communications

Guest Editors: José F. Paris, Paschalis C. Sofotasios, and Theodoros A. Tsiftsis

Advances in Statistical Channel Modeling for Wireless Communications

International Journal of Antennas and Propagation

Advances in Statistical Channel Modeling for Wireless Communications

Guest Editors: José F. Paris, Paschalis C. Sofotasios, and Theodoros A. Tsiftsis

Copyright © 2015 Hindawi Publishing Corporation. All rights reserved.

This is a special issue published in "International Journal of Antennas and Propagation." All articles are open access articles distributed under the Creative Commons Attribution License, which permits unrestricted use, distribution, and reproduction in any medium, provided the original work is properly cited.

Editorial Board

Mohammod Ali, USA
Jaume Anguera, Spain
Charles Bunting, USA
Felipe Cátedra, Spain
Dau-Chyrh Chang, Taiwan
Deb Chatterjee, USA
Z. N. Chen, Singapore
Michael Y. W. Chia, Singapore
Shyh-Jong Chung, Taiwan
Lorenzo Crocco, Italy
Tayeb A. Denidni, Canada
Francisco Falcone, Spain
Miguel Ferrando Bataller, Spain
Vincenzo Galdi, Italy
Wei Hong, China
Tamer S. Ibrahim, USA
Nemai Karmakar, Australia
Se-Yun Kim, Republic of Korea
Ahmed A. Kishk, Canada
Selvan T. Krishnasamy, India
Ju-Hong Lee, Taiwan
Byungje Lee, Republic of Korea
Joshua Le-Wei Li, China
J.S. Mandeep, Malaysia
Atsushi Mase, Japan
Giuseppe Mazzarella, Italy
C. F. Mecklenbruker, Austria
Mark Mirotznik, USA
A. S. Mohan, Australia
P. Mohanan, India
Pavel Nikitin, USA
Symeon Nikolaou, Cyprus
A. D. Panagopoulos, Greece
Matteo Pastorino, Italy
M. Pieraccini, Italy
Sembiam R. Rengarajan, USA
Ahmad Safaai-Jazi, USA
S. Safavi-Naeini, Canada
M. Salazar-Palma, Spain
Stefano Selleri, Italy
Zhongxiang Shen, Singapore
John J. Shynk, USA
Seong-Youp Suh, USA
Parveen Wahid, USA
Yuanxun Ethan Wang, USA
Tat Soon Yeo, Singapore
Young Joong Yoon, Korea
Jong-Won Yu, Republic of Korea
Anping Zhao, China

Contents

Advances in Statistical Channel Modeling for Wireless Communications, José F. Paris, Paschalis C. Sofotasios, and Theodoros A. Tsiftsis
Volume 2015, Article ID 541619, 2 pages

On the Efficient Generation of α-κ-μ and α-η-μ White Samples with Applications, Rausley Adriano Amaral de Souza, Antonio Marcelo Oliveira Ribeiro, and Dayan Adionel Guimarães
Volume 2015, Article ID 873890, 13 pages

Modeling of the Land Mobile Satellite Channel considering the Terminal's Driving Direction, Marie Rieche, Alexander Ihlow, Daniel Arndt, Fernando Pérez-Fontán, and Giovanni Del Galdo
Volume 2015, Article ID 372124, 21 pages

Tracking- and Scintillation-Aware Channel Model for GEO Satellite to Land Mobile Terminals at Ku-Band, Ali M. Al-Saegh, A. Sali, J. S. Mandeep, and Alyani Ismail
Volume 2015, Article ID 392714, 15 pages

On the Bivariate Nakagami-Lognormal Distribution and Its Correlation Properties, Juan Reig, Lorenzo Rubio, and Vicent M. Rodrigo-Peñarrocha
Volume 2014, Article ID 328732, 8 pages

Measurement-Based LoS/NLoS Channel Modeling for Hot-Spot Urban Scenarios in UMTS Networks, Jiajing Chen, Xuefeng Yin, Li Tian, Nan Zhang, Yongyu He, Xiang Cheng, Weiming Duan, and Silvia Ruiz Boqué
Volume 2014, Article ID 454976, 12 pages

Fading Evaluation in the 60 GHz Band in Line-of-Sight Conditions, J. Reig, M.-T. Martínez-Inglés, L. Rubio, V.-M. Rodrigo-Peñarrocha, and J.-M. Molina-García-Pardo
Volume 2014, Article ID 984102, 12 pages

Capacity of κ-μ Shadowed Fading Channels, Celia García-Corrales, Francisco J. Cañete, and José F. Paris
Volume 2014, Article ID 975109, 8 pages

Capacity Estimation of the Very Short-Range Electromagnetic Underwater Channel Based on Measurements, Jesús López-Fernández, Unai Fernández-Plazaola, and Jose F. Paris
Volume 2014, Article ID 318421, 5 pages

Characterization of Path-Loss Disparity in Virtual Multiple-Input-Single-Output Links, Haejoon Jung and Mary Ann Weitnauer
Volume 2014, Article ID 650236, 12 pages

Advances in the Statistical Characterization of Fading: From 2005 to Present, José F. Paris
Volume 2014, Article ID 258308, 5 pages

Relay Selection and Subcarrier-Pair Based Energy-Efficient Resource Allocation for Multirelay Cooperative OFDMA Networks, Wanming Hao, Shouyi Yang, and Wanliang Hao
Volume 2014, Article ID 461713, 13 pages

An Analytical Study of the Impact of Arbitrary Receive Antenna Correlation in TAS/MRC,
Juan P. Peña-Martín and Juan M. Romero-Jerez
Volume 2014, Article ID 798015, 9 pages

Practical and Simple Wireless Channel Models for Use in Multipolarized Antenna Systems,
KwangHyun Jeon, Xin Su, Bing Hui, and KyungHi Chang
Volume 2014, Article ID 619304, 10 pages

Hindawi Publishing Corporation
International Journal of Antennas and Propagation
Volume 2015, Article ID 541619, 2 pages
http://dx.doi.org/10.1155/2015/541619

Editorial

Advances in Statistical Channel Modeling for Wireless Communications

José F. Paris,[1] Paschalis C. Sofotasios,[2,3] and Theodoros A. Tsiftsis[4]

[1]*Department of Communications Engineering, University of Málaga, 29071 Málaga, Spain*
[2]*Department of Electronics and Communications Engineering, Tampere University of Technology, 33720 Tampere, Finland*
[3]*Department of Electrical and Computer Engineering, Aristotle University of Thessaloniki, 54124 Thessaloniki, Greece*
[4]*Department of Electrical Engineering, Technological Educational Institute of Central Greece, 35100 Lamia, Greece*

Correspondence should be addressed to José F. Paris; paris@ic.uma.es

Received 30 November 2014; Accepted 30 November 2014

Copyright © 2015 José F. Paris et al. This is an open access article distributed under the Creative Commons Attribution License, which permits unrestricted use, distribution, and reproduction in any medium, provided the original work is properly cited.

The complex electromagnetic propagation phenomena involved in modern wireless communications are taken into account by appropriate channel modeling. Statistical channel models are a powerful tool for communication engineers since they are able to capture the fundamental behavior of the wireless channel with reasonably simple mathematical formulation. New communication scenarios and services demand novel statistical channel models or extensions of those used in the field of wireless communications.

In the paper by J. Reig et al., the bivariate Nakagami-Lognormal model has been investigated. In particular, they have derived the joint probability density function, the cross moments, and the correlation coefficient in power terms. Also, two procedures to generate two correlated Nakagami-lognormal random variables are described.

In the paper by J. Chen et al., a measurement campaign is introduced for modeling radio channels with either line-of-sight (LoS) or non-line-of-sight (NLoS) connection between user equipment (UE) and Node B (NB) in an operating universal mobile telecommunications system. A space alternating generalized expectation-maximization (SAGE) algorithm is applied to estimate the delays and the complex attenuations of multipath components from the obtained channel impulse responses.

In another paper by J. Reig et al., fading channels in the 60 GHz band have been investigated. An exhaustive analysis of the small-scale fading amplitude in the 60 GHz band is addressed for line-of-sight conditions (LOS). From a measurement campaign carried out in a laboratory, the authors have estimated the distribution of the small-scale fading amplitude over a bandwidth of 9 GHz.

In the paper by C. Garcia-Corrales et al., the ergodic capacity of κ-μ shadowed fading channels is investigated. Considering the importance of the κ-μ shadowed distribution (it includes as special cases other classical distribution models such as one-side Gaussian, Rayleigh, Rician, etc.) the physical meaning of the distribution parameter variations and also their impact on the channel capacity is investigated. These results can be used to study the behavior of various channel models like the ones in underwater acoustic communications, land mobile satellite systems, body centric communications, and other wireless communication applications.

The paper by J. López-Fernández et al. addresses underwater electromagnetic communications, which are particularly important, although largely unexplored. Given that channel characterization and modelling in underwater communications differ substantially due to the different behavior of waves during subsea propagation, a suitable statistical model is proposed. The accuracy of this model is validated by comparisons with frequency response measurements and is shown to provide adequate fittings. Capitalizing on these results, the corresponding ergodic capacity is determined for a 7 MHz bandwidth channel at distances ranging from 0.5 m

to 5 m with different transmits power. This analysis shows capacity values of tens of kbps at distances of around 5 m to several Mbps at distances shorter than 1.5 m.

In the paper by H. Jung and M. A. Weitnauer, cooperative transmissions (CT) formed by spatially separated wireless nodes which collaborate to form a virtual antenna array or virtual multiple-input-multiple-output (VMISO) link are studied. Unlike previous studies where the path loss of the VMISO link is studied as though the elements in the virtual antenna array are colocated, even though they are spread out, in this work the authors show that the spreading causes a signal-to-noise-ratio (SNR) penalty of up to 3 dB. The analysis is also expanded for the high-SNR regime which showed a performance degradation caused by the path-loss disparity. Moreover, this degradation can be characterized equivalently by a log-normal distribution. Considering the above, a new CT link model expressed in closed form as an outage probability based on the log-normal shadowing model is proposed. The quality of the model is evaluated by a statistical test based on Kolmogorov-Smirnov method.

Given the extensive research activity in digital communication over fading channels over the past years, a thorough review by J. F. Paris presents the most important fading models that were proposed during the past decade. These models correspond to multipath, shadowing, and composite fading distributions and have been used extensively over the past years. The most important statistical measures of these models are also presented in a unified manner.

In the paper by W. Hao et al., energy-efficient resource allocation is investigated for a relay-based multiuser cooperation orthogonal frequency division multiple access (OFDMA) uplink system with amplify-and-forward (AF) protocol for all relays. An energy-efficient resource allocation problem that seeks joint optimization of subcarrier pairing, relay selection, subcarrier assignment, and power allocation is formulated. Unlike previous optimization throughput models, the considered EE problem is transformed into an equivalent optimal problem in subtractive form, which is solved by using dual decomposition and subgradient methods. More, two low-complexity suboptimal schemes to reduce computation costs are proposed. The simulation results show EE improvement of the energy-efficient design compared to that of the spectral-efficient design and the proposed suboptimal algorithm ordered subcarrier pairing (OSP) is close to the optimal algorithm.

In the paper by J. P. Peña-Martín and J. M. Romero-Jerez, novel closed-form expressions are derived for the bit error rate (BER) and channel capacity of a multiple-input-multiple-output (MIMO) system in Rayleigh fading using transmit antenna selection (TAS) at the transmitter and maximal ratio combining (MRC) at the receiver.

Practical 2D and 3D wireless channel models multipolarized are proposed in the paper by K. Jeon et al. These models account for both cross polarization discrimination (XPD) and the Rician factor and are claimed to be simpler than existing models for MIMO systems. The offered results are subsequently employed in analyzing the corresponding error rate and achievable throughput for the case of equal-gain combining and maximum-ratio combining in multipolarized antenna systems.

José F. Paris
Paschalis C. Sofotasios
Theodoros A. Tsiftsis

Hindawi Publishing Corporation
International Journal of Antennas and Propagation
Volume 2015, Article ID 873890, 13 pages
http://dx.doi.org/10.1155/2015/873890

Research Article

On the Efficient Generation of α-κ-μ and α-η-μ White Samples with Applications

Rausley Adriano Amaral de Souza,[1] Antonio Marcelo Oliveira Ribeiro,[2] and Dayan Adionel Guimarães[1]

[1]*National Institute of Telecommunications (Inatel), P. O. Box 05, 37540-000 Santa Rita do Sapucaí, MG, Brazil*
[2]*Department of Communications, School of Electrical and Computation Engineering, University of Campinas (DECOM/FEEC/UNICAMP), 13083-852 Campinas, SP, Brazil*

Correspondence should be addressed to Rausley Adriano Amaral de Souza; rausleyaas@gmail.com

Received 8 May 2014; Revised 18 July 2014; Accepted 1 August 2014

Academic Editor: Jose F. Paris

Copyright © 2015 Rausley Adriano Amaral de Souza et al. This is an open access article distributed under the Creative Commons Attribution License, which permits unrestricted use, distribution, and reproduction in any medium, provided the original work is properly cited.

This paper is concerned with a simple and highly efficient random sequence generator for uncorrelated α-κ-μ and α-η-μ variates. The algorithm may yield an efficiency of almost 100%, and this high efficiency can be reached for all special cases such as α-μ, κ-μ, η-μ, Nakagami-m, Nakagami-q, Weibull, Hoyt, Rayleigh, Rice, Exponential, and the One-Sided Gaussian. This generator is implemented via the rejection technique and allows for arbitrary fading parameters. The goodness-of-fit is measured using the Kolmogorov-Smirnov and Anderson-Darling tests. The maximum likelihood parameter estimation for the κ-μ distribution is proposed and verified against true values of the parameters chosen in the generator. We also provide two important applications for the random sequence generator, the first one dealing with the performance assessment of a digital communication system over the α-κ-μ and α-η-μ fading channels and the second one dealing with the performance assessment of the spectrum sensing with energy detection over special cases of these channels. Theoretical and simulation results are compared, validating again the accuracy of the generators.

1. Introduction

In nearly all fields of science, simulation is a strikingly powerful tool widely adopted to help develop a better understanding of some phenomenon under investigation. Particularly in engineering, it is used, for instance, to successfully test equipment, algorithms, and techniques, and, to some extent and whenever applicable, to avoid or minimize time-consuming, costly, and inexhaustible field trials. Wireless communications are no exception and in this challenging, lively, and unkind area, with systems becoming increasingly more complex, both industry and academy engage themselves in developing simulators. Such simulators for wireless communications almost certainly include a block for the fading channel.

The fading channel can be described by a number of models. Among them, the general models, namely, α-κ-μ, α-η-μ [1], and some particular cases such as κ-μ [2], η-μ [2], and α-μ [3], have been gaining wide acceptance [4–25]. Their flexibility renders them adaptable to situations in which none of the traditional distributions yield good fit [2, 3]. In addition, their applicability has been recognized in practical and real scenarios. Field measurements carried out in diverse propagation environments have shown that, in many situations, these models better accommodate the statistical variations of the propagated signal [1, Section VII], [2, 7–10, 26]. In this sense, developing and ameliorating methods in order to simulate the α-κ-μ and α-η-μ fading models and their special cases for *arbitrary* values of their parameters are of paramount importance. One first step in

such a direction is to generate uncorrelated samples and then, if required, correlate them.

This paper is concerned with the generation of uncorrelated samples of α-κ-μ and α-η-μ fading models for arbitrary values of their parameters. Two largely applied methods in this case are the inversion method and the rejection method. The former involves the knowledge of the inverse of the cumulative distribution function (cdf) of the variate, which is either not always available or cannot be easily implemented, but, on the other hand, is highly efficient. The latter is general and applies to any variate but can be rather inefficient.

A useful method for generating independent κ-μ, η-μ, and α-μ sequences with an arbitrary fading parameter was recently investigated in [27]. The method is reported to achieve an efficiency higher than 80% for η-μ and 87.5% for κ-μ. More interestingly, a transformation was proposed in which, from an α-μ sequence, a new α-μ sequence can be obtained with an almost 100% efficiency.

In this paper, we extend the applicability of the approach in [28] to provide an easy-to-implement and highly efficient algorithm that generates α-κ-μ and α-η-μ uncorrelated sequences for arbitrary values of their parameters. A simple transformation is also proposed, in which, from an α-κ-μ or α-η-μ sequence, a new α-κ-μ or α-η-μ sequence can be obtained with an almost 100% efficiency. To the best of the authors' knowledge, the results reported here are new.

With the aim of quantifying the performance of the random sequence generators, we compare empirical cdfs to hypothesized ones by carrying out goodness-of-fit Kolmogorov-Smirnov (KS) and Anderson-Darling (AD) tests. We also generate a large number of κ-μ random variables, as a particular case of the α-κ-μ generator, and perform the maximum likelihood (ML) estimation of the parameters κ and μ. We then verify these estimates against true values of κ and μ defined in the generator. In this context, we use the maximum likelihood technique as its estimators have notable properties, mainly for large sample size [29]. In fact, under regularity conditions, for large sample size ML estimators are consistent and have normal distribution with variance attaining the Cramér-Rao lower bound (CRLB) [29].

In order to demonstrate the usefulness of the proposed method, we provide theoretical and simulated bit error rates of a coherent binary phase-shift keying (BPSK) modulation over the α-κ-μ and α-η-μ fading channels. We also provide the performance assessment of the spectrum sensing with energy detection over special cases of these channels, namely, the κ-μ and η-μ channels.

The remaining of the paper is organized as follows. Section 2 presents the preliminary proposed algorithm and briefly describes the general distributions that are the focus of this paper. Numerical results, including the goodness-of-fit test, and their interpretations are presented in Section 3. In Section 4 a near-100% efficient and definitive algorithm for generating α-κ-μ and α-η-μ variates is discussed in detail. Section 5 verifies the α-κ-μ generator performance by checking ML parameter estimates from κ-μ random samples against true values of the distribution parameters. In Section 6 the average error probability of the BPSK modulation over the α-κ-μ and α-η-μ channels and the performance of the spectrum sensing over the κ-μ and η-μ channels are presented. Some conclusions are drawn in Section 7.

2. Proposed Algorithm: Preliminary Results

In this section we present a preliminary proposed algorithm. However, in Section 4 the definitive and more efficient algorithm will be presented.

The majorizing hat function $g(\rho)$ used here is given as [30]

$$g(\rho) = ch(\rho) = b\exp\left[-a(\rho-\rho_0)^2\right] \geq f_P^{x\text{-}y\text{-}z}(\rho), \quad (1)$$

where $h(\rho)$ is the majorizing density, a, b, and ρ_0 are coefficients to be obtained for the specific fading model so that $g(\rho)$ can majorize $f_P^{x\text{-}y\text{-}z}(\rho)$ for all ρ, and $f_P^{x\text{-}y\text{-}z}(\rho)$ is the desired probability density function (pdf) given in terms of the normalized envelope ρ, with x-y-z standing for α-κ-μ or α-η-μ. The parameter c is given in an exact form as

$$c = \frac{b}{2}\sqrt{\frac{\pi}{a}}\left[1+\operatorname{erf}\left(\sqrt{a}\rho_0\right)\right], \quad (2)$$

where $\operatorname{erf}(\cdot)$ is the error function. The coefficient ρ_0 is obtained as the solution of $(d/d\rho)f_P^{x\text{-}y\text{-}z}(\rho) = 0$. In all cases, the parameter ρ_0 can be easily found numerically using well-known software tools such as Mathematica or MATLAB. The coefficient b is found as the mode of the pdf; that is, $b = f_P^{x\text{-}y\text{-}z}(\rho_0)$. Finally, the coefficient a is found as

$$a = \min\left\{\frac{1}{(\rho-\rho_0)^2}\ln\frac{f_P^{x\text{-}y\text{-}z}(\rho_0)}{f_P^{x\text{-}y\text{-}z}(\rho)}\right\}. \quad (3)$$

Algorithm 1 summarizes the steps for generating the desired sequences. The probability of acceptance in step 7 is $1/c$. $U(0,1)$ is the uniform distribution over the unit interval $(0,1]$. The rejection method is well known and it is described in detail in [31]. Notice that the function $h(\rho)$ has the form of a truncated-Gaussian density. Random variables with pdf $h(\rho)$ can be generated in a fast and accurate way by truncated-Gaussian random variables generation methods (e.g., [32]).

2.1. The α-κ-μ Distribution. For a fading signal with envelope R and normalized envelope $P = R/\sqrt[\alpha]{\mathbb{E}(R^\alpha)}$, the normalized α-κ-μ envelope pdf is given as [1]

$$f_P^{\alpha\text{-}\kappa\text{-}\mu}(\rho) = \frac{\alpha\kappa^{(1-\mu)/2}(1+\kappa)^{(1+\mu)/2}\mu\rho^{(\alpha(1+\mu)/2)-1}}{\exp\left[\mu\left(\kappa+\rho^\alpha+\kappa\rho^\alpha\right)\right]} \times I_{\mu-1}\left(2\sqrt{\kappa(1+\kappa)}\mu\rho^{\alpha/2}\right), \quad (4)$$

where $\alpha > 0$ is a parameter describing the nonlinearity of the propagation medium, $\kappa > 0$ is the ratio between the total power of the dominant components and the total power of the scattered waves, $\mu > 0$ is related to the number of multipath waves, and $I_\nu(\cdot)$ is the modified Bessel function of first kind and order ν [33].

(1) Define the distribution parameters
(2) Find ρ_0, solving $(d/d\rho) f_P^{x\text{-}y\text{-}z}(\rho) = 0$
(3) Find $b = f_P^{x\text{-}y\text{-}z}(\rho_0)$
(4) Find $a = \min\left\{\left(1/(\rho-\rho_0)^2\right)\ln\left(f_P^{x\text{-}y\text{-}z}(\rho_0)/f_P^{x\text{-}y\text{-}z}(\rho)\right)\right\}$, with $0 \le \rho < \infty$
(5) Generate Y from the distribution with density function $h(\rho) = b\exp\left[-a(\rho-\rho_0)^2\right]/c$
(6) Generate U from a $U(0,1)$ distribution
(7) **if** $U \le f_P^{x\text{-}y\text{-}z}(Y)/ch(Y)$ **then**
(8) $P = Y$ as the desired sample
(9) **else**
(10) Return to Step 5
(11) **end if**

Algorithm 1: Preliminary algorithm.

In particular, the first derivative of the α-κ-μ distribution is given by

$$\begin{aligned}
&\frac{df_P^{\alpha\text{-}\kappa\text{-}\mu}(\rho)}{d\rho} \\
&= \frac{1}{2}\alpha^2\sqrt{\kappa(\kappa+1)}\mu^2\kappa^{1/2-\mu/2}(\kappa+1)^{(\mu+1)/2} \\
&\quad\times \rho^{\alpha\mu/2+\alpha-2}\exp\left[\mu\left(-\left(\kappa+(\kappa+1)\rho^\alpha\right)\right)\right] \\
&\quad\times \left[I_{\mu-2}\left(2\sqrt{\rho^\alpha\kappa(\kappa+1)\mu^2}\right) + I_\mu\left(2\sqrt{\rho^\alpha\kappa(\kappa+1)\mu^2}\right)\right. \\
&\qquad + \left(\rho^{-\alpha/2}\left(\alpha\left(\mu-2(\kappa+1)\mu\rho^\alpha+1\right)-2\right)\right. \\
&\qquad \left.\left.\times\ I_{\mu-1}\left(2\sqrt{\rho^\alpha\kappa(\kappa+1)\mu^2}\right)\right)\times\left(\alpha\sqrt{\kappa(\kappa+1)}\mu\right)^{-1}\right].
\end{aligned} \tag{5}$$

2.2. The α-η-μ Distribution. For a fading signal with envelope R and normalized envelope $P = R/\sqrt[\alpha]{\mathbb{E}(R^\alpha)}$, the α-η-μ normalized envelope pdf is given as [1]

$$\begin{aligned}
&f_P^{\alpha\text{-}\eta\text{-}\mu}(\rho) \\
&\quad= \frac{\alpha(\eta-1)^{1/2-\mu}(\eta+1)^{1/2+\mu}\sqrt{\pi}}{\exp\left[(1+\eta)^2\mu\rho^\alpha/2\eta\right]\sqrt{\eta}\Gamma(\mu)} \\
&\qquad\times \mu^{1/2+\mu}\rho^{\alpha(1/2+\mu)-1}I_{\mu-1/2}\left(\frac{\left(\eta^2-1\right)\mu\rho^\alpha}{2\eta}\right),
\end{aligned} \tag{6}$$

where $\eta \ge 0$ is the ratio between the in-phase scattered wave and the quadrature scattered wave and $\Gamma(\cdot)$ is the Euler Gamma function [33].

In particular, the first derivative of the α-η-μ distribution is given by

$$\begin{aligned}
&\frac{df_P^{\alpha\text{-}\eta\text{-}\mu}(\rho)}{d\rho} \\
&= \left(\sqrt{\pi}\alpha^2\left(\eta^2-1\right)\mu^{\mu+3/2}(\eta-1)^{1/2-\mu}(\eta+1)^{\mu+1/2}\right. \\
&\qquad\left.\times\ \rho^{\alpha(\mu+3/2)-2}\exp\left[-\frac{(\eta+1)^2\mu\rho^\alpha}{2\eta}\right]\right)\times\left(4\eta^{3/2}\Gamma(\mu)\right)^{-1} \\
&\quad\times\left[I_{\mu-3/2}\left(\frac{\rho^\alpha\left(\eta^2-1\right)\mu}{2\eta}\right) + I_{\mu+1/2}\left(\frac{\rho^\alpha\left(\eta^2-1\right)\mu}{2\eta}\right)\right. \\
&\qquad + \left(\frac{2\eta(2\alpha\mu+\alpha-2)\rho^{-\alpha}}{\alpha\left(\eta^2-1\right)\mu} - \frac{2(\eta+1)}{\eta-1}\right) \\
&\qquad\left.\times I_{\mu-1/2}\left(\frac{\rho^\alpha\left(\eta^2-1\right)\mu}{2\eta}\right)\right].
\end{aligned} \tag{7}$$

3. Numerical Results

In Figure 1, the empirical pdfs generated by the proposed method using 2^{20} samples are contrasted with the theoretical density for different values of κ, η, μ, and α. In this figure, the solid lines correspond to the theoretical results whereas the symbols correspond to the generated random variates. The excellent agreement between theoretical and simulated results can be noticed.

3.1. Efficiency. The acceptance proportion, or efficiency, is the performance measure of the acceptance-rejection method. It is the ratio between the number of samples accepted by the method and the total number of samples generated from the respective hat function (majorizing function). Figures 2 and 3 depict the efficiency curves for different values of the pdf parameters using the proposed algorithm. Hereafter, the solid lines correspond to the theoretical results whereas the symbols refer to the simulation results.

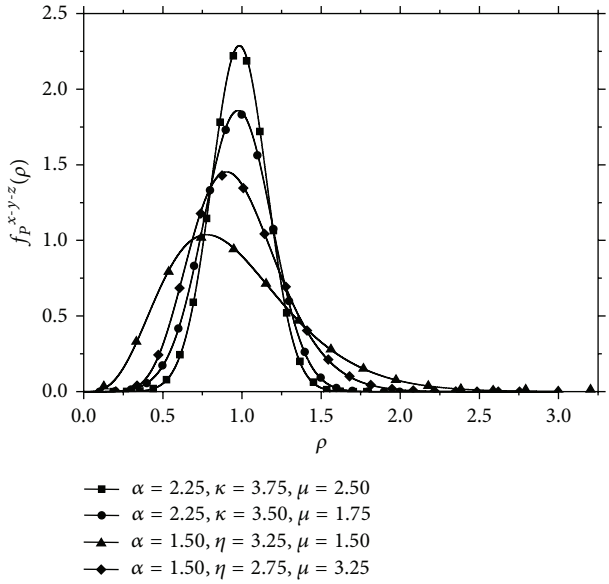

Figure 1: Simulated and theoretical α-κ-μ and α-η-μ densities.

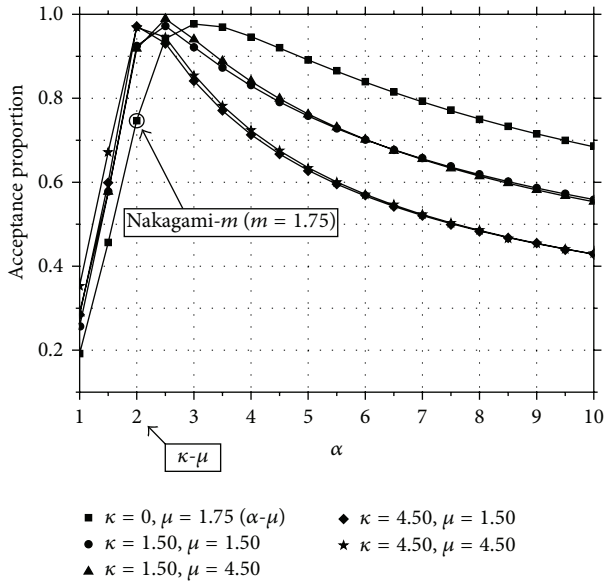

Figure 2: Rejection method efficiency for the α-κ-μ distribution.

The efficiency of the proposed method for the α-κ-μ distribution is shown in Figure 2. Notice that the acceptance proportion decreases with the increasing of the parameter κ. As can be seen, the efficiency is rather small for α below 2 but increases rapidly as α reaches 2. The efficiency increases even further to reach almost 100% for α around 2.2. The well-known Nakagami-m distribution is obtained by setting $\kappa \to 0$ and $\alpha = 2$ in the α-κ-μ distribution in which case $\mu = m$ and the efficiency is around 75%, in agreement with [30].

The efficiency of the proposed method for the α-η-μ distribution is shown in Figure 3. Notice that the acceptance

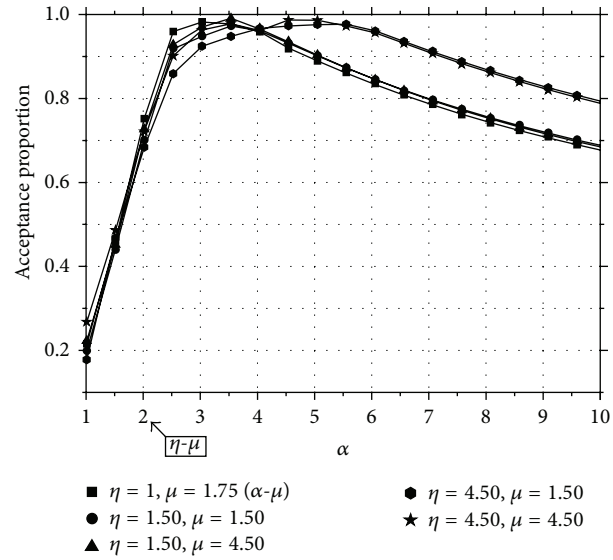

Figure 3: Rejection method efficiency for the α-η-μ distribution.

proportion increases with the increasing of the η parameter for a fixed $\alpha > 4$. The Nakagami-m distribution is obtained by setting $\alpha = 2$, for $\eta \to 1$, in which case $\mu = m/2$, or, equivalently, for $\eta \to 0$, in which case $\mu = m$ in the α-η-μ distribution. In this case, once again, the efficiency stays around 75%, in agreement with [30].

In all the cases, the acceptance ratio does not vary significantly with the variation of μ. In both, Figures 2 and 3, the acceptance proportion decreases with the increase of the fading parameter α. This is a purely mathematical problem, in which we want to find a function (hat function) which is as close as possible to the distribution whose samples are to be generated. As it happens, the variations of the parameters provoke a change in the shape of the curves, which depart from that of the hat function, leading to an increase or a decrease in the efficiency. It is noteworthy that the samples are drawn with arbitrary parameters α, κ, η, and μ. Clearly, the acceptance proportion achieved using the proposed majorizing density is higher than when compared with a traditional uniform majorizing density.

A strikingly interesting result is shown next. Refer to Figure 2 for the efficiency of generating the α-κ-μ random variable. It can be noticed that the efficiency reaches almost 100% for $\alpha \cong 2.2$. For instance, with $\alpha = 2.2$, $\kappa = 3.5$, and $\mu = 4.25$ the efficiency is 99.76%. A similar conclusion can be found for the efficiency of generating the α-η-μ random variable plotted in Figure 3. In this case the efficiency reaches almost 100% for $\alpha \cong 3.5$.

Figure 4 depicts the efficiency curves for the α-κ-μ over different values of κ and μ with fixed $\alpha = 2.2$. Notice that the efficiency starts above 85% ($\kappa = 0$, α-μ case with $\alpha = 2.2$), increases, and decreases but is still above 95% for $\mu > 1$.

Figure 5 plots the efficiency curves for the α-η-μ over different values of η and μ using $\alpha = 3.5$. Notice that the efficiency starts above 95% ($\eta = 1$, α-μ case with $\alpha = 3.5$), increases, and decreases but is still above 92.5% for $\mu > 1$.

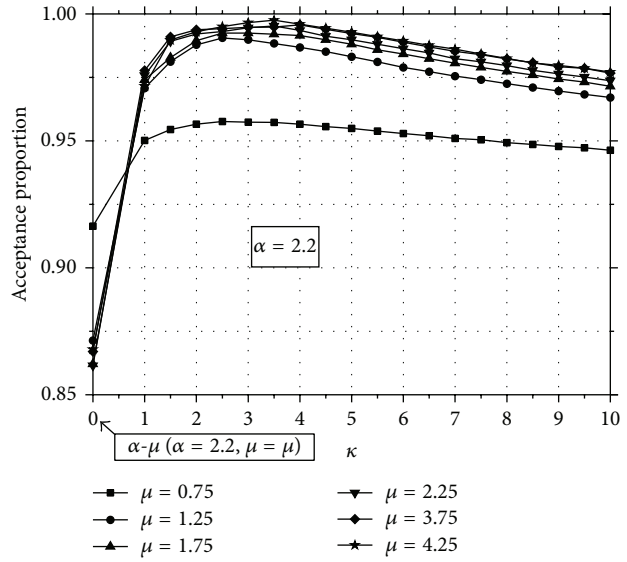

Figure 4: Rejection method efficiency for the α-κ-μ distribution with $\alpha = 2.2$.

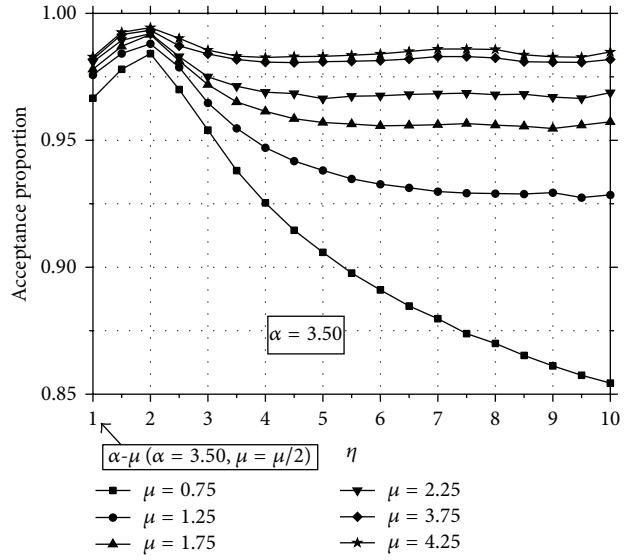

Figure 5: Rejection method efficiency for the α-η-μ distribution with $\alpha = 3.5$.

3.2. Goodness-of-Fit Test. The difference between the theoretical and experimental distributions is minimal as visually perceived in Figure 1. However, in order to objectively quantify the performance of the random sequence generator for the α-κ-μ and α-η-μ fading distributions, the Kolmogorov-Smirnov (KS) test is performed so that the empirical cdf and the hypothesized cdf are compared. As found in the literature (e.g., [29]), the measure of the fit accuracy is given by the P-value. Table 1 reports P-values obtained for the generated sequences with different values of κ, η, μ, and α. In all of the cases, $P > 0.05$, unveiling an excellent goodness-of-fit test result [31].

Table 1: P values of the KS test.

Parameters	P value
$\alpha = 2.25, \kappa = 3.50, \mu = 1.75$	0.8218
$\alpha = 2.25, \kappa = 3.75, \mu = 2.50$	0.6293
$\alpha = 1.50, \eta = 3.25, \mu = 1.50$	0.3654
$\alpha = 1.50, \eta = 2.75, \mu = 3.25$	0.6745

It is well known that the Anderson-Darling test gives more weight to the tails than the KS test. Also, because the Anderson-Darling test is specific for the hypothesized distribution, this test is likely to be more powerful than the traditional KS test [31]. For these reasons, we additionally have performed the Anderson-Darling goodness-of-fit test, with the objective of confirming the adherence of the generated random numbers also in the tails of their probability distributions. In general, critical values of the Anderson-Darling test statistic depend on the specific distribution being tested. We have tested two particular cases of the α-κ-μ and α-η-μ distributions, since for these cases the exact critical values and, consequently, the P value are calculated analytically. The test has been performed for Weibull distribution (α-κ-μ with $\alpha = 3.5, \kappa = 0$, and $\mu = 1$) and for the exponential distribution (α-κ-μ with $\alpha = 1$, $\kappa = 0$, and $\mu = 1$). In the latter case the P value was 0.8352. In the first one the P value was 0.5236. These values reveal the adherence of the generated random numbers also in the tails of their probability distributions.

4. Main Result: A Near-100% Efficient Algorithm for Generating α-κ-μ, α-η-μ Variates, and Their Particular Cases

A modified procedure for a high-efficient and definitive algorithm can be noticed in this section. Let us consider first the α-κ-μ density. From (12) of [3], it is possible to conclude that in the case of the α-κ-μ distribution, for any set (α_1, κ, μ) and (α_2, κ, μ), the following holds: $P^{\alpha_1}_{\alpha_1\text{-}\kappa\text{-}\mu} = P^{\alpha_2}_{\alpha_2\text{-}\kappa\text{-}\mu}$. That is, given an α-κ-μ distribution with parameters (α_1, κ, μ), another α-κ-μ distribution with parameters (α_2, κ, μ), can be obtained by following the given transformation. In particular, knowing that an efficiency of almost 100% is achieved for α-κ-μ samples with $\alpha = 2.2$ (see Figure 4), a transformation of the kind $P^{\alpha}_{\alpha\text{-}\kappa\text{-}\mu} = P^{2.2}_{2.2\text{-}\kappa\text{-}\mu}$ can be used to attain any α-κ-μ samples with this high efficiency.

Considering the α-η-μ distribution, for any set (α_1, η, μ) and (α_2, η, μ), the following holds: $P^{\alpha_1}_{\alpha_1\text{-}\eta\text{-}\mu} = P^{\alpha_2}_{\alpha_2\text{-}\eta\text{-}\mu}$. That is, given an α-η-μ distribution with parameters (α_1, η, μ), another α-η-μ distribution with parameters (α_2, η, μ) can be obtained by following the given transformation. Specifically, knowing that an efficiency of almost 100% is achieved for α-η-μ samples with $\alpha = 3.5$ (see Figure 5), a transformation of the kind $P^{\alpha}_{\alpha\text{-}\eta\text{-}\mu} = P^{3.5}_{3.5\text{-}\eta\text{-}\mu}$ can be used to achieve any α-η-μ samples with this high efficiency. In such cases, the efficiency is kept constant and close to 100%, throughout the variation of the parameters.

Because κ-μ and η-μ are particular cases of the α-κ-μ and α-η-μ distributions (if we set $\alpha = 2$), respectively,

notice that for both, κ-μ and η-μ distributions, the same high efficiency can be attained. In other words, in order to generate κ-μ samples with an almost 100% efficiency, the best choice is to generate α-κ-μ samples with $\alpha = 2.2$ and make the transformation $P^2_{2\text{-}\kappa\text{-}\mu} = P^{2.2}_{2.2\text{-}\kappa\text{-}\mu}$. For the η-μ case, $P^2_{2\text{-}\eta\text{-}\mu} = P^{3.5}_{3.5\text{-}\eta\text{-}\mu}$.

In the same way, one can conclude that the high efficiency can be reached for all the particular cases of α-κ-μ and α-η-μ distributions such as the well-known Nakagami-m, Rayleigh, and Weibull densities. All the particular cases of the α-κ-μ and α-η-μ distributions can be found in [1, Section VI].

The steps for generating the desired sequences using the definitive algorithm are summarized in the Algorithm 2.

5. κ-μ Random Variable Generation and Maximum-Likelihood Parameter Estimation

The generator ability in providing random samples following a given distribution can be alternatively verified by generating a large number of random variables and obtaining maximum likelihood (ML) estimates for the distribution parameters. In this section, as a particular case of the α-κ-μ generator, we generated sample data sets of n independent identically distributed (i.i.d.) κ-μ random variables. Then, for each data set, we applied the ML parameter estimation and verified the estimates against true values of the generator parameters.

5.1. κ-μ Maximum Likelihood Parameter Estimation. Let $\mathbf{P} = [P_1, P_2, \ldots, P_n]$ be n random variables representing normalized envelope observations $P_1 = \rho_1, P_2 = \rho_2, \ldots, P_n = \rho_n$ following a common κ-μ distribution. We assume that this sample data set has a joint probability density function given by $f_{\mathbf{P}}(\rho_1, \rho_2, \ldots, \rho_n; \boldsymbol{\theta})$, where $\boldsymbol{\theta} = [\theta_1, \theta_2] = [\kappa, \mu]$ is the parameter vector to be estimated. The ML estimator $\widehat{\boldsymbol{\Theta}}_{\mathrm{ML}}$ can be determined maximizing the likelihood function $f_{\mathbf{P}}(\rho_1, \rho_2, \ldots, \rho_n; \boldsymbol{\theta})$ as [29]

$$\widehat{\boldsymbol{\Theta}}_{\mathrm{ML}} = \sup_{\boldsymbol{\theta}} f_{\mathbf{P}}\left(\boldsymbol{\rho}; \boldsymbol{\theta}\right). \tag{8}$$

In particular, assuming $P_1, P_2, \ldots, P_n$ as i.i.d. random variables and with [2, Equation (1)], the random samples have a joint pdf given by

$$\begin{aligned} f_{\mathbf{P}}\left(\boldsymbol{\rho}; \boldsymbol{\theta}\right) = {} & \prod_{i=1}^{n} \frac{2\mu(1+\kappa)^{(\mu+1)/2}}{\kappa^{(\mu-1)/2}\exp\left(\kappa\mu\right)} \rho_i^{\mu} \exp\left[-\mu\left(1+\kappa\right)\rho_i^2\right] \\ & \times I_{\mu-1}\left(2\mu\sqrt{\kappa+\kappa^2}\rho_i\right). \end{aligned} \tag{9}$$

Equivalently, we can maximize the log-likelihood function $L(\boldsymbol{\rho}; \boldsymbol{\theta}) = \ln[f_{\mathbf{P}}(\boldsymbol{\rho}; \boldsymbol{\theta})]$, which follows directly from (9) as

$$\begin{aligned} L\left(\boldsymbol{\rho}; \boldsymbol{\theta}\right) = {} & n \ln\left(\frac{2\mu(1+\kappa)^{(\mu+1)/2}}{\kappa^{(\mu-1)/2}\exp\left(\kappa\mu\right)}\right) \\ & + \mu\sum_{i=1}^{n}\ln\left(\rho_i\right) - \mu\left(1+\kappa\right)\sum_{i=1}^{n}\rho_i^2 \\ & + \sum_{i=1}^{n}\ln\left[I_{\mu-1}\left(2\mu\sqrt{\kappa\left(1+\kappa\right)}\rho_i\right)\right], \end{aligned} \tag{10}$$

to write

$$\widehat{\boldsymbol{\Theta}}_{\mathrm{ML}} = \sup_{\boldsymbol{\theta}} L\left(\boldsymbol{\rho}; \boldsymbol{\theta}\right). \tag{11}$$

From (11), one can see that it is necessary to simultaneously solve the following equations:

$$\frac{\partial L\left(\boldsymbol{\rho}; \boldsymbol{\theta}\right)}{\partial \theta_j} = 0, \quad j = 1, 2, \tag{12}$$

in order to obtain $\widehat{\kappa}_{\mathrm{ML}}$ and $\widehat{\mu}_{\mathrm{ML}}$.

Taking the derivative of (10) with respect to κ, after some simplifications we have

$$\begin{aligned} \frac{\partial L\left(\boldsymbol{\rho}; \kappa, \mu\right)}{\partial \kappa} = {} & \frac{n\left(1+\mu\right)}{2\left(1+\kappa\right)} + \frac{n\left(1-\mu\right)}{2\kappa} - n\mu - \mu\sum_{i=1}^{n}\rho_i^2 \\ & + \sum_{i=1}^{n}\frac{\left[I_{\mu-2}\left(y\right) + I_{\mu}\left(y\right)\right]\mu\left(1+2\kappa\right)\rho_i}{2I_{\mu-1}\left(y\right)\sqrt{\kappa+\kappa^2}}, \end{aligned} \tag{13}$$

where $y = 2\mu\sqrt{\kappa(1+\kappa)}\rho_i$. In the same way

$$\begin{aligned} \frac{\partial L\left(\boldsymbol{\rho}; \kappa, \mu\right)}{\partial \mu} = {} & n\left(\frac{1}{\mu} - \kappa\right) + \frac{n}{2}\ln\left(\frac{1+\kappa}{\kappa}\right) + \sum_{i=1}^{n}\ln\left(\rho_i\right) \\ & - \left(1+\kappa\right)\sum_{i=1}^{n}\rho_i^2 + \sum_{i=1}^{n}\frac{1}{I_{\mu-1}\left(y\right)}\frac{\partial I_{\mu-1}\left(y\right)}{\partial \mu}. \end{aligned} \tag{14}$$

Observe that $I_\nu(z)$ in (14) depends on μ with respect to both the order ν and the parameter z. Hence, the derivative with respect to μ in the last term of (14) is the sum of two terms, one only related to z and the other only related to ν. As a result, we have

$$\begin{aligned} \frac{\partial I_{\mu-1}\left(y\right)}{\partial \mu} = {} & \frac{\partial I_{\nu}\left(z\right)}{\partial z}\frac{\partial z}{\partial \mu} + \frac{\partial I_{\nu}\left(z\right)}{\partial \nu}\frac{\partial \nu}{\partial \mu} \\ = {} & \rho_i\sqrt{\kappa\left(1+\kappa\right)}\left[I_{\mu-2}\left(y\right) + I_{\mu}\left(y\right)\right] + I^{(1,0)}_{\mu-1}\left(y\right). \end{aligned} \tag{15}$$

Here $I^{(1,0)}_{\nu}(z)$ is defined as the derivative of $I_\nu(z)$ with respect to the order ν [33, Equation (9.6.42)]; that is

$$\begin{aligned} I^{(1,0)}_{\nu}\left(z\right) = {} & \frac{\partial I_{\nu}\left(z\right)}{\partial \nu} \\ = {} & I_{\nu}\left(z\right)\ln\left(\frac{z}{2}\right) - \left(\frac{z}{2}\right)^{\nu}\sum_{k=0}^{\infty}\frac{\psi_0\left(\nu+k+1\right)}{\Gamma\left(\nu+k+1\right)}\frac{\left(z^2/4\right)^k}{k!}, \end{aligned} \tag{16}$$

(1) Define the distribution parameters
(2) Find ρ_0, solving $(d/d\rho) f_P^{x\text{-}y\text{-}z}(\rho) = 0$
(3) Find $b = f_P^{x\text{-}y\text{-}z}(\rho_0)$
(4) Find $a = \min\left\{\left(1/(\rho-\rho_0)^2\right)\ln\left(f_P^{x\text{-}y\text{-}z}(\rho_0)/f_P^{x\text{-}y\text{-}z}(\rho)\right)\right\}$, with $0 \le \rho < \infty$
(5) Generate Y from the distribution with density function $h(\rho) = b\exp\left[-a(\rho-\rho_0)^2\right]/c$
(6) Generate U from a $U(0,1)$ distribution
(7) **if** $U \le f_P^{x\text{-}y\text{-}z}(Y)/ch(Y)$ **then**
(8) $P = Y$ as the desired sample
(9) **else**
(10) Return to Step 5
(11) **end if**
(12) Make the transformation $P^{\alpha}_{\alpha\text{-}\kappa\text{-}\mu} = P^{2.2}_{2.2\text{-}\kappa\text{-}\mu}$ to obtain α-κ-μ samples or
Make the transformation $P^{\alpha}_{\alpha\text{-}\eta\text{-}\mu} = P^{3.5}_{3.5\text{-}\eta\text{-}\mu}$ to obtain α-η-μ samples

Algorithm 2: Definitive algorithm.

where $\psi_0(\cdot)$ is the Digamma function [33, Equation (6.3.1)]. Fortunately, the function defined in (16) is available for direct usage in current numerical softwares, such as Mathematica, for instance, which makes (16) numerically tractable without additional difficulties.

In general, it is less computationally intensive to evaluate $\widehat{\kappa}_{\mathrm{ML}}$ and $\widehat{\mu}_{\mathrm{ML}}$ iteratively by optimization algorithms, that is, finding $\widehat{\boldsymbol{\Theta}}_{\mathrm{ML}}$ that maximizes $L(\boldsymbol{\rho};\boldsymbol{\theta})$ according to (11). Here we use the iterative optimization algorithm *fmincon*$(\cdot)$, available in the MATLAB software, to estimate the distribution parameters. In this case, we maximize the log-likelihood function applying the algorithm over the negative log-likelihood $-L(\boldsymbol{\rho};\boldsymbol{\theta})$. However, we still make use of (13) and (14) in the estimator variance analysis.

The variance of an estimator is a measurement of its ability to perform reliably as it gives the degree of certainty in which the parameter is being estimated. In this context, the Cramér-Rao lower bound (CRLB) sets a lower limit for the variance of all unbiased estimators for $\boldsymbol{\theta}$ and gives the asymptotic variance for its ML estimator in a large sample size condition [34]. Particularly, we can obtain the CRLB by evaluating the Fisher information matrix $\mathbf{I}_n(\boldsymbol{\theta})$ contained in n random variables $P_1, P_2, \ldots, P_n$ about the parameter $\boldsymbol{\theta}$ as [35]

$$\mathbf{I}_n(\boldsymbol{\theta}) = \mathbb{E}\left[\begin{array}{cc} \left(\dfrac{\partial L(\boldsymbol{\rho};\boldsymbol{\theta})}{\partial\kappa}\right)^2 & \dfrac{\partial L(\boldsymbol{\rho};\boldsymbol{\theta})}{\partial\kappa}\dfrac{\partial L(\boldsymbol{\rho};\boldsymbol{\theta})}{\partial\mu} \\ \dfrac{\partial L(\boldsymbol{\rho};\boldsymbol{\theta})}{\partial\mu}\dfrac{\partial L(\boldsymbol{\rho};\boldsymbol{\theta})}{\partial\kappa} & \left(\dfrac{\partial L(\boldsymbol{\rho};\boldsymbol{\theta})}{\partial\mu}\right)^2 \end{array}\right], \tag{17}$$

where $\mathbb{E}[\cdot]$, meaning the expectation operator, is taken with respect to the random variable P. One can note that $\mathbb{E}[\cdot]$ implies a multiple integration as $L(\boldsymbol{\rho};\boldsymbol{\theta})$ depends on $P_1, P_2, \ldots, P_n$. Fortunately, it has been shown that n i.i.d. random samples, representative of the population $f_{\mathbf{P}}(\rho_1, \rho_2, \ldots, \rho_n;\boldsymbol{\theta})$, have $\mathbf{I}_n(\boldsymbol{\theta}) = n\mathbf{I}(\boldsymbol{\theta})$ [35], where $\mathbf{I}(\boldsymbol{\theta})$ is the Fisher information contained in only one random variable P about $\boldsymbol{\theta}$. In a matrix form we have [35]

$$\mathbf{I}_n(\boldsymbol{\theta}) = n\mathbf{I}(\boldsymbol{\theta}) = n\mathbb{E}\left[\begin{array}{cc} \left(\dfrac{\partial \ln f_P(\rho;\boldsymbol{\theta})}{\partial\kappa}\right)^2 & \dfrac{\partial \ln f_P(\rho;\boldsymbol{\theta})}{\partial\kappa}\dfrac{\partial \ln f_P(\rho;\boldsymbol{\theta})}{\partial\mu} \\ \dfrac{\partial \ln f_P(\rho;\boldsymbol{\theta})}{\partial\mu}\dfrac{\partial \ln f_P(\rho;\boldsymbol{\theta})}{\partial\kappa} & \left(\dfrac{\partial \ln f_P(\rho;\boldsymbol{\theta})}{\partial\mu}\right)^2 \end{array}\right], \tag{18}$$

where the derivatives $\partial \ln f_P(\rho;\boldsymbol{\theta})/\partial\kappa$ and $\partial \ln f_P(\rho;\boldsymbol{\theta})/\partial\mu$ are obtained, respectively, from (13) and (14) by setting $n = 1$. One can readily verify that the derivatives are given by

$$\begin{aligned}\frac{\partial \ln f_P(\rho;\boldsymbol{\theta})}{\partial\kappa} &= \frac{1+\mu}{2(1+\kappa)} + \frac{1-\mu}{2\kappa} - \mu\left(1+\rho^2\right) \\ &\quad + \frac{\left[I_{\mu-2}(y) + I_{\mu}(y)\right]\mu(1+2\kappa)\rho}{2I_{\mu-1}(y)\sqrt{\kappa+\kappa^2}},\end{aligned} \tag{19}$$

$$\begin{aligned}\frac{\partial \ln f_P(\rho;\boldsymbol{\theta})}{\partial\mu} &= \frac{1}{\mu} - \kappa + \ln\left(\sqrt{\frac{1+\kappa}{\kappa}}\rho\right) - (1+\kappa)\rho^2 \\ &\quad + \frac{\rho\sqrt{\kappa(1+\kappa)}\left[I_{\mu-2}(y) + I_{\mu}(y)\right] + I^{(1,0)}_{\mu-1}(y)}{I_{\mu-1}(y)}.\end{aligned} \tag{20}$$

The element $[\mathbf{I}(\boldsymbol{\theta})]_{11}$, for instance, is numerically solved as

$$[\mathbf{I}(\boldsymbol{\theta})]_{11} = \int_0^{\infty}\left(\frac{\partial \ln f_P(\rho;\boldsymbol{\theta})}{\partial\kappa}\right)^2 f_P(\rho;\boldsymbol{\theta})\,\mathrm{d}\rho, \tag{21}$$

where $f_P(\rho;\boldsymbol{\theta})$ is the κ-μ pdf given by [2, Equation (1)]. After numerically evaluating $\mathbf{I}(\boldsymbol{\theta})$, the CRLB or, equivalently, the asymptotic covariance matrix of $\widehat{\boldsymbol{\Theta}}_{\mathrm{ML}}$, based on n i.i.d. observations ρ_i, is given by $(1/n)\mathbf{I}(\boldsymbol{\theta})^{-1}$ [35]. As a consequence, for

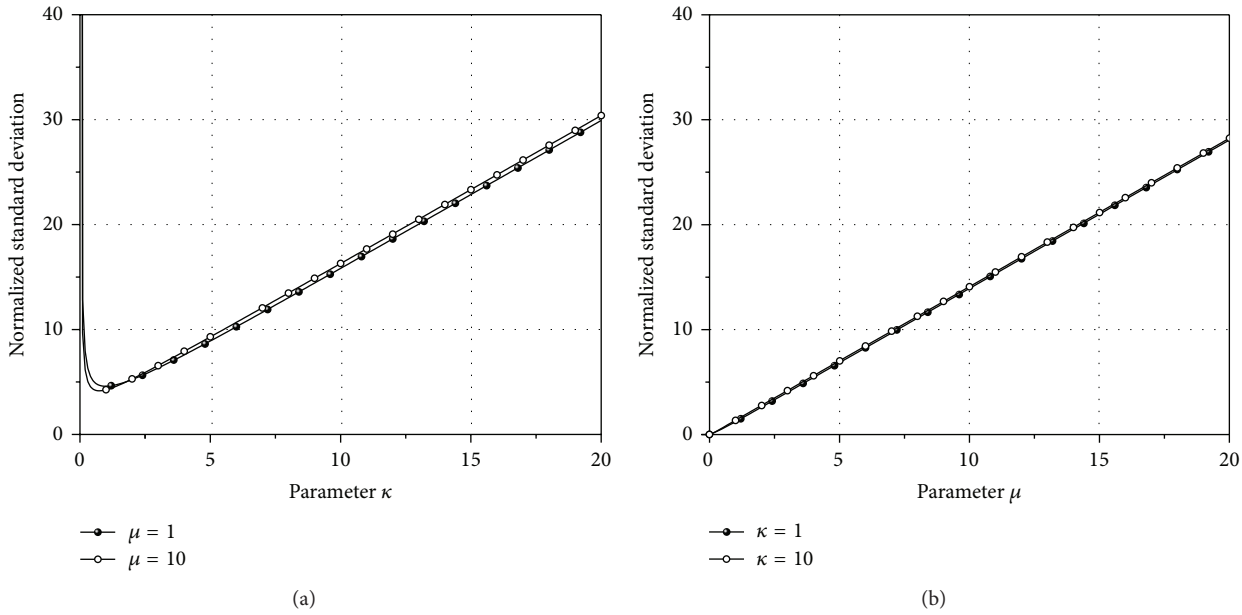

FIGURE 6: Normalized standard deviation curves for the ML estimators of κ and μ. (a) $\sqrt{\text{Var}[\widehat{\kappa}_{\text{ML}}]|_{n=1}}$ as function of κ and for $\mu = \{1, 10\}$. (b) $\sqrt{\text{Var}[\widehat{\mu}_{\text{ML}}]|_{n=1}}$ as function of μ and for $\kappa = \{1, 10\}$.

a large sample size we have $\text{Var}[\widehat{\kappa}_{\text{ML}}] \to (1/n)[\mathbf{I}(\boldsymbol{\theta})^{-1}]_{11}$ and $\text{Var}[\widehat{\mu}_{\text{ML}}] \to (1/n)[\mathbf{I}(\boldsymbol{\theta})^{-1}]_{22}$.

Figure 6 shows the normalized asymptotic variances $\text{Var}[\widehat{\kappa}_{\text{ML}}]|_{n=1}$ and $\text{Var}[\widehat{\mu}_{\text{ML}}]|_{n=1}$, based on the Fisher information contained in only one observation $P = \rho$ about the parameter $\boldsymbol{\theta}$. In particular, Figure 6(a) shows that $\text{Var}[\widehat{\kappa}_{\text{ML}}]|_{n=1}$ has a minimum value about $\kappa = 1$ and does not depend on μ from a practical point of view. Note that this variance increases with the value of κ and tends to infinity when $\kappa \to 0$, denoting large uncertainty in estimating the parameter in a population with $\kappa \approx 0$. Similarly, Figure 6(b) depicts that $\text{Var}[\widehat{\mu}_{\text{ML}}]|_{n=1}$ has no practical dependence with κ and linearly increases with μ.

Also, it has been shown [35] that $\widehat{\boldsymbol{\Theta}}_{\text{ML}}$ has an asymptotic multivariate Gaussian distribution with mean $\boldsymbol{\theta}$ and covariance matrix $(1/n)\mathbf{I}(\boldsymbol{\theta})^{-1}$. Thus, as $n \to \infty$

$$\left(\frac{\widehat{\Theta}_{\text{ML}_i} - \theta_i}{\sqrt{(1/n)\left[\mathbf{I}(\boldsymbol{\theta})^{-1}\right]_{ii}}} \right) \longrightarrow N(0,1), \quad i = 1, 2. \tag{22}$$

Furthermore, it is straightforward to find [36] the confidence interval $(l(\boldsymbol{\rho}), u(\boldsymbol{\rho}))$ for $\widehat{\boldsymbol{\Theta}}_{\text{ML}} = [\widehat{\kappa}_{\text{ML}}, \widehat{\mu}_{\text{ML}}]$, with confidence level of 95%, as

$$\left(\widehat{\Theta}_{\text{ML}_i} - 1.96\sqrt{\left(\frac{1}{n}\right)\left[\mathbf{I}(\boldsymbol{\theta})^{-1}\right]_{ii}}, \right.$$
$$\left. \widehat{\Theta}_{\text{ML}_i} + 1.96\sqrt{\left(\frac{1}{n}\right)\left[\mathbf{I}(\boldsymbol{\theta})^{-1}\right]_{ii}} \right), \quad i = 1, 2. \tag{23}$$

We note that $\mathbf{I}(\boldsymbol{\theta})$ in (23) depends on $\boldsymbol{\theta}$, that is, the true value of the parameter, which is therefore unknown. However, $\widehat{\boldsymbol{\Theta}}_{\text{ML}}$ converges in probability to $\boldsymbol{\theta}$ as $n \to \infty$ [34], which makes it possible to infer that

$$\mathbf{I}\left(\widehat{\boldsymbol{\Theta}}_{\text{ML}}\right) \longrightarrow \mathbf{I}(\boldsymbol{\theta}) \tag{24}$$

as $n \to \infty$. As a result, for large sample sizes we can estimate $\mathbf{I}(\boldsymbol{\theta})$ by $\mathbf{I}(\widehat{\boldsymbol{\Theta}}_{\text{ML}})$ in (23) in order to compute the confidence interval.

5.2. Performance of the κ-μ Random Variable Generator. We use Monte Carlo simulations in order to study the performance of the κ-μ generator. Following the guidelines given in Section II, for each κ in the set $\{0.25, 0.5, 0.75, \ldots, 4.75, 5\}$, $\mu = 1$ and $\alpha = 2$ [1], we generate 500 sequences of $n = 25000$ i.i.d. κ-μ random variables. Similarly, we generate 500 i.i.d. κ-μ sequences of the same length for each μ from the set $\{0.5, 0.75, 1, \ldots, 4.75, 5\}$, $\kappa = 2$ and $\alpha = 2$. In this way we cover a useful range of the parameters κ and μ, found in both indoor and outdoor multipath propagation environments [2, 37].

Taking advantage of notable properties of the ML estimation for large sample sizes, we calculate ML estimates of the parameters κ and μ for each sequence, according to (11), using the already cited algorithm *fmincon*$(\cdot)$, available in the MATLAB software. The starting values of the estimates required by the algorithm are given as the true values of the parameters.

Figure 7 shows the sample mean of $\widehat{\kappa}_{\text{ML}}$, $(1/500)\sum_{i=1}^{500}\widehat{\kappa}_{\text{ML}i}$, against the true value of the parameter. In order to show the estimator variations about its sample mean, we also plotted in Figure 7 a confidence region defined by $\pm 2 \times$ (sample standard deviation of $\widehat{\kappa}_{\text{ML}}$), where the sample standard deviation is given by

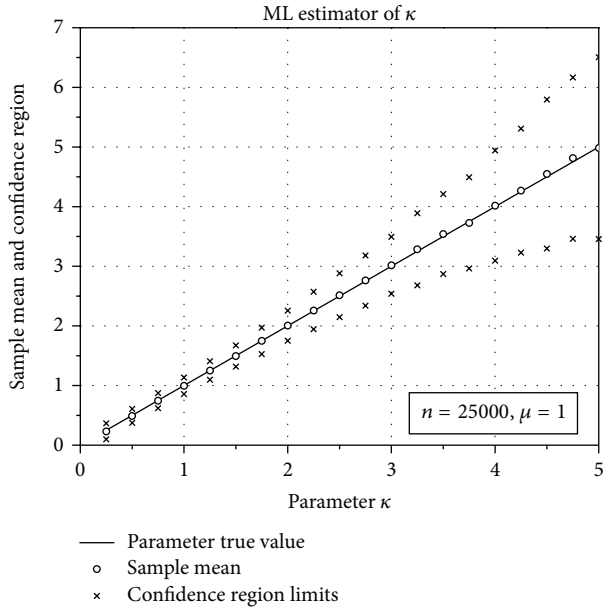

Figure 7: Sample mean and confidence region (±2 × sample standard deviation) of $\widehat{\kappa}_{\mathrm{ML}}$, for $n = 25000$ and $\mu = 1$.

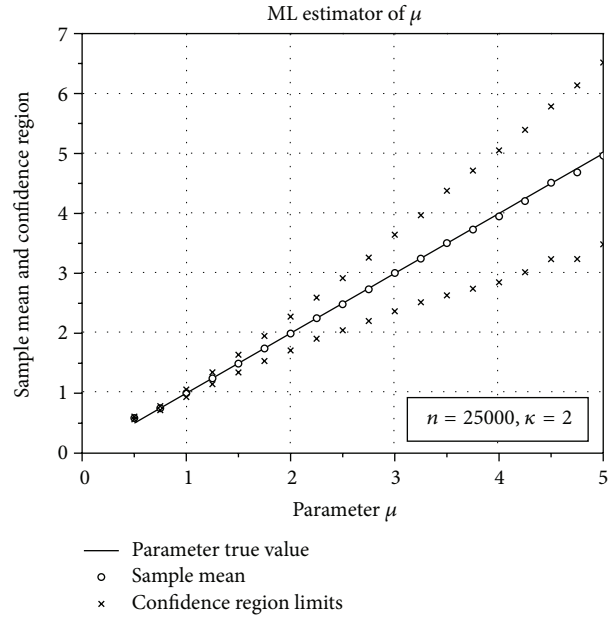

Figure 8: Sample mean and confidence region (±2 × sample standard deviation) of $\widehat{\mu}_{\mathrm{ML}}$, for $n = 25000$ and $\kappa = 2$.

$[(1/500)\sum_{i=1}^{500}\widehat{\kappa}_{\mathrm{ML}i}^2 - ((1/500)\sum_{i=1}^{500}\widehat{\kappa}_{\mathrm{ML}i})^2]^{1/2}$. We verify that, for a large sample size, $\widehat{\kappa}_{\mathrm{ML}}$ is unbiased, from a practical point of view, for the useful range of κ. This is in accordance with the unbiased behavior that the ML estimators have in large sample size conditions [29]. In addition, the confidence region of $\widehat{\kappa}_{\mathrm{ML}}$ becomes broader as κ increases; that is, the variance of $\widehat{\kappa}_{\mathrm{ML}}$ increases with the value of the parameter, as observed from the results in Figure 6(a).

Similar results of the sample mean for $\widehat{\mu}_{\mathrm{ML}}$ against μ are depicted in Figure 8. Likewise, $\widehat{\mu}_{\mathrm{ML}}$ is practically unbiased for the useful range of μ and its variance increases with the value of the parameter, according to the results in Figure 6(b).

The unbiasedness of the ML estimators for large sample sizes, depicted in Figures 7 and 8, reveals the κ-μ generator ability to provide real random samples representative of a population with distribution $f_P(\rho;\kappa,\mu)$. This also alternatively confirms the excellent goodness-of-fit results given by the Kolmogorov-Smirnov and Anderson-Darling tests in Section 3, when applied to the α-κ-μ generator.

6. Applications

In this section we give applications of the proposed random variable generators and use theoretical and simulation results for certifying the accuracy of these generators.

6.1. Average Error Probability of the BPSK Modulation over the α-κ-μ and α-η-μ Fading Channels. Here we analyze the bit error rate (BER) of the BPSK modulation over frequency-flat fading channels modeled by the α-κ-μ and α-η-μ distributions. We assume coherent detection with matched filter or correlator receivers, for which the following vector channel model applies: the decision variable is $y = \rho d + v$, where ρ is the multiplicative fading with $\mathbb{E}[P^2] = 1$, $d = +1$ represents a bit 1, $d = -1$ represents a bit 0, and v is the zero mean, additive white Gaussian noise (AWGN) with variance $N_0/2$.

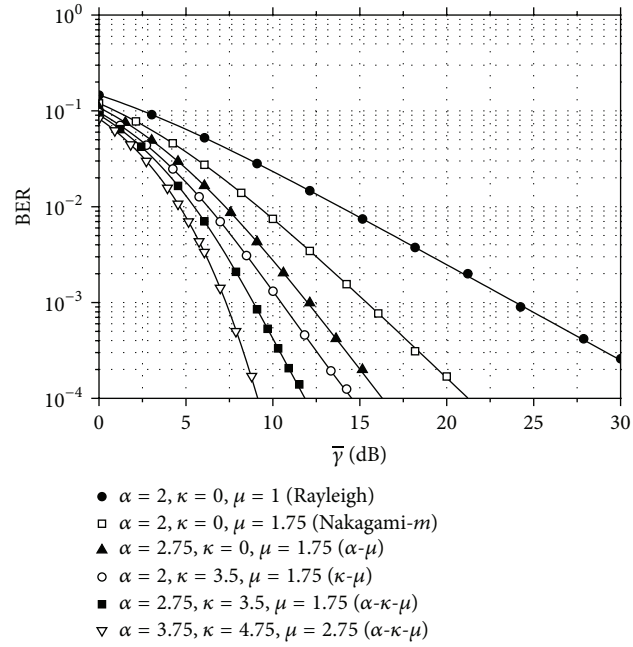

Figure 9: Average error probability for BPSK with α-κ-μ fading.

One possible analytical method employed for determining the performance of a mobile radio communication system is by evaluating the error probability as a function of a fixed signal-to-noise ratio (SNR) and then averaging the result over the probability density function of the SNR variations, which is governed by the particular envelope fading distribution.

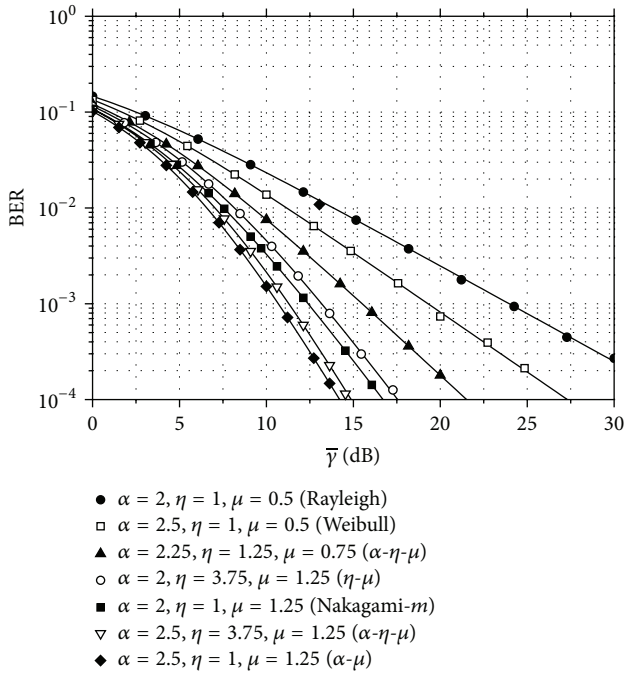

Figure 10: Average error probability for BPSK with α-η-μ fading.

For instance, the bit error probability of the BPSK modulation over the pure AWGN channel as a function of the received SNR γ is given by

$$P_e(\gamma) = \frac{1}{2}\operatorname{erfc}\left(\sqrt{\gamma}\right), \tag{25}$$

where $\gamma = \rho^2 E_b/N_0$ is the SNR for a particular value of the envelope ρ, E_b/N_0 is the ratio between the average energy per bit and the noise power spectral density, and $\operatorname{erfc}(\cdot)$ is the complementary error function.

Now, we must average $P_e(\gamma)$ over the probability density function of γ; that is,

$$P_e = \int_0^\infty P_{\text{BPSK}} f_\Gamma^{x\text{-}y\text{-}z}(\gamma)\, d\gamma, \tag{26}$$

where $f_\Gamma^{x\text{-}y\text{-}z}(\gamma)$ is the pdf of γ for all $\gamma \geq 0$, with x-y-z standing for α-κ-μ or α-η-μ.

Applying a transformation of random variables, from (4) and (6), we have

$$f_\Gamma^{\alpha\text{-}\kappa\text{-}\mu}(\gamma) = \frac{\alpha\kappa^{(1-\mu)/2}(1+\kappa)^{(1+\mu)/2}\mu\left(\sqrt{\gamma/\overline{\gamma}}\right)^{\alpha(1+\mu)/2-1}}{2\sqrt{\gamma\overline{\gamma}}\exp\left[\mu\left(\kappa+\left(\sqrt{\gamma/\overline{\gamma}}\right)^{\alpha}+\kappa\left(\sqrt{\gamma/\overline{\gamma}}\right)^{\alpha}\right)\right]} \times I_{\mu-1}\left(2\sqrt{\kappa(1+\kappa)}\mu\left(\sqrt{\frac{\gamma}{\overline{\gamma}}}\right)^{\alpha/2}\right) \tag{27}$$

$$f_\Gamma^{\alpha\text{-}\eta\text{-}\mu}(\gamma) = \frac{\alpha(\eta-1)^{1/2-\mu}(\eta+1)^{1/2+\mu}\sqrt{\pi}\mu^{1/2+\mu}}{2\sqrt{\gamma\overline{\gamma}}\exp\left[(1+\eta)^2\mu\left(\sqrt{\gamma/\overline{\gamma}}\right)^{\alpha}/2\eta\right]\sqrt{\eta}\Gamma(\mu)} \times\left(\sqrt{\frac{\gamma}{\overline{\gamma}}}\right)^{\alpha(1/2+\mu)-1} I_{\mu-(1/2)}\left(\frac{\left(\eta^2-1\right)\mu\left(\sqrt{\gamma/\overline{\gamma}}\right)^{\alpha}}{2\eta}\right), \tag{28}$$

where $\overline{\gamma} = \mathbb{E}(R^\alpha)E_b/N_0$ is the average SNR when R is α-κ-μ or α-η-μ distributed.

The integral in (26) was evaluated numerically. The average error probabilities curves for the α-κ-μ and α-η-μ fading channels are presented in Figures 9 and 10. In these figures, the theoretical results (solid), from (26), and the simulated results (symbols), from a MATLAB program based on the vector channel model presented above, are plotted for the indicated fading conditions. It is clearly observed that, in spite of the variety of the fading conditions, excellent agreement between the estimated and theoretical results is shown, once more certifying the proposed algorithms for random variable generation. A myriad of different scenarios can be exercised for different values of the fading parameters. We omitted some particular cases (e.g., Rice or Nakagami-q) for the sake of brevity. All the particular cases departing from the general models considered in this paper are in agreement with the particular cases presented in the literature (see, for example, the expressions presented in [38]).

It is worth mentioning that the application just described can be used to check the adherence of the generated random numbers to the tails of their probability distributions as follows. The agreement between theoretical and simulation results in the high E_b/N_0 regime is an evidence of a good adherence in the tail region, since this region governs the performance at high signal-to-noise levels.

6.2. Spectrum Sensing over the η-μ and κ-μ Fading Channels. Modern wireless communication systems are now facing a huge obstacle, spectrum scarcity. New services and applications appear every day, demanding increased bandwidth, new spectrum bands, or both. However, the currently adopted fixed spectrum allocation policy prevents those services and applications to be deployed in adequate pace. Nevertheless, recent studies have demonstrated that, in fact, the radio-frequency spectrum is quite underutilized in some areas and during some time [39]. The cognitive radio (CR) [40] concept then came into scene, aiming at, among other things, opportunistic dynamic spectrum access to idle bands. In this situation, the network which owns the right of using the spectrum is called the primary network, and the cognitive radio network is usually referred to as the secondary network.

To detect the idle bands, also called spectral holes or whitespaces, the CRs must have some sort of *spectrum sensing* capability [41]. Among the spectrum sensing techniques already developed, energy detection is one of the most attractive, since it has low implementation complexity and good detection power. In energy detection, a test statistic

computed from the received signal energy and the noise variance is compared against a threshold so that the decision upon the occupation of the sensed channel is made.

Several studies consider the problem of spectrum sensing with energy detection over the pure AWGN channel, an approach, that is, by far unrealistic since typical wireless communication channels are also subjected to fading. Then, it is of paramount importance to access the performance of a spectrum sensing technique taking into account the channel fading.

There are several fading channel models available in the literature. Among them, two well-accepted models deserve attention due to their ability for accurately modelling several real channel conditions in practice. They are the η-μ [2] and κ-μ [2] fading channel models. Both are special cases of the α-η-μ and α-κ-μ fading models considered in this paper, if $\alpha = 2$ is adopted.

In this section we apply α-η-μ and α-κ-μ random variates, specialized to η-μ and κ-μ variates, to analyze the performance of the energy detection over fading channels.

6.2.1. System Model. The discrete-time model for the hypothesis test associated with the spectrum sensing problem is given by

$$r_i = \begin{cases} z_i : \mathscr{H}_0 \\ hx_i + z_i : \mathscr{H}_1, \end{cases} \tag{29}$$

where $\mathscr{H}_0$ denotes an idle channel state and $\mathscr{H}_1$ denotes a busy channel, r_i is the ith received signal sample collected by the CR, $i = 1, \ldots, n$ during the sensing interval, z_i is the zero mean Gaussian thermal noise sample generated at the receiver input, x_i is the primary transmitted signal sample, and h represents the channel fading envelope, which is assumed to be constant during the sensing interval. From the received signal, the test statistic for the energy detector is computed according to

$$y = \frac{1}{\sigma^2} \sum_{i=1}^{n} r_i^2, \tag{30}$$

where $\sigma^2 = N_0 W$ is the thermal noise variance measured in the bandwidth W, with N_0 being the noise power spectral density. The number of samples n relates with the sensing time T and the bandwidth W through the time-bandwidth product $u = TW$, leading to $n = 2TW$.

The average signal-to-noise ratio (SNR) is defined by $\overline{\gamma} = \mathbb{E}[h^2](E_x/N_0)$, where the primary transmitted signal energy during the sensing interval is $E_x = (1/2W) \sum_{i=1}^{n} x_i^2$ and $\mathbb{E}[h^2]$ is the second moment of the fading envelope. Assuming $\mathbb{E}[h^2] = 1$ without loss of generality and using $N_0 = \sigma^2/W$, the average SNR is simplified to $\overline{\gamma} = (1/2\sigma^2) \sum_{i=1}^{n} x_i^2$. If the primary signal power is $P_x = E_x/T = (1/n) \sum_{i=1}^{n} x_i^2$, the noise variance can be determined from a given SNR by applying

$$\sigma^2 = \frac{nP_x}{2\overline{\gamma}}. \tag{31}$$

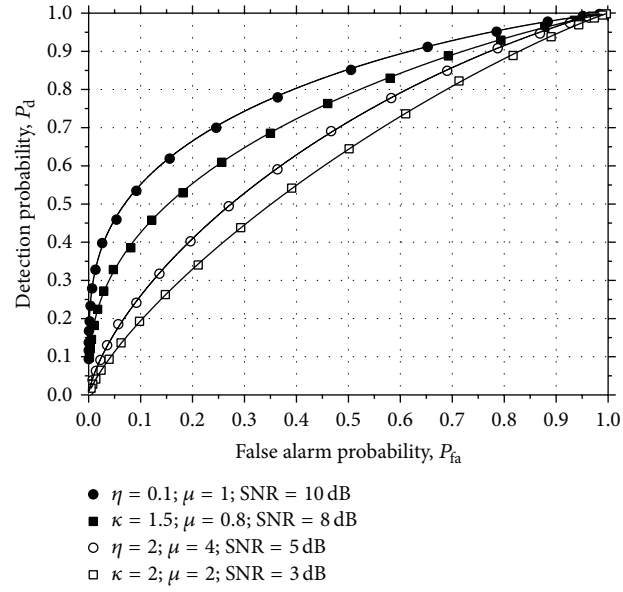

Figure 11: ROC curves for κ-μ and η-μ with different values of κ, η, and μ.

6.2.2. Results. The performance of a spectrum sensing technique is often measured in terms of the probability of detection, P_d, and the probability of false alarm, P_{fa}. When the primary network signal is present in the sensed channel, P_d is the probability of declaring it indeed present. When the primary network signal is absent, P_{fa} is the probability of declaring it present. A large value of P_d translates into a small probability of interference from the secondary in the primary network. A small value of P_{fa} translates into an increased throughput of the secondary network due to a more efficient use of spectral holes. These probabilities are often traded in a receiver operating characteristic (ROC) curve, which shows the values of P_{fa} versus P_d as the decision threshold is varied.

Figure 11 shows analytical (lines) and simulation (symbols) results of the energy detection over the η-μ (α-η-μ with $\alpha = 2$) and κ-μ (α-κ-μ with $\alpha = 2$) fading channels. We have considered $n = 50$ samples ($TW = u = 25$), $\overline{\gamma} = 3$, 5, 8, and 10 dB. The simulation results were obtained from 100,000 Monte Carlo runs. The analytical results were obtained by numerically evaluating (6) and (11) of [42] in the case of η-μ, and by evaluating (3) and (14) of [43] in the case of κ-μ. We have used the Mathematica software package to solve the above equations. The minimum and maximum values of the decision threshold (resp., λ_{min} and λ_{max}) are also reported to facilitate the reproduction of our results. Specifically, for $\eta = 0.1$ and $\mu = 1$, $\lambda_{min} = 31$, and $\lambda_{max} = 100$, for $\kappa = 1.5$ and $\mu = 0.8$, $\lambda_{min} = 30$, and $\lambda_{max} = 85$, for $\eta = 2$ and $\mu = 4$, $\lambda_{min} = 33$, and $\lambda_{max} = 86$, and for $\kappa = 2$ and $\mu = 2$, $\lambda_{min} = 27$, and $\lambda_{max} = 80$.

From Figure 11 the adherence between simulation and analytical results is apparent, validating, again, our random sequence generator.

7. Conclusions

In this paper, sequences of general distributions α-κ-μ and α-η-μ with arbitrary fading parameters were generated using the well-known acceptance-rejection method. Since these densities are general distributions that include a wide range of other distributions, the method is useful for the generation of random numbers of many distinct distributions. The acceptance proportion (more than 95% in some cases) combined with the Kolmogorov-Smirnov and Anderson-Darling tests demonstrate the efficiency and accuracy of the proposed method. The algorithm has been validated by reducing the general case proposed here to special cases already found in the literature. The maximum likelihood parameter estimation was applied to generated κ-μ random samples. The unbiasedness of the κ-μ ML estimators, for large sample size, reveals the generator ability to provide real random samples representative of a population with distribution $f_P(\rho; \kappa, \mu)$. Two applications showed the use of the proposed generators to assess the performance of a digital communication system over the α-κ-μ and α-η-μ fading channels and to assess the performance of the spectrum sensing with energy detection over the κ-μ and η-μ fading channels.

Conflict of Interests

The authors declare that there is no conflict of interests regarding the publication of this paper.

Acknowledgment

This paper was partially supported by the CNPq Postdoctoral Program (501281/2013-4).

References

[1] G. Fraidenraich and M. Yacoub, "The α-η-μ and α-κ-μ fading distributions," in *Proceedings of the 9th IEEE International Symposium on Spread Spectrum Techniques and Applications*, pp. 16–20, August 2006.

[2] M. D. Yacoub, "The κ-μ distribution and the η-μ distribution," *IEEE Antennas and Propagation Magazine*, vol. 49, no. 1, pp. 68–81, 2007.

[3] M. D. Yacoub, "The α-μ distribution: a physical fading model for the Stacy distribution," *IEEE Transactions on Vehicular Technology*, vol. 56, no. 1, pp. 27–34, 2007.

[4] A. Papazafeiropoulos and S. Kotsopoulos, "Second-order statistics for the envelope of α-κ-μ fading channels," *IEEE Communications Letters*, vol. 14, no. 4, pp. 291–293, 2010.

[5] P. C. Sofotasios and S. Freear, "The α-κ-μ/gamma distribution: a generalized non-linear multipath/shadowing fading model," in *Proceedings of the Annual IEEE India Conference: Engineering Sustainable Solutions (INDICON '11)*, pp. 1–6, Hyderabad, India, December 2011.

[6] A. K. Papazafeiropoulos and S. A. Kotsopoulos, "Statistical properties for the envelope and phase of the α-η-μ generalized fading channels," *Wireless Personal Communications*, vol. 66, no. 4, pp. 651–666, 2012.

[7] Q. Wu, D. W. Matolak, and I. Sen, "5-GHz-band vehicle-to-vehicle channels: models for multiple values of channel bandwidth," *IEEE Transactions on Vehicular Technology*, vol. 59, no. 5, pp. 2620–2625, 2010.

[8] P. Karadimas, E. D. Vagenas, and S. A. Kotsopoulos, "On the scatterers' mobility and second order statistics of narrowband fixed outdoor wireless channels," *IEEE Transactions on Wireless Communications*, vol. 9, no. 7, pp. 2119–2124, 2010.

[9] P. K. Chong, S. Yoo, S. H. Kim, and D. Kim, "Wind-blown foliage and human-induced fading in ground-surface narrowband communications at 400 MHz," *IEEE Transactions on Vehicular Technology*, vol. 60, no. 4, pp. 1326–1336, 2011.

[10] A. Michalopoulou, A. A. Alexandridis, K. Peppas et al., "Statistical analysis for on-body spatial diversity communications at 2.45 GHz," *IEEE Transactions on Antennas and Propagation*, vol. 60, no. 8, pp. 4014–4019, 2012.

[11] J. Reig and L. Rubio, "On simple estimators of the α-μ fading distribution," *IEEE Transactions on Communications*, vol. 59, no. 12, pp. 3254–3258, 2011.

[12] Z. Popović, S. R. Panić, J. Anastasov, P. Spalević, and M. Stefanović, "Performance analysis of selection diversity over exponentially correlated α-μ fading environment," *International Journal of Communication Systems*, vol. 24, no. 7, pp. 925–937, 2011.

[13] K. P. Peppas, "A simple, accurate approximation to the sum of gamma-gamma variates and applications in MIMO free-space optical systems," *IEEE Photonics Technology Letters*, vol. 23, no. 13, pp. 839–841, 2011.

[14] P. Cardieri, "Modeling interference in wireless Ad Hoc networks," *IEEE Communications Surveys and Tutorials*, vol. 12, no. 4, pp. 551–572, 2010.

[15] P. C. Spalević, R. S. Panić, and B. Dolicanin, "SSC diversity receiver over correlated α-μ fading channels in the presence of cochannel interference," *EURASIP Journal on Wireless Communications and Networking*, no. 4, pp. 1–7, 2010.

[16] S. R. Panić, M. Č. Stefanović, and A. V. Mosić, "Performance analyses of selection combining diversity receiver over α-μ fading channels in the presence of co-channel interference," *IET Communications*, vol. 3, no. 11, pp. 1769–1777, 2009.

[17] I. B. Djordjevic and G. T. Djordjevic, "On the communication over strong atmospheric turbulence channels by adaptive modulation and coding," *Optics Express*, vol. 17, no. 20, pp. 18250–18262, 2009.

[18] A. M. Magableh and M. M. Matalgah, "Moment generating function of the generalized α-μ distribution with applications," *IEEE Communications Letters*, vol. 13, no. 6, pp. 411–413, 2009.

[19] N. Y. Ermolova and O. Tirkkonen, "Multivariate η-μ fading distribution with constant correlation model," *IEEE Communications Letters*, vol. 16, no. 4, pp. 454–457, 2012.

[20] M. Stefanovic, S. Minic, S. Nikolic et al., "The CCI effect on system performance in κ-μ fading channels," *Technics Technologies Education Management*, vol. 7, no. 1, pp. 88–92, 2012.

[21] K. P. Peppas, "Sum of nonidentical squared κ-μ variates and applications in the performance analysis of diversity receivers," *IEEE Transactions on Vehicular Technology*, vol. 61, no. 1, pp. 413–419, 2012.

[22] S. Atapattu, C. Tellambura, and H. Jiang, "MGF based analysis of area under the ROC curve in energy detection," *IEEE Communications Letters*, vol. 15, no. 12, pp. 1301–1303, 2011.

[23] H. Yu, G. Wei, F. Ji, and X. Zhang, "On the error probability of cross-QAM with MRC reception over generalized η-μ fading

channels," *IEEE Transactions on Vehicular Technology*, vol. 60, no. 6, pp. 2631–2643, 2011.

[24] N. Y. Ermolova and O. Tirkkonen, "The η-μ fading distribution with integer values of η," *IEEE Transactions on Communications*, vol. 10, no. 6, pp. 1976–1982, 2011.

[25] R. Subadar and P. R. Sahu, "Performance of a L-MRC receiver over equally correlated η-μ fading channels," *IEEE Transactions on Wireless Communications*, vol. 10, no. 5, pp. 1351–1355, 2011.

[26] U. S. Dias and M. D. Yacoub, "On the α-μ autocorrelation and power spectrum functions: Field trials and validation," in *Proceedings of the IEEE Global Telecommunications Conference (GLOBECOM '09)*, pp. 1–6, December 2009.

[27] R. Cogliatti, R. A. A. de Souza, and M. D. Yacoub, "Practical, highly efficient algorithm for generating κ-μ and η-μ variates and a near-100% efficient algorithm for generating α-μ variates," *IEEE Communications Letters*, vol. 16, no. 11, pp. 1768–1771, 2012.

[28] R. Cogliatti and R. A. A. de Souza, "A near-100% efficient algorithm for generating α-κ-μ and α-η-μ variates," in *Proceedings of the IEEE 78th Vehicular Technology Conference (VTC '13)*, Las Vegas, Nev, USA, 2013.

[29] A. Papoulis and S. Pillai, *Probability, Random Variables, and Stochastic Processes*, McGraw-Hill, New York, NY, USA, 4th edition, 2002.

[30] Q. M. Zhu, X. Y. Dang, D. Z. Xu, and X. M. Chen, "Highly efficient rejection method for generating Nakagami-*m* sequences," *Electronics Letters*, vol. 47, no. 19, pp. 1100–1101, 2011.

[31] J. E. Gentle, *Random Number Generation and Monte Carlo Methods*, Springer, New York, NY. USA, 2nd edition, 1998.

[32] C. P. Robert, "Simulation of truncated normal variables," *Statistics and Computing*, vol. 5, no. 2, pp. 121–125, 1995.

[33] M. Abramowitz and I. A. Stegun, *Handbook of Mathematical Functions with Formulas, Graphs, and Mathematical Tables*, Dover, New York, NY, USA, 1972.

[34] H. Cramér, *Mathematical Methods of Statistics*, Princeton University Press, Princeton, NJ, USA, 1999.

[35] E. L. Lehmann and G. Casella, *Theory of Point Estimation*, Springer Texts in Statistics, Springer, New York, NY, USA, 2nd edition, 1998.

[36] A. Leon-Garcia, *Probability, Statistics, and Random Processes for Electrical Engineering*, Prentice Hall, Upper Saddle River, NJ, USA, 3rd edition, 2007.

[37] S. L. Cotton, W. G. Scanion, and J. Guy, "The κ-μ distribution applied to the analysis of fading in body to body communication channels for fire and rescue personnel," *IEEE Antennas and Wireless Propagation Letters*, vol. 7, pp. 66–69, 2008.

[38] M. K. Simon and M.-S. Alouini, *Digital Communication over Fading Channels*, John Wiley & Sons, New York, NY, USA, 2005.

[39] R. Engelman, "Report of the spectrum efficiency working group," Tech. Rep., Federal Communication Commission, 2002.

[40] J. Mitola III and G. Q. Maguire Jr., "Cognitive radio: making software radios more personal," *IEEE Personal Communications*, vol. 6, no. 4, pp. 13–18, 1999.

[41] I. F. Akyildiz, B. F. Lo, and R. Balakrishnan, "Cooperative spectrum sensing in cognitive radio networks: a survey," *Physical Communication*, vol. 4, no. 1, pp. 40–62, 2011.

[42] S. Atapattu, C. Tellambura, and H. Jiang, "Energy detection of primary signals over η-μ fading channels," in *Proceedings of the 4th International Conference on Industrial and Information Systems (ICIIS '09)*, pp. 118–122, December 2009.

[43] P. Sofotasios, E. Rebeiz, L. Zhang, T. Tsiftsis, D. Cabric, and S. Freear, "Energy detection based spectrum sensing over κ-μ and κ-μ extreme fading channels," *IEEE Transactions on Vehicular Technology*, vol. 62, no. 3, pp. 1031–1040, 2013.

Hindawi Publishing Corporation
International Journal of Antennas and Propagation
Volume 2015, Article ID 372124, 21 pages
http://dx.doi.org/10.1155/2015/372124

Research Article

Modeling of the Land Mobile Satellite Channel considering the Terminal's Driving Direction

Marie Rieche,[1] Alexander Ihlow,[1] Daniel Arndt,[1] Fernando Pérez-Fontán,[2] and Giovanni Del Galdo[1]

[1] *Institute for Information Technology, Technische Universität Ilmenau, Helmholtzplatz 2, 98693 Ilmenau, Germany*
[2] *Telecommunication Engineering School, University of Vigo, 36310 Vigo, Spain*

Correspondence should be addressed to Marie Rieche; marie.rieche@tu-ilmenau.de

Received 9 May 2014; Revised 4 August 2014; Accepted 5 August 2014

Academic Editor: Jose F. Paris

Copyright © 2015 Marie Rieche et al. This is an open access article distributed under the Creative Commons Attribution License, which permits unrestricted use, distribution, and reproduction in any medium, provided the original work is properly cited.

A precise characterization of the Land Mobile Satellite (LMS) channel, that is, the channel between a satellite and a mobile terminal, is of crucial importance while designing a satellite-based communication system. State-of-the-art statistical LMS channel models offer the advantage of requiring only a few input parameters, which include the environment type and the elevation angle of the satellite. However, the azimuth angle relative to the driving direction of the mobile terminal is usually ignored, as its proper modeling requires either an extensive measurement campaign or a significant effort from the user, as a precise geometrical description of the scenario is required. In this contribution we show that the impact of the driving direction on the channel statistics is not negligible and requires to be modeled explicitly. Moreover, we propose a statistical LMS channel model whose parameters are obtained via an image-based state estimation method. The image-based method is verified by a comparison with measured radio frequency signal levels. The proposed method allows obtaining a complete statistical description of the channel for arbitrary elevation and azimuth angles.

1. Introduction

Satellite communication services need to ensure a certain quality of the received signal. For stationary applications, this is a relatively undemanding task, as it is normally possible to provide a nearly ideal Line-of-Sight (LoS) connection. However, this is not the case for moving terminals. In order to design appropriate systems for this specific application, a profound knowledge of the propagation channel, the so-called land mobile satellite (LMS) channel, becomes necessary.

The LMS channel is mainly impaired by the environment in the direct vicinity of the moving terminal. In fact, the LoS component may be completely obstructed by solid objects (e.g., a building) or may be more or less shadowed by vegetation depending on the density of the foliage and branches. Moreover, diffraction, reflection, and scattering of the transmitted signal generate multipath components.

Looking at the received signal level over traveled distance, as in Figure 1, it is possible to distinguish different effects: the LoS component (which might be blocked or not) gives rise to "very slow fading", while in a partially obstructed condition, it gives rise to "slow fading", for example, due to the vegetation. Furthermore, the multipath propagation introduces "fast fading", which is superimposed to slow and very slow fading. Besides the impact on the signal level described above, the channel also causes temporal dispersion (induced by the different lengths of the propagation paths) and the Doppler shifts, as terminal, satellite, and possibly some objects in the environment are moving.

The LMS channel can be modeled with different approaches, where statistical channel models are frequently used and are able to generate time-series of the received fading signal [1–3]. Their main advantage, compared to other approaches, is that they do not require many input parameters and offer the possibility to generate a large quantity of different channels. These models usually feature two different input parameters: the environment type (e.g., urban, suburban) and the elevation angle of the satellite.

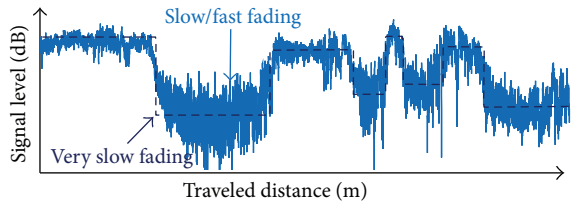

Figure 1: The received satellite signal is characterized by a superposition of very slow, slow, and fast fading effects.

Normally, they do not consider the driving direction of the mobile terminal, that is, the azimuth angle of the satellite. Ignoring the driving direction in the model results in a time-series of the signal fading, which is stationary with respect to the driving direction. This is intuitively an oversimplification for urban scenarios, where a satellite oriented in driving direction leads to a higher signal quality compared to a satellite perpendicular to the driving direction. This is exemplified in Figure 2.

Traditionally, the internal model parameters are derived from statistical distributions, whose parametrization is based on Radio Frequency (RF) measurements. The measurement data utilized by the statistical LMS models, available in the literature, is gathered either from one or more satellites at specific azimuth positions or from a helicopter emulating the satellite. If measurements are carried out for several satellites at different azimuth positions, the average over the available satellite positions in azimuth is calculated. Consequently, the extracted model parameters reflect the flight/satellite conditions and the angle between the radio path and the mobile but do not explicitly consider it. To develop an LMS model which explicitly considers the driving direction, it is necessary to collect enough RF measurements to carry out a statistical analysis in dependence of the relative azimuth angle. For instance, by dividing the full circle (360°) into intervals of 10° each, one needs 36 times the measurement data to achieve an equivalent statistical significance.

In this contribution we extend the statistical LMS model for S-Band proposed by Arndt et al. [5]. We consider the driving direction with a resolution of 1° over the whole azimuthal range of 360°. To solve the challenging task of gathering the necessary large amount of RF measurement data, we follow an alternative image-based approach [23], which allows us to extract the very slow fading of the received signal for arbitrary positions of the satellite, even for those which are not yet in orbit. The method enables the derivation of accurate parameters for different elevations and especially different driving directions with an angular resolution of 1°. Based on the high azimuthal resolution we found that the left-right symmetry assumed in [5] is an oversimplification, because the vehicle travels on one side of the street. We show the significant impact of considering the azimuthal satellite position relative to the driving direction, in contrast to neglecting the azimuthal position, on the quality of the received signal in terms of first order statistics.

The remainder of this contribution is organized as follows: Section 2 gives an overview of state-of-the-art LMS channel models and closer analyzes those, feasible to reflect the effects of the driving direction. Section 3 illustrates the image-based state estimation method, which allows the extraction of the very slow fading, Furthermore, the accuracy of this method is shown by comparing with simultaneously recorded RF signal levels. Section 4 introduces the main components of the LMS model. Section 5 presents the impact of the driving direction on the statistics of the satellite signal. Finally, Section 6 summarizes the main results of the contribution.

2. Modeling Approaches of the Land Mobile Satellite Channel

This section concisely reviews different principles of LMS channel modeling and explains the most common LMS channel models.

It is convenient to distinguish between four basic principles [24].

(i) *Empirical channel models* describe the signal attenuation by fitting mathematical expressions to measurements, without including any physical interpretation. An overview of different empirical LMS channel models can be found in [25].

(ii) *Deterministic channel models* describe the propagation effects for specific environments, while approximating Maxwell's equations. Most of them are based on assumptions of a propagating electromagnetic wave and are so-called ray-based. Ray-tracing approaches applied to the LMS channel are described in [26].

(iii) *Statistical channel models* describe the channel in terms of statistical distributions, which may or may not have physical meaning. The parameters of these models are extracted from a representative number of measurements.

(iv) *Hybrid channel models* are a combination of the approaches mentioned above. In the literature, a large variety of these models can be found, making them difficult to categorize. When deterministic and physical channel models are combined, they are so-called physical-statistical models. A synthetic propagation environment is generated by considering deterministic/physical techniques, whereas statistical distributions are utilized for a description of the environment or the signal propagation.

Furthermore, we can identify more categories of available LMS channel models depending on other features.

(i) One feature for categorizing LMS channel models is the *number of reception states* supported. The received satellite signal can no longer be assumed stationary for a longer time period. Different reception states are introduced to represent the block-wise stationarity of the received signal, which is caused by the slow varying environmental conditions (like LoS or NLoS due to, e.g., buildings, trees), while the terminal moves.

(a) Line-of-sight (LoS) (b) Non-line-of-sight (NLoS)

Figure 2: The mobile user can be situated in different receiving states, which depend on the surrounding objects and the azimuthal angle relative to the driving direction.

Single-state LMS channel models are those which only consider the slow and fast fading of the received satellite signal. Over a short time period these two components (slow and fast fading) are modeled by a stationary stochastic processes, for example, Loo [27–29]. Multistate LMS channel models differentiate two states ("good" and "bad") [30], three states ("line-of-sight," "shadowed," and "blocked") [31] or higher (variable) number of states [32]. The sequence of reception states can either be generated by a Markov process or by physical/geometrical considerations of the environment (see Section 2.2).

(ii) Besides the number of states we can also distinguish between LMS channel models for different *number of satellites*. In the literature, several single-satellite models can be found [1, 2, 5, 30]. Available multisatellite models usually consider dual-satellite systems [3, 4, 6]. Lutz [3] already emphasizes the impact of the correlation between two satellite links, as it provides information about the visibility of satellites and the diversity gain. Propagation models which consider more than two satellites (e.g., [7, 33]) are rather rare in the literature, due to the more complex description of the satellites correlations.

In the following we deal more in detail with the purely statistical and the physical-statistical approaches, as they provide the possibility to include the driving direction and offer less complexity, compared to purely deterministic models.

2.1. Statistical Land Mobile Satellite Channel Models. State-of-the-art purely statistical models [2], which produce time-series of the envelope of the received signal, derive their parameters from RF measurements. They implicitly include the driving direction without evaluating it adequately. If the driving direction was considered explicitly in the channel modeling, the resulting statistics were more realistic for specific situations, as shown in Section 5. Therefore, it would be necessary to collect a sufficient amount of RF data to carry out a statistical analysis in dependence of the relative azimuth angle. In [1] the measurement data was conducted for relative azimuth angles of approximately 0°, 45°, and 90°. Arndt et al. [5] utilize measurement data for different environments, elevation angles, and driving directions. The model consists of a state sequence generator implemented as semi-Markov chains and a Loo-generator simulating slow and fast fading effects within each state. The model parameters are derived from extensive measurements of RF signal levels in S-Band for different environments, elevation angles, and driving directions. The intervals of driving directions with respect to the satellite are $0^\circ \cdots 10^\circ$, $10^\circ \cdots 30^\circ$, $30^\circ \cdots 60^\circ$, and $60^\circ \cdots 90^\circ$. This model assumes a symmetry of 90° for the different driving directions and clusters the data accordingly, which is an oversimplification, as we show in Section 5.

2.2. Physical-Statistical Land Mobile Satellite Channel Models. There are several hybrid LMS channel models available, which consider the driving direction by different geometry-based approaches. The "virtual city" approach represents a special case for the urban environment. Building heights, street widths building block lengths, and so forth are modeled following a statistical distribution. The output of these models are multiple state sequences, which allow to calculate the correlation factors between different satellite links of azimuth and elevation. One of the first physical-statistical LMS models is introduced by Tzaras et al. [8]. The basis is a physical approach based on synthetic environments, where the heights of obstacles follow certain distributions (or are assumed to be constant). The mobile terminal can also be shifted away from the middle of the street. The result is presented in terms of an analytic expression based on diffraction theory, depending only on the azimuth angle separation.

Oestges et al. [9] develop a prediction of the statistical fade distribution based on a conditional Rice distribution. The parameters of the Rician distribution vary with the

physical parameters and depend on the satellite position (elevation and azimuth) and on the environment (building height and street width). The relationship between the Rice parameters and the physical parameters are validated by ray-tracing, based on the Uniform Theory of Diffraction (UTD). Building height and street width are assumed to be log-normally distributed, based on measurements in London and Guildford. The results are shown for an azimuth angle of 90° relative to the street axis and the vehicle was positioned in the middle of the street. Based on this model, the shadowing correlation coefficient for a dual-satellite system as a function of the azimuth separation is presented in [10]. The correlation model is based on the Rician dominant component of the physical-statistical model explained in [9]. Here, the vehicle is positioned at one side of the road, which shows the effect of the right-hand side and left-hand side driving, respectively. In [11], again the same geometry-based approach is used to model time-series, combined with a series of roadside buildings according to measured distributions of geometrical parameters such as building height, street width, and height of the nearest building. This model considers the position of the car to be in the middle of the street.

There are several models based on a street mask concept, mask angle (MKA) or mask function (MKF), respectively [12–16]. These graphical representations of the azimuth and elevation angle indicate the visibility of satellites from the mobile terminal's point of view for different urban scenarios (e.g., street canyons, street crossings). The input parameters are building height, terminal height, and street width, whereby the user is assumed to be in the middle of the street, therefore the correlation between two satellite links is symmetric. To generate the building heights and street widths statistical distributions are used.

A hybrid statistic-deterministic model [17] is based on a Markov chain, considering elevation and street orientation angles (assuming symmetry of 90°). The visibility of the satellite is also described by the MKA, when the terminal is located in the middle of the street. The resulting "on/off" time-series is enhanced by multipath and diffraction effects based on a simple ray-tracing model (statistical distributions for building height and width are used).

A methodology, which uses also fisheye images to derive the state information (clear, shadowed, and blocked) and adding different distributions (i.e., Loo, Rayleigh, and Rice) to simulate the fast fading effects, can be found in [19–21, 34]. Meenan et al. [18] also use fisheye images and apply the approach to the correlated four-state Lutz model [3]. However, none of these models explicitly takes into account the dependency on azimuth angle relative to the street orientation.

Table 1 gives an overview of the statistical and physical-statistical models, which are concisely reviewed in this section. These models are frequently used in the literature and differ in their assumptions, constraints, and outputs. Therefore, the models are compared with respect to their modeling technique, the number of satellites, if they consider the driving direction of the terminal, as well as the correlation coefficient (corr). Further evaluation criteria are the cumulative distribution function (CDF) and the *bad* state probability p_b of a satellite.

In summary, state-of-the-art LMS channel models are either uncapable of describing the influence of the azimuth angle of the satellite due to the lack of data, or they necessitate significant effort from the user, as a precise description of the geometry of the environment is required.

3. State Parameter Extraction

As mentioned in the introduction, to carry out a statistical analysis for different driving directions it is necessary to collect an unfeasible amount of measurement data. To solve this problem, we rely on the image-based method described in [35], which is reviewed in the next Section 3.1. This method is capable of estimating the very slow fading conditions of the LMS channel for an arbitrary position of the satellite using hemispheric images of the environment surrounding the mobile terminal. The very slow fading is modeled with a sequence of the reception states *good* and *bad*, corresponding to line-of-sight (LoS) and nonline-of-sight (NLoS), respectively [2]. Section 3.2 presents the measurement campaign realized to collect the necessary images for the model proposed here. Finally, Section 3.3 addresses the validation of the image-based method by comparing its estimates with actual RF measurements.

3.1. Image-Based State Estimation Method. In the following, we review the image-based method from which we derive the LMS channel reception states [35]. Hemispheric images of the environment are obtained from a fisheye camera pointing towards the sky. Such an image of the upper hemisphere is depicted in Figure 3(a). The image is classified in the region *sky*, where the satellite is visible and the region *obstruction*, where it is shadowed. The result is shown in Figure 3(b) as an overlay of the binary classification result and the original image. Finally, the classified fisheye image is converted into a rectangular image in landscape panoramic form yielding a resolution of one degree in elevation and azimuth (see Figure 3(c)). Knowing the time, location, and heading information of the vehicle we can determine the position of arbitrary satellites within the image given their azimuth and elevation with respect to a known coordinate system. From the position of the satellite within the panoramic image we can directly extract the reception state, where *sky* represents the *good* state and *obstruction* represents the *bad* state, respectively. Based on the extracted state sequence we can determine different state parameters, representing an essential part of the LMS channel model parameters, as explained in detail in Section 4.

3.2. Measurement Data Acquisition. To validate the proposed method we consider extensive measurements conducted in the context of the project Mobile satellite channeL with Angle DiversitY (MiLADY) [36]. During this campaign the received power levels of two geostationary (GEO) satellites of XM Satellite Radio and two of three highly elliptical orbit (HEO)

Table 1: Statistical and physical-statistical LMS channel models are compared with respect to the modeling approach, the number of satellites, considering the driving direction of the terminal, considering the correlation coefficient (Corr) and regarding the evaluation criteria cumulative distribution function (CDF) and the bad state probability of a satellite p_b.

Modeling approach	Proposed by	Year	Number of satellites	Driving direction considered	p_b	Corr	CDF
Statistical	Pérez-Fontán et al. [1]	2001	Single				x
	Prieto-Cerdeira et al. [2]	2010	Single				x
	Lutz [3]	1996	Dual		x	x	
	Arndt et al. [4]	2012	Dual	x			
	Arndt et al. [5]	2012	Single	x	x		x
	Arndt et al. [6]	2012	Dual	x	x	x	
	Arndt et al. [7]	2012	Multi			x	
Physical-statistical	Tzaras et al. [8]	1998	Dual			x	
Ray-tracing	Oestges et al. [9]	1999	Single				x
	Oestges and Vanhoenacker-Janvier [10]	2001	Dual			x	
	Oestges and Vanhoenacker-Janvier [11]	2007	Dual			x	x
MKA	Vázquez-Castro et al. [12]	2001	Dual			x	
	Vázquez-Castro et al. [13]	2002	Dual			x	
	Pérez-Fontán et al. [14]	2002	Multi			x	
	Pérez-Fontán et al. [15]	2002	Multi		x		
	Pérez-Fontán et al. [16]	2003	Multi		x		
Virtual city	Pérez-Fontán et al. [17]	2005	Single	x			
Fisheye	Meenan et al. [18]	1998	Dual			x	
	Akturan et al. [19–21]	1997	Single				x
	Rieche et al. [22]	2014	Single	x			x

(a) Exemplary hemispheric image

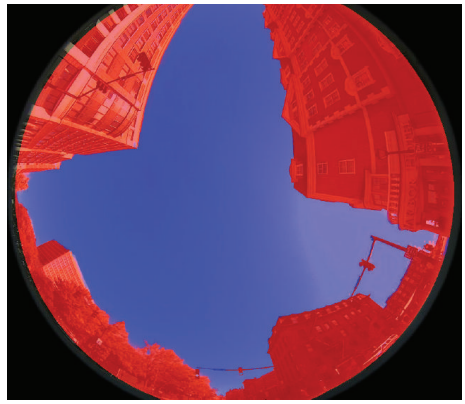

(b) Overlay of the original and the binary classification into *sky* (blue) and *obstruction* (red)

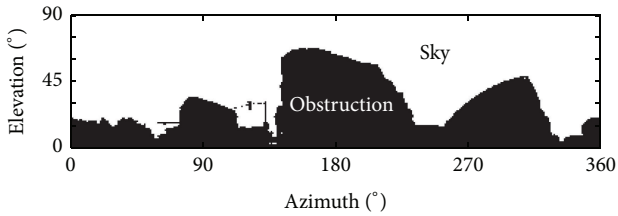

(c) The converted panoramic binary images are of size 90 × 360 pixels, where the resolution is one degree in elevation and in azimuth. White represents the reception state *good* and black *bad*, respectively

Figure 3: The images show the original hemispheric image, the result of the image classification, and the converted panoramic binary image, where the reception state *good* and *bad* is categorized.

Table 2: Semi-Markov parameters (*good* and *bad* state) for *urban* environment for variable driving directions and elevations.

Elevation	Front	Front-right	Right	Back-right	Back	Back-left	Left	Front-left
				Log-normal mean $\mu_{\text{dur,bad}}$				
85	1.28	1.28	1.29	1.33	1.29	1.25	1.24	1.30
80	1.28	1.29	1.32	1.29	1.25	1.15	1.11	1.18
75	1.29	1.41	1.45	1.35	1.20	1.11	1.18	1.19
70	1.30	1.45	1.53	1.39	1.20	1.13	1.25	1.17
65	1.30	1.54	1.60	1.50	1.23	1.22	1.42	1.16
60	1.32	1.60	1.66	1.60	1.27	1.42	1.61	1.29
55	1.39	1.65	1.70	1.64	1.29	1.57	1.71	1.46
50	1.43	1.71	1.81	1.70	1.35	1.68	1.76	1.58
45	1.49	1.80	1.90	1.78	1.40	1.74	1.82	1.66
40	1.55	1.85	1.90	1.85	1.50	1.82	1.85	1.75
35	1.61	1.93	1.99	1.94	1.59	1.85	1.87	1.82
30	1.67	1.99	2.06	2.07	1.68	1.87	1.83	1.84
25	1.72	2.05	2.16	2.22	1.80	1.94	1.96	1.92
20	1.83	2.11	2.22	2.35	1.87	2.10	2.09	2.05
15	2.04	2.21	2.27	2.50	2.09	2.22	2.16	2.18
				Log-normal standard deviation $\sigma_{\text{dur,bad}}$				
85	0.83	0.88	0.88	0.84	0.83	0.83	0.85	0.80
80	0.84	0.88	0.93	0.88	0.84	0.84	0.90	0.86
75	0.85	0.93	0.97	0.92	0.88	0.91	0.93	0.90
70	0.82	0.96	1.06	0.99	0.86	0.94	0.97	0.93
65	0.85	1.02	1.11	1.04	0.87	1.00	1.13	0.97
60	0.86	1.08	1.17	1.10	0.88	1.08	1.23	1.03
55	0.89	1.13	1.17	1.15	0.92	1.14	1.21	1.10
50	0.94	1.17	1.20	1.18	0.93	1.17	1.20	1.14
45	0.99	1.21	1.21	1.21	0.97	1.23	1.20	1.19
40	1.04	1.26	1.26	1.26	1.02	1.25	1.23	1.23
35	1.10	1.31	1.26	1.29	1.07	1.28	1.25	1.27
30	1.20	1.37	1.34	1.34	1.11	1.31	1.32	1.36
25	1.28	1.47	1.39	1.42	1.19	1.36	1.33	1.40
20	1.39	1.56	1.45	1.52	1.29	1.40	1.38	1.48
15	1.52	1.67	1.56	1.67	1.46	1.53	1.47	1.61
				Log-normal mean $\mu_{\text{dur,good}}$				
85	3.89	3.84	3.77	3.86	3.96	4.10	4.08	4.13
80	3.95	3.69	3.61	3.77	3.92	4.09	4.13	4.13
75	4.06	3.54	3.30	3.53	4.03	4.19	4.16	4.25
70	3.91	3.25	2.98	3.37	3.98	4.12	3.96	4.12
65	3.90	3.06	2.77	3.21	3.95	3.86	3.58	3.93
60	3.88	2.88	2.60	3.08	3.87	3.66	3.51	3.77
55	3.84	2.68	2.45	2.90	3.82	3.46	3.18	3.69
50	3.78	2.52	2.30	2.75	3.78	3.26	2.93	3.50
45	3.66	2.38	2.21	2.60	3.70	3.04	2.69	3.26
40	3.53	2.25	2.03	2.46	3.62	2.82	2.50	3.06
35	3.32	2.08	1.92	2.30	3.52	2.59	2.38	2.85
30	3.08	1.88	1.81	2.18	3.39	2.36	2.16	2.57
25	2.79	1.72	1.76	2.04	3.20	2.17	1.98	2.33
20	2.48	1.54	1.64	1.89	2.94	1.99	1.82	2.07
15	2.16	1.36	1.50	1.65	2.71	1.80	1.61	1.76

Table 2: Continued.

Elevation	Front	Front-right	Right	Back-right	Back	Back-left	Left	Front-left
				Log-normal standard deviation $\sigma_{\text{dur,good}}$				
85	1.78	1.71	1.73	1.70	1.72	1.70	1.81	1.72
80	1.70	1.69	1.65	1.61	1.75	1.82	1.82	1.77
75	1.67	1.64	1.62	1.67	1.74	1.78	1.81	1.81
70	1.75	1.66	1.63	1.62	1.75	1.93	1.89	1.86
65	1.77	1.63	1.56	1.59	1.77	1.98	1.87	1.97
60	1.78	1.58	1.49	1.55	1.82	1.90	1.75	1.95
55	1.77	1.54	1.44	1.50	1.79	1.83	1.74	1.85
50	1.77	1.49	1.38	1.45	1.81	1.78	1.67	1.82
45	1.75	1.43	1.31	1.40	1.80	1.72	1.58	1.81
40	1.78	1.36	1.27	1.35	1.79	1.66	1.51	1.76
35	1.81	1.32	1.20	1.29	1.77	1.58	1.43	1.69
30	1.81	1.28	1.20	1.23	1.73	1.50	1.36	1.64
25	1.78	1.23	1.14	1.18	1.67	1.39	1.26	1.52
20	1.71	1.18	1.12	1.12	1.60	1.30	1.22	1.39
15	1.54	1.11	1.09	1.07	1.51	1.21	1.17	1.27

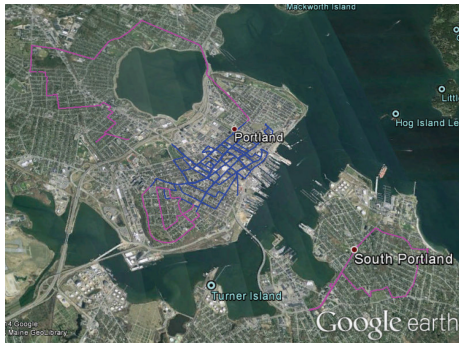

Figure 4: Measurement route in Portland (Maine) across urban (blue) and suburban (magenta) environment.

satellites of Sirius Satellite Radio were recorded at the operational frequency of 2.3 GHz (S-Band) with a sampling rate of 2.1 kHz. The precise measuring time and vehicle position was logged via GPS. In addition, a hemispheric camera was mounted on the van to document the environment, pointing towards the sky (5 frames per second with a resolution of 880 × 768 pixels of the fisheye region). The campaign was carried out along a distance of 3700 km from Jacksonville (Florida) to Portland (Maine) in different environments (urban, suburban, commercial, and highway). In this contribution we focus on data from Portland (Maine) comprising urban and suburban environment. Figure 4 illustrates the measurement route in urban and suburban environments (depicted by the different colors) in Portland, Maine.

3.3. Evaluation of the Image-Based State Estimation Method. In order to validate the image-based method we compare the estimated channel states of the images with actual radio frequency (RF) Data.

In LMS channel models the sequence of states is commonly modeled by Markov/semi-Markov processes [1, 37]. Therefore, parameters like state probabilities and the distribution of state durations are of interest. The state duration statistics are derived for the satellites Sirius 1, Sirius 2, XM-3, and XM-4 with an average elevation of 65°, 68°, 38°, and 23°, respectively. The results based on image and RF data are depicted in Figure 5 for *bad* state and in Figure 6 for *good* state. In order to evaluate the estimation accuracy, we show the Complementary Cumulative Distribution Function (CCDF).

The statistics show very good agreement between the RF-based (dashed lines) and the image-based results (solid lines). Additionally, the log-normal fit is plotted in black. As a result, the image-based approach can be seen as a valid technique for state estimation.

4. Image-Based Model of the Land Mobile Satellite Channel

In the following we explain the proposed LMS channel model. Statistical channel models reproduce the time-series of the received satellite signal comprising two processes, the very slow fading and the slow/fast fading. The nonstationarity of the signal due to the different degrees of shadowing is expressed by states (e.g., LoS, moderate shadowing, and deep shadowing). Well accepted in the literature are LMS models, which describe the very slow fading component by either three states [1], namely, *line-of-sight*, *shadowed*, and *blocked*, or by two states [2], *good* and *bad*. The slow and fast fading caused by varying shadowing and multipath effects are treated as a second process and is commonly reproduced by a stationary stochastic process.

In Figure 7, the LMS model is illustrated, which is based on the versatile two-state approach presented in [2, 5]. The model distinguishes between two states, *good* and *bad*, corresponding to LoS or light shadowing and NLoS or heavy shadowing, respectively. The state modeling is performed by

Table 3: Semi-Markov parameters (*good* and *bad* state) for *suburban* environment for variable driving directions and elevations.

Elevation	Front	Front-right	Right	Back-right	Back	Back-left	Left	Front-left
				Log-normal mean $\mu_{\text{dur,bad}}$				
85	1.87	1.83	1.88	1.81	1.81	1.79	1.81	1.82
80	1.85	1.88	1.89	1.86	1.81	1.78	1.78	1.82
75	1.89	1.94	1.96	1.86	1.78	1.78	1.78	1.82
70	1.92	1.95	1.93	1.91	1.79	1.75	1.75	1.80
65	1.89	1.97	1.96	1.93	1.79	1.79	1.79	1.80
60	1.91	2.02	1.99	1.96	1.83	1.82	1.88	1.83
55	1.94	2.04	2.01	2.02	1.85	1.86	1.90	1.86
50	1.97	2.06	1.98	2.05	1.90	1.88	1.89	1.91
45	1.98	2.05	1.94	2.04	1.94	1.90	1.92	1.90
40	2.04	2.07	1.95	2.07	1.99	1.95	1.94	1.98
35	2.07	2.10	2.01	2.08	2.04	1.99	1.98	1.97
30	2.13	2.14	2.10	2.15	2.11	2.03	1.99	1.99
25	2.10	2.22	2.19	2.24	2.19	2.09	2.07	2.07
20	2.15	2.34	2.32	2.42	2.26	2.22	2.19	2.14
15	2.38	2.57	2.55	2.65	2.41	2.41	2.29	2.35
				Log-normal standard deviation $\sigma_{\text{dur,bad}}$				
85	0.92	0.95	0.93	0.93	0.94	0.96	0.97	0.97
80	0.97	0.96	0.95	0.93	0.95	0.98	0.96	0.96
75	0.95	0.97	0.95	0.98	0.96	0.95	0.95	0.93
70	0.95	0.98	0.98	0.99	0.97	0.95	0.99	0.95
65	0.98	1.00	0.96	0.99	1.00	0.95	1.00	0.98
60	1.00	0.99	0.96	1.00	1.00	0.98	0.97	0.99
55	0.98	1.01	0.97	0.99	1.00	0.97	0.98	1.00
50	1.01	1.03	0.98	0.98	1.00	0.98	1.00	0.99
45	1.06	1.07	1.02	1.02	1.02	1.03	1.00	1.04
40	1.09	1.08	1.03	1.05	1.04	1.04	1.01	1.05
35	1.14	1.10	1.02	1.09	1.08	1.09	1.02	1.10
30	1.18	1.12	1.06	1.12	1.13	1.13	1.07	1.14
25	1.27	1.18	1.13	1.18	1.21	1.18	1.08	1.18
20	1.36	1.27	1.24	1.26	1.31	1.21	1.10	1.26
15	1.47	1.45	1.38	1.47	1.41	1.30	1.21	1.35
				Log-normal mean $\mu_{\text{dur,good}}$				
85	2.94	2.93	2.99	2.92	2.94	2.97	2.98	2.93
80	2.98	2.96	2.98	2.95	2.96	2.95	2.93	2.95
75	3.00	2.99	2.98	2.94	2.90	2.93	2.90	2.97
70	2.99	2.93	2.87	2.94	2.93	2.84	2.87	2.96
65	2.92	2.88	2.78	2.91	2.90	2.86	2.91	2.92
60	2.92	2.80	2.68	2.84	2.89	2.92	2.91	2.92
55	2.89	2.71	2.59	2.77	2.89	2.94	2.90	2.91
50	2.87	2.61	2.49	2.68	2.89	2.89	2.81	2.90
45	2.80	2.51	2.36	2.59	2.87	2.83	2.69	2.81
40	2.76	2.40	2.24	2.52	2.90	2.75	2.59	2.82
35	2.71	2.29	2.08	2.40	2.87	2.68	2.48	2.72
30	2.65	2.13	1.96	2.26	2.83	2.57	2.33	2.56
25	2.50	1.93	1.78	2.08	2.80	2.40	2.18	2.41
20	2.30	1.75	1.65	1.91	2.69	2.22	1.98	2.19
15	2.15	1.55	1.52	1.69	2.38	1.99	1.73	1.93

Table 3: Continued.

Elevation	Front	Front-right	Right	Back-right	Back	Back-left	Left	Front-left
				Log-normal standard deviation $\sigma_{\text{dur,good}}$				
85	1.49	1.49	1.46	1.46	1.49	1.49	1.50	1.52
80	1.47	1.44	1.41	1.44	1.49	1.52	1.51	1.51
75	1.47	1.39	1.34	1.43	1.52	1.53	1.55	1.50
70	1.48	1.36	1.30	1.38	1.53	1.59	1.56	1.54
65	1.51	1.31	1.22	1.33	1.55	1.58	1.58	1.55
60	1.50	1.28	1.22	1.30	1.58	1.57	1.52	1.55
55	1.48	1.26	1.19	1.28	1.57	1.50	1.46	1.56
50	1.49	1.25	1.17	1.25	1.58	1.48	1.41	1.54
45	1.54	1.25	1.15	1.20	1.57	1.47	1.36	1.57
40	1.55	1.25	1.13	1.18	1.52	1.41	1.31	1.53
35	1.57	1.19	1.06	1.17	1.52	1.35	1.28	1.48
30	1.57	1.14	1.01	1.13	1.52	1.30	1.24	1.44
25	1.57	1.11	1.00	1.09	1.51	1.27	1.17	1.38
20	1.55	1.03	0.97	1.05	1.46	1.22	1.11	1.32
15	1.48	1.00	0.95	1.03	1.30	1.16	1.05	1.24

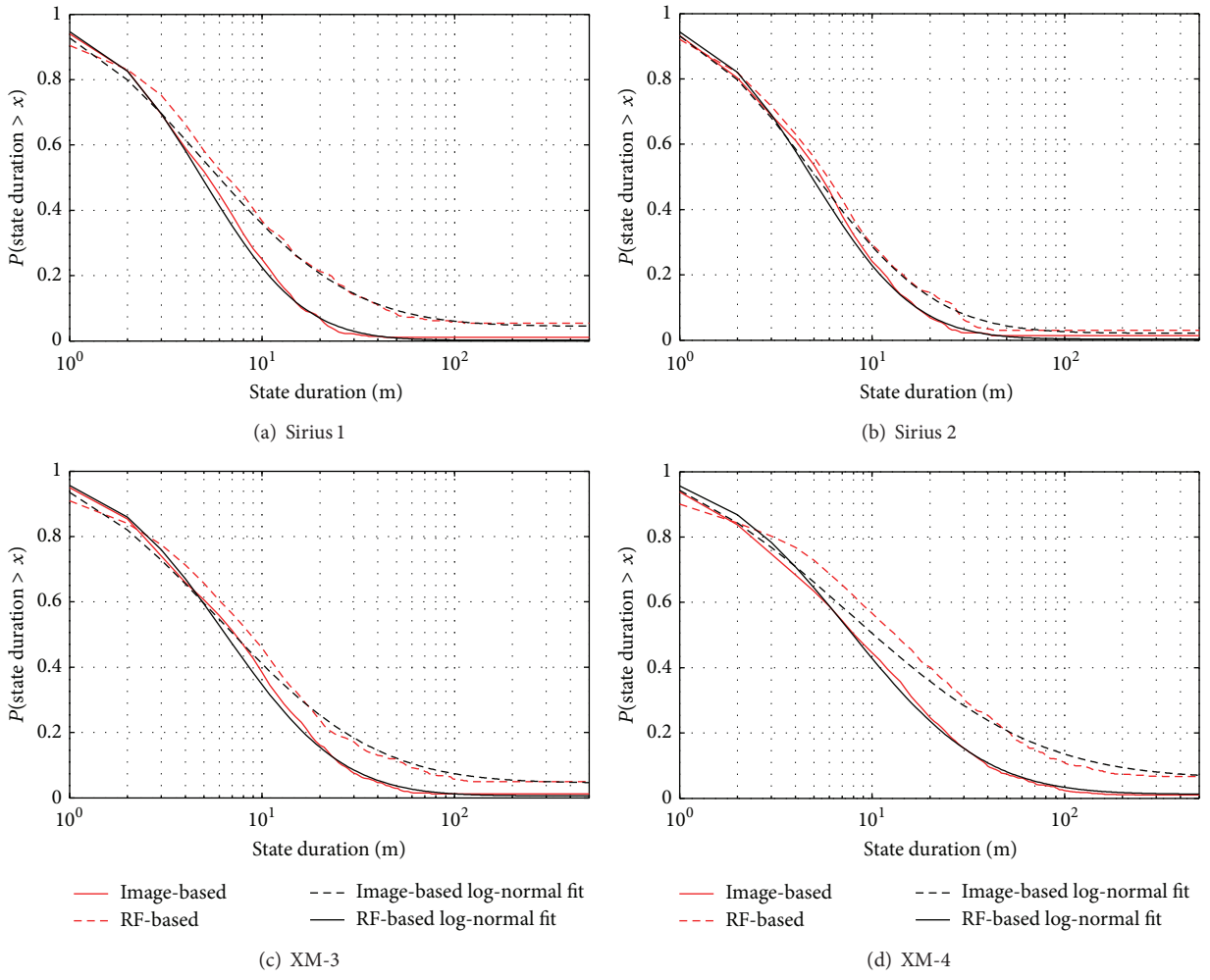

Figure 5: Statistics for *bad* state for each satellite (Sirius 1, Sirius 2, XM-3, and XM-4) obtained from the image-based state estimation method (red solid lines). As a ground truth, the same plots are shown for the states obtained from the RF measurements (red dashed lines). Furthermore, the log-normal fitting is shown based on images and RF data, respectively (black curves).

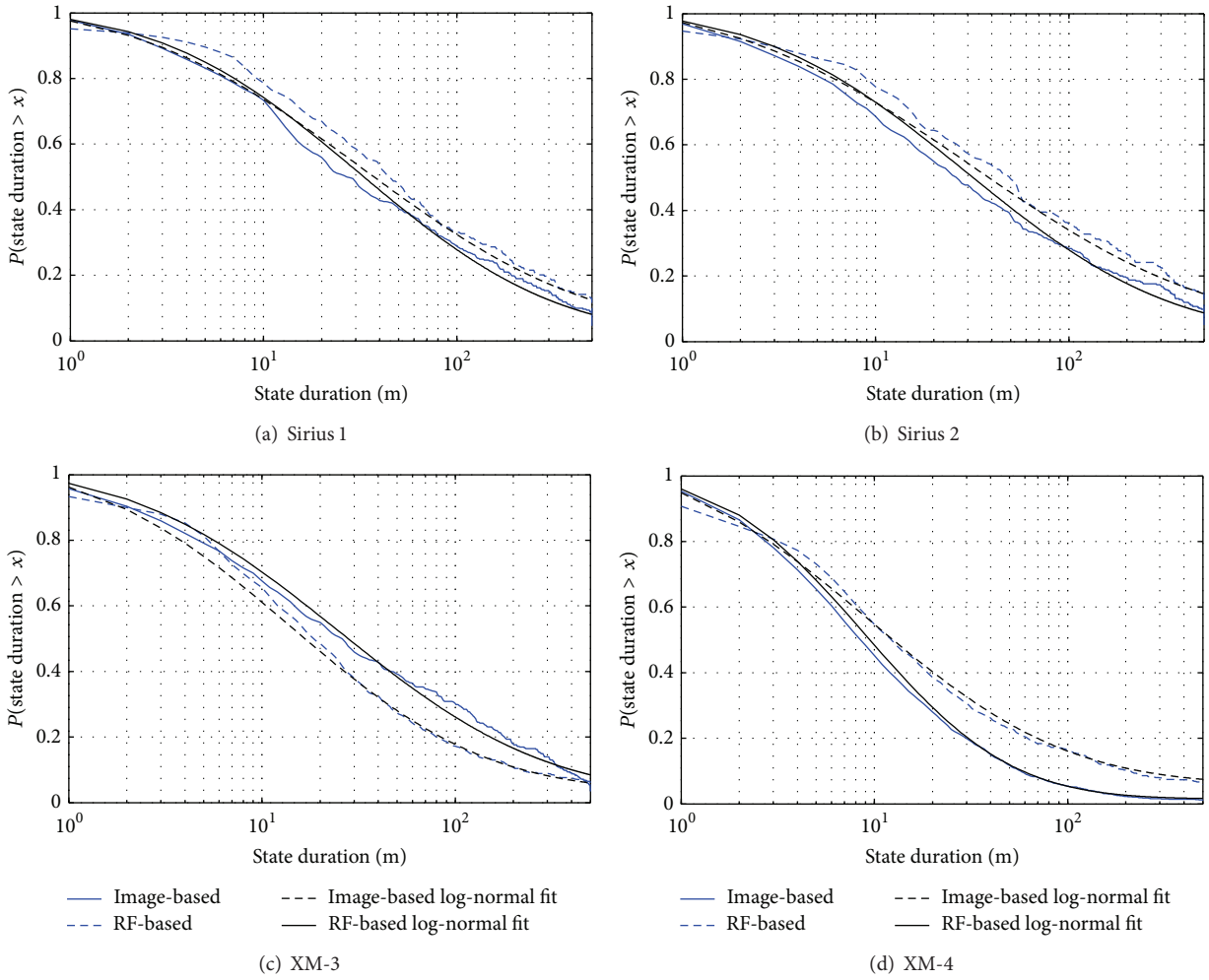

FIGURE 6: Statistics for *good* state for each satellite (Sirius 1, Sirius 2, XM-3, and XM-4) obtained from the image-based state estimation method (blue solid lines). As a ground truth, the same plots are shown for the states obtained from the RF measurements (blue dashed lines). Furthermore, the log-normal fitting is shown based on images and RF data, respectively (black curves).

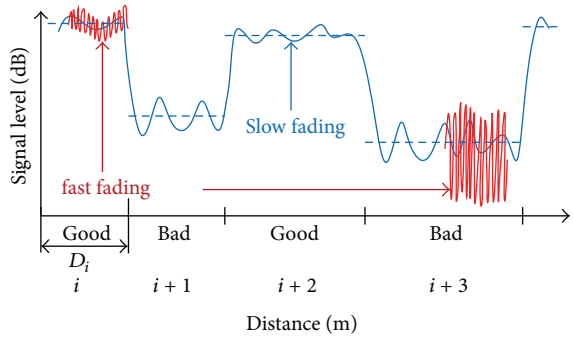

FIGURE 7: Features of the proposed two-state LMS model, where i is the state interval index. Each state has a possibly different interval duration D_i and a new Loo triplet $\mathbf{\Omega}_i$ consisting of $M_{A,i}$, $\Sigma_{A,i}$, and MP_i drawn from random processes.

a semi-Markov chain [37], which improves the accuracy of the state duration modeling, compared to the more common first order Markov chains [1]. Based on the measured state durations, the state duration probability density function (SDPDF) is modeled by a log-normal distribution. It is expressed by

$$P(D) = \frac{1}{D\sigma_{\text{dur}}\sqrt{2\pi}} \exp\left(-\frac{(\ln(D) - \mu_{\text{dur}})^2}{2\sigma_{\text{dur}}^2}\right), \quad (1)$$

where D is the state duration, μ_{dur} is the mean value of $\ln(D)$, and σ_{dur} is the standard deviation of $\ln(D)$. These parameters μ_{dur} and σ_{dur} are called the log-normal mean and log-normal standard deviation, respectively, and are estimated for both *good* and *bad* state. The mean of the state duration (in meter) can be calculated by $e^{\mu_{\text{dur}}+\sigma_{\text{dur}}^2/2}$; the standard deviation (in meter) can be calculated by $\sqrt{(e^{\sigma_{\text{dur}}^2}-1)e^{2\mu_{\text{dur}}+\sigma_{\text{dur}}^2}}$.

The slow and fast signal fading within each state are modeled by a Loo distribution [27]. The Loo distribution considers the received signal as a sum of two signal components. A log-normally distributed direct signal expresses the slow fading component corresponding to varying shadowing

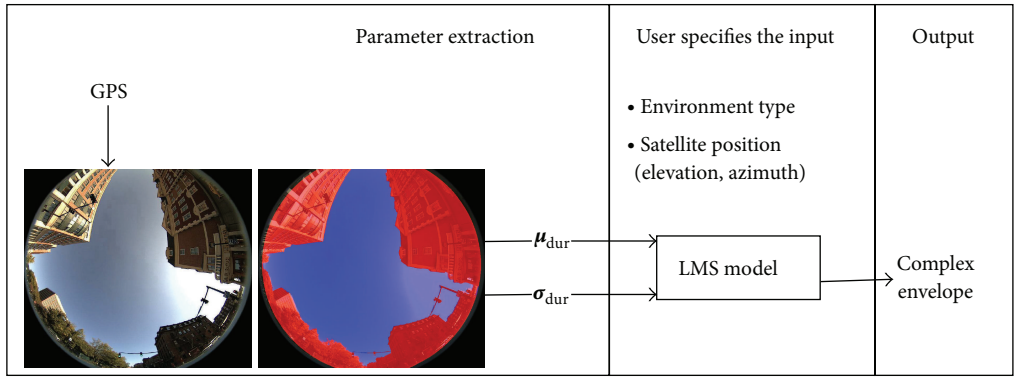

FIGURE 8: High-level overview of the proposed image-based LMS model. The image-based state duration parameters $\boldsymbol{\mu}_{dur}$ and $\boldsymbol{\sigma}_{dur}$ are preprocessed for all possible environments and satellite positions. Depending on the user's input, that is, environment type and satellite position, the specific μ_{dur} and σ_{dur} are chosen.

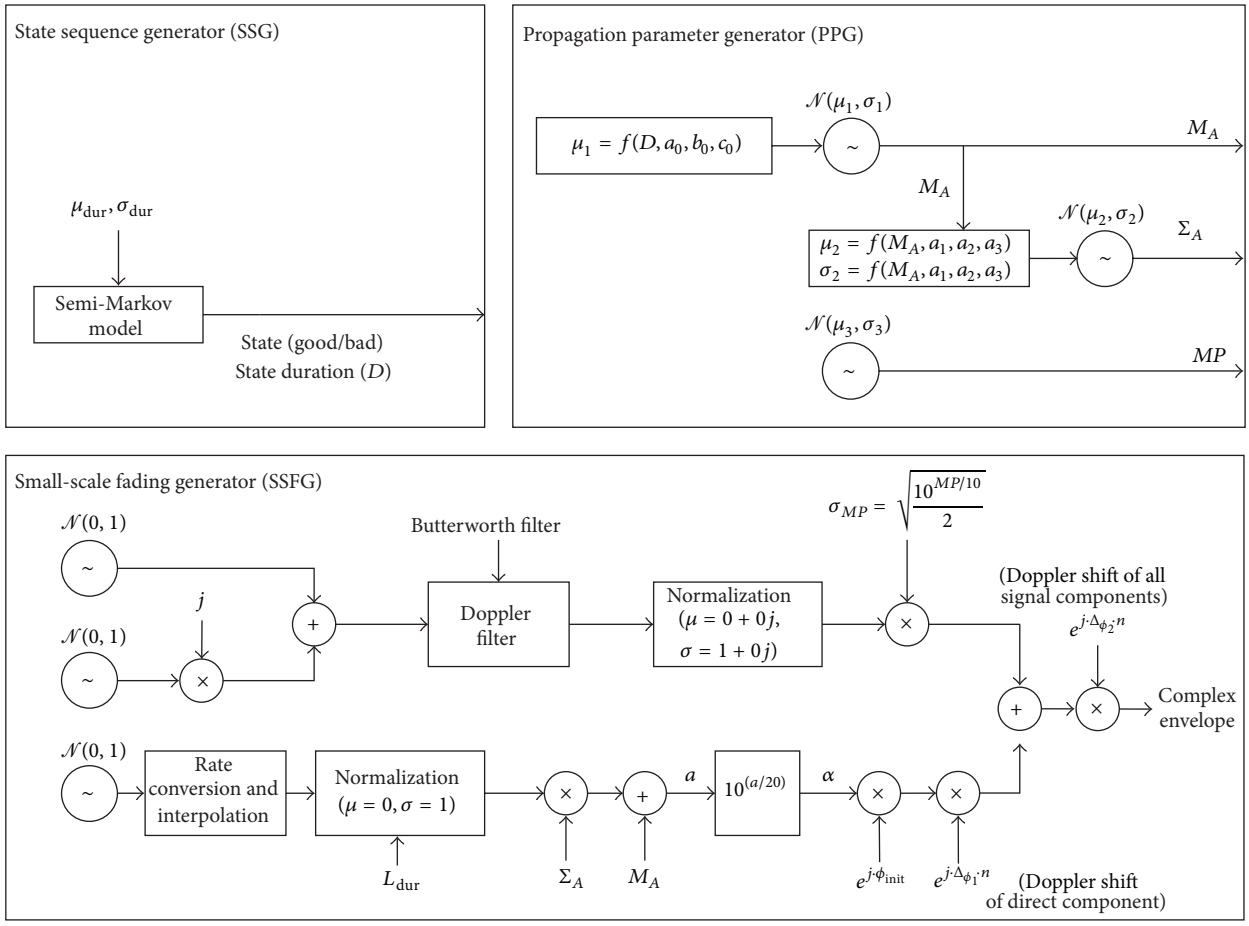

FIGURE 9: Detailed LMS model implementation diagram comprising the three main elements: state sequence generator (SSG), propagation parameter generator (PPG), and small-scale fading generator (SSFG).

conditions of the direct signal. A Rice distribution characterizes the fast fading component due to multipath effects. The Loo parameter triplet $\boldsymbol{\Omega}$ consists of the mean M_A, the standard deviation Σ_A for the log-normally distributed direct signal, and the average multipath power MP. Depending on the current state interval i and on the environment of the terminal, a new random Loo parameter triplet $\boldsymbol{\Omega}_i = (M_{A,i}, \Sigma_{A,i}, MP_i)$ is generated. Compared to an earlier three-state model [1], where the Loo parameter triplet is fixed for each state, the versatile Loo parameter selection enables

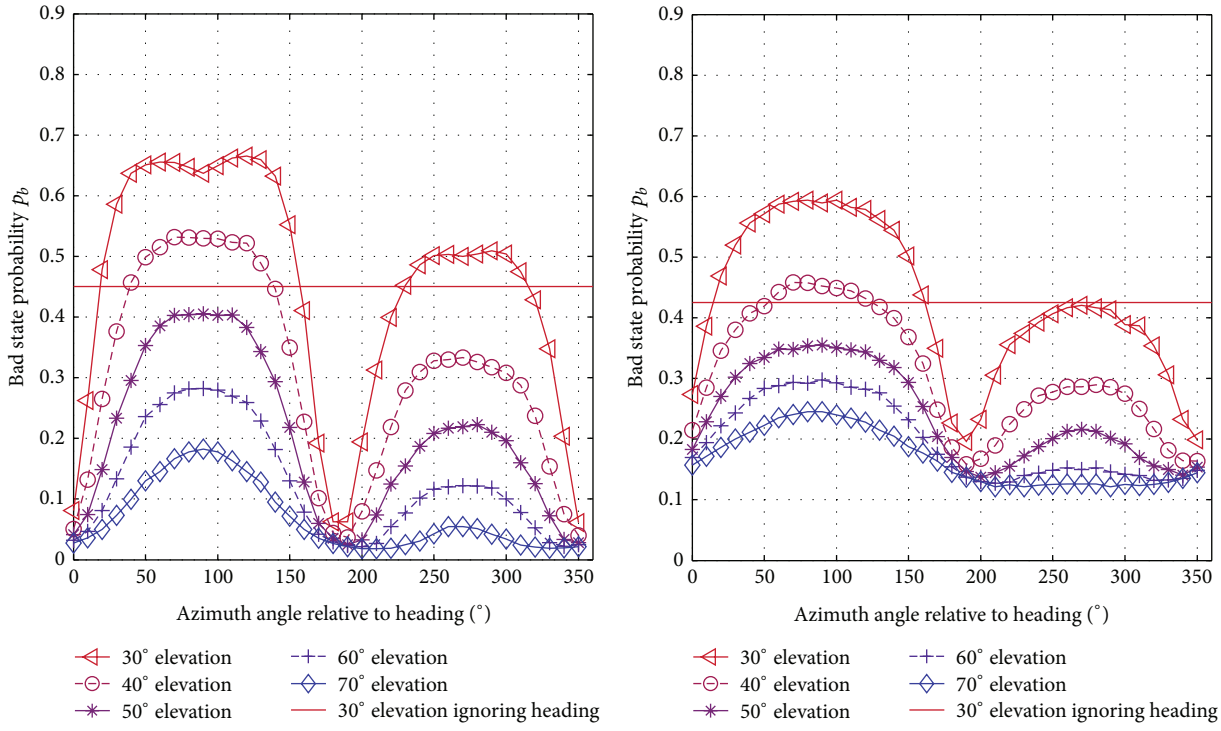

(a) *Urban* environment (b) *Suburban* environment

FIGURE 10: The *bad* state probability (service unavailability) for *urban* (a) and *suburban* (b) environment. The dependency on the azimuth angle (relative to driving direction) is shown for satellites at different elevation angles. For an elevation of 30° also the result of ignoring the heading is plotted as a constant (red line).

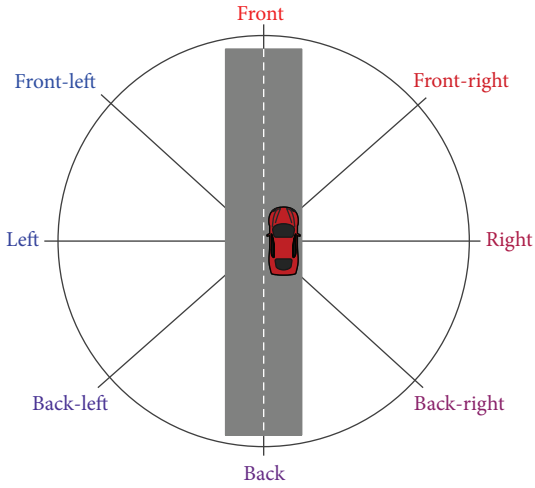

FIGURE 11: Eight exemplary satellite positions relative to the street orientation, which are further investigated.

a more realistic modeling over the full dynamic range of the received signal [2]. The output of the channel model is a time-series of the received signal in form of a complex envelope. For the purpose of comparability, we convert the output to a time-series of the carrier-to-noise ratio (C/N). As the LoS level is dependent on the transmit power, path-loss (distance, weather, and frequency), and the receiver characteristics, we remove it from the signal to obtain a representation of the fading effects exclusively caused by the environment. Thus, we end up with a carrier-to-noise ratio normalized to the LoS level $C/N - (C/N)_{\text{LoS}}$ in dB.

Figure 8 shows how the parameters of the model are preprocessed and how they are applied. First, hemispheric images are binarized into the classes sky and obstruction. Second, a set of parameters for the state duration statistics is extracted from the images, depending on the environment type, satellite elevation, and satellite azimuth. Depending on the user's needs, representative parameters are selected for the actual LMS channel modeling process. Despite the extracted state duration parameters (very slow fading), the Loo-parameters (slow and fast fading) are chosen. Finally, a time-series of the LMS channel in terms of the complex envelope is simulated.

In Figure 9 an overview of the detailed implementation of the LMS channel model is depicted. The model is structured in three different generator types [5].

(1) The State Sequence Generator (SSG) reproduces as sequence of *good* and *bad* states by a semi-Markov model process. The necessary parameters are the log-normal mean μ_{dur} and log-normal standard deviation σ_{dur} of the state duration distribution for the *good* and *bad* state, respectively (cf. (1)). With this approach, an accurate modeling of the state duration and the state probabilities can be provided. At the i-th interval,

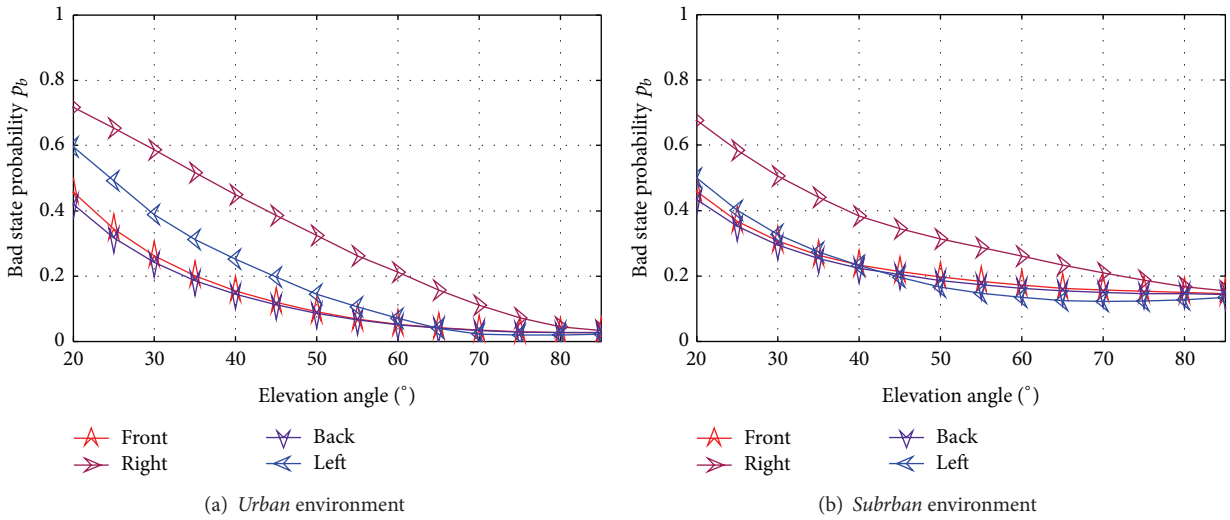

FIGURE 12: *Bad* state probability p_b for different driving directions in *urban* (a) and *suburban* (b) environment.

the SSG outputs the current state, which can be either *good* or *bad*, and the duration D_i for which the channel remains in the same state. The log-normal state duration parameters $(\mu_{\text{dur}}, \sigma_{\text{dur}})$, as input parameters of the semi-Markov model, are provided in Tables 2 and 3.

(2) The Propagation Parameter Generator (PPG) is invoked at each new state interval producing a new random Loo triplet $\mathbf{\Omega}_i$. As depicted in Figure 9, the PPG features three independent standard normal generators, whose means and variances $(\mu_1, \sigma_1, \mu_2, \sigma_2, \mu_3, \sigma_3)$ are estimated from measured RF data by curve-fitting as presented in [38].

(3) The Small-Scale Fading Generator (SSFG) computes the Loo distributed time-series including Doppler shaping for every new state interval, which is the output of the proposed LMS channel model. Furthermore, a Doppler shift of the log-normal varying direct signal is included, which is related to the speed of the vehicle. An optional Doppler shift of all signal components is also possible, to include the movement of the satellite.

5. Results

In the following we show the results obtained by the LMS channel model explained in Section 4, where the model parameters have been obtained with the image-based state estimation presented in Section 3. The first part of this section focuses on the state parameters of the model, which are important for a reliable state sequence generation. Secondly, the output of the whole channel model is evaluated in terms of first order statistics.

Exploiting the image-based state parameter estimation (instead of RF measurements) offers the advantage to perform a reliable analysis of the impact of the driving direction. Without any further geometrical consideration, a statistical availability prediction depending on the direction of the road is possible.

One crucial parameter of satellite service prediction is the service unavailability, or so-called *bad* state probability p_b. Figure 10 depicts p_b with respect to different elevation angles, azimuth angles (one degree resolution), and environment types (urban in Figure 10(a) and suburban in Figure 10(b)). The different curves represent different elevation angles, from which an inverse proportionality of p_b against the elevation angle can be seen. Moreover, a nonsymmetric dependency on the azimuth angle relative to the heading (abscissa) is visible. In both plots two maxima can be identified, one global at 90° azimuth and one local at 270° azimuth, which correspond to the right side and left side of the vehicle, respectively. The global maximum is caused by the right-hand driving on the street; therefore obstacles at the right side of the vehicle appear to be higher in relation to the position of the terminal on the street. This result shows that an assumption of the symmetric dependency of the azimuth angle is an oversimplification. At 0° and 180°, corresponding to *front* and *back* of the vehicle, two minima are found. This clearly reflects the street canyon characteristics, especially in urban scenarios. The influence of the street canyon decreases with an increasing elevation angle. The constant (solid red line) results from a calculation of p_b, which ignores the heading of the vehicle (exemplary for an elevation angle of 30°). Here, the heading is assumed to be uniformly distributed, representing the state-of-the-art LMS channel models, which do not include the azimuth angle of the satellite, for example, [2]. Ignoring the driving direction leads to a significant overestimation or underestimation of the *bad* state probability p_b. The difference between urban (Figure 10(a)) and suburban environment (Figure 10(b))

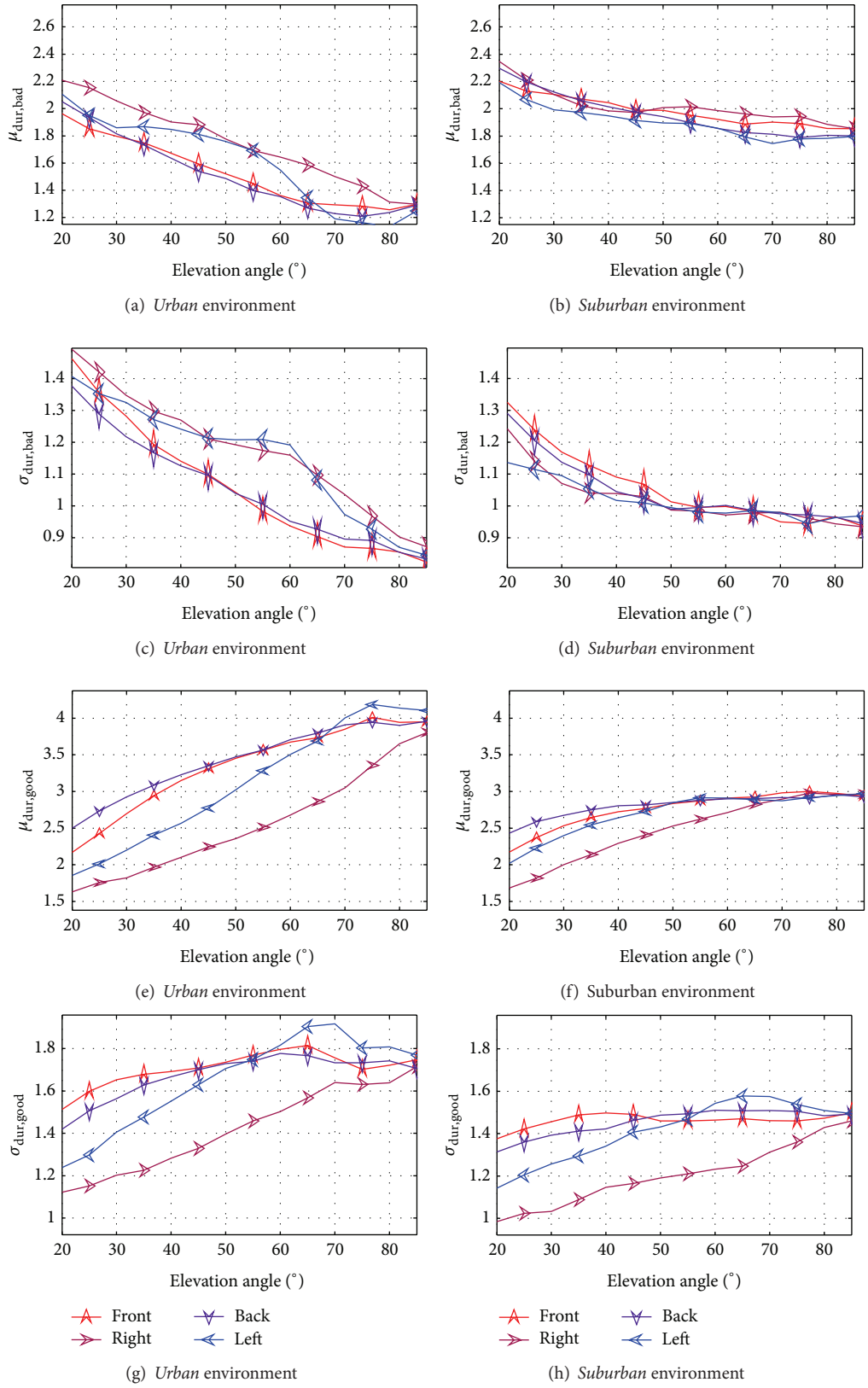

(a) *Urban* environment
(b) *Suburban* environment
(c) *Urban* environment
(d) *Suburban* environment
(e) *Urban* environment
(f) Suburban environment
(g) *Urban* environment
(h) *Suburban* environment

FIGURE 13: The log-normal mean ($\mu_{dur,bad}$, $\mu_{dur,good}$) and the log-normal standard deviation ($\sigma_{dur,bad}$, $\sigma_{dur,good}$) for *bad* and *good* states, respectively. The results refer to *urban* (left) and *suburban* (right) environment for different driving directions.

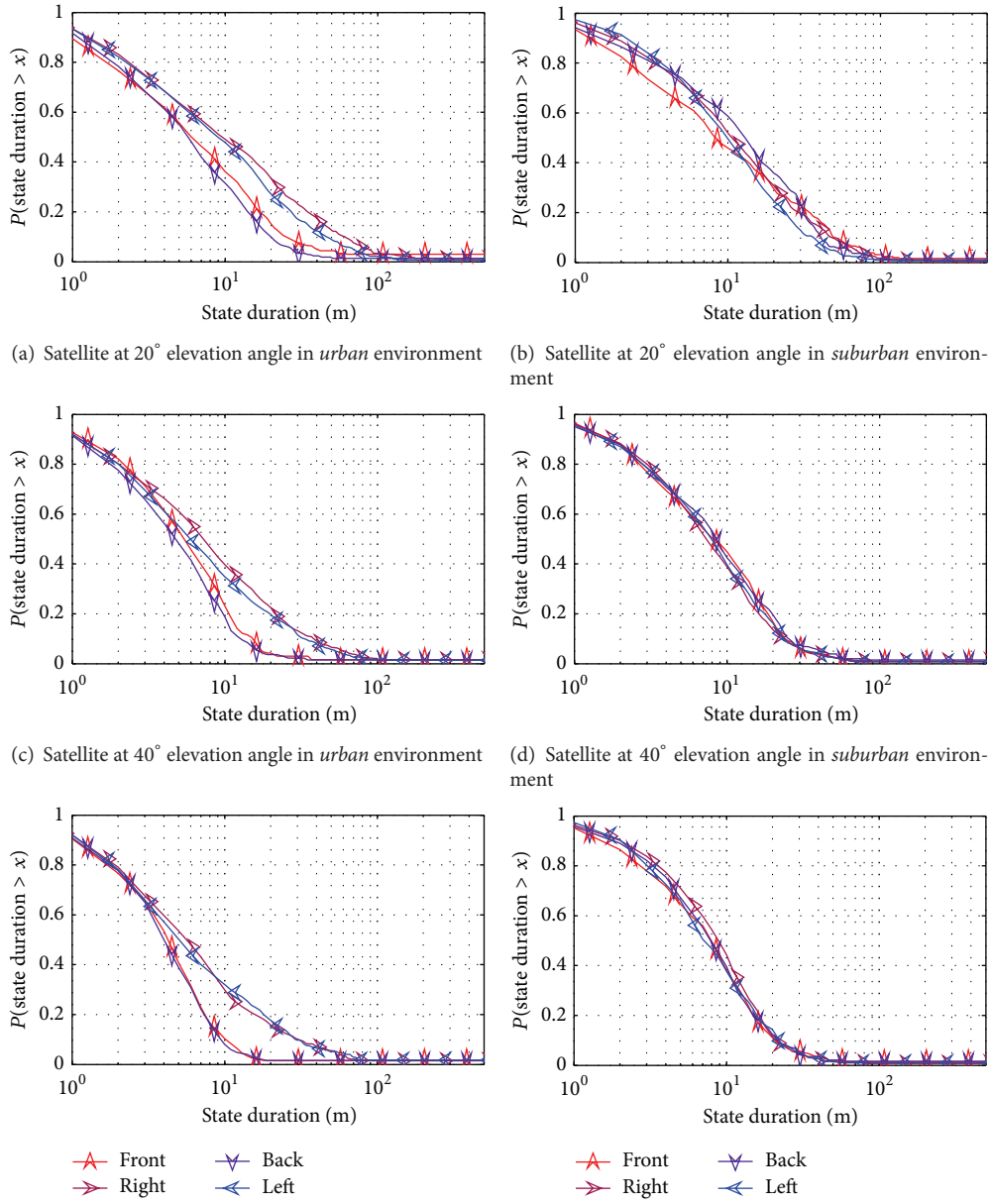

(a) Satellite at 20° elevation angle in *urban* environment

(b) Satellite at 20° elevation angle in *suburban* environment

(c) Satellite at 40° elevation angle in *urban* environment

(d) Satellite at 40° elevation angle in *suburban* environment

(e) Satellite at 60° elevation angle in *urban* environment

(f) Satellite at 60° elevation angle in *suburban* environment

FIGURE 14: State duration statistics for the *bad* state with respect to different driving directions and elevation angles in *urban* (left) and *suburban* environment (right).

becomes visible as approaching higher elevations. In contrast to urban environment, the *bad* state probability for suburban does not become zero due to the trees close to the road, reaching into regions of high elevation.

The hemispheric images offer the possibility to analyze with a resolution of one degree in azimuth and in elevation. Based on the results of Figure 11 we further focus on eight exemplary satellite positions relative to the street orientation, see Figure 11. Turning clockwise, the positions are *front*, *front-right*, *right*, *back-right*, *back*, *back-left*, *left*, and *front-left* and correspond to the azimuthal angles 0°, 45°, 90°, 135°, 180°, 225°, 270°, and 315° relative to the driving direction, respectively.

In order to model the state sequence by a Markov process, the state probability p_b, the log-normal mean of the state duration μ_{dur}, and the log-normal standard deviation σ_{dur} are of prime interest. In Figures 12 and 13 the three parameters are plotted versus the elevation angle (left for urban and on the right for suburban environment). For the sake of clarity we only show four different main positions of the satellite relative to the street orientation (*front*, *right*, *back*, and *left*). In Tables 2 and 3, the log-normal state duration parameters (μ_{dur},

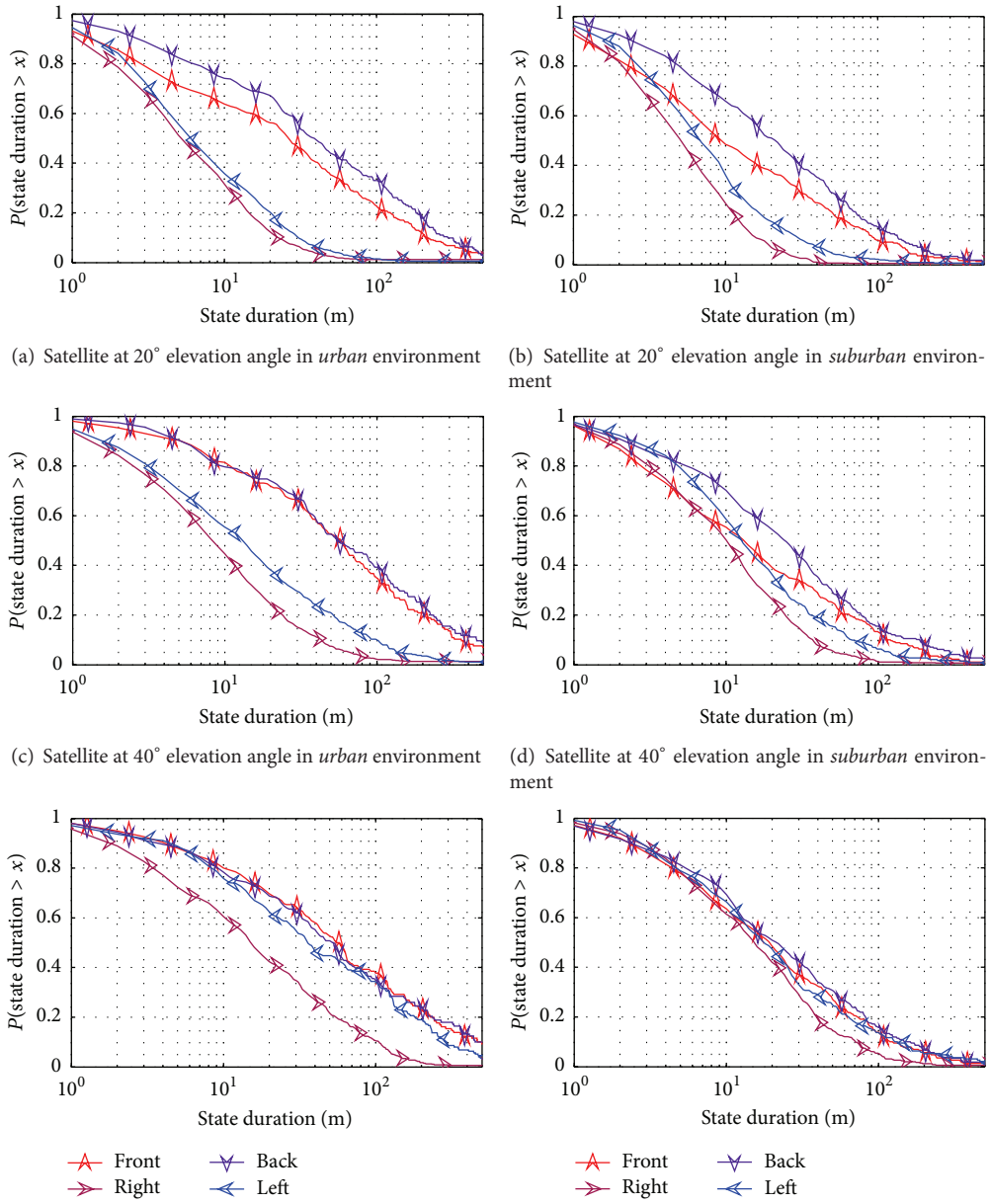

(a) Satellite at 20° elevation angle in *urban* environment

(b) Satellite at 20° elevation angle in *suburban* environment

(c) Satellite at 40° elevation angle in *urban* environment

(d) Satellite at 40° elevation angle in *suburban* environment

(e) Satellite at 60° elevation angle in *urban* environment

(f) Satellite at 60° elevation angle in *suburban* environment

FIGURE 15: State duration statistics for the *good* state with respect to different driving directions and elevation angles in *urban* (left) and *suburban* environment (right).

σ_{dur}) for the urban and suburban environment are provided for eight satellite positions in azimuth and elevation angles ranging from 15° to 85°. Due to the limited building height, the values of the *bad* state probability, the log-normal mean for *bad*, and the log-normal standard deviation for *bad* state decrease with an increasing elevation angle. The log-normal mean *good* state duration and the *good* state log-normal standard deviation show an inverse relationship. In particular, for urban scenarios a strong difference between the values of all the parameters for different satellite positions can be noticed; for example, a difference up to 20% in service unavailability can be seen. The estimated log-normal mean μ_{dur} and the log-normal standard deviation σ_{dur} are crucial parameters to describe the state duration probability density function (SDPDF) of the utilized semi-Markov chain (see Section 4). As we have shown that both parameters are dependent on the driving direction, we present the resulting complementary SDPDFs for the *good* and *bad* state in Figures 14 and 15, respectively. Each figure comprises urban (left) and suburban environment (right). From top to bottom, the elevation angle of the satellite is increasing from 20° to 40° and 60°, and again the four different positions in azimuth are analyzed. In urban

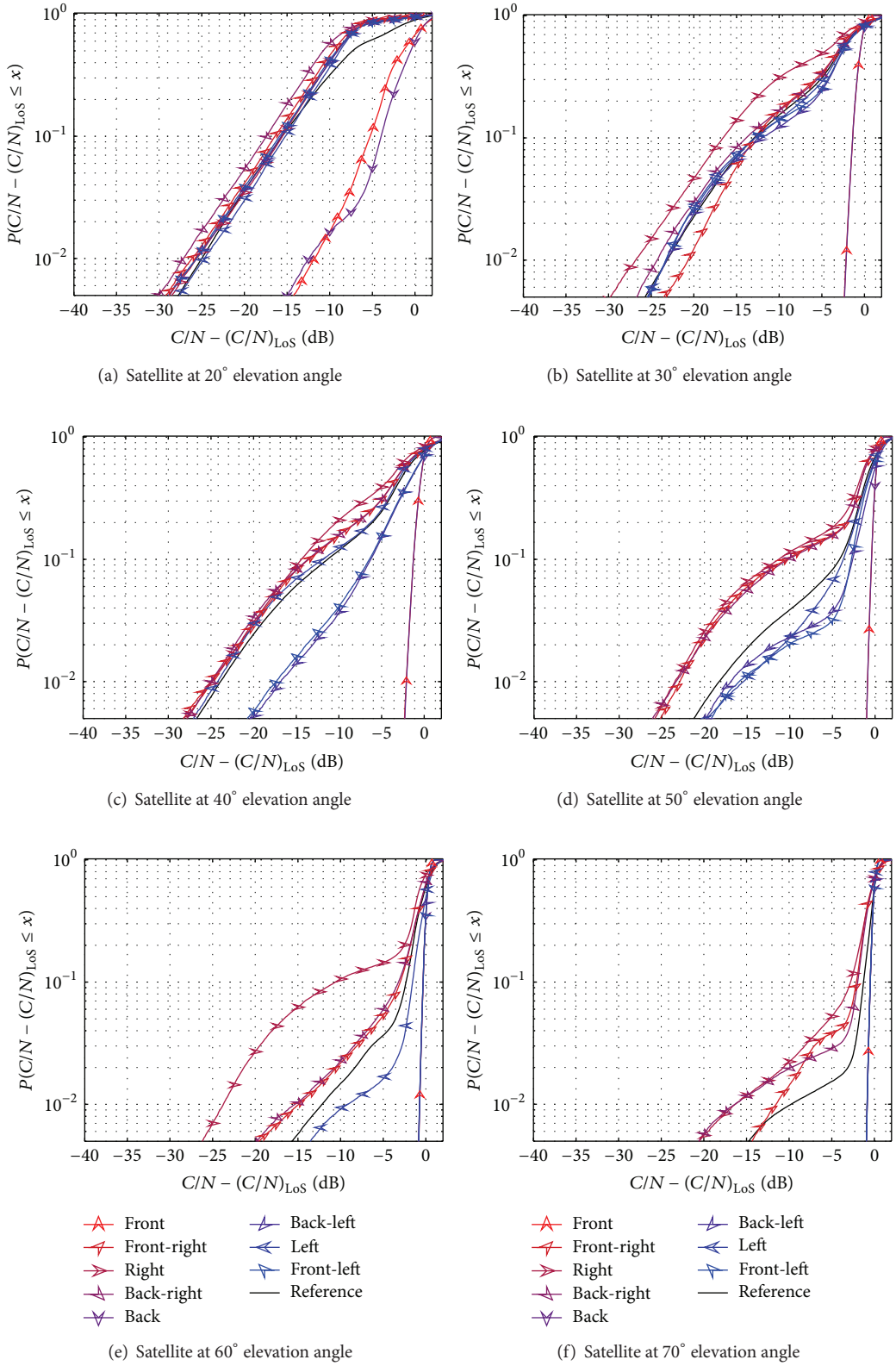

(a) Satellite at 20° elevation angle

(b) Satellite at 30° elevation angle

(c) Satellite at 40° elevation angle

(d) Satellite at 50° elevation angle

(e) Satellite at 60° elevation angle

(f) Satellite at 70° elevation angle

FIGURE 16: Comparison between the traditional and the proposed channel model with respect to the CDF of the received satellite signal envelope. For the results we consider data that has been collected in *urban* environment and each plot is related to a different elevation angle.

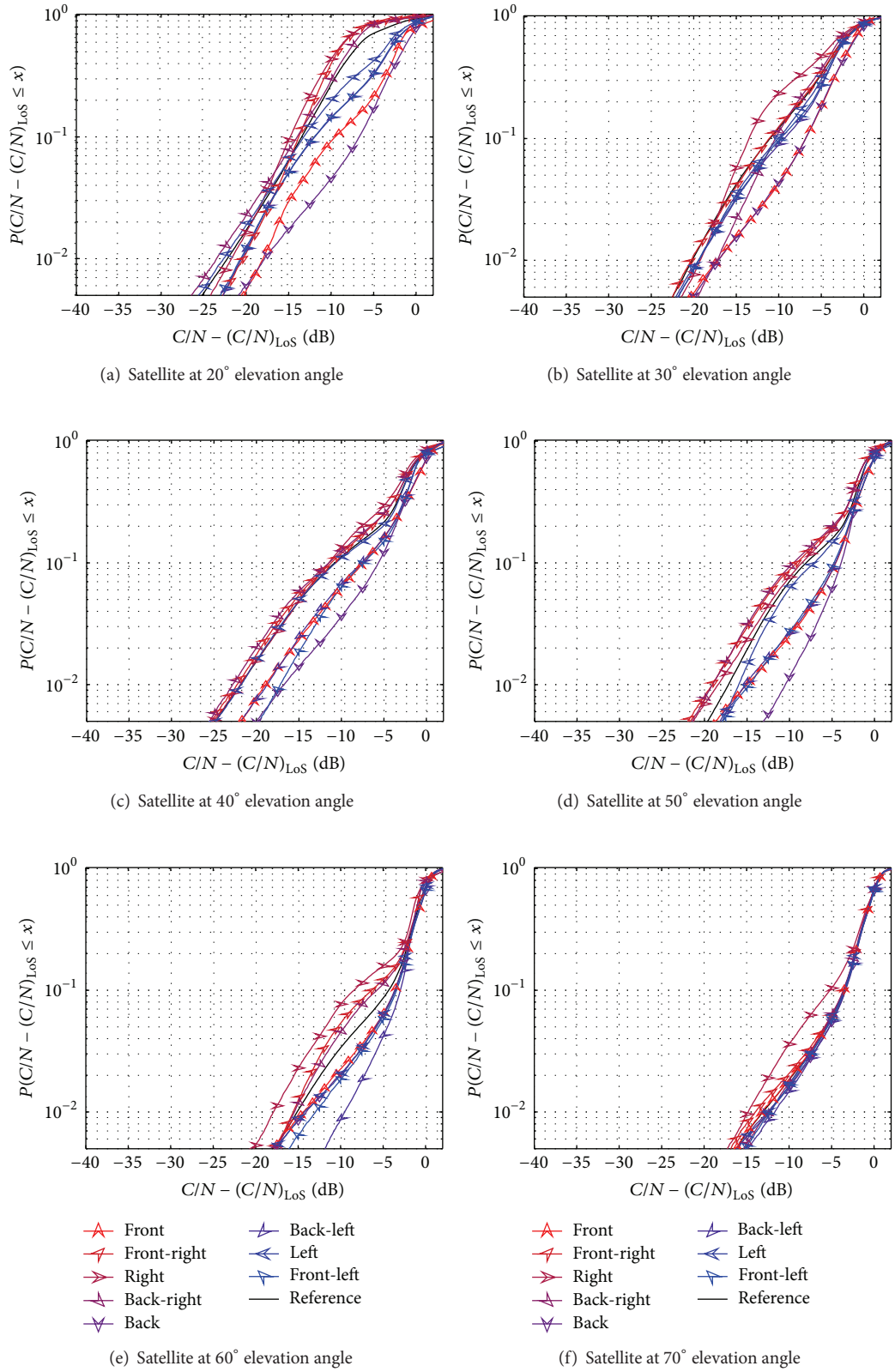

(a) Satellite at 20° elevation angle

(b) Satellite at 30° elevation angle

(c) Satellite at 40° elevation angle

(d) Satellite at 50° elevation angle

(e) Satellite at 60° elevation angle

(f) Satellite at 70° elevation angle

FIGURE 17: Comparison between the traditional and the proposed channel model with respect to the CDF of the received satellite signal envelope. For the results we consider data that has been collected in *suburban* environment and each plot is related to a different elevation angle.

environment considerable differences in the state duration statistics can be identified, where *right* represents the worst case and *front/back* the best case. For suburban scenarios the differences in the statistical behavior decrease. In the first part of this section we reveal significant differences of the state parameters depending on the environment, elevation, and on the azimuth relative to the driving direction.

Building on the results presented so far, we now investigate the impact of the driving direction by comparing the performance of the image-based LMS model output (see Section 4). The evaluation is performed in terms of first order statistics (Cumulative Distribution Functions (CDFs)) of the LoS-normalized carrier-to-noise ratio ($C/N - (C/N)_{\mathrm{LoS}}$ in dB), for eight exemplary satellite positions relative to the street orientation, see Figure 11. Turning clockwise, the positions are *front*, *front-right*, *right*, *back-right*, *back*, *back-left*, *left*, and *front-left* and correspond to the azimuthal angles 0°, 45°, 90°, 135°, 180°, 225°, 270°, and 315° relative to the driving direction, respectively. By extracting the satellite reception states from the images for the particular satellite position (see Section 3.1), the driving direction dependency is considered within the state parameter set. The Loo parameters (M_A, Σ_A, MP), chosen from statistical distributions, depend only on the environment and the elevation angle [5]. The results, corresponding to routes in the urban and suburban environment of Portland (Maine), are depicted in Figures 16 and 17, respectively. Each plot refers to a specific elevation angle (from 20° to 70°) and the colored curves with different markers represent the eight chosen satellite positions with respect to the driving direction. As a reference, the black curve is generated by considering a route in the corresponding environment, while the heading of the vehicle is assumed to be uniformly distributed. This method represents traditional modeling without an explicit consideration of the azimuth angle.

For all plots a clear tendency of an increasing LoS-normalized C/N related to an increasing elevation angle can be seen. The limited height of obstacles in the vicinity of the vehicle leads to better LoS conditions for higher elevations. At low elevation angles of the satellite (20°–30°) the impact of the street canyon becomes obvious (Figures 16(a) and 16(b)). A satellite oriented in the driving direction (*front*) or in the opposite (*back*) leads to an almost 17 dB higher LoS-normalized C/N compared to satellites positioned behind the buildings on the left or right side. The reference curve (ignoring the heading) is very close to the worst case.

In Figures 16(c) and 16(d), a third group with approximately 6 dB better than the worst case can be identified, consisting of the satellite positions *front-left*, *back-left*, and *left*, respectively. Here, the effect of the right-hand driving of the vehicle becomes evident; objects at the right side are closer and in relation to the position of the car, higher in elevation. The reference estimates the channel close to the worst case or close to the CDFs of the left positions. Consequently, modeling the satellite signal without any information of the heading of the vehicle leads to an overly optimistic estimation for satellites positioned at the right side.

Figure 16(e) shows the diversity of the satellite channel at an elevation of 60°. The CDFs of *front-left* and *back-left* superpose with *front* and *back*. The satellite at the *left* position behaves slightly worse. The LoS-normalized C/N decreases even more for *front-left* and *back-left* (≈7 dB) and *right* is still the worst case. The reference CDF is approximately located in the middle of the set of curves.

For 70° elevation (Figure 16(f)) the positions on the right side represent the worst case with a difference of ≈15 dB to the other superposed curves. Again, the reference curve represents almost an average of worst case and best case.

In Figure 17 the results for suburban environment are shown. Not surprisingly, the set of CDFs is closer to each other (≤10 dB); nonetheless the same worst and best cases can be identified.

6. Conclusions

In this contribution, we present a statistical Land Mobile Satellite (LMS) channel model, which includes the azimuth angle of the satellite with respect to the driving direction. To derive the necessary LMS model parameters for different headings and arbitrary satellite positions, an image-based parameter estimation method is used. This allows us to reduce the measurement effort significantly, compared to a conventional RF measurement campaign. We verify the image-based method by comparing the statistical state parameters derived from images with the ones derived from the corresponding measured RF signal levels, serving as a ground truth. The results show a good match, demonstrating that the image-based approach is a reliable method for detecting the very slow fading of the received satellite signal.

The proposed LMS channel model comprises a semi-Markov model using image-based state duration parameters to generate realistic state sequences for different driving directions. In particular, the extracted state duration statistics are strongly influenced by the driving direction. The model is able to generate time-series of the received satellite signal for different azimuth positions relative to the heading. We show that varying headings lead to significant differences in the first order statistics of the carrier-to-noise ratio, demonstrating the considerable nonstationarity of the received satellite signal. Although the proposed approach provides an accurate and realistic model, only a few user input parameters are necessary. This makes it an attractive tool for designing and testing of satellite systems.

Conflict of Interests

The authors declare that there is no conflict of interests regarding the publication of this paper.

Acknowledgment

The measurements were carried out in the context of the project MiLADY (Mobile satellite channeL with Angle DiversitY), funded by the European Space Agency (ESA) under contract no. C21150.

References

[1] F. Pérez–Fontán, M. Vázquez-Castro, C. E. Cabado, J. P. García, and E. Kubista, "Statistical modeling of the LMS channel," *IEEE Transactions on Vehicular Technology*, vol. 50, no. 6, pp. 1549–1567, 2001.

[2] R. Prieto-Cerdeira, F. Pérez–Fontán, P. Burzigotti, A. Bolea-Alamaac, and I. Sanchez-Lago, "Versatile two-state land mobile satellite channel model with first application to DVB-SH analysis," *International Journal of Satellite Communications and Networking*, vol. 28, no. 5-6, pp. 291–315, 2010.

[3] E. Lutz, "A Markov model for correlated land mobile satellite channels," *International Journal of Satellite Communications*, vol. 14, no. 4, pp. 333–339, 1996.

[4] D. Arndt, T. Heyn, A. Heuberger, R. Prieto-Cerdeira, and E. Eberlein, "State modeling of the land mobile satellite channel with angle diversity," in *Proceeding of the 6th European Conference on Antennas and Propagation (EuCAP '12)*, pp. 3140–3144, Prague, Czech Republic, March 2012.

[5] D. Arndt, T. Heyn, J. König et al., "Extended two-state narrowband LMS propagation model for S-Band," in *Proceedings of the IEEE International Symposium on Broadband Multimedia Systems and Broadcasting (BMSB '12)*, pp. 1–6, Seoul, Republic of Korea, June 2012.

[6] D. Arndt, A. Ihlow, T. Heyn, A. Heuberger, R. Prieto-Cerdeira, and E. Eberlein, "State modelling of the land mobile propagation channel for dual-satellite systems," *EURASIP Journal on Wireless Communications and Networking*, vol. 2012, article 228, 2012.

[7] D. Arndt, A. Ihlow, A. Heuberger, and E. Eberlein, "State modelling of the land mobile propagation channel with multiple satellites," *International Journal of Antennas and Propagation*, vol. 2012, Article ID 625374, 15 pages, 2012.

[8] C. Tzaras, S. R. Saunders, and B. G. Evans, "A physical-statistical pro pagation model for diversity in mobile satellite PCN," in *Proceedings of the 48th IEEE Vehicular Technology Conference (VTC '98)*, vol. 1, pp. 525–529, Ottawa, Canada, May 1998.

[9] C. Oestges, S. R. Saunders, and D. Vanhoenacker-Janvier, "Physical statistical modelling of the land mobile satellite channel based on ray tracing," *IEE Proceedings: Microwaves, Antennas and Propagation*, vol. 146, no. 1, pp. 45–49, 1999.

[10] C. Oestges and D. Vanhoenacker-Janvier, "A physical-statistical shadowing correlation model and its application to low-earth-orbit systems," *IEEE Transactions on Vehicular Technology*, vol. 50, no. 2, pp. 416–421, 2001.

[11] C. Oestges and D. Vanhoenacker-Janvier, "Time series-based prediction of fade dynamics and shado wing correlation statistics for navigation systems," in *Proceedings of the 2nd European Conference on Antennas and Propagation (EuCAP '07)*, pp. 1–6, IET, Edinburgh, UK, 2007.

[12] M. A. Vázquez–Castro, F. Pérez–Fontán, H. Iglesias-Salgueiro, and M. A. Barcia-Fernandez, "A simple three-segment model for shadowing cross correlation in multisatellite systems in street canyons," *Microwave and Optical Technology Letters*, vol. 28, no. 3, pp. 160–164, 2001.

[13] M. A. Vázquez-Castro, F. Pérez–Fontán, and S. R. Saunders, "Shadowing correlation assessment and modeling for satellite diversity in urban environments," *International Journal of Satellite Communications*, vol. 20, no. 2, pp. 151–166, 2002.

[14] F. Pérez–Fontán, M. A. Vázquez–Castro, C. Enjamio, and J. Pita, "Modeling the building blockage cross-correlation in multi-satellite systems," in *Proceedings of the 55th Vehicular Technology Conference (VTC '02)*, vol. 2, pp. 928–932, May 2002.

[15] F. Pérez–Fontán, M. A. Vázquez–Castro, C. Enjamio-Cabado, and J. Pita, "Simplified multi-satellite system availability calculations using street masking functions," in *Proceedings of the 55th IEEE Vehicular Technology Conference (VTC '02)*, vol. 4, pp. 1864–1868, May 2002.

[16] F. Pérez–Fontán, M. A. Vázquez–Castro, C. Enjamio, P. Mariño, and J. Pita, "Approximate urban area call drop-out probability estimation in mobile multi-satellite systems," *International Journal of Satellite Communications and Networking*, vol. 21, no. 2, pp. 183–197, 2003.

[17] F. Pérez–Fontán, S. Martínez, B. Sanmartin, C. Enjamio, P. Mariño, and F. Machado, "An enhanced Markov chain based model for the narrowband LMS channel in built-up areas," *International Journal of Satellite Communications and Networking*, vol. 23, no. 2, pp. 111–128, 2005.

[18] C. Meenan, M. Parks, R. Tafazolli, and B. Evans, "Availability of 1st generation satellite personal communication network service in urban environments," in *Proceedings of the IEEE 48th Vehicular Technology Conference (VTC Spring '98)*, vol. 2, pp. 1471–1475, IEEE, Ottawa, Canada, May 1998.

[19] R. Akturan and W. J. Vogel, "Optically derived elevation angle dep endence of fading for satellite PCS," *Proceedings of the 19th NASA Propagation Experimenters Meeting (NAPEX '95)*, vol. 1, pp. 127–132, 1995.

[20] R. Akturan and W. J. Vogel, "Path diversity for LEO satellite-PCS in the urban environment," *IEEE Transactions on Antennas and Propagation*, vol. 45, no. 7, pp. 1107–1116, 1997.

[21] R. Akturan, H.-P. Lin, and W. J. Vogel, "Propagation modeling in land mobile satellite systems using photogrammetry," in *Proceedings of the IEEE 46th Vehicular Technology Conference*, pp. 1018–1022, Atlanta, Ga, USA, May 1996.

[22] M. Rieche, D. Arndt, A. Ihlow, F. Pérez-Fontán, and G. Del Daldo, "Impact of driving direction on land mobile satellite channel modeling," in *Proceedings of the 8th European Conference on Antennas and Propagation (EuCAP '14)*, The Hague, The Netherlands, 2014.

[23] R. Akturan and W. J. Vogel, "Photogrammetric mobile satellite service prediction," *Electronics Letters*, vol. 31, no. 3, pp. 165–166, 1995.

[24] L. Castanet, "Influence of the variability of the propagation channel on mobile, fixed multimedia and optical satellite communications," in *Mobile/Indoor Multipath*, L. Castanet, Ed., Shaker, Aachen, Germany, 2008.

[25] A. G. Kanatas and P. Constantinou, "A narrowband land mobile satellite channel software simulator for urban environments," *International Journal of Satellite Communications*, vol. 18, no. 1, pp. 17–45, 2000.

[26] M. Döttling, A. Jahn, D. Didascalou, and W. Wiesbeck, "Two- and three-dimensional ray tracing applied to the land mobile satellite (LMS) propagation channel," *IEEE Antennas and Propagation Magazine*, vol. 43, no. 6, pp. 27–37, 2001.

[27] C. Loo, "A statistical model for a land mobile satellite link," *IEEE Transactions on Vehicular Technology*, vol. 34, no. 3, pp. 122–127, 1985.

[28] G. E. Corazza and F. Vatalaro, "A statistical model for land mobile satellite channels and its application to nongeostationary orbit systems," *IEEE Transactions on Vehicular Technology*, vol. 43, no. 3, pp. 738–742, 1994.

[29] H. Suzuki, "A statistical model for urban radio propogation," *IEEE Transactions on Communications*, vol. 25, no. 7, pp. 673–680, 1977.

[30] E. Lutz, D. Cygan, M. Dippold, F. Dolainsky, and W. Papke, "The land mobile satellite communication channel: recording, statistics, and channel model," *IEEE Transactions on Vehicular Technology*, vol. 40, no. 2, pp. 375–386, 1991.

[31] Y. Karasawa, K. Minamisono, and T. Matsudo, "A propaga tion channel model for personal mobilesatellite services," in *Proceedings of Progress of Electromagnetic Research Symposium of the European Space Agency (ESA '95)*, pp. 11–15, Noordwijk , The Netherlands, July 1995.

[32] S. Scalise, C. Alasseur, L. Husson, and H. Ernst, "Accurate and novel modeling of the land mobile satellite channel using reversible jump markov chain monte carlo technique," in *Proceedings of the IEEE Global Telecommunications Conference (GLOBECOM '06)*, pp. 1–6, San Francisco, Calif, USA, November 2006.

[33] M. Milojević, M. Haardt, A. Heuberger, and E. Eberlein, "Channel state modeling for single and multiple satellite broadcasting systems," in *Proceedings of the International Workshop on Satellite and Space Communications (IWSSC '08)*, pp. 102–106, Toulouse, France, October 2008.

[34] H.-P. Lin, R. Akturan, and W. J. Vogel, "Satellite-PCS channel simulation in mobile user environments using photogrammetry and Markov chains," *Wireless Networks*, vol. 3, no. 4, pp. 299–308, 1997.

[35] M. Rieche, D. Arndt, A. Ihlow, and G. Del Galdo, "State modeling of the land mobile satellite channel by an image-based approach," in *Proceedings of the 7th European Conference on Antennas and Propagation (EuCAP '13)*, pp. 672–676, Gothenburg, Sweden, April 2013.

[36] E. Eberlein, A. Heuberger, and T. Heyn, "Channel models for systems with angle diversity—the MiLADY project," in *Proceedings of the ESA Workshop on Radiowave Propagation Models, Tools and Data for Space Systems*, Noordwijk, The Netherlands, December 2008.

[37] L. E. Bråten and T. Tjelta, "Semi-Markov multistate modeling of the land mobile propagation channel for geostationary satellites," *IEEE Transactions on Antennas and Propagation*, vol. 50, no. 12, pp. 1795–1802, 2002.

[38] J. König, D. Arndt, A. Ihlow, and A. Heuberger, "Estimation of fading parameter correlation for modeling the land mobile satellite channel," in *Proceedings of the IEEE International Symposium on Broadband Multimedia Systems and Broadcasting (BMSB '12)*, Seoul, Republic of Korea, June 2012.

Hindawi Publishing Corporation
International Journal of Antennas and Propagation
Volume 2015, Article ID 392714, 15 pages
http://dx.doi.org/10.1155/2015/392714

Research Article

Tracking- and Scintillation-Aware Channel Model for GEO Satellite to Land Mobile Terminals at Ku-Band

Ali M. Al-Saegh,[1] A. Sali,[1] J. S. Mandeep,[2] and Alyani Ismail[1]

[1]*Department of Computer and Communication Systems Engineering, Universiti Putra Malaysia (UPM), 43400 Serdang, Selangor, Malaysia*
[2]*Department of Electrical, Electronic and Systems Engineering, Universiti Kebangsaan Malaysia (UKM), 43600 Bangi, Selangor, Malaysia*

Correspondence should be addressed to Ali M. Al-Saegh; ali.alsaegh84@gmail.com

Received 28 March 2014; Accepted 9 July 2014

Academic Editor: Paschalis Sofotasios

Copyright © 2015 Ali M. Al-Saegh et al. This is an open access article distributed under the Creative Commons Attribution License, which permits unrestricted use, distribution, and reproduction in any medium, provided the original work is properly cited.

Recent advances in satellite to land mobile terminal services and technologies, which utilize high frequencies with directional antennas, have made the design of an appropriate model for land mobile satellite (LMS) channels a necessity. This paper presents LMS channel model at Ku-band with features that enhance accuracy, comprehensiveness, and reliability. The effect of satellite tracking loss at different mobile terminal speeds is considered for directional mobile antenna systems, a reliable tropospheric scintillation model for an LMS scenario at tropical and temperate regions is presented, and finally a new quality indicator module for different modulation and coding schemes is included. The proposed *extended LMS channel (ELMSC)* model is designed based on actual experimental measurements and can be applied to narrow- and wide-band signals at different regions and at different speeds and multichannel states. The proposed model exhibits lower root mean square error (RMSE) and significant performance observation compared with the conventional model in terms of the signal fluctuations, fade depth, signal-to-noise ratio (SNR), and quality indicators accompanied for several transmission schemes.

1. Introduction

The recent applications and services in the broadcasting satellite communication to land mobile terminal have increased the demand for higher data rate and thus higher transmission frequency. Therefore, land mobile satellite (LMS) channel estimation at high frequency has become a necessity to develop efficient adaptive transmission models and techniques as solutions for channel impairments. Considerable interest has been directed recently toward LMS communication at Ku-band [1], which is the main concern of this study, owing to the high number of existing transponders and the large amount of available bandwidth. Nevertheless, Ku-band receivers require a high-gain directional antenna [1]. A new generation of statistical LMS channel models capable of producing time series generative models was initially introduced for lower frequencies, particularly for L and S bands. These models have replaced the ones that solely provide cumulative distribution functions (CDFs), which are insufficient for appropriate investigations [2].

The LMS channel condition at Ku-band depends on mobility impairments and tropospheric scintillation. The latter, which causes rapid fluctuations in satellite signal level, occurs due to the irregularities in radio refractivity as the wave travels along different medium densities in the troposphere [3, 4]. Several researchers [1, 2, 5–10] have created well-designed LMS channel models. The accuracy of the estimated models has increased notably over time through the addition of several features for approaching the real-world environment along with recent LMS technologies and services. This condition has motivated researchers, as well as the authors of this paper, to design more reliable LMS channel models.

However, existing channel models do not consider tropospheric scintillation under nonrainy conditions, which significantly affect the signal performance at Ku-band, particularly at high humidity regions, such as tropical areas [4]. Moreover,

these models do not consider the impairments caused by different vehicle speeds at Ku-band for systems utilizing mobile directional antenna. Therefore, a comprehensive LMS channel modeling that considers these significant impairments is needed to be designed with lower root mean square error (RMSE).

This paper presents a channel model for satellite to land mobile terminals based on actual measured channel conditions. The proposed model is referred to as *extended LMS channel (ELMSC) model*. The term "extended" refers to four new features included in the model design. Firstly, the improvement is based on actual signal measurements to enhance the accuracy and reliability of the previously developed multistate LMS model at Ku-band. Secondly, the impairment attributed to the variable vehicular speeds is modeled concerning the clear line-of-sight (LOS) and shadowing scenarios. Thirdly, an LMS tropospheric scintillation model is developed. Lastly, a quality indicator module is developed and added to the ELMSC model. The model considers tropospheric scintillation and vehicular environments as well as its application to narrow- and wide-band signals worldwide because the LMS environment varies with respect to different regions in the world, particularly in temperate and tropical regions.

The LMS channel characteristics and impairments regarding the mobility and tropospheric scintillation effects are presented in the next section. The experimental setup is enlightened in Section 3 taking into account the mobility impairments for different states accompanied with tropospheric scintillation. The proposed ELMSC model is presented in Section 4. Section 5 provides a discussion of the results obtained from the measurements and proposed model, along with comparisons made concerning the existing models. The conclusion is presented in Section 6.

2. LMS Channel Characterizations and Impairments

Transmission parameters considerably affect the channel characteristics, the amount of signal attenuation, and the quality of service (QoS) of the LMS signal. In particular, the transmitted frequency, bandwidth, and elevation angle exert effects that should be identified by satellite system designers prior to the design process. The amount of signal attenuation is directly proportional to the carrier frequency and inversely proportional to the elevation angle; thus, the signal quality indication metrics, such as the signal-to-noise ratio (SNR) and energy of bit to noise ratio (E_b/N_o), are affected. For signal frequencies below 3 GHz, ionospheric scintillation has a paramount effect on signal performance. This effect begins to disappear as the frequency increases above the said value [11]. The bandwidth effect will be explained in Section 2.1. The mobility impairments and channel states are presented in Sections 2.2 and 2.3, respectively. The tropospheric scintillation effect is discussed in Section 2.4.

2.1. Bandwidth and Directional Antenna. The bandwidth of the signal is considered narrow-band when it is smaller than the coherence bandwidth; otherwise, it is wide-band. The coherence bandwidth, which is inversely proportional to the delay spread, is typically in the range of 7 MHz to 11 MHz at L-band and approximately 30 MHz at EHF band [1, 12]. Under the narrow-band condition, which is the most probable condition in the LMS channel [13], the channel causes signal amplitude variations, whereas the time dispersion (time delay of the received echoes) is insignificant. Under the wide-band condition, the channel not only causes variations in signal amplitude but also experiences significant time dispersion in the received signal. This condition will cause distortion effects, such as frequency selectivity or intersymbol interference; this distortion effect is attributed to the arrival of the signal echoes at the receiver at different excess delays with respect to the direct signal [2].

Practically, the radiation pattern of a directional antenna, which is commonly used in LMS scenarios at Ku-band, filters out the echoes with significant delays; therefore, narrow-band models are typically employed for Ku-band signals for narrow- and wide-band signals [1, 12, 14].

2.2. Mobility. Advanced technologies for satellite communication services have resulted in a significant increase in mobile satellite terminals. This condition gave rise to the demand for the estimation of the mobility effect on the satellite link channel. Mobility impairments are typically produced by the shadowing or blockage of signal energy, multipath, and antenna tracking error. Shadowing is usually caused by roadside trees, whereas blockage is normally caused by surrounding tall buildings or bridges. The multipath effect, which can be modeled by Rayleigh distribution [15], is primarily attributed to nearby buildings in urban areas or mountains.

These major factors affect the performance and quality of the received signal and have motivated LMS system designers to build well-formulated mobility channel models to predict the signal performance of mobile scenarios. For accurate modeling, the model design should be based on actual channel condition measurements. Thus, a number of experiments are conducted to compare the measured results with that of our estimated model (discussed in Section 3). The received signal strength in a tropical region is measured in consideration of the scenarios of signal quality degradation using a mobile receiver system mounted at the roof of a car. To the best of our knowledge, this is the first experiment conducted to determine the mobility effects on satellite link channel conditions in tropical regions.

2.3. Channel States and Conventional Model. According to the type of impairments encountered during the movements, LMS channel models can be categorized into single-state and multistate models [16, 17]. The single-state model describes the signal level distribution of a specific propagation environment over time, such as clear LOS, direct signal blockage, or shadowing states. Typically, in a single-state LMS channel, the unblocked LOS signal is modeled by Rice distribution. The

Rice factor (K) is defined as the ratio of carrier to multipath normalized average power. Consider

$$K = \frac{a^2}{2\sigma^2}, \quad (1)$$

where a is the amplitude of the direct signal and σ is the standard deviation. If the signal is totally blocked, it is usually represented by Rayleigh distribution.

Meanwhile, several researchers have established single-state channel models that focus on the shadowing condition; they defined this state as a combination of two distributions. The most used models for the LMS scenario are Suzuki and Loo models, which have gained global attention [13]. Loo model assumes that, in the case of shadowing, the Rician-distributed direct signal amplitude varies according to a log-normal distribution, and the received complex envelope consists of the sum of the two phasors. The model considers the change in the phase caused by the Doppler effect, which is practically detected by the omnidirectional antenna. Loo model is applied to multistate LMS channel models at L and S bands [10, 16, 18]. Suzuki model is a combination of Rayleigh and log-normal distributions and is conventionally applied to the modeling of multistate LMS channels at Ku-band using directional antenna [1].

However, in a real-world environment, two or more LMS channel states may occur during normal satellite terminal movement. Therefore, the signal performance exhibits several significant transformations in its characteristics over time unlike the terrestrial scenario whose behavior is usually described by a single distribution [2]. In such case, multistate statistical models should be used to design LMS channel models [2, 19].

Based on data obtained from measurement campaigns in Europe, Lutz et al. [8] designed a two-state model that estimates the LMS signal performance under clear sky (Rician distribution) and signal blockage (Rayleigh distribution) conditions. A high-state channel model is typically based on the Markov chain approach [15, 19]. The Markov chain is a stochastic model in which a system takes on discrete states. This approach is commonly used to model the variations in signal performance attributed to shadowing or blockage effects [10]. The correlation between rain impairment and mobility impairment at Ku-band is presented in [9]; they modified the Rice factor to include the rainy sky scenario.

The first stochastic multistate model based on received signal measurements at Ku-band was supported by the European Space Agency (ESA) [1]. A three-state channel model that reflects the proper approach for the real-world environment, including clear sky, shadowing, and blockage scenarios with multipath effect, was employed. The model was built based on the measurement campaign in Germany with a constant high speed of 120 Km/h in a highway environment and lower than 60 Km/h in other environments. However, the receiver antenna was mounted on a mechanically steerable platform during measurements; this condition may cause pointing misalignments and hence a high tracking accuracy error.

The International Telecommunication Union (ITU) [20] recommended the use of a three-state model for statistical-approach LMS channel modeling. Moreover, [2] stated that the three-state model provides a tradeoff between complexity and accuracy. For the aforementioned reasons, a three-state channel is utilized in the proposed model. Thus, the model is compared with the conventional model [1] that also implemented the three-state scenarios at Ku-band, as explained in the previous paragraph. Nevertheless, other states can be added besides the aforementioned three states; however, this condition represents only special case modeling, such as that presented in [10, 18], where a fourth state was added. The former described the fourth state as signal unavailability attributed to the failure of the satellite tracking process for very low elevation angles (lower than 10°), whereas the fourth state of the latter represented multisatellite diversity (angle diversity).

2.4. Tropospheric Scintillation. Tropospheric scintillation occurs inherently as the wave travels along different medium densities in the troposphere and causes rapid fluctuations in satellite signal level due to irregularities in radio refractivity [3, 21]. The standard deviation of fluctuations in tropical regions differs from that in temperate regions owing to their different related weather parameters, particularly the temperature and humidity of the medium. Accordingly, this condition results in different satellite channel assessments and signal quality performance. However, tropical regions are warmer and have higher relative humidity (H_R) than temperate regions for most time of the year [22]. ITU [23] claimed that the fade depth of tropospheric scintillation may reach a few dBs based on its probability of exceedance time.

3. Experimental Setup

To achieve accurate channel estimation, the model design should be based on the measured values of the LMS channel conditions. Several experiments were therefore conducted to measure the received signal level at the receiver (installed in a vehicle) at different mobility impairments. The impairments that occur typically in everyday life were considered (Figure 1), namely, effects attributed to different vehicle speeds (up to 150 Km/h), shadowing by roadside trees, and blockage by crossroad bridges.

The experimental measurements obtained in the southernmost region of Kuala Lumpur in Malaysia are shown in Figure 2. The measurements are represented by the three states listed in Table 1.

A mobile antenna system (upper right image of Figure 2) was used in the measurements setup mounted at the roof of a car (upper left image of Figure 2). The system consists of a 0.44 m mobile autosteerable antenna pointed at MEASAT 3/3A broadcasting satellite (91.5°E) at 76.5° elevation angle. A high tracking rate (75°/sec) antenna was employed to reduce the tracking error as much as possible. The antenna system also includes a built-in motor and gyroscope to point to the satellite automatically. The detection, filtering, and amplification processes were performed by the antenna system

Table 1: Measurements scenarios.

State number	Scenario	Details
State 1	Clear sky/different speeds	The vehicle moved at different speeds (from 0 km/h up to 150 km/h) during clear LOS. Measurements at zero speed (stationary) were obtained as well.
State 2	Shadowing	The vehicle moved at constant speed (40 km/h) under link shadowing by tall trees (approximately 12 m tall and 7 m away from the vehicle on the average) on the roadsides.
State 3	Blockage	The vehicle moved at constant speed (40 km/h) under blockage by road bridges.

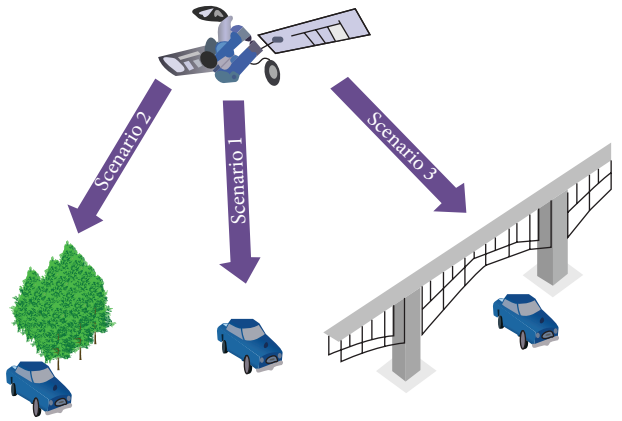

Figure 1: LMS link scenarios.

Figure 2: Measurements campaign.

before the down conversion to L-band IF by a 9.75 GHz local oscillator.

As the signals pass through the mobile antenna system, they are split into two directions as shown in Figure 3; the first direction is toward the decoder, and the second is toward the spectrum analyzer for data evaluation and analysis.

Meanwhile, the relative humidity was obtained on the day of the measurement campaign from the Malaysian Meteorological Department (MMD). The satellite and receiver systems parameters are listed in Table 2.

Typically, when the directional antenna is used, the reflections from buildings come from angles that are different from those in the satellite direction. This condition causes

Table 2: LMS system parameters.

EIRP	57 dBW
Antenna elevation angle	76.5°
Polarization	Horizontal
Antenna local oscillator	9.75 GHz
Radio frequency (RF)	11.68 GHz
Intermediate frequency (IF)	1.93 GHz
Antenna diameter	0.44 m
Antenna tracking rate	75°/s

Table 3: Channel states probabilities.

Probability	Value
P_1	$\frac{836}{875} = 0.955$
P_2	$\frac{21}{875} = 0.024$
P_3	$\frac{18}{875} = 0.021$

the reflections from the buildings to be rarely measured [1]. The measurement campaign was conducted in highway and suburban areas as shown in Figure 2. The areas contain many crossroad bridges, tunnels, and road toll counters (whose sheds cause signal blockages) as well as roadside trees that cause shadowing because of their dense leaves and branches. During the continuous measurements, 837 data recordings were obtained at a clear sky state at various vehicle speeds, whereas 21 and 17 recordings were obtained during signal shadowing and blockage, respectively. The probability of accordance of each state is obtained depending on the aforementioned numbers of recordings and shown in Table 3.

The large number of measured samples is used in the comparison with the measured data to improve the accuracy of the ELMSC model. However, the probability of each state can be assumed in the design of the LMS channel model according to the environment of the specified region of interest.

4. ELMSC Model

Fading channel model and characterization gain the outmost importance for systems utilizing LMS link adaptive techniques and channel-aware modeling performance evaluation and assessment. The proposed model consists of several sections as shown in Figure 4. These sections include the

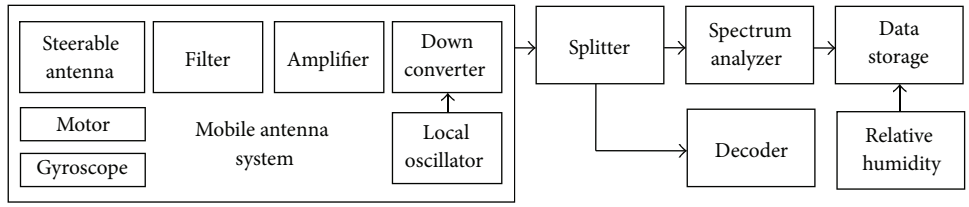

Figure 3: Measurement setup.

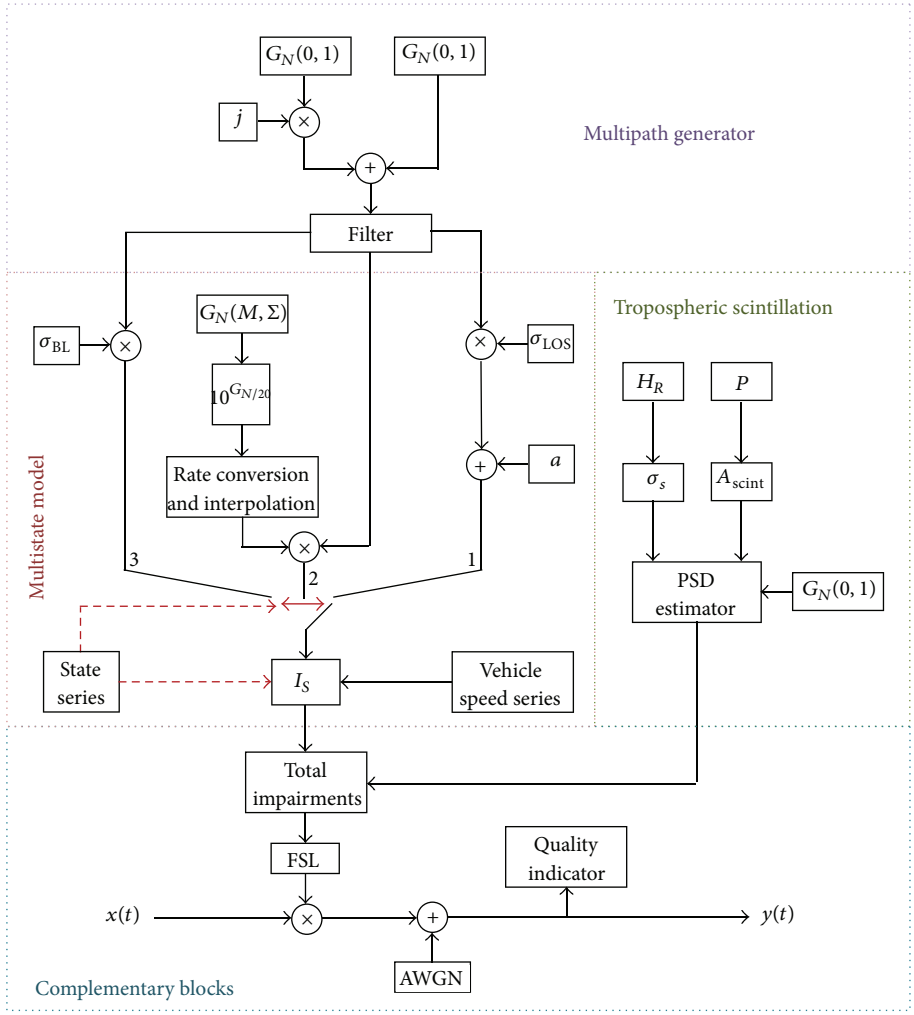

Figure 4: Proposed ELMSC model.

multipath generation, the multistate model, the tropospheric scintillation model, the complementary blocks, and the quality indicator module. The model is designed based on the actual experimental measurements presented in Section 3.

In an actual LMS environment, channel output $y(t)$ can be defined as

$$y(t) = x(t) f(t) + n(t), \tag{2}$$

where $x(t)$ is the transmitted signal, $f(t)$ is the LMS channel fading, and $n(t)$ is the signal noise. The proposed ELMSC model imposes a comprehensive impairments estimation effect which includes the impairments of mobility $m(t)$ and tropospheric scintillation $s(t)$. Consider

$$f_m(t) = m(t) s(t), \tag{3}$$

where $f_m(t)$ is the total mobility impairments. The mobility impairments of the LMS channel include the attenuation attributed to the satellite terminal speed, shadowing or blockage attributed to physical obstacles in the link, and the multipath effect. In practice, both impairments are modeled separately to produce the time series for correlated scintillation and mobility impairments. Afterwards, their values are correlated according to the mobility state environment. The

details of the proposed model blocks are explained in the subsequent subsections.

4.1. Multipath Generator. The diffused multipath fading model can be characterized by Rayleigh distribution [15]. The envelope is a result of the reflected signals from number of paths N as illustrated in (4). Consider

$$r(t) = \sum_{i=1}^{N} A_i(t) \exp\left[j\,\Gamma_i(t)\right], \tag{4}$$

where $A_i(t)$ is the reflected power of the ith signals and $\Gamma_i(t)$ is a coefficient that depends on angular Doppler frequency ω_D as well as angle of arrival β and phase ϕ as expressed in (5). Consider

$$\Gamma_i(t) = \omega_D \cos\beta_i(t) + \phi(t). \tag{5}$$

Therefore, (4) can be rewritten as (6) or (7). Consider

$$r(t) = A(t) \sum_{i}^{N} \cos\Gamma_i(t) + jA(t) \sum_{i}^{N} \sin\Gamma_i(t), \tag{6}$$

$$r(t) = r_I(t) + jr_Q(t), \tag{7}$$

where $r_I(t)$ and $r_Q(t)$ represent the inphase and quadrature components of the Rayleigh distribution, respectively. These two components, as predicted by the central limit theorem, can be produced by first generating two, zero-mean white Gaussian distributions [13, 24] as shown in Figure 4. The standard deviation σ varies with respect to the clear sky, shadowing, and blockage states because the fluctuation level attributed to the multipath effect differs with respect to each state [13]. σ reaches the maximum in the blockage state and minimum in the state of clear LOS. Therefore, σ is included in the multistate model (explained in Section 4.2).

Power spectral shaping is achieved by coloring "filtering" the resultant complex signal. The inphase and quadrature trails are filtered with a Doppler filter to shape "reproduce" the Doppler effects for the fading channel attributed to the motion of the terminal. The filtering process is necessary in simulating the channel. Without this process, the resultant signal variations would be unnaturally fast for a given satellite terminal speed and would thus produce error bursts and distribution of outage durations [25]. Therefore, a Butterworth filter is used in the proposed model; this filter is commonly used in LMS channel modeling because it provides a more realistic approach [13, 24, 26, 27]. The filtering process is designed based on [13, 27].

4.2. Multistate Model. Three states, namely, clear LOS, shadowing, and blockage states, were implemented in the ELMSC model. The model introduces one of the extensions of the ELMSC model that represents the losses of satellite terminal attributed to movements at different speeds (I_S); the new extension is applied to the clear LOS and shadowing states.

The cumulative distribution of the resultant signal should be the weighted combination of the three states [10, 23]. Therefore, the probability behavior for the three states is expressed in (8). Consider

$$P(n \le N) = P_1 m_1 + P_2 m_2 + P_3 m, \tag{8}$$

where n is the sample number from the total number of samples N. P_i is the probability of occurrence of the ith state ($P_1 + P_2 + P_3 = 1$). The probabilities were obtained from the experimental measurements as mentioned in Section 3 and were used to generate random state series. The total time (or number of samples) of being in a specific state depends on the probability of occurrence. The output discrete signal is a result of switching between the generated signal samples of the aforementioned states according to the state series.

4.2.1. Clear LOS Signal Model. The signal received by the mobile satellite terminal moving at different speeds in a clear (unblocked) channel environment is usually modeled with Rician distribution as discussed in Section 2.3. The model includes the constant direct signal with multipath fluctuations. The latter, Rician multipath, is designed by first multiplying the resultant signal from the multipath model discussed in Section 4.1 with its specific standard deviation (σ_{LOS}). The direct signal component (a) is then added to the Rician multipath signal. a is extracted using (1), where K represents the ratio between the direct signal level and the noise floor level. Therefore, our assumption on the Rice factor is based on the actual measurements of the signal. Typically, the noise floor level is assumed based on the measurement setup [1, 2].

Moreover, to estimate the signal losses that may occur because of the antenna tracking error attributed to terminal movements, a new formula is proposed (see (9)) to estimate the signal losses for satellite terminal movements at different speeds in dB based on the actual measurement explained in Section 3. Consider

$$I_S = k_a s^2 + k_b s + k_c, \tag{9}$$

where s is the satellite terminal speed in km/h and the constant values k_a, k_b, and k_c are -4.667×10^{-5}, 1.468×10^{-2}, and -1.364×10^{-3}, respectively. These values were obtained with nonlinear curve-fitting optimization technique; the proposed formula provides accurate mobility impairment estimation with a RMSE of 0.02407. Terminal speed is used as an input to the module. This input series can be generated using sinusoidal distribution random numbers with a minimum value of 0. The maximum value can be assumed based on the nature of the road of interest and its highest permitted speed. Moreover, the probability of speed values can be obtained through statistical observations.

4.2.2. Shadowed Signal Model. The shadowing (state 2) attributed to roadside trees causes additional attenuation to the received signal and thus results in a slow variation in the direct signal simultaneous with the diffuse multipath components. Typically, the shadowed signal at Ku-band is modeled with the Suzuki model [1]. This model involves the combination of log-normal and Rayleigh distributions.

Normal distribution signal G_N is generated with its specific mean M and standard deviation Σ obtained from [1] in dB before being converted to a log-normal distribution using the relation $10^{G_N/20}$. The resultant signal passes through two stages: rate conversation (to identify the slope of the envelop and number of the added samples based on f_S of the fast multipath fluctuations) and interpolation (adding samples between two different leveled samples corresponding to the rate conversation and then convolution for envelope shaping of the interpolated samples). In summary, these steps were implemented to add an interpolated sloped envelop sample to approach the number of multipath samples and to avoid sharp multipath fluctuations. For periods with no state transitions, this rate is utilized to generate rapid variations with a low sampling period to account for the Doppler spread bandwidth [13].

The multipath fluctuations of this state were generated as discussed in Section 4.1. The resultant combination of the two distributions is then obtained to reflect the performance of the signal in the shadowing environment. The impairments that occur primarily because of the antenna tracking error due to the terminal movements, expressed in (9), affect the shadowed signal as well because the direct signal component still exists despite being shadowed. Therefore, in the case of a partially shadowed environment (state 2), the I_S module is also involved in the simulated shadowed signal.

4.2.3. Blocked Signal Model. LMS signal blockage (state 3) is typically caused by bridges across the highway, sheds of the road tolls counters, tunnels, or tall buildings in urban areas. The received signal power vanishes, and the fade depth can be expressed by the noise floor level below the LOS. The LMS signal blockage model is typically designed with Rayleigh distribution with specific standard deviation σ_{BL} as discussed earlier. Therefore, σ_{BL} is applied to the resultant fluctuated signal from the multipath model discussed in Section 4.1. Considering that the direct signal is totally blocked in this state, the signal would be unaffected by the I_S module. The status of the current state is obtained from state series block as shown in Figure 4 to switch the I_S module on during the clear LOS and shadowing states and off during the blockage state.

4.3. Tropospheric Scintillation Model. Tropospheric scintillation depends on its standard deviation (σ_S) [21, 23]. The modeling of tropospheric scintillation effect begins with the generation of a zero-mean white Gaussian distribution and with standard deviation conventionally set to 1 [23, 28]. However, σ_S depends mainly on the relative humidity and the temperature [23], which is different in tropical regions compared with temperate regions according to their weather parameters. For temperate regions, Cioni et al. [28] assumed that the value of σ_S is 0.066. However, it is declared by [22] that the standard deviation of scintillation in tropical regions is larger than that in temperate regions. Therefore, σ_S is adjusted to 0.117 to increase the accuracy of the estimated scintillation standard deviation. The value of σ_S is estimated based on two steps. First, the H_R value was obtained from the MMD as discussed in Section 3. Second, the mean value is used to estimate σ_S according to (10) [23]. Consider

$$\sigma_S = \sigma_0 \, f^{0.583} \frac{g}{(\sin\theta)^{1.2}}, \tag{10}$$

where f is the frequency in GHz, θ is the angle of elevation, and g is the antenna averaging factor that depends mainly on the frequency and antenna parameters. σ_0 can be obtained in dB from the wet term of radio refractivity N_{wet} which, in turn, depends on the value of temperature T and H_R [29]. Consider

$$\begin{aligned} \sigma_0 &= 0.0036 + N_{\mathrm{wet}} \times 10^{-4}, \\ N_{\mathrm{wet}} &= 3732 \times \frac{H_R e_S}{T^2}, \end{aligned} \tag{11}$$

where e_S is the temperature-dependent saturation vapor pressure that can be calculated from [29]. The mean value of H_R measured by MMD is 82.375%. With σ_S, the tropospheric scintillation fade depth A_{scint} is estimated using the ITU model [23] for different probabilities of occurrence (P).

The power spectral density (PSD) of the fading is time variant and can be approximated by low-pass filter (LPF) [28]. The LPF in [28] is used, and the resultant signal is then uniformly distributed and combined with A_{scint} to obtain the estimated signal series of tropospheric scintillation.

4.4. Complementary Blocks and Quality Indicator. The total performance of the correlated impairments is a combination of the LMS multistate mobility and tropospheric scintillation models as declared in (2). However, as the signal passes through the channel, several other constraints cause additional losses, such as system loss and free space loss (FSL). The latter depends on the transmitted frequency and the distance difference between the satellite and the mobile terminal as revealed in (12). Consider

$$\mathrm{FSL} = 20 \log\left(\frac{4\pi d}{\lambda}\right). \tag{12}$$

Consequently, the estimation of the received SNR, which is the received signal power P_r to noise [$P_n = 10\log(k_B \mathrm{TBW})$] ratio is included in the design. Equation (13) [30, 31] is utilized to estimate the received power P_r in dBW. Consider

$$P_r = \mathrm{EIRP} + G_r - \mathrm{FSL} - L_S - L_{\mathrm{LMS}}, \tag{13}$$

where EIRP is the effective isotropic radiated power in dBW that depends on the transmitted power and the transmitter antenna gain; G_r is the receiver gain; L_S is the total system loss; and L_{LMS} is the total LMS channel loss that has not been considered in previous studies, which represents the total fading losses that can be obtained from the ELMSC model. After the insertion of the channel fading effect to the transmitted signal, additive white Gaussian noise (AWGN) is added.

The atmospheric impairments have a negative effect on the data after being demodulated in the receiver. The effect appears, for example, as a decrease in E_b/N_o or packet error

rate. These ratios can be utilized to generate the proposed indexing for optimal physical or link layer adaptations for the current instantaneous transmission time interval (TTI). Equation (14) is used to obtain E_b/N_o (in dB) for widely used modulation schemes and code rates (MODCOD) in satellite communications. Consider

$$\frac{E_b}{N_o} = \frac{E_S}{N_o} - 10\log(K), \tag{14}$$

$$\frac{E_S}{N_o} = \text{SNR} + 10\log\left(\frac{\text{BW}}{R}\right), \tag{15}$$

where $K = \log_2(M) \times R_C$, M is the modulation order, R_C is the code rate, E_s/N_o is the symbol energy to noise ratio, BW is the bandwidth, and R is the symbol rate. For fixed R and BW, E_b/N_o is directly proportional to SNR and inversely proportional to M and R_C. Therefore, after substituting ((12)–(14)) to (15), the estimated E_b/N_o is obtained as shown in (16). Consider

$$\frac{E_b}{N_o} = \text{EIRP} + \frac{G}{T} - 20\log\left(\frac{4\pi d}{\lambda}\right) - L_{\text{LMS}} - L_S - k_B + 10\log\left(\frac{K}{R}\right), \tag{16}$$

where G/T is the figure of merit of the receiver antenna and k_B is the Boltzmann constant. E_b/N_o is used as a quality indicator for the ELMSC model.

5. Results and Discussion

For realistic channel estimation, the estimation was based on the actual measurements of signal performance under dynamic weather conditions. The model design results are organized based on the arrangements of the blocks in Figure 4.

The generated signal (Figure 5(a)) exhibits rapid variation at a transmission frequency of 11.6 GHz. Figure 5(b) shows that the distribution of the resultant signal did not change after filtering.

The state series shown in Figure 5(c) comprises the three states distributed randomly with respect to the probability of occurrence of each state. Figure 6 provides a zoomed in version of Figure 5 to recognize the generated samples clearly. The succeeding results are presented based on the zoomed in version to identify clearly the effect of each block in the ELMSC model. For accurate comparison with other models and better modeled signal resolution, the comparison was based on extended samples as in Figure 5.

The resultant multipath signal passes through the multi-state model with respect to the state series. If the current state is 1, then the multipath signal samples will pass through the clear LOS model, which is composed of three stages. First, the samples are multiplied by σ_{LOS} to obtain the Rician multipath signal. Second, the direct signal component (a) is added. Lastly, I_S is added at different speeds. The resultant clear LOS fading is shown in Figure 7.

The direct signal component (a) is calculated based on (1), where Rice factor $K = 11.5$ dB. The value of K is assumed based on the measurements discussed in Section 3. The channel parameters are listed in Table 4.

During the measurement campaign, vehicle speed was recorded simultaneously with the measurement data to account for the additional losses from the movement of the satellite terminal at different speeds. These losses are mainly due to the pointing misalignment caused by the antenna

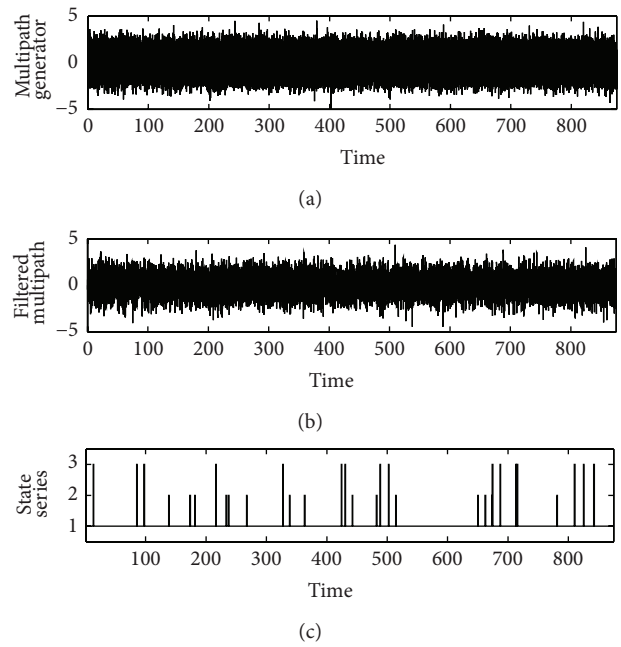

Figure 5: Multipath generated signal and state series: (a) generated samples, (b) filtered signal, and (c) state series.

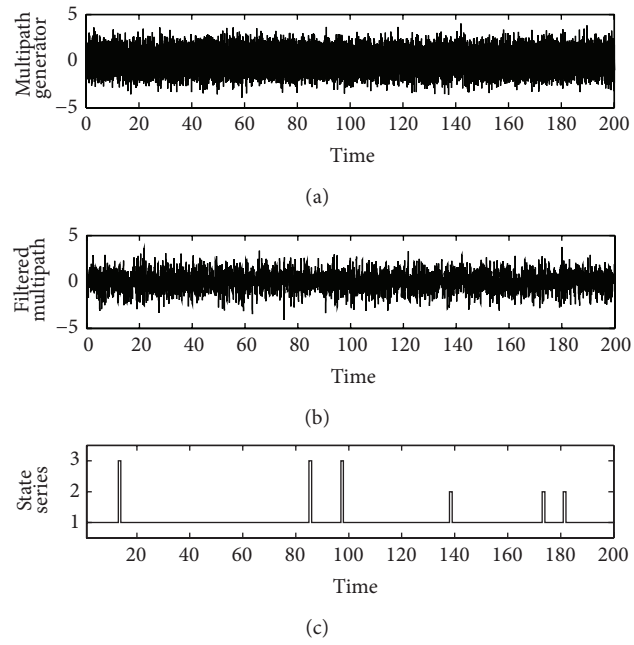

Figure 6: Zoomed in version of the generated signal and state series: (a) generated samples, (b) filtered signal, and (c) state series.

Table 4: Models' parameters.

Parameter	ELMSC	Conventional [1]
Satellite orbit	GEO	GEO
Frequency band	Ku	Ku
Rice K factor	11.5 dB	17 dB
Climatic area	Temperate-tropical	Temperate
Antenna type	Directional antenna	Directional antenna

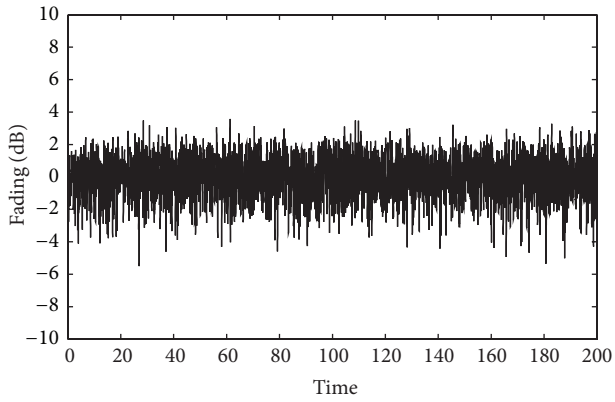

Figure 7: Fading in the clear LOS state.

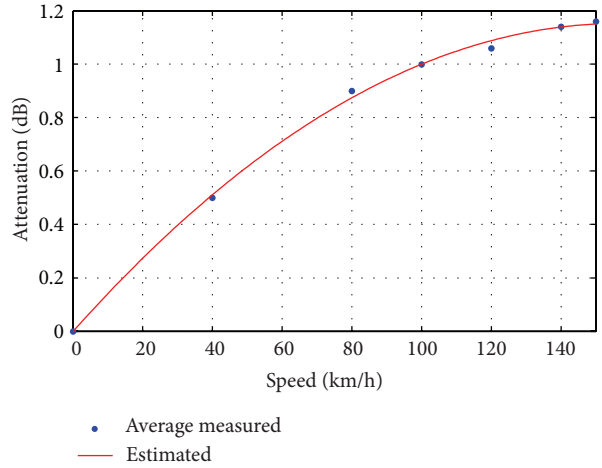

Figure 8: Signal losses with respect to satellite terminal speed.

tracking error. The resultant average measurement data of signal attenuation with respect to satellite terminal speed is shown in Figure 8.

With respect to terminal speed, the average values of several measured signal samples have been obtained. The speed of approximately 40, 80, 100, 120, 140, and 150 km/h has been considered in the measurement campaign as well as the stationary (zero speed) case. The measurements show that the signal is further attenuated by 0.6 dB when the terminal moves at 60 km/h. The attenuation slope changes when the speed reaches 80 km/h. The attenuation level increases more slightly than when speed is below 80 km/h. The losses reach approximately 1 dB at 100 Km/h, 1.15 dB at 140 Km/h, and 1.18 dB at 150 Km/h. However, as discussed in Section 4.2 and expressed in Figure 8, the proposed equation (9) provides an accurate estimation of signal performance at different terminal speeds with RMSE equal to 0.02407. To the best of our knowledge, this model is the first to be designed for the estimation of LMS channel impairments at different terminal speeds based on measurement data at the Ku-band.

Based on the experimental measurements in the clear LOS scenario, the signal model at state 1 provides less RMSE estimation than the conventional model proposed earlier. This finding can be clearly proven by comparing the CDF and PDF of the measured SNR and the conventional model with the proposed model. After adding the effect of FSL from (12) to obtain the channel fade and AWGN to the transmitted signal carrier, the CDF and PDF of the estimated received power were obtained as shown in Figure 9.

To identify the effect of the proposed multistate part of the ELMSC model with respect to the clear LOS measured signal and conventional model, Figure 9 shows the CDF and PDF of the received SNR prior to the addition of the proposed tropospheric scintillation model. The effect of the proposed I_S module appeared as a change in the slope difference of CDF as shown in Figure 9(a). This leads to a decrease in the RMSE of the proposed model, whereas the change in the K factor shifted the CDF for few dBs towards the measured value, which approaches the CDF slope of the measured SNR compared with the conventional model. Until this point, the PDF performance of the proposed model exhibits a significant enhancement compared with the conventional model such that it approaches the PDF of the measured SNR and will be further enhanced if tropospheric scintillation is included.

In the case of state 2, the shadowing model is applied to the generated multipath signal in Figure 5(b). The model is a combination of two distributions. The slow variation trail is composed of three stages before the addition of rapid variation. Finally, the signal passes through the proposed I_S block as discussed in Section 4.2. The effect of these steps is shown in Figure 10.

The slow variation trail begins with the generation of random normal distribution samples. One of the objectives of the experimental measurements is to measure the average power absorption for each scenario. 13 dB mean value is used as proposed in [32].

The distribution is then converted to a log-normal distribution before rate conversion and interpolation as discussed in Section 4.2 and shown in Figure 10(a). Figure 10(b) shows that the signal variation performance does not change after this step, except for the higher number of samples that accounts for the generated rapid variations. Figure 10(c) shows the simulated shadowing fade.

The signal level in a full blocking environment (state 3) usually reaches the noise floor level, as discussed in Section 4.2, with multipath fluctuations of specific standard deviation σ_{BL} that is typically greater than σ_{LOS} [13]. Therefore, the resultant signal from the multipath generator is multiplied by the value of σ_{BL}, which is assumed according to

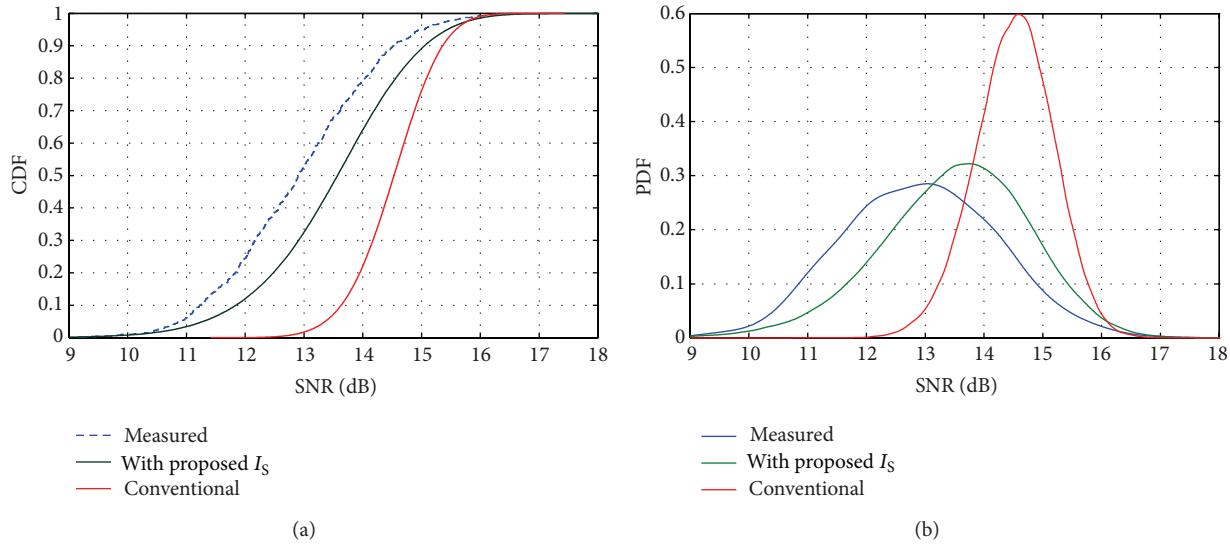

Figure 9: Received SNR in clear LOS state: (a) CDF and (b) PDF.

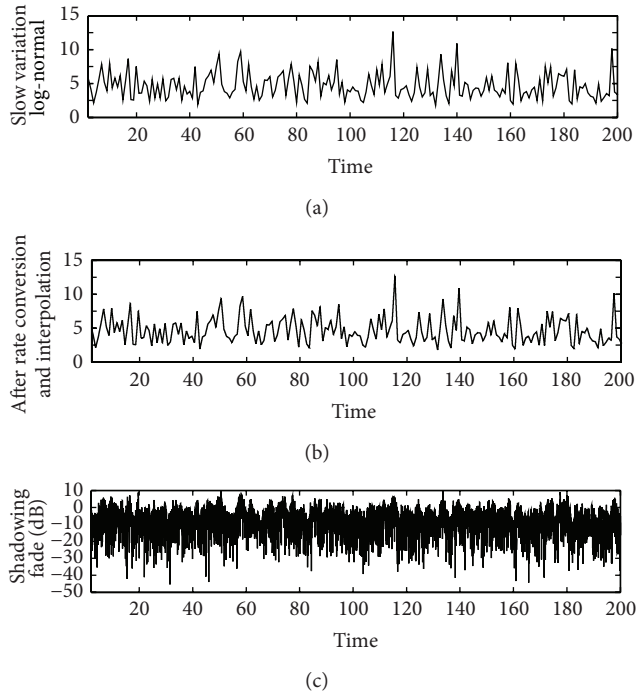

Figure 10: Simulated fade attributed to shadowing: (a) the generated slow variation lognormal distribution, (b) signal after rate conversion and interpolation, and (c) the aggregated fade.

[1]. However, the simulated signal of the multistate model is a result of the switching process of the three aforementioned states. Switching control is based on the state series generated (shown in Figure 5(c)).

Another remarkable impairment to the LMS channel is tropospheric scintillation which gives rise to signal turbulence because of the rapid change in the refractive index of the medium. The change in the refractive index of the medium is because of the water particles in the troposphere. Therefore, the H_R percentage has a vital role in the signal performance and standard deviation of fluctuations.

H_R is varied from one region to another according to their different weather parameters. Therefore, two different signals were modeled each with its specific region, one with lower standard deviation of fluctuation as proposed by [28] represents a temperate region and the other proposed in this study for higher humidity regions as in tropics based on the measured H_R discussed in Section 4.3. Figure 11 shows the

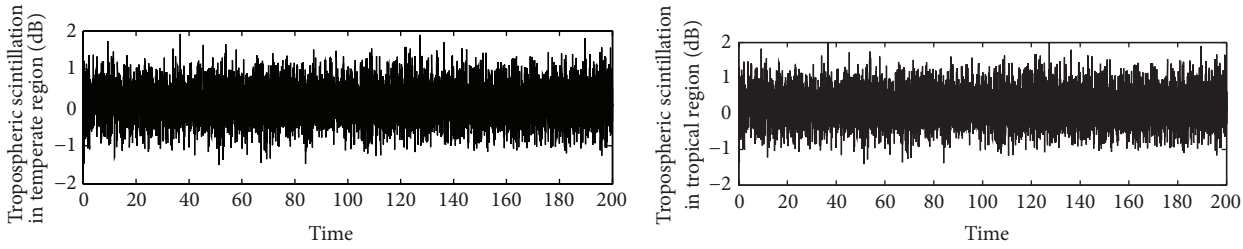

Figure 11: Modeled fluctuations caused by tropospheric scintillation: (a) temperate region and (b) tropical region LMS link scenarios.

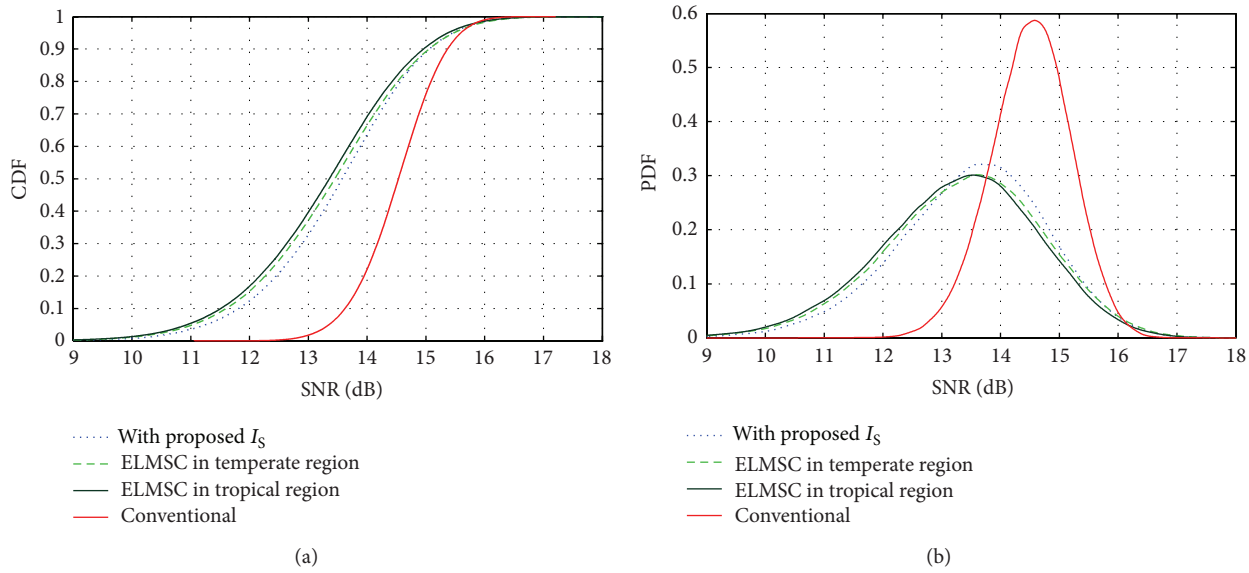

Figure 12: Tropospheric scintillation effect: (a) CDF and (b) PDF.

estimated tropospheric scintillation performance according to the proposed model.

Figure 11 shows the difference in the estimated signal samples between temperate and tropical regions. To identify the effect of tropospheric scintillation clearly in both regions, Figure 12 shows the CDF and PDF of the received SNR in temperate and tropical regions for clear LOS state after adding the tropospheric scintillation effect.

It is shown in Figure 12 that the distribution of the samples in tropical regions is different from the temperate regions according to its weather parameters especially the higher relative humidity and hence higher water particles which cause extra fluctuations compared with the temperate regions. Therefore, the fluctuation performance reflects a change in CDF and PDF with respect to the original distribution functions when tropospheric scintillation is excluded. It can be noticed that the peak value of the PDF of the estimated SNR in tropical region is moved to lower SNR because of the different weather parameters and approaches the peak value of the measured SNR (as seen later in Figure 14). As discussed in Section 2.4, fade depth depends on the probability of exceedance time (P). Figure 13 shows the tropospheric scintillation effect for several fade depths at different P.

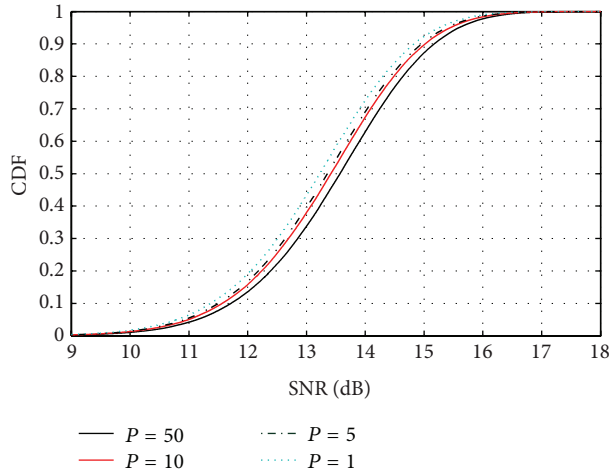

Figure 13: Tropospheric scintillation effect at different P.

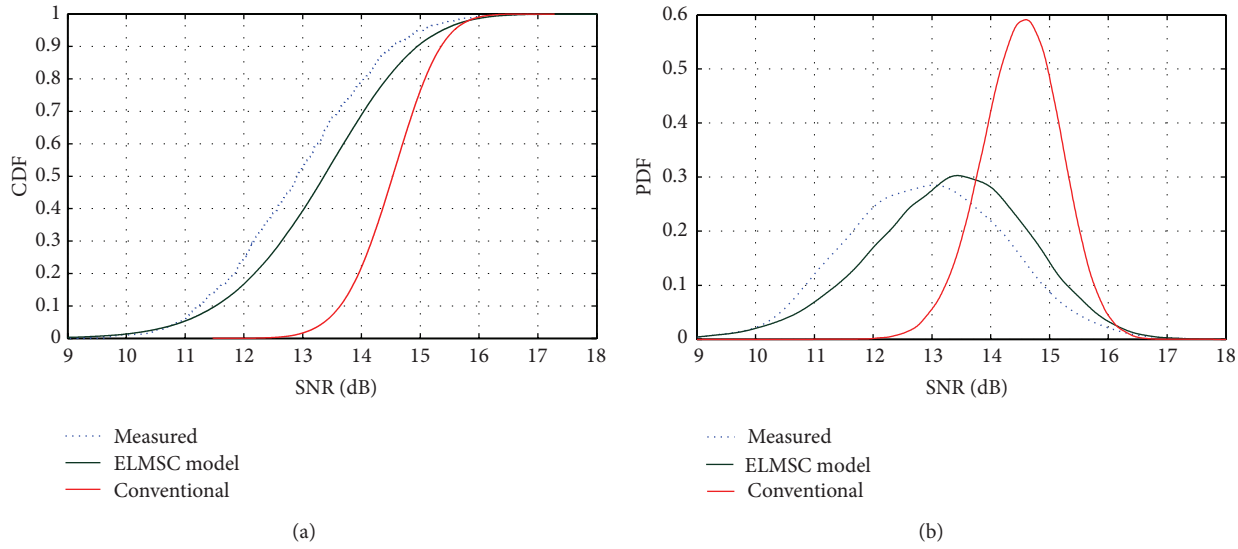

Figure 14: Comparison of channel models with the measured SNR: (a) CDF and (b) PDF.

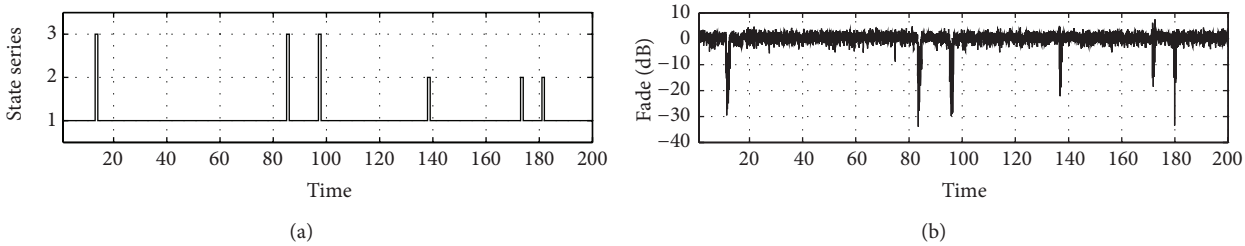

Figure 15: Signal performance of the ELMSC model: (a) state series and (b) signal fade.

The probability of exceedance time significantly affects the distribution function. P is directly proportional to fade depth; the highest level reached $P \geq 1$.

The effect of P was predicted based on the experimental measurements obtained by ITU [23]. The proposed ELMSC model at tropical regions in clear LOS is compared with the measurement data (discussed in Section 3) and the conventional model used, as shown in Figure 14.

The CDF and PDF show that the ELMSC model provides less RMSE regarding the estimation of the channel compared with the conventional model. The PDF of the proposed model reached a peak value of approximately 0.3 among 8 dBs. This value approaches the measured value (difference = 0.02). By contrast, the conventional model reached the peak value of approximately 0.59 among 5 dBs, which significantly differs from the measured value (difference = 0.31). Table 5 shows the RMSE and the differences in variance and PDF's peak values of the ELMC and conventional model compared with the measured time series signal. The proposed fade for three states is shown in Figure 15.

The variance in fluctuation during state 1 is equal to 1.8133, which approaches the measured value of 1.6408 and is closer than the value of conventional variance (0.4508). The minimum duration for one state is set to four times the sampling period to reflect the real-world environment, such that, when the mobile terminal passes under trees, it usually stays in this environment for more than one sample period.

Table 5: Comparison with the measured data.

Parameter	ELMSC	Conventional [1]
RMSE	0.0262	0.1268
PDF's peak value difference	0.02	0.31
Variance difference	0.1725	1.3625

The quality indicator included in the model is used to identify the channel quality in several widely used modulation schemes and code rates (MODCODs) that are used in video broadcasting protocols such as digital video broadcasting via satellite-second generation (DVB-S2) [33]. Figure 16 shows the mean E_b/N_o value for the three states. These values were estimated at the input of the decoder.

E_b/N_o is used as a quality indicator for the ELMSC model. The value is examined at different MODCODs. E_b/N_o determines the availability of the received signal as well as its quality. Availability is determined based on the value of a quality indicator. Therefore, to achieve signal availability for systems that use, for example, a minimum E_b/N_o value of 4 dB, the signal is available in the clear LOS scenario at all times. In the shadowing scenario, the signal is available

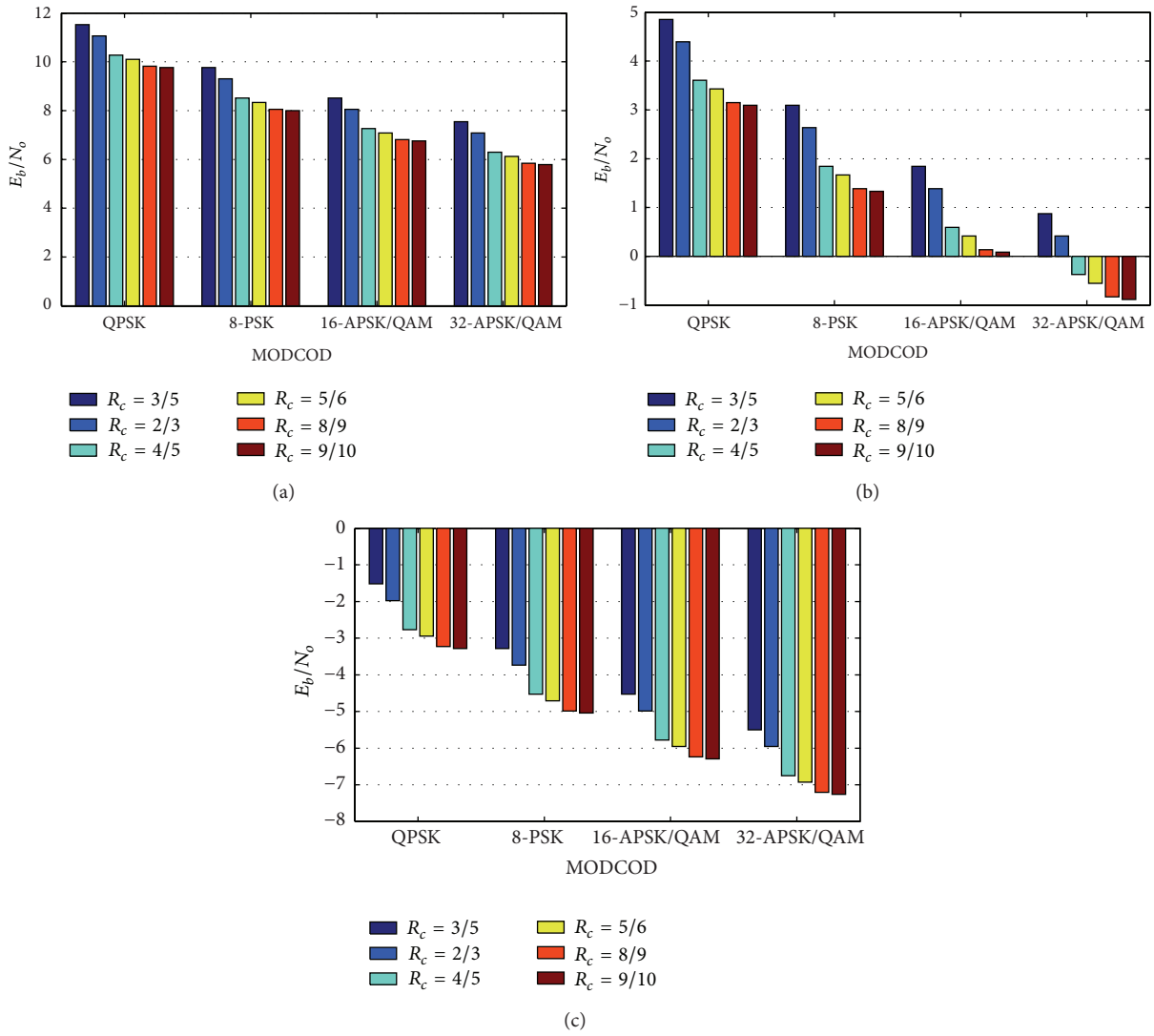

FIGURE 16: E_b/N_o (in dB) at different MODCODs: (a) clear LOS, (b) shadowing, and (c) blockage scenarios.

when QPSK at $R_C = 3/5$ and 2/3 only, whereas no signal is available in the blockage state. Moreover, the values of E_b/N_o at different MODCODs and environments can determine the error rates in the data received. Therefore, the quality indicator is essential in the design of the channel model to specify the availability and error rates for the signal under different channel conditions and system parameters.

6. Conclusion

A model for LMS channel modeling at the Ku-band was presented in this study based on experimental measurements. The design considers the three typical channel states, namely, clear LOS, shadowing, and blockage states. The proposed model has new features and was proven to be comprehensive, reliable, and less RMSE than conventional model. The channel states were modeled and combined with the new module to account for the satellite tracking error attributed to the dynamic terminal speeds. The tropospheric scintillation impairments were presented and modeled for the LMS scenario at temperate and tropical regions. Finally, a quality indicator module was presented and included in the proposed ELMSC model. The measurement data were provided, and the time series synthesizer, PDF, and CDF of the proposed model were presented and compared with the conventional model. A fairly good agreement was observed between the proposed ELMSC model outputs and the measurements. The model can be applied to temperate and tropical regions for narrow- and wide-band signals at various modulation and coding schemes and different satellite terminal speeds. The model and its associated modules can be used to study the signal performance, availability, and error rates of different services, including communications, broadcast, and navigation, as well as to develop fade mitigation techniques for channel-aware strategies.

Conflict of Interests

The authors declare that there is no conflict of interests regarding the publication of this paper.

Acknowledgment

The support provided by the Ministry of Higher Education in Malaysia through project grant code ERGS/1-2012/5527096 is duly acknowledged.

References

[1] S. Scalise, H. Ernst, and G. Harles, "Measurement and modeling of the land mobile satellite channel at Ku-band," *IEEE Transactions on Vehicular Technology*, vol. 57, no. 2, pp. 693–703, 2008.

[2] F. P. Fontán, M. Vázquez-Castro, C. E. Cabado, J. P. García, and E. Kubista, "Statistical modeling of the LMS channel," *IEEE Transactions on Vehicular Technology*, vol. 50, no. 6, pp. 1549–1567, 2001.

[3] A. M. Al-Saegh, A. Sali, J. S. Mandeep, and A. Ismail, "Extracted atmospheric impairments on earth-sky signal quality in tropical regions at Ku-band," *Journal of Atmospheric and Solar-Terrestrial Physics*, vol. 104, pp. 96–105, 2013.

[4] J. S. Mandeep and Y. Y. Ng, "Satellite beacon experiment for studying atmospheric dynamics," *Journal of Infrared, Millimeter, and Terahertz Waves*, vol. 31, no. 8, pp. 988–994, 2010.

[5] C. Loo and N. Secord, "Computer models for fading channels with applications to digital transmission," *IEEE Transactions on Vehicular Technology*, vol. 40, no. 4, pp. 700–707, 1991.

[6] G. E. Corazza and F. Vatalaro, "Statistical model for land mobile satellite channels and its application to nongeostationary orbit systems," *IEEE Transactions on Vehicular Technology*, vol. 43, no. 3, pp. 738–742, 1994.

[7] M. Pätzold, U. Killat, and F. Laue, "An extended suzuki model for land mobile satellite channels and its statistical properties," *IEEE Transactions on Vehicular Technology*, vol. 47, no. 2, pp. 617–630, 1998.

[8] E. Lutz, D. Cygan, M. Dippold, F. Dolainsky, and W. Papke, "The land mobile satellite communication channel—recording, statistics, and channel model," *IEEE Transactions on Vehicular Technology*, vol. 40, no. 2, pp. 375–386, 1991.

[9] K. P. Liolis, A. D. Panagopoulos, and S. Scalise, "On the combination of tropospheric and local environment propagation effects for mobile satellite systems above 10 GHz," *IEEE Transactions on Vehicular Technology*, vol. 59, no. 3, pp. 1109–1120, 2010.

[10] D. Rey Iglesias and M. G. Sanchez, "Semi-Markov model for low-elevation satellite-earth radio propagation channel," *IEEE Transactions on Antennas and Propagation*, vol. 60, no. 5, pp. 2481–2490, 2012.

[11] A. D. Panagopoulos, P. D. M. Arapoglou, and P. G. Cottis, "Satellite communications at KU, KA, and V bands: propagation impairments and mitigation techniques," *IEEE Communications Surveys & Tutorials*, vol. 6, no. 3, pp. 2–14, 2004.

[12] S. Scalise, R. Mura, and V. Mignone, "Air interfaces for satellite based digital TV broadcasting in the railway environment," *IEEE Transactions on Broadcasting*, vol. 52, no. 2, pp. 158–166, 2006.

[13] F. P. Fontan, A. Mayo, D. Matote et al., "Review of generative models for the narrowband land mobile satellite propagation channel," *International Journal of Satellite Communications and Networking*, vol. 26, no. 4, pp. 291–316, 2008.

[14] A. Vanelli-Coralli, G. E. Corazza, G. K. Karagiannidis et al., "Satellite communications: research trends and open issues," in *Proceedings of the International Workshop on Satellite and Space Communication (IWSSC '07)*, pp. 71–75, September 2007.

[15] Z. K. Adeyemo, O. O. Ajayi, and F. K. Ojo, "Simulation model for a frequency-selective land mobile satellite communication channel," *Innovative Systems Design and Engineering*, vol. 3, pp. 71–84, 2012.

[16] M. Milojević, M. Haardt, E. Eberlein, and A. Heuberger, "Channel modeling for multiple satellite broadcasting systems," *IEEE Transactions on Broadcasting*, vol. 55, no. 4, pp. 705–718, 2009.

[17] A. Abdi, W. C. Lau, M. Alouini, and M. Kaveh, "A new simple model for land mobile satellite channels: first- and second-order statistics," *IEEE Transactions on Wireless Communications*, vol. 2, no. 3, pp. 519–528, 2003.

[18] D. Arndt, A. Ihlow, T. Heyn, A. Heuberger, R. Prieto-Cerdeira, and E. Eberlein, "State modelling of the land mobile propagation channel for dual-satellite systems," *EURASIP Journal on Wireless Communications and Networking*, vol. 2012, pp. 1–21, 2012.

[19] A. Mehmood and A. Mohammed, "Characterisation and channel modelling for satellite communication systems," in *Satellite Communications*, N. Diodato, Ed., pp. 133–152, InTech, Rijeka, Croatia, 2010.

[20] ITU, *Propagation Data Required for the Design of Earth-Space Land Mobile Telecommunication Systems*, International Telecommunication Union—Recommandation, 2009.

[21] A. Adhikari and A. Maitra, "Studies on the inter-relation of Ku-band scintillations and rain attenuation over an Earth-space path on the basis of their static and dynamic spectral analysis," *Journal of Atmospheric and Solar-Terrestrial Physics*, vol. 73, no. 4, pp. 516–527, 2011.

[22] A. Adhikari, A. Bhattacharya, and A. Maitra, "Rain-induced scintillations and attenuation of ku-band satellite signals at a tropical location," *IEEE Geoscience and Remote Sensing Letters*, vol. 9, no. 4, pp. 700–704, 2012.

[23] ITU, "Propagation data and prediction methods required for the design of Earth-space telecommunication systems," Tech. Rep. P.618-11, International Telecommunication Union—Recommandation, 2013.

[24] P. Burzigotti, R. Prieto-Cerdeira, A. Bolea-Alamañac, F. Perez-Fontan, and I. Sanchez-Lago, "DVB-SH analysis using a multi-state land mobile satellite channel model," in *Proceeding of the 4th Advanced Satellite Mobile Systems (ASMS '08)*, pp. 149–155, Bologna, Italy, August 2008.

[25] F. Pérez Fontán and P. Mariño Espiñeira, "Multipath: narrowband channel," in *Modeling the Wireless Propagation Channel*, chapter 5, pp. 105–135, John Wiley & Sons, 2008.

[26] R. Prieto-Cerdeira, F. Perez-Fontan, P. Burzigotti, A. Bolea-Alamaac, and I. Sanchez-Lago, "Versatile two-state land mobile satellite channel model with first application to DVB-SH analysis," *International Journal of Satellite Communications and Networking*, vol. 28, no. 5-6, pp. 291–315, 2010.

[27] F. Pérez Fontán and P. Mariño Espiñeira, "The land mobile satellite channel," in *Modeling the Wireless Propagation Channel*, chapter 9, pp. 213–227, John Wiley & Sons, New York, NY, USA, 2008.

[28] S. Cioni, R. de Gaudenzi, and R. Rinaldo, "Channel estimation and physical layer adaptation techniques for satellite networks

exploiting adaptive coding and modulation," *International Journal of Satellite Communications and Networking*, vol. 26, no. 2, pp. 157–188, 2008.

[29] ITU, "The radio refractive index: its formula and refractivity data," in *International Telecommunication Union—Recommandation*, pp. 453–510, 2012.

[30] L. J. Ippolito, *Satellite Communications Systems Engineering: Atmospheric Effects, Satellite Link Design and System Performance* , Wiley, New York, NY, USA, 2008.

[31] V. K. Sakarellos, D. Skraparlis, A. D. Panagopoulos, and J. D. Kanellopoulos, "Outage performance analysis of a dual-hop radio relay system operating at frequencies above 10 GHz," *IEEE Transactions on Communications*, vol. 58, no. 11, pp. 3104–3109, 2010.

[32] F. Pérez Fontán and P. Mariño Espiñeira, "Shadowing and multipath," in *Modeling the Wireless Propagation Channel*, chapter 6, pp. 137–151, John Wiley & Sons, New York, NY, USA, 2008.

[33] ETSI, "Digital Video Broadcasting (DVB) ; second generation framing structure, channel coding and modulation systems for broadcasting interactive services, news gathering and other broadband satellite applications (DVB-S2)," Tech. Rep. EN 302 307 V1.3.1, ETSI, 2013.

Hindawi Publishing Corporation
International Journal of Antennas and Propagation
Volume 2014, Article ID 328732, 8 pages
http://dx.doi.org/10.1155/2014/328732

Research Article

On the Bivariate Nakagami-Lognormal Distribution and Its Correlation Properties

Juan Reig, Lorenzo Rubio, and Vicent M. Rodrigo-Peñarrocha

Grupo de Radiación Electromagnètica (GRE), Universitat Politècnica de València, Camino de Vera s/n, 46022 Valencia, Spain

Correspondence should be addressed to Juan Reig; jreigp@dcom.upv.es

Received 9 May 2014; Accepted 27 June 2014; Published 18 August 2014

Academic Editor: Jose F. Paris

Copyright © 2014 Juan Reig et al. This is an open access article distributed under the Creative Commons Attribution License, which permits unrestricted use, distribution, and reproduction in any medium, provided the original work is properly cited.

The bivariate Nakagami-lognormal distribution used to model the composite fast fading and shadowing has been examined exhaustively. In particular, we have derived the joint probability density function, the cross-moments, and the correlation coefficient in power terms. Also, two procedures to generate two correlated Nakagami-lognormal random variables are described. These procedures can be used to evaluate the robustness of the sample correlation coefficient distribution in both macro- and microdiversity scenarios. It is shown that the bias and the standard deviation of this sample correlation coefficient are substantially high for large shadowing standard deviations found in wireless communication measurements, even if the number of observations is considerable.

1. Introduction

In wireless communications, the received signal is subjected to fading due to two physical mechanisms. On one hand, the multipath components cause rapid and deep fading in displacements of few wavelengths (small-scale area). This is the well-known short-term fading or fast fading, which has been extensively analyzed in the literature [1, 2]. This fast fading has been modeled statistically using the Rice, Rayleigh, Nakagami-m, and Weibull distributions. The Nakagami-m distribution is frequently employed to model the fast fading since it fits better than the other distributions in many measurement campaigns [3, 4]. On the other hand, the received signal fluctuates slowly around a mean in displacements of hundreds of wavelengths (large-scale area). This variation is known as long-term fading or shadowing. This shadowing is due to the temporal blockage of the direct component between the transmitter and receiver terminals. The shadowing is commonly modeled statistically by a lognormal distribution. Values of standard deviations for shadowing reported in the literature range from 5 to 12 dB in macrocells, from 6 to 10 dB in microcells, and from 3 to 10 dB in indoor environments [5].

In the analysis of wireless propagation channels, these components are traditionally separated to model both the fast fading and shadowing. Nevertheless, this separation is troublesome in scenarios as in indoor and vehicular channels, where the variation of the received signals is considerably high, with few displacements in terms of the wavelength, and thus these effects are severely overlapped.

Therefore, several distributions have been proposed to describe the composite fast fading and shadowing. Initially, the Rayleigh-lognormal distribution was used by Suzuki to model this compound fading [6]. Also, the Nakagami-lognormal distribution has been employed to model the composite fading [7–9]. Recently, some other distributions as the α-μ [10], the generalized-K [11], or the mixture gamma (MG) distribution [12] have been proposed in the literature. Nevertheless, the results derived from a measurement campaign carried out in a macrocellular urban environment [13] have shown that the Nakagami-lognormal is the best-fit distribution compared with the Rayleigh-lognormal, α-μ, and generalized-K distributions.

The effect of the correlated shadowing or correlated fast fading on the performance parameters in wireless communication diversity has attracted the attention of several researches [14–19]. Nevertheless, all the above works have assumed either correlated fast fading with independent shadowing or correlated shadowing with independent fast fading.

Therefore, to the best of the authors' knowledge an analysis of the general bivariate distribution Nakagami-lognormal with correlated both fading and shadowing and arbitrary fading parameters is novel in the literature.

Thus, in this paper the joint probability density function (PDF) and the cross-moments of the bivariate Nakagami-lognormal distribution are derived. Also, we have focused our attention on calculating the correlation coefficient between the composite signals. This correlation coefficient is particularized for two wireless scenarios of interest: macro- and microdiversity cases.

Two procedures to generate two correlated Nakagami-lognormal random variables (RVs) are proposed and several examples for the sample correlation coefficient are evaluated in both macro- and microdiversity scenarios.

This paper is organized as follows. First, the joint PDF, the central moments, and the correlation coefficient of the Nakagami-lognormal distribution are derived in Section 2. Second, in Section 3 we describe two procedures for generating Nakagami-lognormal RVs and several results are analyzed. Finally, the conclusions are discussed in Section 4.

2. Bivariate Nakagami-Lognormal Distribution

2.1. Joint Probability Density Function. Let r_{f_1} and r_{f_2} be correlated Nakagami-m RVs, representing fast fading processes with the same mean power equal to unity, whose marginal PDFs are given by

$$p_{r_{f_j}}\left(r_{f_j}\right) = \frac{2}{\Gamma\left(m_j\right)} m_j^{m_j} r_{f_j}^{2m_j-1} \exp\left(-m_j r_{f_j}^2\right), \quad r_{f_j} \geq 0, \quad j = 1, 2, \tag{1}$$

where m_j is the fading parameter and $\Gamma(z) = \int_0^\infty t^{z-1}e^{-t}dt$ is the Gamma function [20, (6.1.1)].

The correlation coefficient between r_{f_1} and r_{f_2} in power terms can be expressed as

$$\rho_f = \frac{E\left(r_{f_1}^2 r_{f_2}^2\right) - E\left(r_{f_1}^2\right)E\left(r_{f_2}^2\right)}{\sqrt{\operatorname{var}\left(r_{f_1}^2\right)\operatorname{var}\left(r_{f_2}^2\right)}}, \tag{2}$$

where var(·) denotes the variance.

We can define r_{s_1} and r_{s_2} as correlated lognormal RVs corresponding to shadowing processes, whose marginal PDFs can be written as

$$p_{r_{s_j}}\left(r_{s_j}\right) = \frac{1}{\sqrt{2\pi}\sigma_j r_{s_j}} \exp\left(-\frac{\left(\ln\left(r_{s_j}\right) - \mu_j\right)^2}{2\sigma_j^2}\right), \quad r_{s_j} \geq 0, \quad j = 1, 2, \tag{3}$$

where

$$\mu_j = \frac{\ln(10)}{10}\mu_{dj}, \tag{4}$$

$$\sigma_j = \frac{\ln(10)}{10}\sigma_{dj}, \tag{5}$$

μ_{dj} being the mean of the associated Gaussian process of the shadowing, expressed in dBV/m, σ_{dj} the standard deviation of the associated normal distribution corresponding to the lognormal shadowing, expressed in dB. The power correlation coefficient between the associated Gaussian processes, $x_1 = 20\log r_{s_1}$ and $x_2 = 20\log r_{s_2}$, is denoted by ρ_s and it is defined in the same way as (2), by substituting x_1 and x_2 for r_{f_1} and r_{f_2}, respectively.

If we calculate $r_j = r_{f_j} \cdot r_{s_j}$, $j = 1, 2$, then r_j is Nakagami-lognormal distributed, with PDF given by

$$p_{r_j}\left(r_j\right) = \int_0^\infty \frac{2}{\Gamma\left(m_j\right)}\left(\frac{m_j}{\Omega_j}\right)^{m_j} r_j^{2m_j-1} \exp\left(-\frac{m_j r_j^2}{\Omega_j}\right) \times \frac{1}{\sqrt{2\pi}\sigma_j\Omega_j} \exp\left(-\frac{\left(\ln\left(\Omega_j\right) - \mu_j\right)^2}{2\sigma_j^2}\right) d\Omega_j \quad r_j \geq 0, \tag{6}$$

where Ω_j is a lognormal RV which represents the shadowing process. Note that the PDF given by (6) corresponds to the Nakagami-lognormal PDF in power terms given by [8, (8)].

The nth moment of r_j, $j = 1, 2$, is calculated as

$$E\left(r_j^n\right) = \frac{\Gamma\left(m_j + n/2\right)}{m_j^{n/2}\Gamma\left(m_j\right)} \exp\left(\frac{n}{2}\mu_j + \frac{n^2}{8}\sigma_j^2\right), \tag{7}$$

where $E(\cdot)$ denotes expectation. Note that (7) is equivalent to [21, (2.59)] by substituting $2n$ instead of n in (7), which corresponds to the nth moment of the Gamma-lognormal distribution.

Combining [22, (2.1)] and [23, (12)], the joint PDF of r_1 and r_2 can be obtained as

$$p_{r_1,r_2}(r_1, r_2) = 4\left(1-\delta_f\right)^{m_2} \sum_{k=0}^{\infty} \frac{(m_1)_k}{\Gamma(m_1+k)\Gamma(m_2+k)k!} \times \delta_f^k r_1^{2(m_1+k)-1} r_2^{2(m_2+k)-1} \times \int_0^\infty \int_0^\infty \left(\frac{m_1}{\Omega_1\left(1-\delta_f\right)}\right)^{m_1+k} \left(\frac{m_2}{\Omega_2\left(1-\delta_f\right)}\right)^{m_2+k} \times \exp\left[-\left(\frac{m_1 r_1^2}{\Omega_1\left(1-\delta_f\right)} + \frac{m_2 r_2^2}{\Omega_2\left(1-\delta_f\right)}\right)\right] \times {}_1F_1\left(m_2 - m_1, m_2 + k; \frac{m_2\delta_f}{\Omega_2\left(1-\delta_f\right)} r_2^2\right) \times \frac{1}{2\pi\Omega_1\Omega_2\sigma_1\sigma_2\sqrt{1-\rho_s^2}} \exp\left(-\frac{q}{2}\right) d\Omega_1 d\Omega_2, \tag{8}$$

being

$$q = \frac{1}{1-\rho_s^2}\left[\left(\frac{\ln\Omega_1-\mu_1}{\sigma_1}\right)^2+\left(\frac{\ln\Omega_2-\mu_2}{\sigma_2}\right)^2 -2\rho_s\left(\frac{\ln\Omega_1-\mu_1}{\sigma_1}\right)\left(\frac{\ln\Omega_2-\mu_2}{\sigma_2}\right)\right], \tag{9}$$

where $(a)_b = \Gamma(a+b)/\Gamma(a)$ is the Pochhammer symbol [20, (6.1.22)], ${}_1F_1(\cdot,\cdot;\cdot)$ is the confluent hypergeometric function [20, (13.1.2)], and $\delta_f = \rho_f\sqrt{m_2/m_1}$. The Nakagami-$m$ variables in (8) are ordered to fulfill the condition $m_2 \geq m_1$ [23]. Thus, the correlation coefficient between the Nakagami-m processes in power terms is limited to $\rho_f < \sqrt{m_1/m_2}$.

The joint bivariate Nakagami-lognormal PDF can be simplified for $m = m_1 = m_2$ using [24, (1)], [3, (126)] as

$$\begin{aligned} p_{r_1,r_2}(r_1,r_2) &= \int_0^\infty\int_0^\infty \frac{4m(mr_1r_2)^m}{\Gamma(m)\,\Omega_1\Omega_2\left(1-\rho_f\right)\left(\sqrt{\Omega_1\Omega_2\rho_f}\right)^{m-1}} \\ &\times \exp\left[-\left(\frac{m_1r_1^2}{\Omega_1\left(1-\delta_f\right)}+\frac{m_2r_2^2}{\Omega_2\left(1-\delta_f\right)}\right)\right] I_{m-1} \\ &\times\left(\frac{2m\sqrt{\rho_f}r_1r_2}{\sqrt{\Omega_1\Omega_2}\left(1-\rho_f\right)}\right) \\ &\times \frac{1}{2\pi\Omega_1\Omega_2\sigma_1\sigma_2\sqrt{1-\rho_s^2}}\exp\left(-\frac{q}{2}\right)d\Omega_1 d\Omega_2, \end{aligned} \tag{10}$$

where $I_\nu(\cdot)$ is the modified Bessel function of the first kind [20, (9.6.3)], and q is given by (9).

Assuming $\rho_s = 1$ in (8) and (10), the infinite summation is not convergent. In order to overcome it, we can alternatively express the joint PDF for $\rho_s = 1$, $m = m_1 = m_2$, $\mu = \mu_1 = \mu_2$, and $\sigma = \sigma_1 = \sigma_2$ as

$$\begin{aligned} p_{r_1,r_2}(r_1,r_2) &= \int_0^\infty \frac{4m(mr_1r_2)^m}{\Gamma(m)\left(1-\rho_f\right)\rho_f^{(m-1)/2}\Omega^{m+1}} \\ &\times \exp\left[-\frac{m}{\Omega\left(1-\rho_f\right)}\left(r_1^2+r_2^2\right)\right] \\ &\times I_{m-1}\left(\frac{2m\sqrt{\rho_f}r_1r_2}{\Omega\left(1-\rho_f\right)}\right)\frac{1}{\sqrt{2\pi}\sigma\Omega} \\ &\times \exp\left(-\frac{\left(\ln(\Omega)-\mu\right)^2}{2\sigma^2}\right)d\Omega. \end{aligned} \tag{11}$$

2.2. Correlation Coefficient. Using [23, (16)] and [25, (2.1)], the cross-moments of the bivariate Nakagami-lognormal distribution can be calculated as

$$\begin{aligned} &E\left(r_1^n r_2^p\right) \\ &= \frac{\Gamma\left(m_1+n/2\right)\Gamma\left(m_2+p/2\right)}{\Gamma\left(m_1\right)\Gamma\left(m_2\right)m_1^{n/2}m_2^{p/2}}\,{}_2F_1\left(-\frac{n}{2},-\frac{p}{2};m_2;\delta_f\right) \\ &\times\exp\left(\frac{n}{2}\mu_1+\frac{p}{2}\mu_2+\frac{n^2}{8}\sigma_1^2+\frac{p^2}{8}\sigma_2^2+\frac{np}{4}\rho_s\sigma_1\sigma_2\right), \end{aligned} \tag{12}$$

where ${}_2F_1(\cdot,\cdot;\cdot;\cdot)$ is the Gauss hypergeometric function [20, (15.1.1)].

From (7) and (12), the correlation coefficient in power terms between two Nakagami-lognormal variables can be derived as

$$\begin{aligned} \rho &= \left(\frac{m_2+\rho_f\sqrt{m_2/m_1}}{m_2}\exp\left(\rho_s\sigma_1\sigma_2\right)-1\right) \\ &\times\left(\sqrt{\left(\frac{m_1+1}{m_1}\exp\left(\sigma_1^2\right)-1\right)\left(\frac{m_2+1}{m_2}\exp\left(\sigma_2^2\right)-1\right)}\right)^{-1}. \end{aligned} \tag{13}$$

Note that this power correlation coefficient is not affected by the means of the associated Gaussian processes, μ_j, $j = 1, 2$, corresponding to the shadowing.

Next, we analyze the correlation coefficient between the composite fast fading shadowing of the received powers in two wireless communication scenarios.

Case 1 (macrodiversity). The macrodiversity is the technique used to combat the effects of the shadowing, by combining the signals received in several antennas separated by hundreds of wavelengths. For instance, in the macrodiversity scenario depicted in Figure 1, the mobile terminal is connected simultaneously to two base stations (BSs), BS1 and BS2. The gain obtained with macrodiversity in this scenario depends strongly on the cross-correlation coefficient of the received field strengths at BS1 and BS2.

The behavior of the site-to-site shadowing correlation coefficient has been extensively analyzed in the literature [5, 26, 27]. In [5], a model of the shadowing correlation has been proposed where the cross-correlation coefficient is given by

$$\rho_s = \begin{cases} \sqrt{\dfrac{d_1}{d_2}} & 0 \leq \phi < \phi_T, \\ \left(\dfrac{\phi_T}{\phi}\right)^\gamma\sqrt{\dfrac{d_1}{d_2}} & \phi_T \leq \phi \leq \pi, \end{cases} \tag{14}$$

where d_1 is the smallest of the two path lengths d_1 and d_2; γ is a parameter of adjustment which depends on the size and

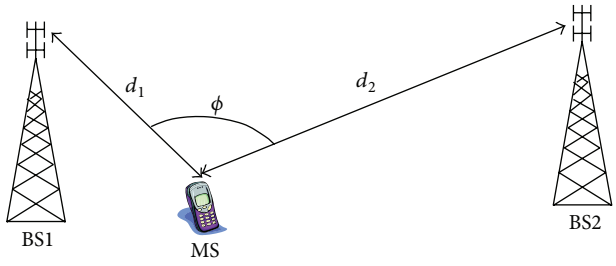

BS: base station
MS: mobile station

Figure 1: Cross-correlation shadowing scenario.

height of terrain and clutter, and according to the height of the BS antenna relative to them; and

$$\phi_T = 2\sin^{-1}\frac{d_c}{2d_1}, \tag{15}$$

d_c being the shadowing correlation distance.

In this situation, it is reasonable to assume that the short-term variations of the signal envelopes at BS1 and BS2 are independent, and consequently $\rho_f = 0$. Hence, the correlation coefficient between the instantaneous powers received at BS1 and BS2 can be easily simplified from (13) as

$$\rho = \left(\exp\left(\rho_s\sigma_1\sigma_2\right) - 1\right) \times \left(\sqrt{\left(\frac{m_1+1}{m_1}\exp\left(\sigma_1^2\right) - 1\right)\left(\frac{m_2+1}{m_2}\exp\left(\sigma_2^2\right) - 1\right)}\right)^{-1}, \tag{16}$$

where ρ_s is given by (14).

Case 2 (microdiversity). The microdiversity has been extensively used to reduce the harmful effects of the fast fading. The most common methods employed in microdiversity are spatial, polarization, frequency, angular, and temporal [2]. In order to obtain a high degree of improvement using microdiversity, two conditions should be fulfilled: (i) low cross-correlation coefficients between individual diversity branches and (ii) similar mean power available from each branch of the combiner [5]. For instance, the correlation coefficient using spatial microdiversity at the BS depends basically on the antenna separation, the direction of arrival of the main contribution arriving from the mobile station (MS), and the angular spread corresponding to the scatterers surrounding the MS [28].

It is reasonable to assume the following hypotheses in a microdiversity scenario: (i) total shadowing correlation, that is, $\rho_s = 1$; (ii) identical distributions for shadowing processes, that is, $\sigma = \sigma_1 = \sigma_2$; and (iii) identical fading parameters for the short-term distributions, that is, $m = m_1 = m_2$. Accordingly, the correlation coefficient between the composite distributions, whose joint PDF is given by (11), is simplified from (13) to

$$\rho = \frac{\left(m + \rho_f\right)\exp\left(\sigma^2\right) - m}{(m+1)\exp\left(\sigma^2\right) - m}. \tag{17}$$

In this case, the correlation coefficient in power terms is limited to

$$\frac{m\left(\exp\left(\sigma^2\right) - 1\right)}{m\left(\exp\left(\sigma^2\right) - 1\right) + \exp\left(\sigma^2\right)} \le \rho \le 1. \tag{18}$$

3. Numerical Results

In this section, we compare the values of the correlation coefficient given by (13) to those obtained by generating two correlated Nakagami-lognormal RVs using two methods.

3.1. Nakagami-Lognormal RV Generation. First, two correlated Gaussian variables will be generated following the next method. Let x_1 be a Gaussian RV with mean μ_{d1} and standard deviation σ_{d1}, denoted as $x_1 \sim \mathcal{N}(\mu_{d1}, \sigma_{d1})$. If we generate a Gaussian RV, symbolized as $y \sim \mathcal{N}(\mu_{d2} - \rho_s(\sigma_{d2}/\sigma_{d1})\mu_{d1}, \sigma_{d2}\sqrt{1-\rho_s^2})$, the variable $x_2 = \rho_s(\sigma_{d2}/\sigma_{d1})x_1 + y$ is a Gaussian RV represented as $x_2 \sim \mathcal{N}(\mu_{d2}, \sigma_{d2})$, correlated ρ_s with x_1. The pair of Gaussian correlated RVs, x_1 and x_2, are denoted as $\{x_1, x_2\} \sim \mathcal{N}(\mu_{d1}, \sigma_{d1}; \mu_{d2}, \sigma_{d2}; \rho_s)$.

Second, we generate two correlated lognormal variables using the following transformations:

$$\Omega_1 = 10^{x_1/10}, \qquad \Omega_2 = 10^{x_2/10}. \tag{19}$$

Hence, Ω_1 and Ω_2 are lognormal distributed, denoted as $\{\Omega_1, \Omega_2\} \sim \mathcal{L}(\mu_1, \sigma_1; \mu_2, \sigma_2; \rho_s)$. Note that the mean, the variance, and the correlation coefficient between Ω_1 and Ω_2 are given by Mostafa and Mahmoud [22]

$$E\left(\Omega_j\right) = \exp\left(\mu_j + \frac{\sigma_j^2}{2}\right), \quad j = 1, 2,$$

$$\operatorname{var}\left(\Omega_j\right) = \exp\left(2\mu_j + \sigma_j^2\right)\left(\exp\left(\sigma_j^2\right) - 1\right), \quad j = 1, 2,$$

$$\rho_l = \frac{\exp\left(\rho_s\sigma_1\sigma_2\right) - 1}{\sqrt{\left(\exp\left(\sigma_1^2\right) - 1\right)\left(\exp\left(\sigma_2^2\right) - 1\right)}}, \tag{20}$$

where μ_j and σ_j are related to the logarithmic parameters, μ_{dj} and σ_{dj}, in (4) and (5), respectively.

Finally, we generate two correlated Nakagami-m variables with arbitrary fading parameters, whose mean powers are correlated lognormal RVs. These RVs, denoted as $\{r_1, r_2\} \sim \mathcal{M}(m_1, \Omega_1; m_2, \Omega_2; \rho_f)$, can be generated by following the method described in [29]. Each RV, r_j, $j = 1, 2$, follows a Nakagami-m distribution, whose PDF is given by

$$p\left(r_j\right) = \frac{2}{\Gamma\left(m_j\right)}\left(\frac{m_j}{\Omega_j}\right)^{m_j} r_j^{2m_j-1}\exp\left(-\frac{m_j r_j^2}{\Omega_j}\right), \tag{21}$$

where m_j is the fading parameter; Ω_j is the mean power calculated in this case from (19); and ρ_f is the power correlation coefficient. Note that $m_2 \geq m_1$ and $\rho_f < \sqrt{m_1/m_2}$. Estimated values of the fading parameter typically range from 1 to 3. For example, a mean of 1.56 and a standard deviation of 0.34 for the estimated fading parameters were reported in [4].

To improve in computation efficiency, we can alternatively generate the two correlated Nakagami-lognormal RVs by using a logarithmic procedure, since a log Nakagami-lognormal RV can be calculated as the sum of a log Nakagami-m and a Gaussian RVs [13]. Therefore, first two correlated Gaussian RVs, that is, $\{x_1, x_2\} \sim \mathcal{N}(\mu_{d1}, \sigma_{d1}; \mu_{d2}, \sigma_{d2}; \rho_s)$, are calculated as previously. Second, we generate two correlated Nakagami-m RVs with average powers equal to 1, that is, $(v_1, v_2) \sim \mathcal{M}(m_1, 1; m_2, 1; \rho_f)$. Next, two log Nakagami-m RVs are generated by calculating $\epsilon_1 = 20 \log v_1$ and $\epsilon_2 = 20 \log v_2$. Finally, the two correlated Nakagami-lognormal RVs are obtained as $r_1 = 10^{(x_1+\epsilon_1)/20}$ and $r_2 = 10^{(x_2+\epsilon_2)/20}$.

3.2. Sample Correlation Coefficient. We have generated N observations of correlated Nakagami-lognormal RVs following the methods described above. Hence, the sample coefficient correlation, R, is calculated. K samples of the sample correlation coefficient are obtained in order to estimate the bias and the variance of R. The variance of R depends strongly on the skewness of the marginal Nakagami-lognormal distributions as it was shown for different examples of the lognormal distribution in [30]. The skewness of the marginal Nakagami-lognormal distributions can be evaluated from (7) as

$$
\begin{aligned}
s_j &= \frac{E\left[\left(r_j - \bar{r}_j\right)^3\right]}{E\left[\left(r_j - \bar{r}_j\right)^2\right]^{3/2}} \\
&= \left(\frac{2\Gamma\left(m_j + 1/2\right)^3}{m_j^{3/2}\Gamma\left(m_j\right)^3} + \frac{\Gamma\left(m_j + 3/2\right) e^{3\sigma_j^2/4}}{m_j^{3/2}\Gamma\left(m_j\right)} \right. \\
&\quad \left. - \frac{3\Gamma\left(m_j + 1/2\right) e^{\sigma_j^2/4}}{\sqrt{m_j}\Gamma\left(m_j\right)} \right) \\
&\quad \times \left(\left(e^{\sigma_j^2/4} - \frac{\Gamma\left(m_j + 1/2\right)^2}{m_j \Gamma(m)^2} \right)^{3/2} \right)^{-1}, \\
&\qquad\qquad\qquad\qquad\qquad\qquad\qquad\qquad\qquad\qquad j = 1, 2,
\end{aligned}
\tag{22}
$$

where $\bar{r}_j$ is the mean of r_j, $j = 1, 2$. The skewness, s_j, increases with σ_j. For instance, the skewness oscillates from 3.55 to 12.11 with $m_j = 1$ for shadowing standard deviations from 6 to 10 dB, respectively. Nevertheless, the skewness decreases slightly with the fading parameter, m_j. For instance, $s_j = 3.55$ for $\sigma_{dj} = 6$ dB and $m_j = 1$ and $s_j = 3.15$ for $\sigma_{dj} = 6$ dB and $m_j = 3$.

Figures 2, 3, and 4 show the bias and the standard deviation of R as a function of the fast fading correlation coefficient, ρ_f. The results correspond to spatial microdiversity, with $\rho_s = 1$, $m = m_1 = m_2$, and $\sigma_d = \sigma_{d1} = \sigma_{d2}$. In particular, the effect of the sample size, N, and the number of samples, K, on the variation of the standard deviation is illustrated in Figure 2. In this figure, the parameters of the distribution are $m = m_1 = m_2 = 1.2$ and $\sigma_d = \sigma_{d1} = \sigma_{d2} = 8$ dB. The sample size, which corresponds to the number of observations used in simulations, is $N = 1000$ and 100000, and the number of samples is $K = 25$, 50, and 100. Obviously, the higher the number of observations, N, the smaller the standard deviation. Also, the standard deviation reduces as the fast fading correlation coefficient, ρ_f, grows. Nevertheless, the standard deviation of R is scarcely affected by the number of samples calculated; that is, K equals 25, 50, and 100.

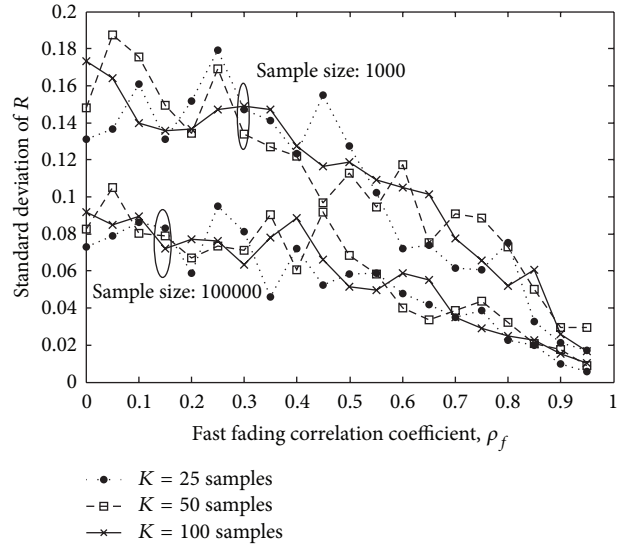

Figure 2: Standard deviation of the sample correlation coefficient as a function of the fast fading correlation coefficient for a number of observations $N = 1000, 100000$ and number of samples $K = 25, 50, 100$. The distribution parameters are $m_1 = 1.2$, $m_2 = 1.2$; $\sigma_{d1} = \sigma_{d2} = 8$ dB.

In Figure 3, the effect of both the fading parameter, m, and the shadowing standard deviation, σ_{dj}, on the standard deviation of the sample correlation coefficient is analyzed for $N = 100000$ and $K = 50$. The standard deviation of the sample correlation coefficient depends strongly on the shadowing standard deviation. Also, it can be observed that the standard deviation of R for $\sigma_d = 10$ dB decreases as m grows. In general, the standard deviation of R tends to reduce for high correlation coefficient values.

Figure 4 shows the mean of the sample correlation coefficient and the correlation coefficient ρ given by (17), that is, the analytical prediction, as a function of the fast fading correlation coefficient. The simulations are performed for $m = m_1 = m_2 = 1.2$, $\sigma_d = \sigma_{d1} = \sigma_{d2} = 10$ dB and $m = m_1 = m_2 = 3.2$, $\sigma_d = \sigma_{d1} = \sigma_{d2} = 8$ dB. The number of observations is $N = 100000$ and the number of samples is $K = 25, 50$, and 100. Generally speaking, the sample correlation coefficient is slightly positive biased for these values. This bias

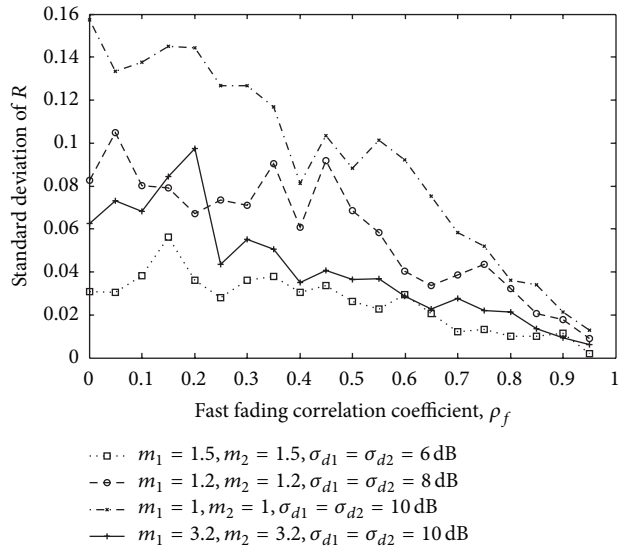

Figure 3: Standard deviation of the sample correlation coefficient as a function of the fast fading correlation coefficient for different parameters of the marginal distributions. The number of observations and number of samples are $N = 100000$ and $K = 50$, respectively.

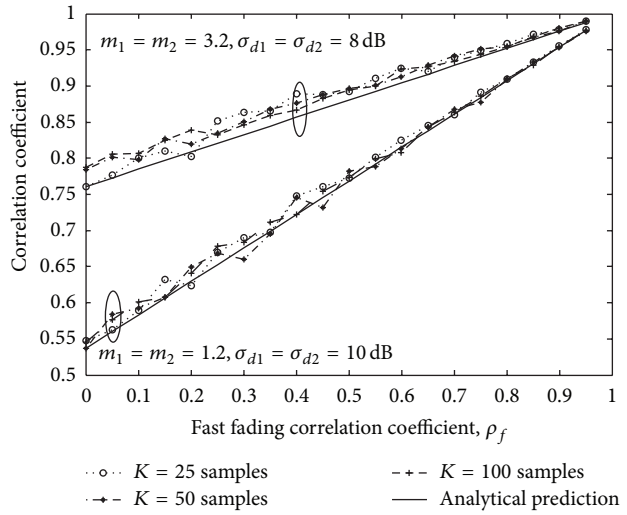

Figure 4: Correlation coefficient and mean of the sample correlation coefficient as a function of the fast fading correlation coefficient for $m_1 = m_2 = 1.2$, $\sigma_{d1} = \sigma_{d2} = 10$ dB and $m_1 = m_2 = 3.2$, $\sigma_{d1} = \sigma_{d2} = 8$ dB. The correlation coefficient (analytical prediction) is in solid lines and the mean of the sample correlation coefficient in dashed lines. The number of observations is $N = 100000$ and the number of samples is $K = 25, 50, 100$.

is higher for small fast fading correlation coefficients and for $m = m_1 = m_2 = 3.2$; $\sigma_d = \sigma_{d1} = \sigma_{d2} = 8$ dB.

In Figure 5, the correlation coefficient given by (16) and the mean of the sample correlation coefficient are plotted as a function of the angle between the MS and the base stations, ϕ, for $d_1 = 1000$ m, $d_2 = 2000$ m, $d_c = 300$ m, and $\gamma = 0.3$. Curves have been drawn for $N = 10000$, 100000, and 1000000, and $K = 50$. The marginal distributions parameters

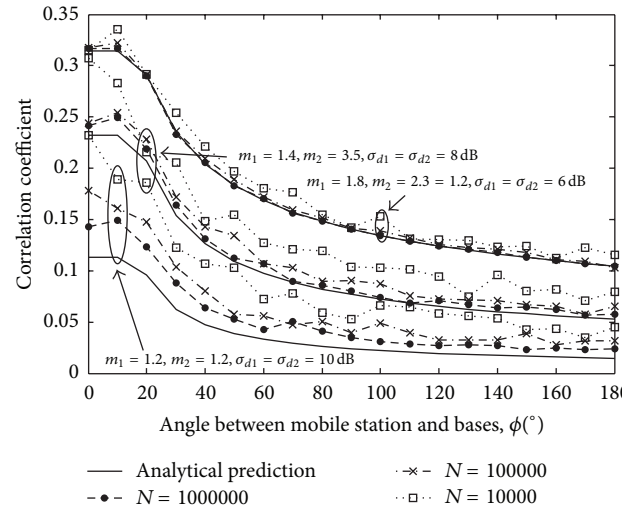

Figure 5: Correlation coefficient and mean of the sample correlation coefficient as a function of the angle between the mobile station and the two base stations. The parameters of the shadowing cross-correlation scenario are $d_1 = 1000$ m, $d_2 = 2000$ m, $d_c = 300$ m, and $\gamma = 0.3$. The marginal distributions parameters are $m_1 = m_2 = 1.2$, $\sigma_{d1} = \sigma_{d2} = 10$ dB; $m_1 = 1.4$, $m_2 = 3.2$, $\sigma_{d1} = \sigma_{d2} = 8$ dB; and $m_1 = 1.8$, $m_2 = 2.3$, $\sigma_{d1} = \sigma_{d2} = 6$ dB. The correlation coefficient (analytical prediction) is in solid lines and the mean of the sample correlation coefficient in dashed lines. The number of observations is $N = 10000$, 100000, 1000000 and the number of samples is $K = 50$.

are $m = m_1 = m_2 = 1.2$, $\sigma_d = \sigma_{d1} = \sigma_{d2} = 10$ dB; $m_1 = 1.4$, $m_2 = 3.5$, $\sigma_d = \sigma_{d1} = \sigma_{d2} = 8$ dB; and $m_1 = 1.8, m_2 = 2.3$, $\sigma_d = \sigma_{d1} = \sigma_{d2} = 6$ dB. It is observed that the sample correlation coefficient is positive biased for such parameter values. This bias is considerably high for a small number of observations, that is, $N = 10000$ and $N = 100000$, specially for ϕ close to 0°. Also, from the results shown in Figure 5, the higher the shadowing standard deviation is, the larger the values of the bias are using the same number of observations and ϕ. This bias is large for $\sigma_d = \sigma_{d1} = \sigma_{d2} = 10$ dB and low values of ϕ even for a high number of observations; for example, the bias is around 0.035 for $m = m_1 = m_2 = 1.2$, $\phi \leq 10^\circ$, and $N = 1000000$.

4. Conclusions

In this paper, we have analytically derived the PDF of bivariate Nakagami-lognormal distribution with arbitrary distribution parameters of the marginal distributions and arbitrary correlation. Also, the correlation coefficient between the compound signals has been obtained as a function of the distribution parameters and both the fast fading and shadowing correlation coefficients. This correlation coefficient has been particularized for specific scenarios of wireless communications: micro- and macrodiversity. In microdiversity, the correlation coefficient between the composite signals is substantially higher than the fast fading correlation coefficient. Otherwise, the composite correlation coefficients are small (in the examples lower than 0.32) in the macrodiversity scenario.

Two procedures to generate two correlated Nakagami-lognormal variables have been described. In examples of both microdiversity and macrodiversity scenarios, we have evaluated the sample correlation coefficient between the composite Nakagami-lognormal signals, comparing it to the analytical correlation coefficient derived previously. In general, this sample correlation coefficient is positive biased. From those examples, it can be observed that the bias and the standard deviation of the sample correlation coefficient depend substantially on the shadowing standard deviation.

The results reported in this work can be of interest in the assessment of performances (outage probabilities, bit error rates, etc.) in diversity receivers with highly dynamical environments, such as vehicular or indoor wireless channels. In these scenarios, the separation of the fast fading and shadowing processes is cumbersome, and the received signals at each branch of the diversity combiner can be accurately modeled as Nakagami-lognormal composite distributions.

Conflict of Interests

The authors declare that there is no conflict of interests regarding the publication of this paper.

Acknowledgment

This work was supported by the Spanish Ministerio de Ciencia e Innovación TEC-2010-20841-C04-1.

References

[1] J. D. Parsons, *Mobile Radio Propagation Channel*, John Wiley & Sons, Chichester, UK, 2nd edition, 2000.

[2] A. F. Molisch, *Wireless Communications*, John Wiley & Sons, Chichester, UK, 2nd edition, 2011.

[3] M. Nakagami, "The m-distribution—a general formula of intensity distribution of rapid fading," in *Statistical Methods of Radio Wave Propagation*, W. G. Hoffman, Ed., pp. 3–35, Pergamon Press, Oxford, UK, 1960.

[4] L. Rubio, J. Reig, and N. Cardona, "Evaluation of Nakagami fading behaviour based on measurements in urban scenarios," *International Journal of Electronics and Communications*, vol. 61, no. 2, pp. 135–138, 2007.

[5] S. R. Saunders and A. Aragón-Zavala, *Antennas and Propagation for Wireless Communication Systems*, John Wiley & Sons, Chichester, UK, 2nd edition, 2007.

[6] H. Suzuki, "A statistical model for urban radio propagation," *IEEE Transactions on Communications*, vol. 25, no. 7, pp. 673–680, 1977.

[7] A. A. Abu-Dayya and N. C. Beaulieu, "Micro- and macrodiversity NCFSK (DPSK) on shadowed Nakagami-fading channels," *IEEE Transactions on Communications*, vol. 42, no. 9, pp. 2693–2702, 1994.

[8] M. Ho and G. Stuber, "Co-channel interference of microcellular systems on shadowed Nakagami fading channels," in *Proceedings of the 43rd IEEE Vehicular Technology Conference (VTC '93)*, pp. 568–571, May 1993.

[9] T. T. Tjhung and C. C. Chai, "Fade statistics in Nakagami-lognormal channels," *IEEE Transactions on Communications*, vol. 47, no. 12, pp. 1769–1772, 1999.

[10] M. D. Yacoub, "The α-μ distribution: a physical fading model for the Stacy distribution," *IEEE Transactions on Vehicular Technology*, vol. 56, pp. 122–124, 2007.

[11] P. M. Shankar, "Error rates in generalized shadowed fading channels," *Wireless Personal Communications*, vol. 28, no. 3, pp. 233–238, 2004.

[12] S. Atapattu, C. Tellambura, and H. Jiang, "A mixture gamma distribution to model the SNR of wireless channels," *IEEE Transactions on Wireless Communications*, vol. 10, no. 12, pp. 4193–4203, 2011.

[13] J. Reig and L. Rubio, "Estimation of the composite fast fading and shadowing distribution using the log-moments in wireless communications," *IEEE Transactions on Wireless Communications*, vol. 12, no. 8, pp. 3672–3681, 2013.

[14] S. Mukherjee and D. Avidor, "Effect of microdiversity and correlated macrodiversity on outages in a cellular system," *IEEE Transactions on Wireless Communications*, vol. 2, no. 1, pp. 50–58, 2003.

[15] R. Zhang, J. Wei, D. G. Michelson, and V. C. M. Leung, "Outage probability of MRC diversity over correlated shadowed fading channels," *IEEE Wireless Communications Letters*, vol. 1, no. 5, pp. 516–519, 2012.

[16] G. C. Alexandropoulos, A. Conti, and P. T. Mathiopoulos, "Adaptive M-QAM systems with diversity in correlated Nakagami-m fading and shadowing," in *Proceedings of the 53rd IEEE Global Communications Conference (GLOBECOM '10)*, pp. 1–5, December 2010.

[17] R. Zhang, J. Wei, and V. C. M. Leung, "Outage probability of composite microscopic and macroscopic diversity over correlated shadowed fading channels," *China Communications*, vol. 10, pp. 129–142, 2013.

[18] M. Abdel-Hafez and M. Cafak, "Performance analysis of digital cellular radio systems in Nakagami fading and correlated shadowing environment," *IEEE Transactions on Vehicular Technology*, vol. 48, no. 5, pp. 1381–1391, 1999.

[19] P. M. Shankar, "Macrodiversity and microdiversity in correlated shadowed fading channels," *IEEE Transactions on Vehicular Technology*, vol. 58, no. 2, pp. 727–732, 2009.

[20] M. Abramowitz, *Handbook of Mathematical Functions, with Formulas, Graphs, and Mathematical Tables*, Dover, New York, NY, USA, 9th edition, 1972.

[21] M. K. Simon and M. S. Alouini, *Digital Communication over Fading Channels*, vol. 86, Wiley-IEEE Press, 2nd edition, 2005.

[22] M. D. Mostafa and M. W. Mahmoud, "On the problem of estimation for the bivariate lognormal distribution," *Biometrika*, vol. 51, pp. 522–527, 1964.

[23] J. Reig, L. Rubio, and N. Cardona, "Bivariate Nakagami-m distribution with arbitrary fading parameters," *Electronics Letters*, vol. 38, no. 25, pp. 1715–1717, 2002.

[24] C. C. Tan and N. C. Beaulieu, "Infinite series representations of the bivariate Rayleigh and Nakagami-m distributions," *IEEE Transactions on Communications*, vol. 45, no. 10, pp. 1159–1161, 1997.

[25] D. Lien and N. Balakrishnan, "Moments and properties of multiplicatively constrained bivariate lognormal distribution with applications to futures hedging," *Journal of Statistical Planning and Inference*, vol. 136, no. 4, pp. 1349–1359, 2006.

[26] K. Zayana and B. Guisnet, "Measurements and modelisation of shadowing cross-correlations between two base-stations," in *Proceedings of the IEEE International Conference on Universal Personal Communications (ICUPC '98)*, vol. 1, pp. 101–105, Florence, Italy, October 1998.

[27] T. B. Sørensen, "Slow fading cross-correlation against azimuth separation of base stations," *Electronics Letters*, vol. 35, no. 2, pp. 127–129, 1999.

[28] W. C. Jakes, *Microwave Mobile Communications*, IEEE Press, Piscataway, NJ, USA, 2nd edition, 1994.

[29] J. Reig, M. A. Martinez-Amoraga, and L. Rubio, "Generation of bivariate Nakagami-m fading envelopes with arbitrary not necessary identical fading parameters," *Wireless Communications and Mobile Computing*, vol. 7, no. 4, pp. 531–537, 2007.

[30] C. D. Lai, J. C. W. Rayner, and T. P. Hutchinson, "Robustness of the sample correlation—the bivariate lognormal case," *Journal of Applied Mathematics and Decision Sciences*, vol. 3, no. 1, pp. 7–19, 1999.

Hindawi Publishing Corporation
International Journal of Antennas and Propagation
Volume 2014, Article ID 454976, 12 pages
http://dx.doi.org/10.1155/2014/454976

Research Article

Measurement-Based LoS/NLoS Channel Modeling for Hot-Spot Urban Scenarios in UMTS Networks

Jiajing Chen,[1] Xuefeng Yin,[1] Li Tian,[1] Nan Zhang,[1] Yongyu He,[1] Xiang Cheng,[2] Weiming Duan,[3] and Silvia Ruiz Boqué[4]

[1] *College of Electronics and Information Engineering, Tongji University, Shanghai, China*
[2] *School of Electronics Engineering and Computer Science, Peking University, Beijing, China*
[3] *Huawei Technology Company, Shanghai, China*
[4] *Department of Signal Theory and Communications, Polytechnic University of Catalonia, Castelldefels, Spain*

Correspondence should be addressed to Xuefeng Yin; yinxuefeng@tongji.edu.cn

Received 5 May 2014; Revised 14 July 2014; Accepted 29 July 2014; Published 17 August 2014

Academic Editor: Jose F. Paris

Copyright © 2014 Jiajing Chen et al. This is an open access article distributed under the Creative Commons Attribution License, which permits unrestricted use, distribution, and reproduction in any medium, provided the original work is properly cited.

A measurement campaign is introduced for modeling radio channels with either line-of-sight (LoS) or non-line-of-sight (NLoS) connection between user equipment (UE) and NodeB (NB) in an operating universal mobile telecommunications system. A space-alternating generalized expectation-maximization (SAGE) algorithm is applied to estimate the delays and the complex attenuations of multipath components from the obtained channel impulse responses. Based on a novel LoS detection method of multipath parameter estimates, channels are classified into LoS and NLoS categories. Deterministic models which are named "channel maps" and fading statistical models have been constructed for LoS and NLoS, respectively. In addition, statistics of new parameters, such as the distance between the NB and the UE in LoS/NLoS scenarios, the life-distance of LoS channel, the LoS existence probability per location and per NB, the power variation at LoS to NLoS transition and vice versa, and the transition duration, are extracted. These models are applicable for designing and performance evaluation of transmission techniques or systems used by distinguishing the LoS and NLoS channels.

1. Introduction

Distinctive characteristics of signals coming from a line-of-sight (LoS) or non-line-of-sight (NLoS) path in a wireless environment raised great concerns in mobile radio system design. The probability of whether the LoS path exists in the channel or not depends on various factors, for example, terrain features, building density and locations of users. Statistical models have been employed by the 3GPP spatial channel model (SCM) [1] and the WINNER II SCM-enhanced [2] to describe the LoS existence probability. Recently, characterization of LoS/NLoS channel becomes highly demanded in some applications, such as massive multiple-input-multiple-output (MIMO), mobile back-hauling, user-specific beamforming, and other adaptive techniques used in future heterogeneous networks [3–6]. Newly introduced multipath access scheme—nonorthogonal multiple access (NOMA)—for future radio access also relies on the distinction of LoS and NLoS channels [7–9]. Additionally, some ad-hoc wireless communication scenarios and the implementation of some new technologies also prefer the LoS channel, for example, dedicated short range communication (DSRC) system for device-to-device, vehicle-to-vehicle, and machine-to-machine communications [10–15]. Furthermore, the LoS existence has been considered in localization applications, such as the distance estimation between the base station (BS) and the mobile station in [16]. Modeling realistic characteristics of LoS/NLoS channels based on measurements are important for designing and optimizing these techniques or systems.

A problem arising when characterizing the LoS/NLoS channels based on measurements is how to categorize a channel as LoS or NLoS. Detection methods addressed in the literature can be split into two groups, that is, the range-measurement-based and channel-impulse-response- (CIR-) based methods. The former method, such as those introduced in

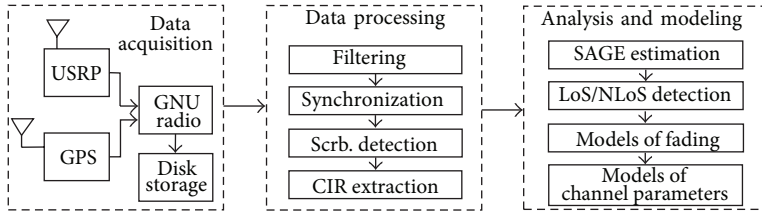

Figure 1: A diagram of channel measurement, data analysis, and modeling procedure adopted for LoS/NLoS channel characterization.

[16–18], was adopted for LoS detection in the early stage. The latter approach is mainly based on the shape or statistical properties of the CIRs, for example, the confidence matrix [19], the delay spread [19], the power delay profile (PDP) [20], and the narrowband K-factor [21, 22]. In our contribution, the LoS detection is performed based on the power difference among estimated multipath components, which has been proven to be effective through measurement campaigns.

Some LoS/NLoS propagation models have been reported in the literature. According to measurement environments, these models characterize channels in either indoor or outdoor scenarios. In indoor cases, the distribution of the channel gains for the LoS/NLoS scenarios is presented [23, 24]. Coherence bandwidth and delay spread in LoS/NLoS scenarios have been studied at 5 GHz [25, 26] and 60 GHz [27]. In [28, 29], statistical models characterizing the shadowing in LoS and NLoS scenarios were extracted from indoor measurements. In outdoor scenarios, path loss models have been attracting more attention [30–34]. Furthermore, statistics of the LoS coverage rate in urban areas for broadband wireless access systems and the LoS existence probability versus elevations of departure of downlink channels have been investigated in [35, 36], respectively.

Experiment-based stochastic channel modeling relies on measurement campaigns to be conducted extensively in the environments of interest. Many conventional models have been extracted based on dedicated channel sounding activities. However, due to practical concerns, such as power constraints, poor mobility of the sounding equipment, and limited number of measurement routes, the channel observations do not possess sufficient randomness to characterize the channels ergodically, leading to limited applicability of the resultant models. As an alternative, using in-service public wireless communication systems or networks to measure channels in large areas can be adopted. In [37], a public base station was used as a transmitter, and the received signal strength was measured in the whole coverage of the base station. The advantage of channel measurements in in-service networks is that the channel characteristics observed are identical with those experienced by the user equipment (UE); thus the channel statistics extracted are more realistic. Compared with hundreds of MHz bandwidth usually adopted in the dedicated wideband channel measurement campaigns, the measurement based on the conventional 2G public system usually utilizes hundreds of KHz bandwidth, which facilitates the study of narrowband channel properties, such as the fading-related parameters [38] or performance-related parameters, for example, the out-of-channel interference [39]. Along with fast developing commercial systems, such as LTE-Advanced, wideband characteristics of channels can be measured based on the in-service networks. Channel modeling based on these data began to attract more attention recently [36, 40].

In this work, a receiver was constructed to collect the downlink signals at a hot-spot area of Shanghai in a commercial in-service UMTS network. The impulse responses of the channels are calculated, and a high-resolution estimation algorithm derived based on the SAGE scheme is applied to extract multipath parameters. After appropriately detecting the LoS and NLoS channels by using the novel LoS detection, various aspects of LoS/NLoS channels are investigated and the corresponding models are established based on the extensive observations. They include the deterministic channel maps, which are the geographic map overlaid with spots color-coded by channel characteristics, and statistical models characterizing the channel gain, shadowing, and multipath fading. Furthermore, the statistics of some newly defined channel parameters are studied, which include (i) the distance between NBs and the user equipment in LoS and NLoS conditions, (ii) the life-distance of LoS and NLoS channels, (iii) the LoS existence probability per carrier for a UE, (iv) the LoS existence probability per carrier for a NB, and (v) power variation at LoS-NLoS transition and the transition duration. These models are useful for the design and performance evaluation of communication techniques adaptive to the LoS and NLoS scenarios.

The rest of this paper is organized as follows. Section 2 introduces the measurement equipment, environments, and the specifications applied for data acquisition in an in-service UMTS network. The main steps of processing the measurement data to obtain the estimates of channel impulse responses are also described. In Section 3, the LoS/NLoS detection method is introduced. Section 4 elaborates details of the models established based on the LoS/NLoS channel characteristics obtained. Finally conclusive remarks are addressed in Section 5.

2. Measurement Equipment, Campaigns, Setup, and Postprocessing

Figure 1 illustrates the diagram of the data acquisition, processing, and modeling procedure adopted for characterizing LoS/NLoS channels based on the signals of a UMTS network. The equipment used to acquire the signals consists of the following components: a Universal Software-Defined Radio Peripheral (USRP) device of type N210 [41] controlled by the GNU radio software in a computer and a global positioning

Figure 2: A photograph of the Nanjing Road.

system (GPS) module that reports the longitude and latitude of the measurement location to the computer through a serial port, the storage disk, an omnidirectional antenna working in 2-3 GHz UMTS frequency band, and a lead-acid battery. All this equipment was loaded in a trolley moving along predefined routes during the field measurements.

The measurement campaign was performed in the pedestrian zone along Nanjing Road, Shanghai, China. This area is a typical hot-spot of the local UMTS network where complex streets and densely distributed skyscrapers jointly create a city canyon environment. Multiple macro-, micro-, or pico-cellular UMTS stations were deployed in the area. Figure 2 shows a photograph taken on the Nanjing Road during the measurements. Measurements along the streets with different styles of corners provide a large amount of channel observations which are sufficient statistically for modeling the realistic LoS/NLoS channels, including the channel evolution characteristics during the LoS-to-NLoS transitions and vice versa.

During the measurements, the receiver moves at a walking speed of about 1.2 m/s. Data acquisition was triggered when the receiver departed from its previous location by 5 meters, and the duration of collecting the data at each location is 1 second. The carrier frequency was 2.1376 GHz and the receiving bandwidth was 20 MHz. The scrambling code existing in more than 5 consecutive frames is considered to be a valid code. It was found later that the data collected in the whole campaign was from 78 NBs, each with a distinctive combination of a scrambling code and a physical carrier.

The raw data collected during the measurements was post-processed in the following five steps.

Step 1 (filtering). The measurement results show that three UMTS carriers were used with central frequencies of 2.1326 GHz, 2.1376 GHz, and 2.1426 GHz, respectively. The raw data received with 20 MHz effective bandwidth at the center frequency of 2.1376 GHz is first filtered to obtain three baseband signals $r_c(t)$, $c = 1, 2, 3$, for these carriers individually.

Step 2 (synchronization). The beginnings of time-slots in the downlink synchronization channels are detected by correlating the baseband signals with the primary synchronization code (PSC). Multiple NBs are found by checking the dominant peaks in the PDPs of the obtained CIRs. In addition, the estimates of the starting time t_0 of individual data frame in the common pilot channels (CPICHs) and the index i of estimating scrambling code group are obtained by solving the maximization problem:

$$\left(\widehat{t}_0, \widehat{i}\right) = \arg \max_{t_0, i} \left| \int_0^T r_c(t) \left(c_s^i(t - t_0)\right)^* dt \right|^2, \quad c = 1, 2, 3, \tag{1}$$

where $c_s^i(t)$, $i \in [1, 2, \ldots, 64]$, consists of 15 secondary synchronization codes permuted according to the ith predefined sequence, $T = 10$ ms is the duration of a CPICH frame [42], and $(\cdot)^*$ denotes the complex conjugate of given argument.

Step 3 (scrambling code detection). The detection of scrambling code is necessary in our case due to the fact that the information that how the scrambling codes are allocated in the carriers is unknown. The index j of the scrambling code used to modulate the CPICH is detected by

$$\widehat{j} = \arg \max_{j \in J_{\widehat{i}}} \left| \int_{\widehat{t}_0}^{\widehat{t}_0 + T} r_c(t)\, s_j^*\left(t - \widehat{t}_0\right) dt \right|^2, \quad c = 1, 2, 3, \tag{2}$$

where the vector $J_{\widehat{i}} = (\widehat{i} - 1) \cdot 8 + [1, 2, \ldots, 8]$ contains the indices of 8 scrambling codes in the $\widehat{i}$th group and $s_j(t)$ denotes the jth scrambling code. Notice that, for some channels, although the index of scrambling code group can be detected in Step 2, none of the scrambling codes within the group exhibits significantly higher likelihood of being the correct code than the others. This is probably due to the fact that the frequency offset between the NBs and USRP is non-negligible, resulting in low SNR or signal to interference and noise power ratio (SINR) in the CPICHs. In such cases, the data acquired at this location will not be considered for modeling.

Step 4 (CIR extraction). For the channels identified with the $\widehat{j}$th scrambling code at carrier c, the impulse response $h_{c,k}(\tau)$ of the channels observed in the kth CPICH frame is calculated as

$$h_{c,k}(\tau) = \int_{\widehat{t}_0}^{\widehat{t}_0 + T} r_c(t + kT)\, s_{\widehat{j}}^*(t - \tau)\, dt. \tag{3}$$

Step 5 (parameter estimation). It can be shown that the channel coherence time is beyond the duration of one frame even in the worst case where the people in the environment are moving at the largest speed of 3 m/s. Thus, the channel observations obtained in one data frame are considered to be coherent and applicable for multipath extraction. A SAGE algorithm is derived and used to estimate the delays and complex attenuations of multiple specular propagation paths from the CIRs observed in individual data frames. Readers may refer to [43] for the derivation of the SAGE algorithm and the steps for implementation. Based on a practical principle that the paths estimated with power 20 dB lower than the maximum are negligible, we found that 10 paths per CIR are sufficient for reconstructing the dominant portion of the CIRs in most cases. Furthermore, observations not reported

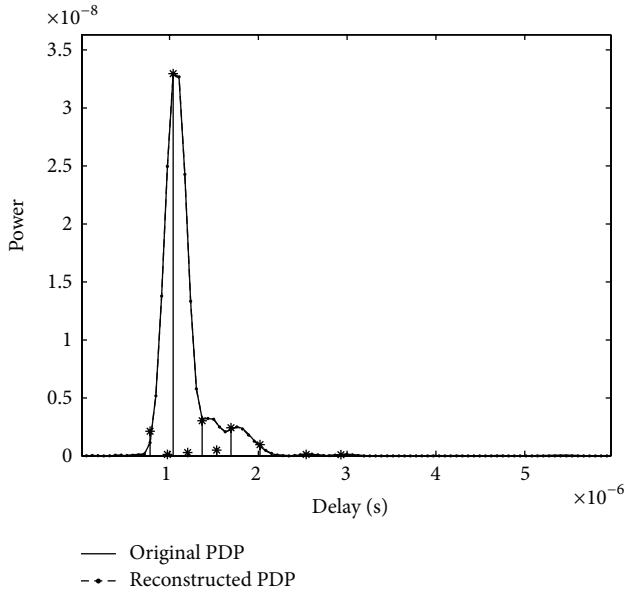

Figure 3: An example of an original channel PDP and the PDP of the channel reconstructed based on the multipath parameter estimates. The powers of the estimated paths versus the path delays are also illustrated.

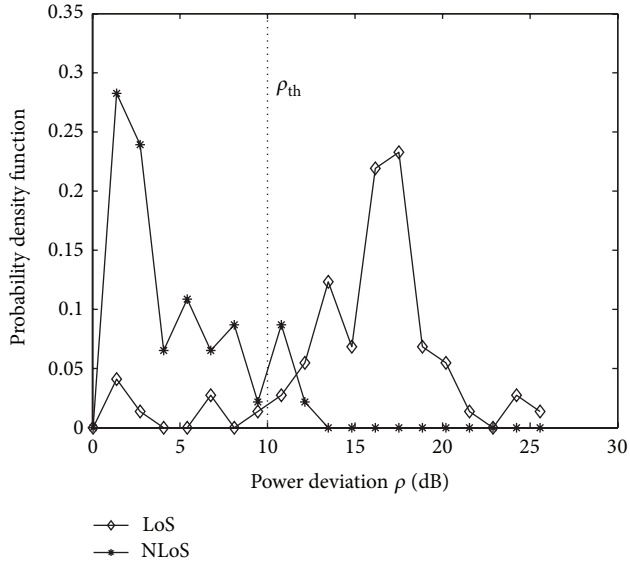

Figure 4: The pdfs of the deviation ρ between the powers of the strongest path and the first-arrival path in the case where the first-arrival path does not have the largest power among all estimated paths.

here also show that the parameter estimates usually converge within 30 iterations. Figure 3 depicts the comparison between the original PDP for the channel observed in a CPICH frame and that calculated from the reconstructed signals that are computed based on the estimated 10 specular paths. The stem plot for the powers of the estimated paths with the asteroid marker is also illustrated in Figure 3. It is obvious that the original PDP is well approximated by the reconstructed PDP, indicating that the path components estimated by using the SAGE algorithm can represent the channel impulse response accurately.

3. LoS/NLoS Detection

The LoS detection method considered here is based on the estimated multipath parameters. It is a common belief that the LoS path arrives at the UE with the shortest delay. However, due to the limited delay resolution of the communication signals, a LoS path may be combined with NLoS paths which have slightly larger delays than the former. Thus, a multipath cluster can be identified in the vicinity of the true LoS path. This is particularly the case in urban environments where the local clutter around the NB may generate a large amount of diffraction or reflection paths with delays close to the LoS path. Considering these situations, the LoS detection method adopted here is designed for two cases. In the first case where the first-arrival path has the largest power among all estimated paths, a clear decision that the channel is a LoS channel is made without further analysis. In the second case where the first-arrival path does not have the largest power, the deviation ρ between the powers of the strongest path and this first-arrival path is calculated and used to determine the channel scenarios based on a hypothesis testing. A predefined threshold ρ_{th} is applied in the testing, where the channel is LoS for $\rho > \rho_{\text{th}}$ and NLoS for $\rho \leq \rho_{\text{th}}$, respectively. The suitable value of ρ_{th} was identified through the measurements collected at a corner on Nanjing Road, where the receiver moved from LoS to NLoS scenarios. Figure 4 depicts the empirical probability density functions (pdfs) of ρ observed in the true LoS and NLoS cases. It can be observed that the two pdfs interset to overlap around $\rho = 9$–12 dB. Our calculation shows that, by setting $\rho_{\text{th}} = 10$ dB, the accumulative probability for detection error in this case can be kept less than 0.1. Thus, practically, $\rho_{\text{th}} = 10$ dB is chosen for the hypothesis testing of a channel being LoS or NLoS in the environment considered here.

It is worth mentioning that the measurement environments were time-variant with people walking around, which can significantly influence the accuracy of LoS detection based on a signal observation. To improve the detection accuracy, it is necessary to select the decision in majority when multiple decisions are available. In the case considered here, the decision with higher occurrence frequency among 49 CPICH frames per location is selected. In most locations, more than 35 frames were observed to provide common LoS detection result.

By using the aforementioned detection method, LoS and NLoS channels observed with valid scrambling codes are identified for all measurement locations. Figures 5(a) and 5(b) demonstrate an example of the LoS and NLoS channel maps for Nanjing Road where the geometric map or the photograph of the environment is overlaid with spots marking the channel categories observed by the UE. Notice that since there are many NBs deployed along the Nanjing Road transmitting signals with different scrambling codes at three carriers, Figure 5 illustrates the LoS detection results at all measured

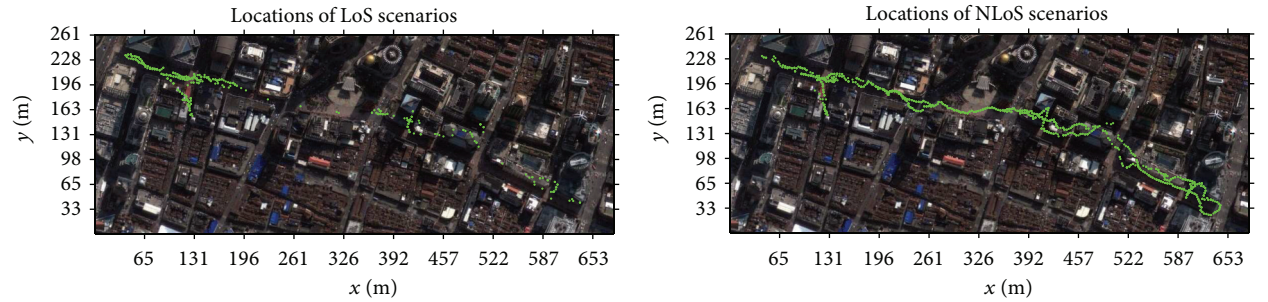

(a) Locations where LoS channels are observed

(b) Locations where NLoS channels are observed

Figure 5: The locations where the channels are found to be LoS and NLoS channels along the Nanjing Road.

locations for the channel with the largest power among all valid channels identified. It can be observed that more LoS channels are found than the NLoS channels at the left end of the Nanjing Road. This is reasonable as that area is an open cross with two main roads intersect. Furthermore, NLoS channels are widely observed along the Nanjing Road, a typical street canyon environment where the diffraction and the reflections from skyscrapers are the major propagation mechanisms.

4. LoS/NLoS Channel Models

In this section, various aspects of the LoS and NLoS channels are analyzed, and the corresponding stochastic models are established based on 664 LoS and 1181 NLoS channel observations. These characteristics include the conventional fading statistics and the distributions of some novel parameters. For notational convenience, we use $h_{\mathrm{LoS},m}(\tau)$ and $h_{\mathrm{NLoS},n}(\tau)$ to denote the CIR of the mth observation of LoS channel and the nth observation of NLoS channel, respectively. The corresponding narrowband channel coefficients $h_{\mathrm{LoS},m}$ and $h_{\mathrm{NLoS},n}$ are calculated as $h_{\mathrm{LoS},m} = \int h_{\mathrm{LoS},m}(\tau)d\tau$ and $h_{\mathrm{NLoS},n} = \int h_{\mathrm{NLoS},n}(\tau)d\tau$, respectively. The channel gains $P_{\mathrm{LoS},m}$ and $P_{\mathrm{NLoS},n}$ represented in dB are calculated as $P_{\mathrm{LoS},m} = 20\log_{10}|h_{\mathrm{LoS},m}|$ and $P_{\mathrm{NLoS},n} = 20\log_{10}|h_{\mathrm{NLoS},n}|$, respectively.

4.1. Channel Gain, Shadowing, and Multipath Fading. The channel gain $P_{\mathrm{LoS},m}$ can be written as $P_r = P_t - P_p + P_s + P_m$ where P_t, P_p, P_s, and P_m represent the transmission power, path loss, shadowing, and multipath fading denoted in dB, respectively. Figure 6 depicts the empirical cumulative distribution functions (cdfs) of the channel gains $P_{\mathrm{LoS},m}$ and $P_{\mathrm{NLoS},n}$, respectively. It can be observed that the channel gains for LoS are concentrated in the region more to the right of the abscissa than to the NLoS scenario. Different kinds of distributions including the m-Nakagami, Rice, Weibull, normal, and α-μ are used to fit with the empirical results. The Kolmogorov-Smirnov test (K-S test) has been conducted for evaluating the consistency of the analytical pdf and the empirical graphs. The results show that both cdfs are well fitted by normal distributions with appropriately chosen parameters reported in Table 1. It can be observed from the table that the average of $P_{\mathrm{LoS},m}$ is 6.12 dB higher than that in the NLoS scenario, and the standard deviation of the channel gain in the LoS scenario is 4.65 dB less than that in the NLoS scenario. These statistical differences indicate that the existence of the LoS path in the channel can not only bring 6 dB gain in average for the received signal but also reduce the variation of the channel gain significantly.

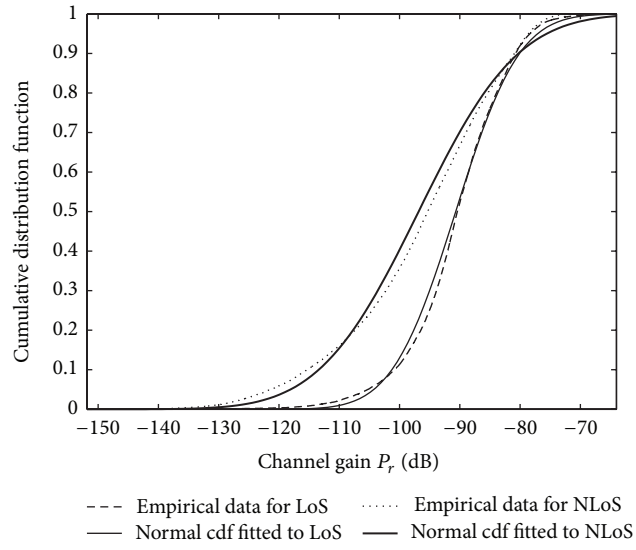

Figure 6: The empirical and fitted cdfs of the channel gains in the LoS and NLoS scenarios.

Table 1: Parameters of analytical pdfs fitted to the empirical data.

	LoS scenarios	NLoS scenarios
Channel gain (normal)	$\mu = -90.68$, $\sigma = 8.27$	$\mu = -96.80$, $\sigma = 12.92$
Shadowing (α-μ)	$\alpha = 0.9184$, $\mu = 4.5918$	$\alpha = 1.6327$, $\mu = 0.9184$
Multipath (α-μ)	$\alpha = 2.4490$, $\mu = 2.1429$	$\alpha = 2.5510$, $\mu = 1.0204$

To calculate the gain due to the shadowing P_s which attributes to the large structures around the receiver, it is necessary to subtract the path loss P_p caused by free-space propagation and the terrain features. In our case, since the exact locations of the NBs are unknown, the path loss may not be calculated analytically by using existing models. As

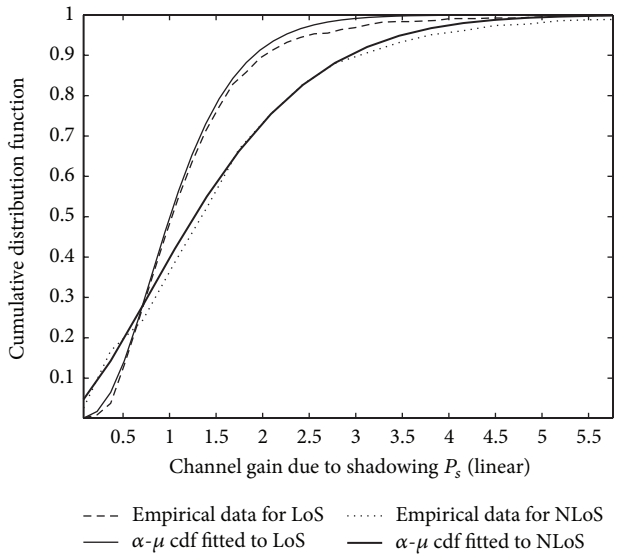

Figure 7: The empirical and fitted cdfs of shadowing in the LoS and NLoS scenarios.

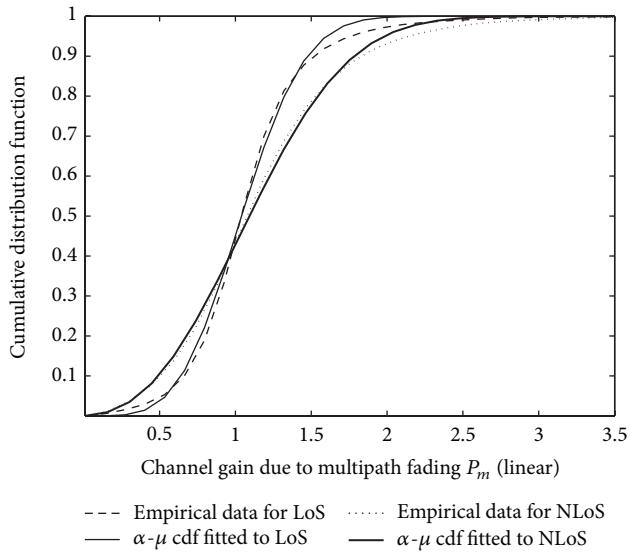

Figure 8: The empirical and fitted cdfs of multipath fading in the LoS and NLoS scenarios.

an alternative, the empirical path loss is computed in the following manner. For any location, say A, channel gains observed in the surrounding locations within 50-m radius are averaged to obtain the estimate of the path losses $P_{p,\mathrm{LoS}}$ and $P_{p,\mathrm{NLoS}}$ at A for LoS and NLoS scenarios, respectively. The shadowing of a LoS channel $P_{s,\mathrm{LoS}}$ at the location A is then calculated by taking the mean of $P_{\mathrm{LoS},m} - P_{p,\mathrm{LoS}}$, where $P_{\mathrm{LoS},m}$ is the channel gain observed in a LoS scenario at any location less than 10-m deviation from A. Similar calculations are applied to calculate the shadowing of a NLoS channel $P_{s,\mathrm{NLoS}}$.

Figure 7 depicts the empirical cdfs of the shadowing in the LoS and NLoS scenarios, respectively. The cdfs of α-μ distributions which were found to fit the best with the empirical graphs among multiple candidates are also illustrated in Figure 7. The parameters of the pdfs of the adopted distributions are reported in Table 1. It can be observed from Figure 7 that the mean of the gain due to shadowing both in LoS and NLoS scenarios are around 1 in linear scale, which indicates that the path loss has been correctly removed in the calculation. The spread of the shadowing is larger in the NLoS channels than that in the LoS channels. This observation shows that more complex environments exist around the receiver in the NLoS scenarios, which create larger variation of the shadowing than in the LoS scenarios.

Multipath fading in a channel can be calculated by subtracting the path loss and shadowing from the over channel gain. Figure 8 depicts the empirical cdfs of channel gain attributed to the multipath fading in the LoS and NLoS scenarios, respectively. The α-μ distributions which were shown by the K-S test to fit the best to the empirical graphs are also depicted in Figure 8. It can be observed that the multipath fading magnitudes in the linear scaling are distributed within the interval of [0, 3] with mean values equal to 1 for both scenarios. Furthermore, the cdf is more concentrated in the LoS than in the NLoS scenarios, indicating that the variation of the multipath fading is more severe in NLoS scenarios. Table 1 reports the parameters of the α-μ cdfs that fit well with the empirical data.

4.2. Distance between the NB and the UE. As the locations of the NBs are unknown in our case, it is difficult to establish the path loss models for both LoS and NLoS scenarios. However, the distributions of the path loss, which can be calculated based on a method that will be introduced later, are applicable to deducing the statistics of the distances between NBs and UE in either LoS or NLoS cases. Such information is considered to be useful for channel simulations and designing the transmission power for NBs and UE with respect to the LoS and NLoS scenarios.

Here P_t can be considered to be deterministic, P_p depends on the direct distance d between the NB and the UE, and P_s, P_m are uncorrelated random variables. In the case considered here, the unknown d can be viewed as a random variable, and consequently P_p, as a deterministic function of d, is a random variable as well. The pdf of P_r is the convolution of the pdfs of $-P_p$, P_s, and P_m. Under the condition that the empirical pdfs of P_s and P_m are known, we can calculate the pdf of P_p by the deconvolution operation. Figure 9 depicts the estimated empirical pdf of the P_p in LoS and NLoS scenarios. It is worth mentioning that, since P_t is unknown, the absolute value of the abscissa of Figure 9 may be incorrect. It can be observed that the mean path loss is 7 dB less in LoS than in NLoS scenarios and the spread of the path loss is larger in NLoS than in LoS scenarios.

Since the path loss is a deterministic function of the distance d between the NB and the UE, we may deduce the distribution of d from the estimated pdf of P_p. For simplicity, the following path loss model [44, Section 2.6] is used:

$$P_p = -10\gamma \log_{10}\left(\frac{d}{d_0}\right) + 20\log_{10}\left(\frac{\lambda}{4\pi d_0}\right), \qquad (4)$$

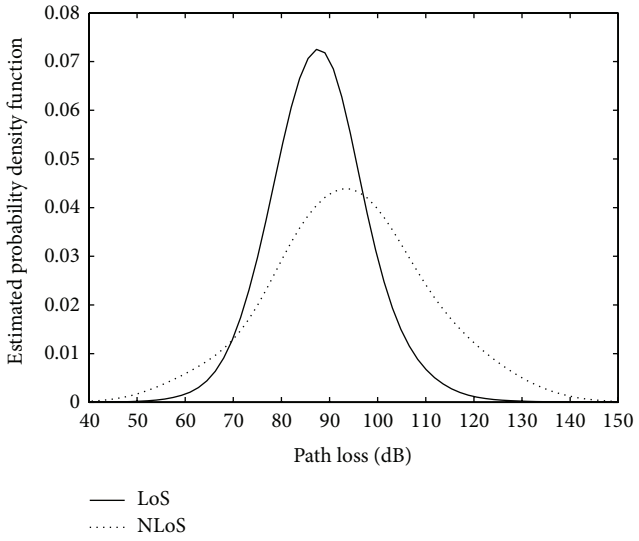

Figure 9: The empirical pdfs of estimated path loss in LoS and NLoS scenarios.

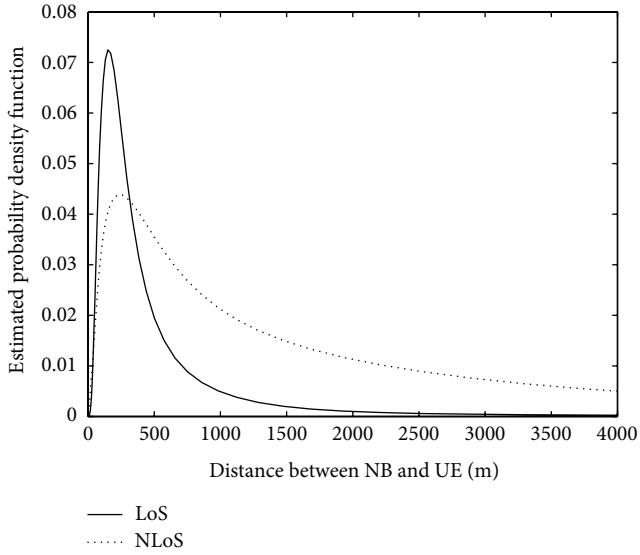

Figure 10: The empirical pdfs of the distance between the NB and the UE in LoS and NLoS scenarios.

where the path loss exponent γ should be selected within $[2.7, 3.5]$ and the reference distance d_0 is between 10 and 100 m for urban micro-cellular environments. In our case, $\gamma = 3$ and $d_0 = 50$ are selected, which can be changed if more accurate path loss model is available for the environment considered. By assuming that the transmit power $P_t = 0$ dB, the pdf of d is obtained from the empirical pdf of P_p by replacing P_p with (4). Figure 10 illustrates the resultant pdfs of direct distance from the NB to UE in LoS and NLoS scenarios, respectively. It can be observed from Figure 10 that the LoS users are maximum 2.5 km from the NB. The most of the LoS users are located at 200 m from the NB. The NLoS users are widely spread within the range from 0 to 4 km, and their majority is around 300 m from the NBs. The nonzero probability observed for large range up to 4 km indicates that this may be due to the existence of macro-cellular NBs. These results clearly demonstrate that the LoS users are located closer to the NB than the NLoS users. In other words, the NBs with small coverage areas tend to serve more LoS users than the NBs with larger coverage ranges in the Nanjing Road environments.

4.3. Life-Distance of LoS Channel. To implement, for example, the user-specific beamforming technique, a UE is usually expected to experience LoS scenarios in a long distance. Thus, it is important to investigate the statistics of the so-called "life-distance of the LoS/NLoS channel" d_c within which a UE experiences the LoS channel constantly. Based on the location information of the measured spots, the measurement routes are accurately reproduced. In the case where the LoS or NLoS channel appears in a certain number of consecutive locations, d_c can be calculated as the displacement from the first to the last location. Figure 11 illustrates an example of the fragments where LoS or NLoS channels were constantly observed for the NB with the scrambling code number 188. In this example, the maximum of the life-distance of LoS channel is calculated as

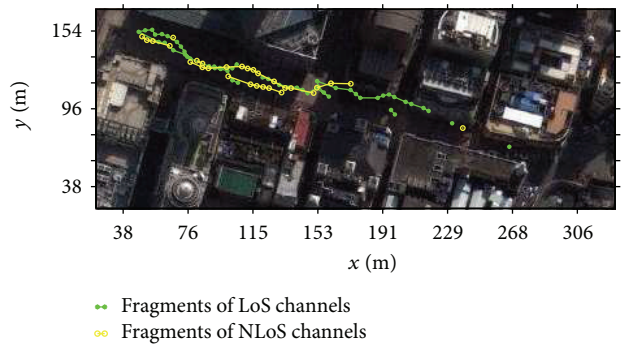

Figure 11: An example of calculating life-distance of LoS and NLoS channels for a NB with the scrambling code number 188.

25 meters which was found along the spacious street. Notice that, due to the limited GPS resolution and the fixed distance of 5 m between adjacent measured spots, the minimum life-distance of LoS or NLoS channel is lower-bounded by 5 m.

Figure 12 depicts the cdf of the life-distance of LoS and NLoS channels calculated based on the observations of totally 148 fragments for LoS and 298 fragments for the NLoS channels. It can be observed from Figure 12 that the longest LoS and NLoS life-distance can be up to 28.1 m and 160 m, respectively. Furthermore, nearly 50% of the LoS and NLoS life-distances observed are 5 meters, and 20% of the LoS and NLoS life-distances are within the range of 5 to 10 meters. The majority of the life-distances observed are below 10 meters which indicates that the LoS and NLoS scenarios transit frequently when a UE walks on the city canyon environments as in the case of Nanjing Road.

4.4. LoS Existence Probability for a UE and for a NB. The probability of a UE experiencing the LoS channel at an arbitrary location in the network is of interest to know. Considering

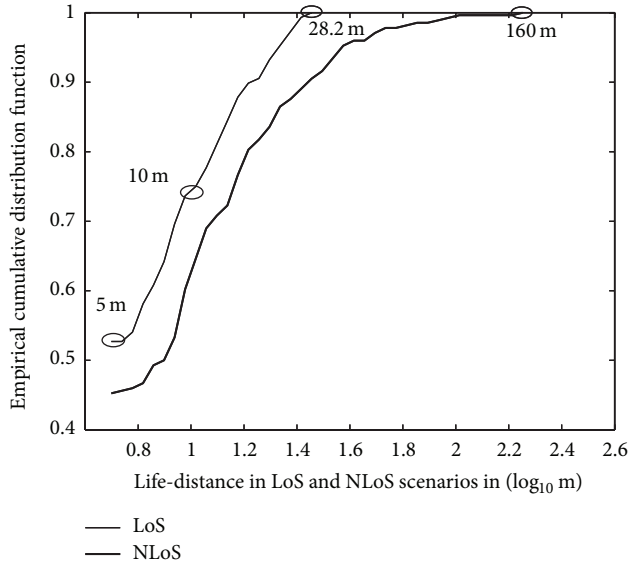

Figure 12: The empirical cdfs of the LoS and NLoS life-distance.

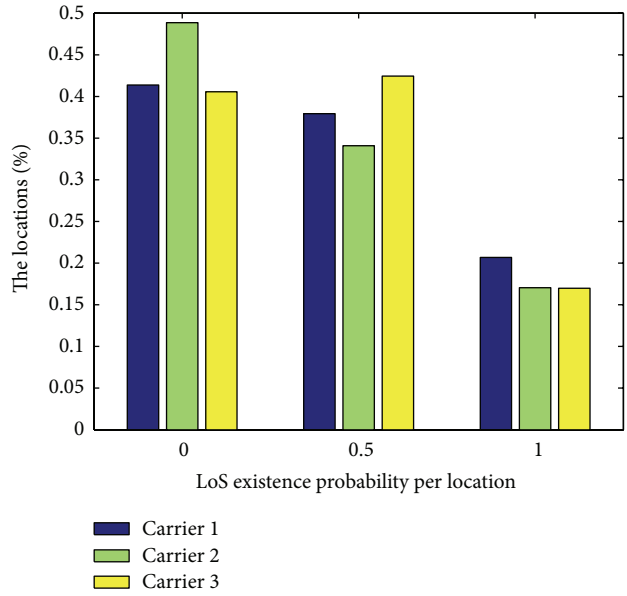

Figure 13: The empirical percentage of LoS existence probability per location.

that the UE may receive signals from more than one NB, the "LoS existence probability for a UE" $P_{\text{LoS/UE}}$ is defined as the percentage of the NBs with the fact that the UE can set up a LoS channel among all valid NBs. In the measurement data, the case of receiving two scrambling codes per carrier is the majority. The $P_{\text{LoS/UE}}$ for the two-scrambling-code cases is investigated based on available observations. Figure 13 depicts the empirical percentage of $P_{\text{LoS/UE}}$ for three carriers. It can be observed that the distributions of $P_{\text{LoS/UE}}$ are similar for all three carriers, which is probability due to the fact that every NB in Nanjing Road makes use of three carriers. Furthermore, the case of no LoS path existed to the two NBs has the probability larger than 0.4. The opposite situation that all NBs have LoS connections to UE has the probability around 0.15. It is easy to deduce that the case where the UE has at least one LoS connection to the surrounding NBs can happen with probability 0.6. These results may be used to provide probabilistic assumptions for designing the cooperative multipoint (CoMP) techniques when the coexisting multilinks involve both LoS and NLoS channels.

For individual NBs, it is important to know the distribution of a specific percentage of UE that are categorized as LoS users among all UE served by the NB. The "LoS existence probability per NB" $P_{\text{LoS/NB}}$ is defined as the ratio of number of LoS UE to the number of all UE in the coverage of a NB. Figure 14 illustrates the empirical percentages of LoS existence probability per NB per carrier, calculated based on the observations in total 78 NBs. It can be observed from Figure 14 that, for three carriers, the situation of all UE in a NB experiencing LoS channel is zero, the situation in which 20% of the UE in a NB are LoS users occurs with 0.4 probability, and the case with 80% of the UE being LoS users happens with probability close to 0.2. This result indicates that, on the Nanjing Road, the existing NBs can be categorized into two groups, one with the most users being LoS users and the other with the most users being NLoS

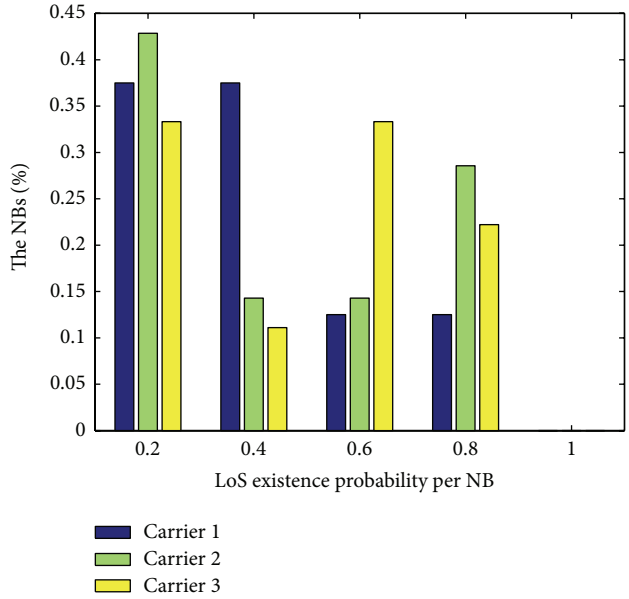

Figure 14: The empirical percentage of LoS existence probability per NB.

users. This categorizing scheme probability is due to the fact that the most NBs deployed on Nanjing Road are either micro- or pico-cellular NBs. Depending on the type of the NB, distinctive distribution of "LoS existence probability per NB" may be caused.

In addition, an interesting phenomenon observed from Figure 14 is that, for the carriers 2 and 3, higher $P_{\text{LoS/NB}}$ is observed with larger probability than in the case of carrier 1. This is probably due to the reason that the carriers 2 and 3 might be more widely used in the pico-cellular NBs than the

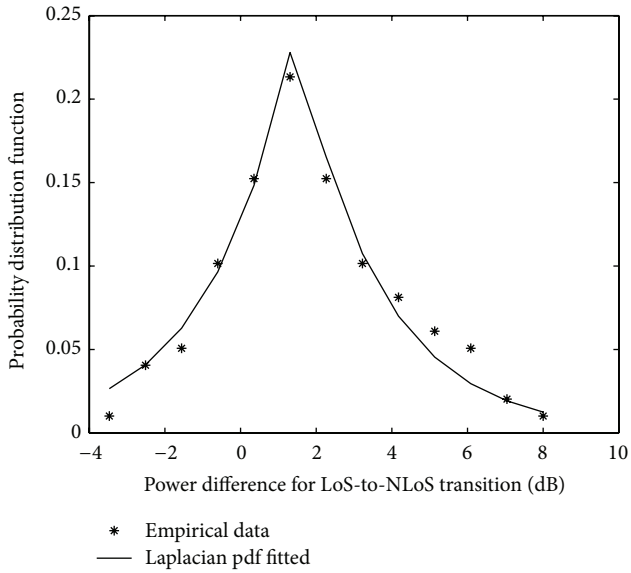

Figure 15: The empirical pdf and fitted Laplacian pdf for the power difference of the channels before and after the LoS-to-NLoS transition.

carrier 1. Since more LoS users exist in the pico-cellular NBs than other types of NBs [45], the carriers 2 and 3 exhibit higher probability than the carrier 1 for larger $P_{\text{LoS/NB}}$.

4.5. Channel Characterization of LoS-NLoS Transition. Power diversity techniques used in the NOMA systems mitigate the multipath fading by adapting the transmission power, for example, allocating low power for UE in LoS scenarios and higher power for UE in NLoS scenarios. Designing such techniques requires accurate modeling of the power difference between the LoS and NLoS channels, particularly during the transition process. To design the transmission techniques used in the LoS and NLoS scenarios specifically, adaptation operations, such as switching the techniques or modifying operational parameters, are necessary when the channel changes from the LoS scenario to the NLoS scenario or vice versa. Thus, it is necessary to characterize the channel variations during the period of LoS-to-NLoS or NLoS-to-LoS transition. Measurements were conducted around multiple crosses along Nanjing Road to acquire the downlink data for 1 minute while the receiver was moving. The transitions between LoS and NLoS channels are identified and the interested parameters are analyzed.

4.5.1. Power Difference at LoS-NLoS Transition. Figure 15 demonstrates that the empirical pdf of the power differences $\Delta P_{\text{LoS–NLoS}} = P_{\text{LoS}} - P_{\text{NLoS}}$ at LoS-to-NLoS transition points. The fitted analytical graph is also illustrated. It can be observed from Figure 15 that the majority of the distribution of $\Delta P_{\text{LoS–NLoS}}$ is located above 0 dB in the abscissa. The Laplace distribution with its parameters $\mu = 1.42$ dB and $b = 2.22$ fits well with the empirical data. Furthermore, the observation that $\Delta P_{\text{LoS–NLoS}}$ is less than 0 dB indicates that, for some transitions, the NLoS scenarios have higher received

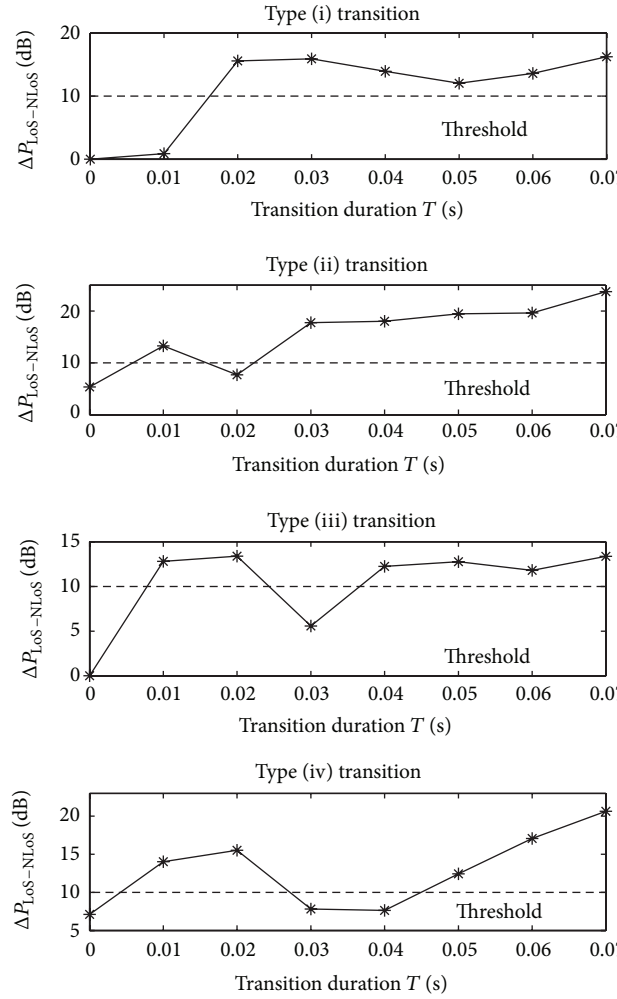

Figure 16: Examples of the four types of transition behavior.

power than the LoS scenarios. This phenomenon may be due to the fact that, for some locations such as the corners of streets, when a UE turns its moving direction significantly, the LoS-to-NLoS transition occurs, and the constellation of multipath propagation may include new NLoS paths which add more power to the channel than the power lost due to the absence of the LoS path. This is different with the obstruction cases where the overall propagation constellation is retained with only the LoS path absent due to blockage.

4.5.2. LoS-to-NLoS Transition Duration. The LoS-to-NLoS transition duration T is defined as the time spent on the period from the starting of transition to the moment that the NLoS channel begins to stabilize. Here the channel is considered stabilized if the LoS or NLoS status is maintained for no less than 10 frames. The observations show that all LoS-to-NLoS transitions can be categorized into four types depending on the times of back-and-forth between LoS and NLoS scenarios. Figure 16 illustrates examples for the four transition types. Type (i) is referred to as the case where a LoS channel changes to a NLoS channel which stabilizes immediately. For such cases, T is regarded to be 1 frame. Type (ii)

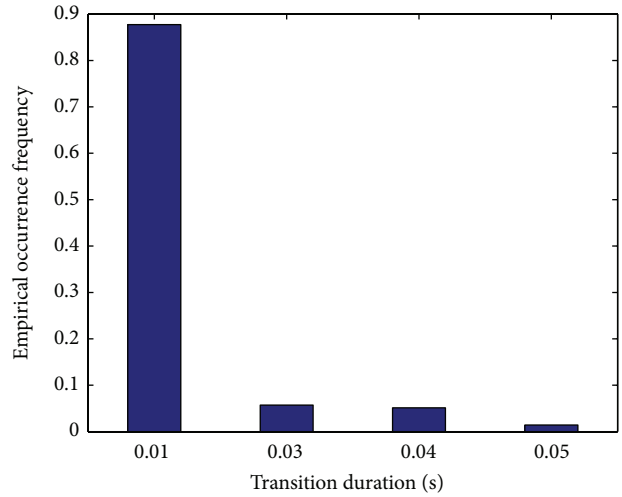

Figure 17: The empirical occurrence frequency of transition duration from LoS points to NLoS points or NLoS points to LoS points.

denotes the situation that, after the transition starts, the NLoS channel changes back to the LoS scenario once and then transits again to the NLoS scenario. For this case, T is considered to be 3 frames. Type (iii) is similar with type (ii) but the difference is that, during the transition, the NLoS scenario lasts for two frames before transiting back to the LoS. Type (iv) is similar with type (iii) except for the fact that the LoS channel remains for two frames before transiting to the NLoS scenario in the second time. For the latter two types, T is considered to be 4 and 5 frames, respectively. Figure 17 depicts the empirical probability of T for the four types considered. It can be observed that the type I transition occurs with the highest probability of 0.9 among all types. Only a small amount of transitions undergoes the fluctuations in types (ii) to (iv) which cost a longer time for channel being stabilized. These results show that, for the walking speed in a city canyon environment, most of the LoS-to-NLoS transitions are accomplished rapidly in one frame, that is, 10 ms. Longer transitions lasting for more than one frame can be neglected when designing systems for their low occurrence probabilities.

5. Conclusions

A channel measurement campaign has been conducted aiming at characterizing LoS/NLoS channels by using the downlink signals in a commercial UMTS network for a pedestrian zone in Nanjing Road, Shanghai. Techniques were developed for extracting the channel impulse responses, and multipath parameters were estimated by using the SAGE algorithm. Channels observed were categorized into LoS and NLoS by using a novel multipath-based LoS detection method. A map overlaid by the channel properties observed at multiple locations demonstrated that LoS channels mostly exist in open areas, while NLoS channels are dominant in the city canyons with densely distributed skyscrapers. Statistical models for the fading coefficients were first established, which have shown that the existence of the LoS path can bring 6 dB gain on average and reduce the gain variation by 5 dB. Additionlly, the statistics of some newly defined parameters were also investigated, which include the distributions of the LoS and NLoS life-distance, the LoS existence probability per user equipment and per NB, power difference at the LoS-to-NLoS transition, and the transition duration. Important findings were discovered; for example, the LoS and NLoS life-distances are usually less than 10 m, the LoS-to-NLoS transition can be accomplished less than 10 ms, and so forth. These characteristics are important for the design and preference evaluation of the techniques or systems adaptive to LoS and NLoS scenarios.

Conflict of Interests

The authors declare that there is no conflict of interests regarding the publication of this paper.

Acknowledgments

The authors wish to acknowledge Dr. Junhe Zhou, Tongji University, for his valuable comments on the paper. This work is jointly supported by Huawei Technology Company in the research Project "Analysis and Verification of Channel Fingerprinting Characteristics in In-Service UMTS Networks" (YBWL2010KJ010), Huawei innovation research Project "High Dimensional MIMO Channel Estimation, Modeling, and Measurement Combined with Antenna Status," the Science and Technology Commission of Shanghai Municipality "System Design and Demo-Construction for Cooperative Networks of High-Efficiency 4G Wireless Communications in Urban Hot-Spot Environments" (13510711000), and the Key Program of National Natural Science Foundation of China (Grant no. 61331009).

References

[1] *Universal Mobile Telecommunications System (UMTS); Spacial Channel Model for Multiple Input Multiple Output (MIMO) Simulations (3GPP TR 25.996 Version 8.0.0 Release 8)*, ETSI Std.

[2] WINNER II interim channel models, IST-4-027756 WINNER D1.1.1 Std.

[3] D. Gesbert, M. Shafi, D. Shiu, P. J. Smith, and A. Naguib, "From theory to practice: an overview of MIMO space-time coded wireless systems," *IEEE Journal on Selected Areas in Communications*, vol. 21, no. 3, pp. 281–302, 2003.

[4] M. Coldrey, H. Koorapaty, J. Berg et al., "Small-cell wireless backhauling: a non-line-of-sight approach for point-to-point microwave links," in *Proceedings of the 76th IEEE Vehicular Technology Conference (VTC Fall '12)*, September 2012.

[5] S. Mukherjee, *WiMAX Antennas Primer—A Guide to MIMO and Beamforming*, 2010.

[6] B. Furht and S. A. Ahson, *Long Term Evolution: 3GPP LTE Radio and Cellular Technology*, 2009.

[7] Y. Saito, Y. Kishiyama, A. Benjebbour, T. Nakamura, A. Li, and K. Higuchi, "Non-orthogonal multiple access (NOMA) for future radio access," in *Proceedings of the IEEE 77th Vehicular Technology Conference (VTC '13)*, 2013.

[8] K. Higuchi and Y. Kishiyama, "Non-orthogonal access with random beamforming and intra-beam SIC for cellular mimo downlink," in *Proceedings of the IEEE 78th Vehicular Technology Conference (VTC '13)*, pp. 1–5, Las Vegas, Nev, USA, September 2013.

[9] J. Umehara, Y. Kishiyama, and K. Higuchi, "Enhancing user fairness in non-orthogonal access with successive interference cancellation for cellular downlink," in *Proceedings of the IEEE 14th International Conference on Communication Systems (ICCS '12)*, pp. 324–328, Singapore, November 2012.

[10] D. Jiang and L. Delgrossi, "IEEE 802.11p: towards an international standard for wireless access in vehicular environments," in *Proceedings of the 67th IEEE Vehicular Technology Conference (VTC '08)*, pp. 2036–2040, May 2008.

[11] X. Cheng, C. Wang, B. Ai, and H. Aggoune, "Envelope level crossing rate and average fade duration of nonisotropic vehicle-to-vehicle Ricean fading channels," *IEEE Transactions on Intelligent Transportation Systems*, vol. 15, no. 1, pp. 62–72, 2014.

[12] X. Cheng, Q. Yao, M. Wen, C. Wang, L. Song, and B. Jiao, "Wideband channel modeling and intercarrier interference cancellation for vehicle-to-vehicle communication systems," *IEEE Journal on Selected Areas in Communications*, vol. 31, no. 9, pp. 434–448, 2013.

[13] V. Nurmela, T. Jämsä, P. Kyösti, V. Hovinen, and J. Medbo, "Channel modelling for device-to-device scenarios," IC 1004 TD(13)08009, 2013.

[14] D. W. Matolak, "Channel modeling for vehicle-to-vehicle communications," *IEEE Communications Magazine*, vol. 46, no. 5, pp. 76–83, 2008.

[15] Y. Zhang, R. Yu, M. Nekovee, Y. Liu, S. Xie, and S. Gjessing, "Cognitive machine-to-machine communications: visions and potentials for the smart grid," *IEEE Network*, vol. 26, no. 3, pp. 6–13, 2012.

[16] J. Borras, P. Hatrack, and N. B. Mandayam, "Decision theoretic framework for NLOS identification," in *Proceedings of the 48th IEEE Vehicular Technology Conference (VTC '98)*, pp. 1583–1587, May 1998.

[17] M. Wylie-Green and J. Holtzman, "Locating mobile stations with non-line-of-sight measurements," *Advances in Wireless Communications*, p. 359, 1998.

[18] S. Venkatraman, J. Caffery Jr., and H.-. You, "Location using LOS range estimation in NLOS environments," in *Proceedings of the 55th IEEE Vehicular Technology Conference (VTC '02)*, vol. 2, pp. 856–860, May 2002.

[19] J. Schroeder, S. Galler, K. Kyamakya, and K. Jobmann, "NLOS detection algorithms for ultra-wideband localization," in *Proceedings of the 4th Workshop on Positioning, Navigation and Communication (WPNC '07)*, pp. 159–166, March 2007.

[20] A. Maali, H. Mimoun, G. Baudoin, and A. Ouldali, "A new low complexity NLOS identification approach based on UWB energy detection," in *Proceedings of the IEEE Radio and Wireless Symposium (RWS '09)*, pp. 675–678, San Diego, Calif, USA, January 2008.

[21] A. Lakhzouri, E. S. Lohan, R. Hamila, and M. Rentors, "Extended Kalman filter channel estimation for line-of-sight detection in WCDMA mobile positioning," *EURASIP Journal on Applied Signal Processing*, vol. 2003, no. 13, pp. 1268–1278, 2003.

[22] F. Benedetto, G. Giunta, A. Toscano, and L. Vegni, "Dynamic LOS/NLOS statistical discrimination of wireless mobile channels," in *Proceedings of the 65th IEEE Vehicular Technology Conference (VTC '07)*, pp. 3071–3075, 2007.

[23] T. Svantesson and J. Wallace, "Statistical characterization of the indoor mimo channel based on los/nlos measurements," in *Proceedings of the 36th Asilomar Conference on Signals, Systems and Computers*, vol. 2, pp. 1354–1358, IEEE, 2002.

[24] K. Yu, M. Bengtsson, B. Ottersten, D. McNamara, P. Karlsson, and M. Beach, "Modeling of wide-band MIMO radio channels based on NLoS indoor measurements," *IEEE Transactions on Vehicular Technology*, vol. 53, no. 3, pp. 655–665, 2004.

[25] C. Bergljung and P. Karlsson, "Propagation characteristics for indoor broadband radio access networks in the 5 GHz band," in *Proceedings of the 9th IEEE International Symposium on Personal, Indoor and Mobile Radio Communications (PIMRC '98)*, vol. 2, pp. 612–616, September 1998.

[26] K. Yu, M. Bengtsson, B. Ottersten, D. McNamara, P. Karlsson, and M. Beach, "Second order statistics of NLOS indoor MIMO channels based on 5.2 GHz measurements," in *Proceedings of the IEEE Global Telecommunicatins Conference (GLOBECOM '01)*, pp. 156–160, November 2001.

[27] H. Yang, P. F. M. Smulders, and M. H. A. J. Herben, "Frequency selectivity of 60 GHz LOS and NLOS indoor radio channels," in *Proceedings of the 63rd IEEE Vehicular Technology Conference (VTC '06)*, vol. 6, pp. 2727–2731, July 2006.

[28] Z. Lin, X. Peng, K. B. Png, and F. Chin, "Kronecker modelling for correlated shadowing in UWB MIMO channels," in *Proceedings of the IEEE Wireless Communications and Networking Conference (WCNC '07)*, pp. 1585–1589, March 2007.

[29] J. C. Liberti and T. S. Rappaport, "Statistics of shadowing in indoor radio channels at 900 and 1900 MHz," in *Proceedings of the IEEE Military Communications Conference (MILCOM '92)*, pp. 1066–1070, 1992.

[30] J. E. Berg, R. Bownds, and F. Lotse, "Path loss and fading models for microcells at 900 MHz," in *Proceedings of the 42th IEEE Vehicular Technology Conference (VTC '92)*, pp. 666–671, 1992.

[31] S. Y. Tan and H. S. Tan, "Propagation model for microcellular communications applied to path loss measurements in Ottawa City streets," *IEEE Transactions on Vehicular Technology*, vol. 44, no. 2, pp. 313–317, 1995.

[32] V. Erceg, L. J. Greenstein, S. Y. Tjandra et al., "Empirically based path loss model for wireless channels in suburban environments," *IEEE Journal on Selected Areas in Communications*, vol. 17, no. 7, pp. 1205–1211, 1999.

[33] E. Green and M. Hata, "Microcellular propagation measurements in an urban environment," in *Proceedings of the IEEE Personal, Indoor and Mobile Radio Communications (PIMRC '91)*, pp. 324–328, 1991.

[34] Y. Oda, K. Tsunekawa, and M. Hata, "Advanced LOS path-loss model in microcellular mobile communications," *IEEE Transactions on Vehicular Technology*, vol. 49, no. 6, pp. 2121–2125, 2000.

[35] G. Bauer and R. Jakoby, "Analysis and estimation of line-of-sight coverage in urban areas for fixed broadband wireless access systems," in *Proceedings of the 10th European Conference on Wireless Technology (ECWT '07)*, pp. 229–232, October 2007.

[36] J. Yu, X. Yin, J. Chen et al., "Channel maps and stochastic models in elevation based on measurements in operating networks," in *Proceedings of the IEEE Wireless Communications and Signal Processing (WCSP '13)*, pp. 1–6, 2013.

[37] M. Ylitervo and M. Vayrynen, "Methods for making active channel measurements in a personal base station environment," US Patent 5 726 981, 1998.

[38] K. Pentikousis, M. Palola, M. Jurvansuu, and P. Perälä, "Active goodput measurements from a public 3G/UMTS network," *IEEE Communications Letters*, vol. 9, no. 9, pp. 802–804, 2005.

[39] J. Potman, F. W. Hoeksema, and C. H. Slump, "Adjacent channel interference in UMTS networks, prorisc," in *Proceedings of the 17th Annual Workshop on Circuits, Systems and Signal Processing*, Veldhoven, The Netherlands, 2006.

[40] X. Yin, N. Zhang, Z. Zhong et al., "System-level channel modeling based on active measurements from a public 3G/UMTS network," in *Proceedings of the 78th IEEE Vehicular Technology Conference (VTC '13)*, pp. 1–5, 2013.

[41] "USRP n210 datasheet," Tech. Rep., https://www.ettus.com/product/details/UN210-KIT.

[42] Technical Specification Group Radio Access Network, *Physical Channels and Mapping of Transport Channels onto Physical Channels (FDD)(Release 9)*, 3rd Generation Partnership Project 3GPP TS 25.211 V9.2.0 (2010-09) Std.

[43] B. H. Fleury, M. Tschudin, R. Heddergott, D. Dahlhaus, and K. I. Pedersen, "Channel parameter estimation in mobile radio environments using the SAGE algorithm," *IEEE Journal on Selected Areas in Communications*, vol. 17, no. 3, pp. 434–450, 1999.

[44] A. Goldsmith, *Wireless Communications*, Cambridge University Press, 2005.

[45] L. Thiele, M. Peter, and V. Jungnickel, "Statistics of the Ricean k-factor at 5.2 GHz in an urban macro-cell scenario," in *Proceedings of the 17th IEEE International Symposium on Personal, Indoor and Mobile Radio Communications (PIMRC '06)*, pp. 1–5, September 2006.

Hindawi Publishing Corporation
International Journal of Antennas and Propagation
Volume 2014, Article ID 984102, 12 pages
http://dx.doi.org/10.1155/2014/984102

Research Article

Fading Evaluation in the 60 GHz Band in Line-of-Sight Conditions

J. Reig,[1] M.-T. Martínez-Inglés,[2] L. Rubio,[1] V.-M. Rodrigo-Peñarrocha,[1] and J.-M. Molina-García-Pardo[2]

[1] *Grupo de Radiación Electromagnética (GRE), Universitat Politècnica de València, Camino de Vera s/n, 46022 Valencia, Spain*
[2] *Grupo de Sistemas de Comunicaciones Móviles (SiCoMo), Universidad Politécnica de Cartagena, Antigones, 30202 Cartagena, Spain*

Correspondence should be addressed to J. Reig; jreigp@dcom.upv.es

Received 9 May 2014; Revised 10 July 2014; Accepted 10 July 2014; Published 7 August 2014

Academic Editor: Jose F. Paris

Copyright © 2014 J. Reig et al. This is an open access article distributed under the Creative Commons Attribution License, which permits unrestricted use, distribution, and reproduction in any medium, provided the original work is properly cited.

An exhaustive analysis of the small-scale fading amplitude in the 60 GHz band is addressed for line-of-sight conditions (LOS). From a measurement campaign carried out in a laboratory, we have estimated the distribution of the small-scale fading amplitude over a bandwidth of 9 GHz. From the measured data, we have estimated the parameters of the Rayleigh, Rice, Nakagami-m, Weibull, and α-μ distributions for the small-scale amplitudes. The test of Kolmogorov-Smirnov (K-S) for each frequency bin is used to evaluate the performance of such statistical distributions. Moreover, the distributions of the main estimated parameters for such distributions are calculated and approximated for lognormal statistics in some cases. The matching of the above distributions to the experimental distribution has also been analyzed for the lower tail of the cumulative distribution function (CDF). These parameters offer information about the narrowband channel behavior that is useful for a better knowledge of the propagation characteristics at 60 GHz.

1. Introduction

There is an increasing interest in using the unlicensed 60 GHz frequency band for commercial applications because of its capability to provide extremely high data rates beyond 5 Gbps over short distances [1–4].

The IEEE 802.15.3c task group (TG3c) has recently published the standard for the millimeter-wave- (mmW-) based alternative physical layer extension for IEEE802.15.3, that is, physical layer (PHY) and media access control layer (MAC) specifications. The IEEE 802.15.3c [5] is a standard in the 60 GHz band for wireless personal area networks (WPAN) devices in the named wireless gigabit ethernet. Simultaneously, the industry has created the consortium wireless gigabit alliance, commonly called WiGig [6], which is devoted to the development and promotion of wireless communications in the 60 GHz band. This band offers the following advantages: (i) huge and readily available spectrum allocation with 7 GHz in both USA and Japan and 9 GHz in Europe, (ii) dense deployment and high frequency reuse, and (iii) reduced size of devices due to the small wavelength [2]. The output power of 60 GHz devices is mainly limited to 10 mW due to regulations. Moreover, the free space losses in the 60 GHz band are considerably higher than those in the microwave band. Thus, the mmW WPAN devices will be designed to operate mainly in short-range line-of-sight (LOS) environments.

Since high data rates available in the IEEE 802.15.3c standard are achieved with multiple-input and multiple-output (MIMO) techniques [5], it is of paramount importance to characterize adequately the propagation channel in such band.

Several measurement campaigns have been carried out to model adequately the propagation channel at the 60 GHz band [7–15]. In [7], a stochastic channel model has been derived from measurements conducted in office, private house, library, and laboratory environments. The Triple-S and Valenzuela (TSV) statistical model has been proposed in [8] for the mmW band from the well-known Saleh and Valenzuela (SV) model. A modified SV model has been

derived in [9] where the deterministic two-path model is extended to a statistical two-path model by introducing random variables for the antenna position and merging with the conventional SV model which is suitable to express non-line-of-sight (NLOS) path components. In [10], power delay profiles (PDPs) and power angle profiles (PAPs) have been measured in various indoor and short-range outdoor environments. These experimental functions have been compared to results provided with image based on ray tracing techniques, by separating the multipath components (MPCs) in angle of arrival (AOA) and time of arrival (TOA). Measurements in a modern office block addressed to characterize the path loss were carried out in [11]. In [12], Smulders has reviewed the statistical description of an extensive number of measurements campaigns and channel modeling published previously.

As a result of some of such works, the TG3c channel modeling subcommittee released a report where a comprehensive channel model is presented based on measurements conducted in several environments [16].

The high speed interface (HSI) mode of the IEEE 802.15.3c standard is designed for devices with low-latency and bidirectional high-speed data and uses orthogonal frequency domain multiplexing (OFDM) [5]. Since the guard interval in the OFDM-HSI mode is higher than the root mean square (rms) delay spread in the majority of indoor environments [7, 10, 11], an accurate characterization of the narrowband channel is required for the 60 GHz frequency band.

Concretely, small-scale fading analyses in the 60 GHz have been addressed in some works to characterize the received amplitude [12–14]. In [13], the small-scale amplitude in LOS measurements conducted in three corridors of an office block with a bandwidth of 1 GHz was modeled as a Rice distribution. Values of mean and standard deviation of the Rice K-factor have been reported for two antenna types: an open-ended waveguide (OWG) and lens. The small-scale amplitude has been found to follow a Rayleigh distribution in an urban environment with ranges up to 400 m [14].

In spite of the numerous researches' efforts, an extensive study of the small-scale fading amplitude in the 60 GHz frequency band remains still open in the technical literature. Furthermore, the performance of MIMO techniques depends strongly on the multipath characteristics of the signal at the receiver device. Therefore, an exhaustive analysis of the fading phenomenon in the 60 GHz band is vital for the deployment of such systems.

In this paper, we will address an extensive study of the fading distribution in the 60 GHz band with LOS conditions from a measurement campaign carried out in a laboratory. The small-scale amplitude of the received signal is modeled as distributions proposed in the literature for modeling the fading amplitude: Rayleigh, Rice, Weibull, Nakagami-m, and α-μ distributions. Recently, several distributions have been proposed to model the small-scale fading in LOS condition [17, 18]. Nevertheless, to the best of the authors' knowledge, no estimators have been derived for the two-wave with diffuse power (TWDP) fading distribution proposed in [17]. In [18], the estimators of the κ-μ fading distribution

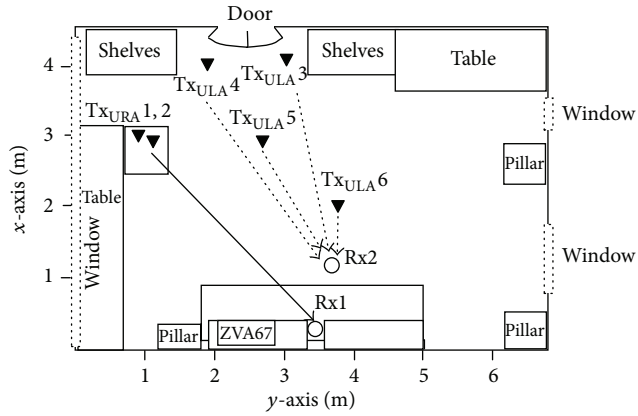

Figure 1: Map of measurements.

are calculated by using the method of moments with the moments of orders 4th and 6th. It is well known that the higher the order of moments used in the method of moments is, the poorest performance of such estimators is. Therefore, we have not analyzed both distributions in this paper. From experimental data, we have obtained the best-fit distribution and the distribution of the parameters inferred for Rayleigh, Rice, Weibull, Nakagami-m, and α-μ distributions.

This paper is organized as follows: firstly, the measurement campaign and the measuring setup are exposed in Section 2. In Section 3, the estimators of the distributions used to model the small-scale fading are presented. Next, Section 4 includes the results of the best-fitting distributions. Finally, the conclusions are discussed in Section 5.

2. Measurement Setup

Measurements have been performed in a laboratory of the Universidad Politécnica de Cartagena, Spain. The scenario consists of a room of dimensions approximately 4.5 × 7 × 3 m and it is furnished with several closets, desktops, and computers. The walls are made of plasterboard, whereas the floor is made of concrete. Figure 1 shows a top view of the room where measurements have been performed.

The channel sounder is based on the vector network analyzer (VNA) Rhode ZVA67, which has a dynamic range of 110 dB at 60 GHz. A resolution bandwidth of 10 Hz has been used and the band is 57–66 GHz. Both ports have V/1.85 mm female connectors. The antennas used in the measurements have a 5 dBi gain (manufacturer: Q-par 55 to 65 GHz omnidirectional antennas with V/1.85 mm type connector). A scheme of the channel sounder can be found in Figure 2.

The receiving antenna (Rx) is connected to the receiving port of the VNA using a 2 m coaxial cable, while the signal of the transmitting port of the VNA is twice amplified before being connected to the transmitter antenna (Tx), with a total length cable of 6.5 m (4 m + 2 m + 0.5 m). The reference of the two 25 dB amplifiers is HXI HLNA-465. The insertion losses of the cable are around 6 dB/m at 66 GHz. The polarization of antennas is vertical. For each combination of the Tx/Rx,

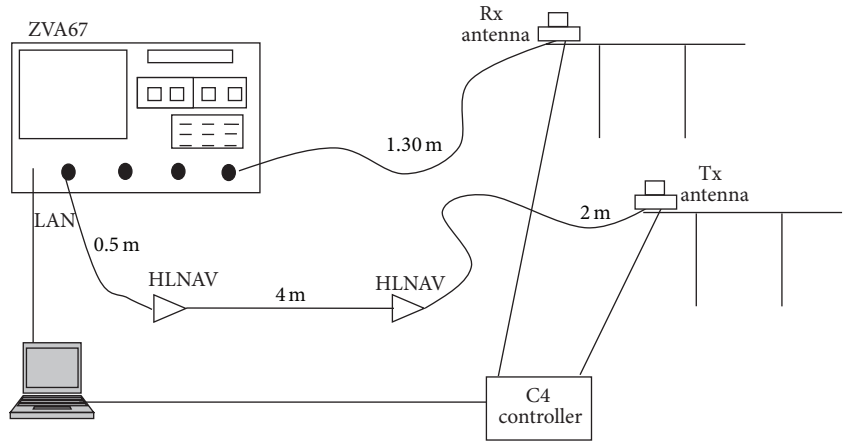

Figure 2: Scheme of the channel sounder.

we use virtual arrays by means of a linear positioning system moved by a C4 controller, and measurements can be distinguished into two groups.

Tx1-2 (corresponding to Rx1-2): in this case, the transmitter is placed in a bidimensional virtual array, uniform rectangular array (URA) 2D positioner, while the receiver uses a unique position.

Tx3-6 (corresponding to Rx3-6 each): both the transmitter and the receiver use uniform linear array (ULA).

The ULA are oriented in the y-axis corresponding to Figure 1. The URA are oriented in the x- and y-axes.

More details can be found in Table 1. The space between positions is 2 mm in both ULA and URA. The measurement process is controlled by a Matlab-based software executed from a laptop, which is connected to the VNA by a local area network (LAN) and to the C4 controller by a RS232 connection.

Each configuration has a bandwidth of 9 GHz and number of equal space frequency points, which are also summarized in Table 1. The transmitted power by the VNA was set to −10 dBm (in order not to saturate the first amplifier), giving a dynamic range of more than 100 dB at 66 GHz; that is, all of the cable attenuation is compensated by the two amplifiers and the measurement is calibrated using the through method. During the measurement process, nobody was in the room, so the channel can thus be considered as stationary. All of the measurement process has been carefully checked by analyzing the frequency response and by measuring the LOS component in the time domain. An analysis of the path-loss, correlation coefficients, and throughput in such scenario is carried out in [19].

3. Estimators of the Small-Scale Fading Distribution

In this section, estimators of the most employed distributions for small-scale modeling are described besides both the probability density functions (PDFs) and the cumulative distribution functions (CDFs). The Rayleigh, Rice, Weibull, Nakagami-m, and α-μ distributions can adequately characterize different fading conditions.

There are several methods to estimate parameters in distributions. The maximum likelihood estimation (MLE) is superior to the other estimation methods. Nevertheless, the derivation of MLE estimators cannot be straightforward [20]. For instance, a scalar nonlinear equation system is obtained in MLE method for the α-μ distribution without a single solution. The method of moments (MM) provides in many distributions consistent estimators and the estimating equations are simple in many situations [20]. For the α-μ distribution and Nakagami-m distributions, we have used the log-moments method, since it offers more superior performance than MM.

Let r be the instantaneous received field strength amplitude expressed in V/m. Thus, the received field strength in dBV/m is given by $\varepsilon = A \ln r$, where

$$A = \frac{20}{\ln 10}. \tag{1}$$

From the measurements records, we assume a sample size of N. Thus, $r_i, \varepsilon_i,\ i = 1, \ldots, N$ correspond to each observation in linear and logarithmic units, respectively. The sample nth raw moments of r and ε are defined as

$$\widehat{\mu}'_{r_n} = \frac{1}{N}\sum_{i=1}^{N} r_i^n, \tag{2}$$

$$\widehat{\mu}'_{\varepsilon_n} = \frac{1}{N}\sum_{i=1}^{N} \varepsilon_i^n, \tag{3}$$

respectively. We can calculate the sample nth central moments of r and ε as

$$\widehat{\mu}_{r_n} = \frac{1}{N}\sum_{i=1}^{N}\left(r_i - \widehat{\mu}'_{r_1}\right)^n, \tag{4}$$

$$\widehat{\mu}_{\varepsilon_n} = \frac{1}{N}\sum_{i=1}^{N}\left(\varepsilon_i - \widehat{\mu}'_{\varepsilon_1}\right)^n. \tag{5}$$

3.1. Rayleigh Distribution. If both the inphase and quadrature components of the complex baseband received signal follow a Gaussian distribution with 0 mean and standard deviation σ, then the amplitude of the received signal r, is a Rayleigh random variable (RV). This situation frequently occurs in the NLOS case, where the real and imaginary parts of the MPC fulfill these conditions since they are composed of the sum of a large number of waves. Thus, the sum of enough independent RVs provided the fact that no one of the RV dominates very closely to a normal distribution [21]. Nevertheless, the Rayleigh distribution has been extensively used to model the small-scale received amplitude in several environments due to its simplicity.

Assuming that r follows a Rayleigh distribution, the PDF of r is given by

$$p(r) = \frac{r}{\sigma^2} \exp\left(-\frac{r^2}{2\sigma^2}\right), \quad r \geq 0, \tag{6}$$

where $\sigma = \sqrt{E[r^2]/2}$, denoting $E[\cdot]$ expectation.

Likewise, the PDF of ε can be written as

$$p(\varepsilon) = \frac{1}{A\sigma^2} \exp\left(\frac{2\varepsilon}{A} - \frac{e^{2\varepsilon/A}}{2\sigma^2}\right), \quad -\infty < \varepsilon < \infty, \tag{7}$$

where A is given by (1).

The CDF in linear and logarithm units are given by

$$F(r) = 1 - \exp\left(-\frac{r^2}{2\sigma^2}\right), \quad r \geq 0, \tag{8}$$

$$F(\varepsilon) = 1 - \exp\left(-\frac{e^{2\varepsilon/A}}{2\sigma^2}\right), \quad -\infty < \varepsilon < \infty, \tag{9}$$

respectively.

Using the MLE method, σ can be estimated from the samples r_i, $i = 1, \ldots, N$ as

$$\widehat{\sigma} = \sqrt{\frac{1}{2}\widehat{\mu}'_{r_2}}. \tag{10}$$

3.2. Rice Distribution. In LOS situations, very often the received signal is composed of random MPCs, whose amplitude is described by the Rayleigh distribution plus a coherent LOS component which has essentially constant power. The power of this component, denoted by ν^2, is frequently higher than the total multipath power, symbolized as $2\sigma^2$.

Hence, the PDF of a Rice distribution can be expressed as

$$p(r) = \frac{r}{\sigma^2} \exp\left(-\frac{r^2 + \nu^2}{2\sigma^2}\right) I_0\left(\frac{\nu r}{\sigma^2}\right), \quad r \geq 0, \tag{11}$$

where $I_a(\cdot)$ is the modified Bessel function of the first kind with order a[22, 8.406].

The Rice factor, K, extensively used in radio propagation is defined as

$$K = \frac{\nu^2}{2\sigma^2}, \tag{12}$$

which represents the ratio between power of the coherent LOS component and the power in the other scattered MPCs.

The PDF of ε is expressed as

$$p(\varepsilon) = \frac{1}{A\sigma^2} \exp\left(\frac{2\varepsilon}{A} - \frac{e^{2\varepsilon/A} + \nu^2}{2\sigma^2}\right) I_0\left(\frac{\nu e^{\varepsilon/A}}{\sigma^2}\right), \quad -\infty < \varepsilon < \infty, \tag{13}$$

where A is given by (1).

The CDF of r and ε can be written as

$$F(r) = 1 - Q\left(\frac{\nu}{\sigma}, \frac{r}{\sigma}\right), \quad r \geq 0, \tag{14}$$

$$F(\varepsilon) = 1 - Q\left(\frac{\nu}{\sigma}, \frac{\exp(2\varepsilon/A)}{\sigma}\right), \quad -\infty < \varepsilon < \infty, \tag{15}$$

respectively, where $Q(a, b) = \int_b^\infty x \exp(-(x^2+a^2)/2) I_0(ax) dx$ is the Marcum Q function [23].

In [24], an efficient algorithm to estimate the υ and σ parameters of the Rice distribution with the MM has been derived using the sample mean and the sample standard deviation. This recursive algorithm defines the function

$$g(\theta) = \sqrt{\xi(\theta)(1 + r^2) - 2}, \tag{16}$$

where

$$\xi(\theta) = 2 + \theta^2 - \frac{\pi}{8} \exp\left(-\frac{\theta^2}{2}\right) \left[\left(2 + \theta^2\right) I_0\left(\frac{\theta^2}{4}\right) + \theta^2 I_1\left(\frac{\theta^2}{4}\right)\right]^2, \tag{17}$$

$$r = \frac{\widehat{\mu}'_{r_1}}{\widehat{\mu}_{r_2}}.$$

From a starting point of iteration $\theta_0 > 0$, we recursively evaluate $g^m(\theta_0) = \underbrace{g(g(\cdots g(\theta_0)))}_{m \text{ times}}$ until $|g^i(\theta_0) - \theta_{i-1}| \leq \Delta$, where Δ is the required accuracy. From this point, the parameters of the Rice distribution can be calculated as

$$\widehat{\sigma} = \sqrt{\frac{\widehat{\mu}_{r_2}}{\xi(\theta_i)}}, \tag{18}$$

$$\widehat{\nu} = \sqrt{\widehat{\mu}'^2_{r_1} + \left(\xi(\theta_i) - 2\right)\widehat{\sigma}^2}, \tag{19}$$

where $\theta_i = g^i(\theta_0)$ has been obtained in the ith iteration. Note that the minimum theoretical value of r is $\sqrt{\pi/(4-\pi)}$ that corresponds to a Rayleigh distribution; that is, $\upsilon = 0$. Hence, if $r < \sqrt{\pi/(4-\pi)}$, then υ is fixed to 0, and from (11) the estimated distribution becomes Rayleigh.

3.3. Nakagami-m Distribution. In several environments, the Rayleigh and Rice distributions cannot characterize satisfactorily the behavior of the received signal amplitude. For

instance, if two paths are of comparable power and are stronger than all the others, the amplitude signal does not fit neither Rice nor Rayleigh distributions.

The Nakagami-m distribution [25] assumes that the received signal is a sum of vectors with random magnitude and random phases with less restriction than both the Rice and Rayleigh distributions, thus providing more accuracy in matching experimental data than the use of such distributions [26].

The PDF of the Nakagami-m distribution in linear and logarithmic units is given by

$$p_r(r) = \frac{2}{\Gamma(m)}\left(\frac{m}{\Omega}\right)^m r^{2m-1}\exp\left(-\frac{mr^2}{\Omega}\right), \quad r \geq 0, \quad m > \frac{1}{2},$$
$$p_\varepsilon(\varepsilon) = \frac{2}{A\Gamma(m)}\left(\frac{m}{\Omega}\right)^m \exp\left(\frac{2m\varepsilon}{A} - \frac{me^{2\varepsilon/A}}{\Omega}\right), \quad -\infty < \varepsilon < \infty, \tag{20}$$

where A is given by (1), $\Omega = E[r^2]$, $\Gamma(\cdot)$ is the gamma function [22, (8.310)], and $m = \Omega^2/\mathrm{var}(r^2)$ is the fading parameter which provides information about the severity of fading, being $\mathrm{var}(\cdot)$ the variance operator. For $m = 1$, the Nakagami-m becomes a Rayleigh distribution. Compound small-scale fading and shadowing amplitudes can be modeled with Nakagami-m distributions with $1/2 < m < 1$. That is why the standard deviation of the logarithmic amplitude distribution exceeds the maximum theoretical value for a small-scale distribution of 5.57 dB which corresponds to the Rayleigh fading distribution ($m = 1$). Note that the smaller fading parameter, m, the higher standard deviation of the log distribution. If we assume that the small-scale and shadowing distribution are independent processes, the variance of the log composite distribution is the sum of the variance of the log small-scale and the log shadowing distributions.

We can easily calculate the CDF of the Nakagami-m in linear and logarithmic units as

$$F_r(r) = \frac{\gamma\left(m, (m/\Omega)\, r^2\right)}{\Gamma(m)}, \quad r \geq 0, \tag{21}$$

$$F_\varepsilon(\varepsilon) = \frac{\gamma\left(m, (m/\Omega)\exp(2\varepsilon/A)\right)}{\Gamma(m)}, \quad -\infty < \varepsilon < \infty, \tag{22}$$

where $\gamma(a, b) = \int_0^b t^{a-1}\exp(-t)dt$ is the lower incomplete gamma function [22, (8.350)].

In [27, 28], an approximation of the log-moments method for m was derived as

$$\widehat{m} = \frac{4.4}{\sqrt{\widehat{\mu}_{\varepsilon_2}}} + \frac{17.4}{\widehat{\mu}_{\varepsilon_2}^{1.29}}, \quad \widehat{\Omega} = \widehat{\mu}'_{r_2}, \tag{23}$$

where $\widehat{\mu}'_{r_2}$ and $\widehat{\mu}_{\varepsilon_2}$ are the second sample raw moment of r given by (2) and the second sample central moment of ε given by (3), respectively.

3.4. Weibull Distribution. The Weibull distribution has been used to model fading amplitudes mainly in indoor environments [29, 30] where the separation of the small-scale and long-term fading is frequently cumbersome and this distribution can fit well the measurements.

The PDF of the Weibull distribution in both linear and logarithmic units is given by

$$p_r(r) = \frac{\alpha r^{\alpha-1}}{\Omega^\alpha}\exp\left(-\frac{r^\alpha}{\Omega^\alpha}\right), \quad r \geq 0,\ \alpha > 0, \tag{24}$$

$$p_\varepsilon(\varepsilon) = \frac{1}{A}\frac{\alpha\varepsilon^{\alpha-1}}{\Omega^\alpha}\exp\left(\frac{\alpha}{A}\varepsilon - \frac{1}{\Omega^\alpha}e^{\alpha\varepsilon/A}\right), \quad -\infty < \varepsilon < \infty, \tag{25}$$

where A is given by (1) and α and Ω are the shape and scale parameters of the Weibull distribution, respectively.

From (24) and (25), we can easily obtain the CDF of the Weibull distribution in both linear and logarithmic units as

$$F_r(r) = 1 - \exp\left(-\frac{r^\alpha}{\Omega^\alpha}\right), \quad r \geq 0, \tag{26}$$

$$F_\varepsilon(\varepsilon) = 1 - \exp\left(-\frac{e^{(\alpha/A)\varepsilon}}{\Omega^\alpha}\right), \quad -\infty < \varepsilon < \infty. \tag{27}$$

The Weibull distribution turns into the Rayleigh distribution for $\alpha = 2$. Composite small-scale and shadowing distributions can be modeled as Weibull distributions with $0 < \alpha < 2$.

Combining the methods of log-moments and moments, we can easily estimate the parameters of the Weibull distribution as [30]

$$\widehat{\alpha} = \frac{A\pi}{\sqrt{6}}\frac{1}{\sqrt{\widehat{\mu}_{\varepsilon_2}}} = \frac{11.14}{\sqrt{\widehat{\mu}_{\varepsilon_2}}}, \quad \widehat{\Omega} = \frac{\widehat{\mu}'_{r_1}}{\Gamma\left(1 + \dfrac{1}{\alpha}\right)}, \tag{28}$$

where $\widehat{\mu}'_{r_1}$ and $\widehat{\mu}_{\varepsilon_2}$ are the first sample raw moment of r given by (2) and the second sample central moment of ε given by (3), respectively.

3.5. α-μ Distribution. Recently, in [31], Yacoub proposed the use of the α-μ or generalized gamma distribution to model the fading in nonlinear environments where the surfaces which cause diffuse scattering are correlated spatially. Nevertheless, this distribution had been employed previously in [32] to characterize shadowed channels, that is, composed long-term and small-scale fading effects. The main advantage of the α-μ distribution is its mathematical simplicity and versatility even though it includes important distributions as gamma, Nakagami-m, one-side Gaussian, and Rayleigh as particular cases.

The PDF of the α-μ distribution in linear units can be written as

$$p_r(r) = \frac{\alpha\mu^{\mu} r^{\alpha\mu-1}}{\Omega^{\alpha\mu}\Gamma(\mu)} \exp\left(-\mu\frac{r^{\alpha}}{\Omega^{\alpha}}\right), \quad r \geq 0, \quad \alpha > 0,\ \mu > 0, \tag{29}$$

where α is a parameter which controls the linearity, $\mu = E^2[r^{\alpha}]/\mathrm{var}(r^{\alpha})$, and $\Omega = \sqrt[\alpha]{E[r^{\alpha}]}$. For $\alpha = 2$, the α-μ distribution becomes a Nakagami-m distribution. If $\alpha = 2$ and $\mu = 1$, the α-μ distribution turns into a Rayleigh distribution. For $\mu = 1$, the α-μ distribution converts into a Weibull distribution.

From (29), the PDF of ε is obtained as

$$p_{\varepsilon}(\varepsilon) = \frac{1}{A}\frac{\alpha\mu^{\mu}\varepsilon^{\alpha\mu-1}}{\Omega^{\alpha\mu}\Gamma(\mu)} \exp\left(\frac{\alpha\mu}{A}\varepsilon - \frac{\mu}{\Omega^{\alpha}}e^{\alpha\varepsilon/A}\right), \quad -\infty < \varepsilon < \infty, \tag{30}$$

where A is given by (1).

We can calculate the CDF of r and ε as

$$F_r(r) = \frac{\gamma\left(\mu, (\mu/\Omega^{\alpha})\, r^{\alpha}\right)}{\Gamma(\mu)}, \quad r \geq 0, \tag{31}$$

$$F_{\varepsilon}(\varepsilon) = \frac{\gamma\left(\mu, (\mu/\Omega^{\alpha}) \exp\left((\alpha/A)\,\varepsilon\right)\right)}{\Gamma(\mu)}, \quad -\infty < \varepsilon < \infty. \tag{32}$$

In [33], an estimation of such parameters has been derived based on the log-moments method as

$$\widehat{\mu} = \begin{cases} \widehat{\eta}^2 + \dfrac{1}{2} & \widehat{\eta} \leq -2.85 \\ -0.0773\widehat{\eta}^4 - 0.6046\widehat{\eta}^3 - 0.7949\widehat{\eta}^2 & \\ \quad -2.4675\widehat{\eta} - 0.9208 & -2.85 < \widehat{\eta} \leq -0.6 \\ -132.8995\widehat{\eta}^3 - 232.0659\widehat{\eta}^2 & \\ \quad -137.6303\widehat{\eta} - 27.3616 & -0.6 < \widehat{\eta} < -0.5, \end{cases} \tag{33}$$

$$\widehat{\alpha} = A\sqrt{\frac{\psi'(\widehat{\mu})}{\widehat{\mu}_{\varepsilon_2}}}, \tag{34}$$

$$\widehat{\Omega} = \sqrt[\alpha]{E[\widehat{r}^{\alpha}]}, \tag{35}$$

where

$$\widehat{\eta} = \frac{\widehat{\mu}_{\varepsilon_2}^{3/2}}{\widehat{\mu}_{\varepsilon_3}}, \qquad E[\widehat{r}^{\alpha}] = \frac{1}{N}\sum_{i=1}^{N} r_i^{\alpha}, \tag{36}$$

$\psi'(x) = \partial\psi(x)/\partial x = \partial^2 \ln\Gamma(x)/\partial x^2$ is the polygamma function of first order [34, (6.4.1)], and $\widehat{\mu}_{\varepsilon_2}$ and $\widehat{\mu}_{\varepsilon_3}$ are the sample central moments of second and third order of ε, calculated as (5).

4. Results

In this section, we present results of the fading amplitude distributions for the six measurements shown in Table 1 with positions depicted in Figure 1. Firstly, the main parameters of each measurement such as the coherence bandwidth, rms delay spread, and mean delay are calculated. Next, the statistical Kolmogorov-Smirnov (K-S) test is used to evaluate the goodness-of-fit of the above distributions, and finally we obtain the distribution of the most important estimators for such distributions. Finally, we have analyzed the matching of the estimated distributions in their lower tails to the experimental distribution.

4.1. Main Wideband Parameters. The principal wideband parameters for each measurement have been included in Table 2. Both mean excess delay and rms delay spread have been calculated from the measured power delay profile (PDP). To mitigate the noise effect on the rms derivation, we have considered a threshold level of 10 dB above the noise level floor. Since the rms delay spreads calculated for all the measurements are considerably smaller than 24.24 ns, which is the guard interval in the OFDM-HSI mode [5], the behavior of the PDP profile does not affect substantially the performance of this mode; that is, the intersymbol interference (ISI) is negligible.

The coherence bandwidth has been calculated for a high normalized frequency autocorrelation function value of 0.9; that is, $R_T(\Delta f) = 0.9$. The coherence bandwidths for all measurements are larger than the subcarrier spacing of 5.15625 MHz in the OFDM-HSI mode [5] except for the measurement #4, which is around 5 MHz. Therefore, we can also ignore the time dispersion effect on the system performance.

4.2. Best-Fit Distribution and Kolmogorov-Smirnov Test. Using the estimators detailed in Section 3, we have evaluated the inferred Rayleigh, Rice, Nakagami-m, Weibull, and α-μ distributions for each point of frequency in each measurement. These distributions are compared to the experimental distributions. To estimate the parameters of the Rice distribution, the accuracy parameter Δ is fixed to 10^{-8}.

In Figure 3, the PDFs of the above distributions in logarithmic units given by (7), (13), (25), (27), and (30) are plotted beside the experimental logarithmic PDF for the 2nd bin (frequency of 57.002 GHz) of the measurement #1. Note that the relationship between the received power in dBm, $\varepsilon_{\mathrm{dBm}}$, and the field strength in dBV/m, $\varepsilon_{\mathrm{dBV/m}}$, is given by

$$\varepsilon_{\mathrm{dBm}} = \varepsilon_{\mathrm{dBV/m}} + 10\log\left(\frac{\lambda^2}{480\pi^2}\right) + G_{\mathrm{dB}} + 30, \tag{37}$$

where λ is the wavelength and G_{dB} is the receiver antenna gain in dB.

The α-μ, Weibull, and Rice distributions match rather well the experimental distribution. In fact, the best-fit is the Weibull distribution in this case.

The statistical K-S test has been assessed for these distributions over all the bins of frequency in each measurement.

Table 1: Main parameters in each measurement experiment in the 57–66 GHz band.

Number of measurement	Tx—Rx	Number of points	Positions	Separation
1	1—1	4096	40 × 20 Tx; 1 Rx	3.79 m
2	2—1	10001	5 × 5 Tx; 1 Rx	3.84 m
3	3—2	8192	10 Tx; 10 Rx	3.40 m
4	4—2	8192	10 Tx; 10 Rx	3.70 m
5	5—2	8192	10 Tx; 10 Rx	2.20 m
6	6—2	2048	156 Tx; 8 Rx	1.24 m

Table 2: Wideband parameters in each measurement experiment.

Number of measurement	Mean excess delay (ns)	rms delay spread (ns)	Coherence bandwidth for $R_T = 0.9$ (MHz)
1	5.8	6.09	11.5
2	3.39	5.39	6.5
3	3.48	4.8	6
4	4.9	5.4	5
5	4.58	5.2	11
6	3.03	3.74	15

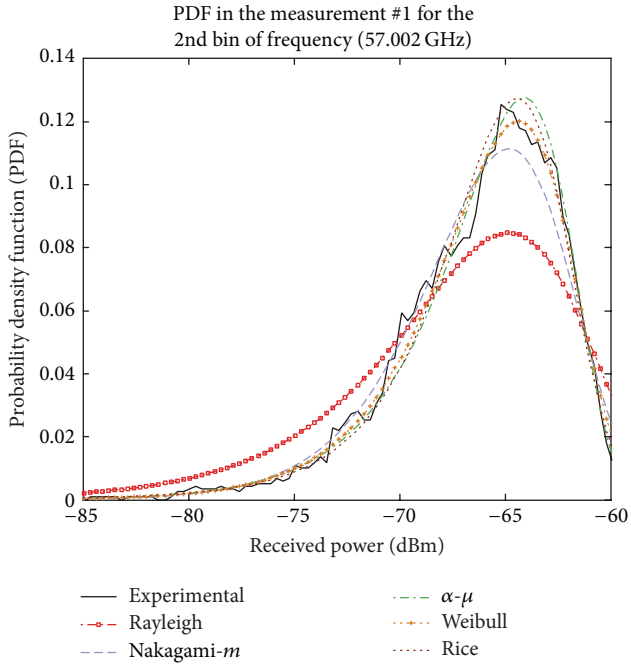

Figure 3: Probability density functions of the experimental, Rayleigh, Nakagami-m, α-μ, Weibull and, Rice distributions for the 2nd bin (frequency of 57.002 GHz) of the measurement #1.

The K-S confidence interval used is 5%. Moreover, we have calculated the best-fit distribution using the K-S test in each measurement. The best-fit distribution is calculated from the minimum value of

$$\max_{-\infty<\varepsilon_j<\infty} \left| F_{\varepsilon_{\text{experimental}}}(\varepsilon_j) - F_{\varepsilon_{\text{estimated}}}(\varepsilon_j) \right|, \tag{38}$$

where $F_{\varepsilon_{\text{experimental}}}(\varepsilon_j)$ is the experimental logarithmic CDF and $F_{\varepsilon_{\text{estimated}}}(\varepsilon_j)$ is the inferred logarithmic Rayleigh, Rice, Nakagami-m, Weibull, and α-μ CDFs given by (9), (15), (22), (27), and (32), both of them evaluated in ε_j.

Table 3 shows the percentage of the best-fist for the above distributions besides the K-S test accomplishment percentage over all the frequency bins in each measurement.

Note that the sum of the best-fit percentages for each measurement is 100%. In bold letters, we have highlighted the maximum best-fit distribution of each measurement. Since the measurements have been carried out in LOS condition, and in accordance with [13, 14], the Rice distribution is the most frequently best-fit distribution in the measurements from #1 to #5. In measurement #6, the Nakagami-m is the most frequently best-fit distribution even though the K-S test success of 90.5% for this distribution is less than the value of the percentage for the Rice distribution of 94.7%. Furthermore, the K-S test for the Rice distribution is fulfilled in at least 84.4% of frequency bins in the worst case, corresponding to the measurement #2. In measurements #3–#5, the K-S test percentage for the Rice distribution is very close to 100%.

4.3. Distribution of Estimated Parameters. Once the parameters of the Rayleigh, Rice, Nakagami-m, Weibull, and α-μ distributions are estimated from (10), (16)–(19), (23), (28), and (34)–(36), we can obtain the distribution of the main parameters of these distributions for each measurement.

Let γ_{P_2} and β_{P_2} be the skewness and kurtosis of the distribution of the parameter P defined as

$$\gamma_{P_2} = \frac{\mu_{P_3}}{\mu_{P_2}^{3/2}}, \qquad \beta_{P_2} = \frac{\mu_{P_4}}{\mu_{P_2}^{2}}, \tag{39}$$

respectively, where μ_{P_n} is the nth central moment of the distribution of P. The skewness is a measure of the asymmetry of the PDF of a real-valued RV whereas the kurtosis is an estimation of the "peakedness" of the PDF. A null skewness corresponds to a symmetrical PDF. A left-tailed PDF provides negative skewness and a positive skewness is obtained for right-tailed PDFs. Note that the skewness and kurtosis of a Gaussian distribution are equal to 0 and 3, respectively. We can also define the sample skewness, $\widehat{\gamma}_{P_2}$, and sample kurtosis, $\widehat{\beta}_{P_2}$, of the distribution of P in the same way of (2)–(5).

Table 3: Best-fit distributions percentages and Kolmogorov-Smirnov test accomplishment percentage for a confidence interval of 5%.

Number of measurement	1	2	3	4	5	6
α-μ						
K-S 5%	61	73.3	89.7	87.7	91	72.8
Best-fit	19.7	29	26.3	22.6	32.5	16.8
Rayleigh						
K-S 5%	4.4	6	42.7	59.8	15.1	0
Best-fit	0.3	1.4	1.1	1.8	0.2	0
Nakagami						
K-S 5%	71.3	66.4	98.3	97	98.7	**90.5**
Best-fit	23.6	17.6	15.9	12.7	19.1	**46.2**
Weibull						
K-S 5%	85.3	73.1	99.5	99.4	99.6	46.8
Best-fit	18	17	15.9	18	13.7	2.2
Rice						
K-S 5%	**91.9**	**84.4**	**99.9**	**100**	**99.9**	94.7
Best-fit	**38.4**	**35**	**40.9**	**45**	**34.4**	34.7

We have observed that the PDF of all the estimated parameters is highly right-skewed. That fact suggests that a lognormal distribution could approximate the distribution of some of these parameters. Therefore, we can evaluate the skewness and kurtosis of the distribution parameters expressed in dB.

Table 4 shows the sample log skewness, log kurtosis, sample mean, and sample standard deviation of the main estimated parameters of the Rice, Nakagami-m, Weibull, and α-μ distributions.

Following these results, both the fading parameter, m, of the Nakagami-m distribution and the shape parameter, α, of the Weibull distribution can be clearly modeled as a lognormal distribution. The Rice K-factor in dB could also fit a Gaussian distribution in measurements #3, #5, and #6. Nevertheless, both α and μ parameters of the α-μ distribution cannot be modeled as a lognormal distribution in spite of the PDF symmetry due to the small sample skewness values. Figure 4 shows the PDF of the Rice K-factor in dB and the Gaussian approximation for the measurements #1 and #5. Since the skewness of both K-factor distributions are very close to 0, the experimental PDFs are symmetrical. In spite of the fact that the kurtosis of the K-factor distribution, which is equal to 4 in the measurement #1, is slightly different from the theoretical value for the Gaussian distribution that is 3, the appearance of experimental and estimated PDFs is similar.

The mean of the K-Rice parameter oscillates from 3.21 to 8.45 dB. The values of the K-Rice parameter mean are equal to or higher than 4 dB except for the measurement #4. Note that the separation between Tx and Rx in the measurement #4 is the highest of all the experiments and the scatterers are closer to the Rx than the rest of the measurements.

The mean of the Rice K-factor can be related to the mean of the fading parameter, m, of the Nakagami-m distribution following the method of moments as follows [35]:

$$m = \frac{(1+K)^2}{1+2K}. \quad (40)$$

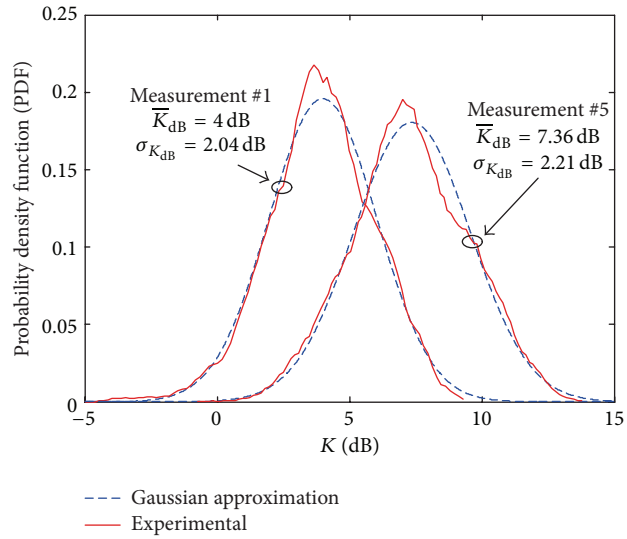

Figure 4: Probability density functions of the Rice K-factor in dB and the Gaussian approximation for the measurements #1 and #5.

From (40), the smaller Rice K parameter is, the lower fading parameter, m, is for $m \geq 1$. Mean fading parameters vary from 1.54 to 3.87. The standard deviation of the fading parameter is low with a maximum value of 2.06 for the measurement #2. We can compare $\overline{m}$, defined as the sample mean of the estimated fading parameter with the log-moments method (see Table 4), to $\overline{m}_{\text{Rice}}$, calculated from the sample mean of the estimated Rice K-factors using (40). Table 5 shows both parameters and the mean of the estimated Rice K parameter in both linear and logarithmic units.

From Table 5, it can be observed that $\overline{m}$ and $\overline{m}_{\text{Rice}}$ values are similar with a maximum difference between them of 0.4 for the measurement #6.

Table 4: Sample mean, standard deviation, log skewness, and log kurtosis of the main parameters of the estimated distributions.

Number of measurement	1	2	3	4	5	6
Rice						
K_{dB}						
Skewness	−0.4	−0.53	−0.2	−0.8	−0.1	−0.7
Kurtosis	4	4.33	3.59	5.88	2.73	3.82
Mean (dB)	4	5.46	4.97	3.21	7.36	8.45
St. dev. (dB)	2.04	3.1	3.01	2.23	2.21	1.68
Nakagami						
m						
L. skew.	0.53	0.46	0.65	0.52	0.24	−0.4
L. kurtosis	3.24	3.46	2.88	3.24	2.71	3.06
Mean	1.71	2.52	2.27	1.54	3.28	3.87
St. dev.	0.53	2.06	1.32	0.45	1.61	1.3
Weibull						
α						
L. skew.	0.55	0.15	0.43	0.33	0.01	−0.6
L. kurtosis	2.94	2.78	2.53	3.01	2.63	3.36
Mean	2.88	3.53	3.35	2.7	4.23	4.71
St. dev.	0.55	1.2	1.08	0.51	1.13	0.9
α-μ						
α						
L. skew.	1.05	0.54	0.81	0.84	0.62	2.1
L. kurtosis	3.96	5.36	4.69	3.47	5.3	10.4
Mean	5.58	4.31	4.73	4.97	4.72	4.34
St. dev.	5.22	5.81	5.58	5.27	6.07	3.71
μ						
L. skew.	−0.3	0.61	0.33	−0.2	0.41	−0.8
L. kurtosis	3.84	6.45	6.13	4.48	5.95	5.34
Mean	0.86	23.22	15.7	2.41	10.3	1.78
St. dev.	1.02	$1.2 \cdot 10^3$	875	72.4	186	1.37

Table 5: Sample mean of the Rice K-factor in logarithmic units and linear units. Sample mean of the fading parameter and mean of fading parameter calculated from the Rice K-factor.

Number of measurement			1	2	3	4	5	6
Rice	$\overline{K}_{\mathrm{dB}}$	Mean (dB)	4	5.46	4.97	3.21	7.36	8.45
	$\overline{K}$	Mean	2.51	3.51	3.14	2.09	5.44	6.99
Nakagami	$\overline{m}$	Mean	1.71	2.52	2.27	1.54	3.28	3.87
	$\overline{m}_{\mathrm{Rice}}$	Mean	2.05	2.54	2.35	1.85	3.49	4.27

Figure 5 shows the PDF of the fading parameter in dB, $10 \log m$, and the Gaussian approximation for the measurements #2 and #5. In spite of the fact that the kurtosis value of $10 \log m$ for the measurement #2 is not so different from 3, the difference between the experimental and the Gaussian PDFs is not negligible due to the significant value of skewness of 0.46 which provides a right-tailed or right-skewed experimental PDF. Similar conclusion can be extracted for the fading parameter distribution of the measurement #5.

The mean of the shape parameter, α, of the Weibull distribution oscillates from 2.7 to 4.71. On the one hand, the distribution is very different from the Rayleigh distribution since the mean of α is substantially higher than 2. On the other hand, the long-term fading is negligible in our measurements, since the standard deviation of the distribution in logarithmic units is considerably smaller than 5.57 dB which is the value for the log Rayleigh distribution ($\alpha = 2$). The higher α value of the Weibull distribution is, the smaller standard deviation of the logarithmic Weibull distribution is. A composite small-scale and log-term fading logarithmic distribution usually reaches a standard deviation that exceeds 5.57 dB which corresponds to estimated α values of the Weibull distribution lower than 2. The standard deviation of the α parameter of the Weibull distribution is low varying from 0.51 to 1.2. For the α-μ distribution, we have obtained considerably high standard deviations of the μ estimated parameter. Therefore,

Table 6: Mean and standard deviation of the difference between the relative received power of the estimated CDFs and the relative received power of the experimental CDF for the same value of the CDF, $p = 10^{-1}$, in the measurements #1 and #6.

Distribution		α-μ	Rayleigh	Nakagami	Weibull	Rice
Measurement #1	Mean (dB)	**0.088**	−3.12	−0.396	−0.16	0.135
	Standard deviation (dB)	**0.369**	1.137	0.34	0.315	0.368
Measurement #6	Mean (dB)	0.031	−4.39	−0.16	**−0.022**	0.053
	Standard deviation (dB)	0.228	0.861	0.1814	**0.1516**	0.1215

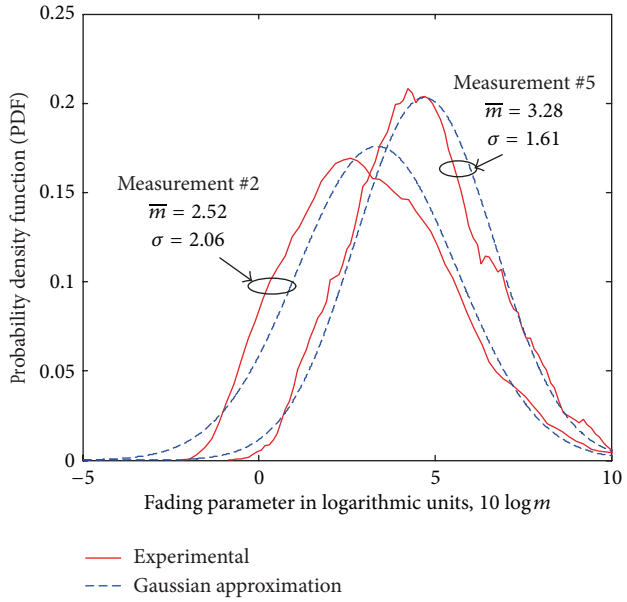

Figure 5: Probability density functions of the fading parameter in logarithmic units, $10 \log m$, and the Gaussian approximation for the measurements #2 and #5.

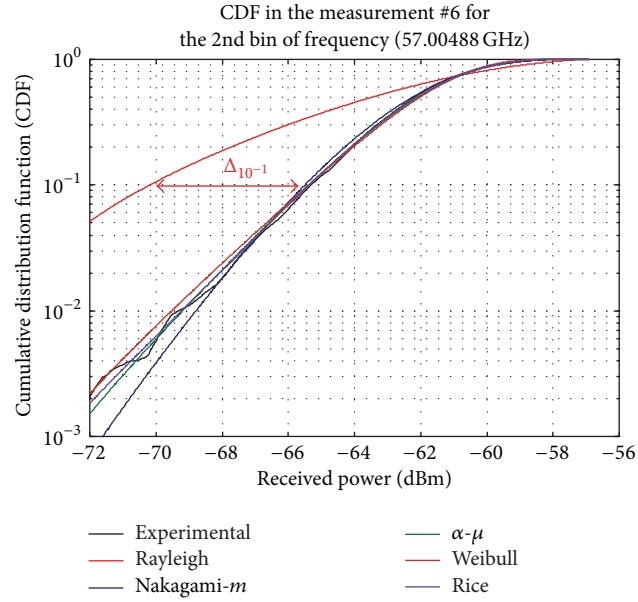

Figure 6: Cumulative distribution of the 2nd bin of frequency (57.00488 GHz) in the measurement #6. The difference between the relative received power of the estimated CDF and the relative received power of the experimental CDF for the same value of the CDF, $p = 10^{-1}$, is shown for the Rayleigh distribution.

the stability of this estimated parameter is substantially small. Nevertheless, the variation of the mean of the α estimated parameter for the α-μ distribution is not considerable since it oscillates from 4.31 to 5.58.

4.4. Lower Tail of the Distributions. In the analysis of performance in wireless communication systems, the lower tail of the distribution influences substantially the parameters, such as the outage probability, the bit error rate (BER), and the symbol error rate (SER), for high average signal-to-interference ratios. That is why the matching of the analytical distributions considered in this paper to the experimental distribution in the lower tails has been deeply analyzed in this subsection.

We have defined a relative received power, $\varepsilon_{\text{experimental}}$, for a given value of the experimental CDF, p, which can be written as

$$F_{\varepsilon_{\text{experimental}}}\left(\varepsilon_{\text{experimental}}\right) = p. \tag{41}$$

The relative received power for the Rayleigh, Rice, Nakagami-m, Weibull, or α-μ estimated CDFs, $\varepsilon_{\text{estimated}}$, for the same value of the CDF, p, is given by

$$F_{\varepsilon_{\text{estimated}}}\left(\varepsilon_{\text{estimated}}\right) = p. \tag{42}$$

Let Δ_p be the difference between the relative received power of the estimated CDF and the relative received power of the experimental CDF for the same value of the CDF, p, defined as

$$\Delta_p = \varepsilon_{\text{estimated}} - \varepsilon_{\text{experimental}}\Big|_p. \tag{43}$$

In Figure 6, $\Delta_{p=10^{-1}}$ is shown for the Rayleigh distribution in the measurement #6 and the 2nd bin of frequency (57.00488 GHz).

Since the number of samples of each observation is not high, we cannot calculate Δ_p for low values of p, provided that the experimental CDF is not stable for such low values as it can be observed in Figure 6. We can only evaluate this parameter for $p = 10^{-1}$ in the measurements #1 and #6, where the number of samples per record is significantly high.

In Table 6, the mean value $\Delta_{p=10^{-1}}$ and the standard deviation of $\Delta_{p=10^{-1}}$ are calculated for the measurements #1 and #6.

Surprisingly, the best-fit distribution for the low tails is not the same as the best-fit distribution using the K-S test for both measurements. In the measurement #1, the best-fit

distribution for the low tails is the α-μ instead of the Rice distribution obtained with the K-S test. In the same way, the best-fit distribution for the low tails is the Weibull instead of the Nakagami-m distribution calculated using the K-S test in the measurement #6.

5. Conclusions

In this work, an extensive study of the small-scale amplitude distribution in the 60 GHz band has been carried out for a LOS laboratory environment. Parameters of the Rayleigh, Rice, Nakagami-m, Weibull, and α-μ distributions have been estimated and such inferred distributions are compared to the experimental distribution using the Kolmogorov-Smirnov test. The Rice is the best-fit distribution followed by the α-μ and Nakagami-m distributions using the K-S test. However, the best-fit distributions for the low tails do not agree to the best-fit distributions obtained using the K-S test in the measurements #1 and #6. The K-S test for a confidence interval of 5% is fulfilled in over 84.4% of frequency bins for the Rice distribution in the worst-case experiment. From the calculation of the skewness and kurtosis of the logarithmic distribution, we have observed that both the Weibull shape parameter and the Nakagami-m fading parameter can be modeled as a lognormal distribution with small standard deviations, with maxima of 1.2 and 2.06, respectively.

Conflict of Interests

The authors declare that there is no conflict of interests regarding the publication of this paper.

Acknowledgments

This work was supported in part by the Spanish Ministerio de Ciencia e Innovación TEC-2010-20841-C04-1 and by the Universitat Politècnica de València, PAID 05-11 ref. 2702. The authors thank the anonymous reviewers for their valuable remarks and suggestions which have considerably enriched the final paper.

References

[1] P. Smulders, "Exploiting the 60 GHz band for local wireless multimedia access: prospects and future directions," *IEEE Communications Magazine*, vol. 40, no. 1, pp. 140–147, 2002.

[2] C. Park and T. S. Rappaport, "Short-range wireless communications for next-generation networks: UWB 60 GHz millimeter-wave wpan, and ZigBee," *IEEE Wireless Communications*, vol. 14, no. 4, pp. 70–78, 2007.

[3] R. C. Daniels and R. W. Heath Jr., "60 GHz wireless communications: emerging requirements and design recommendations," *IEEE Vehicular Technology Magazine*, vol. 2, no. 3, pp. 41–50, 2007.

[4] S. K. Yong, P. Xia, and A. Valdes-Garcia, *60 GHz Technology for Gbps WLAN and WPAN: From Theory to Practice*, Wiley, Chichester, UK, 2011.

[5] IEEE 802.15.3, *Wireless Medium Access Control (MAC) and Physical Layer (PHY) Specifications for High Rate Wireless Personal Area Networks (WPANs) Amendment 2: Millimeter-Wave-Based Alternative Physical Layer Extension*, IEEE, New York, NY, USA, 2009.

[6] WiGig White Paper: Defining the Future of Multi-Gigabit Wireless Communication, http://wilocity.com/resources/WiGigWhitepaper_FINAL5.pdf.

[7] T. Zwick, T. J. Beukema, and H. Nam, "Wideband channel sounder with measurements and model for the 60 GHz indoor radio channel," *IEEE Transactions on Vehicular Technology*, vol. 54, no. 4, pp. 1266–1277, 2005.

[8] H. Sawada, Y. Shoji, and C. Choi, "Proposal of novel statistic channel model for millimeter-wave WPAN," in *Proceedings of the Asia-Pacific Microwave Conference (APMC '06)*, pp. 1855–1858, Yokosuka, Japan, December 2006.

[9] Y. Shoji, H. Sawada, C.-S. Choi, and H. Ogawa, "A modified SV-model suitable for line-of-sight desktop usage of millimeter-wave WPAN systems," *IEEE Transactions on Antennas and Propagation*, vol. 57, no. 10, pp. 2940–2948, 2009.

[10] H. Xu, V. Kukshya, and T. S. Rappaport, "Spatial and temporal characteristics of 60-GHZ indoor channels," *IEEE Journal on Selected Areas in Communications*, vol. 20, no. 3, pp. 620–630, 2002.

[11] C. R. Anderson and T. S. Rappaport, "In-building wideband partition loss measurements at 2.5 and 60 GHz," *IEEE Transactions on Wireless Communications*, vol. 3, no. 3, pp. 922–928, 2004.

[12] P. F. M. Smulders, "Statistical characterization of 60-GHz indoor radio channels," *IEEE Transactions on Antennas and Propagation*, vol. 57, no. 10, pp. 2820–2829, 2009.

[13] H. J. Thomas, R. S. Cole, and G. L. Siqueira, "Experimental study of the propagation of 55 GHz millimeter waves in an urban mobile radio environment," *IEEE Transactions on Vehicular Technology*, vol. 43, no. 1, pp. 140–146, 1994.

[14] M. Choi, G. Grosskopf, and D. Rohde, "Statistical characteristics of 60 GHz wideband indoor propagation channel," in *Proceedings of the IEEE 16th International Symposium on Personal, Indoor and Mobile Radio Communications (PIMRC '05)*, vol. 1, pp. 599–603, September 2005.

[15] M. Kyrö, K. Haneda, J. Simola, K. Takizawa, H. Hagiwara, and P. Vainikainen, "Statistical channel models for 60 GHz radio propagation in hospital environments," *IEEE Transactions on Antennas and Propagation*, vol. 60, no. 3, pp. 1569–1577, 2012.

[16] S. K. Yong et al., "TG3c channel modeling sub-committee final report," IEEE 802.15-07-584-01, 2007.

[17] G. D. Durgin, T. S. Rappaport, and D. A. De Wolf, "New analytical models and probability density functions for fading in wireless communications," *IEEE Transactions on Communications*, vol. 50, no. 6, pp. 1005–1015, 2002.

[18] M. D. Yacoub, "The κ-μ distribution and the η-μ distribution," *IEEE Antennas and Propagation Magazine*, vol. 49, no. 1, pp. 68–81, 2007.

[19] M.-T. Martinez-Ingles, C. Sanchis-Borras, J.-M. Molina-Garcia-Pardo, J.-V. Rodriguez, and L. Juan-Llácer, "Experimental evaluation of an indoor MIMO-OFDM system at 60 GHz based on the IEEE802.15.3c standard," *IEEE Antennas and Wireless Propagation Letters*, vol. 12, pp. 1562–1565, 2013.

[20] K. D. Rao, *Linear Statistical Inference and Its Applications*, John Wiley & Sons, New York, NY, USA, 2nd edition, 1973.

[21] J. G. Proakis, *Digital Communications*, McGraw-Hill, Singapore, 3rd edition, 1995.

[22] I. S. Gradshteyn and I. M. Ryzhik, *Table of Integrals, Series and Products*, Academic Press, San Diego, Calif, USA, 7th edition, 2007.

[23] J. I. Marcum, *Table of Q Functions, U.S. Air Force RAND Research Memorandum M-339*, Rand Corporation, Santa Monica, Calif, USA, 1950.

[24] C. G. Koay and P. J. Basser, "Analytically exact correction scheme for signal extraction from noisy magnitude MR signals," *Journal of Magnetic Resonance*, vol. 179, no. 2, pp. 317–322, 2006.

[25] M. Nakagami, "The *m*-distribution—a general formula of intensity distribution of rapid fading," in *Statistical Methods of Radio Wave Propagation*, W. G. Hoffman, Ed., Pergamon Press, Oxford, UK, 1960.

[26] U. Charash, "Reception through nakagami fading multipath channels with random delays," *IEEE Transactions on Communications*, vol. 27, no. 4, pp. 657–670, 1979.

[27] R. W. Lorenz, "Theoretical distribution functions of multipath propagation and their parameters for mobile radio communication in quasi-smooth terrain," in *AGARD Terrain Profiles and Contours in Electromagnetic Wave Propagation*, SAO/NASA ADS, 1979.

[28] J. D. Parsons, *The Mobile Radio Propagation Channel*, John Wiley & Sons, New York, NY, USA, 2nd edition, 2000.

[29] H. Hashemi, "Indoor radio propagation channel," *Proceedings of the IEEE*, vol. 81, no. 7, pp. 943–968, 1993.

[30] R. Ganesh and K. Pahlavan, "On the modeling of fading multipath indoor radio channels," in *Proceedings of the IEEE Global Telecommunications Conference & Exhibition (GLOBECOM '89)*, vol. 3, pp. 1346–1350, November 1989.

[31] M. D. Yacoub, "The α-μ distribution: a physical fading model for the Stacy distribution," *IEEE Transactions on Vehicular Technology*, vol. 56, no. 1, pp. 27–34, 2007.

[32] A. J. Coulson, A. G. Williamson, and R. G. Vaughan, "Improved fading distribution for mobile radio," *IEE Proceedings—Communications*, vol. 145, pp. 197–202, 1998.

[33] J. Reig and L. Rubio, "On simple estimators of the α-μ fading distribution," *IEEE Transactions on Communications*, vol. 59, no. 12, pp. 3254–3258, 2011.

[34] M. Abramowitz and I. Stegun, *Handbook of Mathematical Functions*, National Bureau of Standards, Washington, DC, USA, 10th edition, 1972.

[35] M. K. Simon and M.-S. Alouini, *Digital Communications over Fading Channels*, John Wiley & Sons, New York, NY, USA, 2nd edition, 2005.

Hindawi Publishing Corporation
International Journal of Antennas and Propagation
Volume 2014, Article ID 975109, 8 pages
http://dx.doi.org/10.1155/2014/975109

Research Article

Capacity of κ-μ Shadowed Fading Channels

Celia García-Corrales, Francisco J. Cañete, and José F. Paris

Departamento Ingeniería de Comunicaciones, ETS Ingeniería de Telecomunicacion, Universidad de Malaga, E-29071 Málaga, Spain

Correspondence should be addressed to Celia García-Corrales; celia@ic.uma.es

Received 9 May 2014; Accepted 10 July 2014; Published 24 July 2014

Academic Editor: Theodoros Tsiftsis

Copyright © 2014 Celia García-Corrales et al. This is an open access article distributed under the Creative Commons Attribution License, which permits unrestricted use, distribution, and reproduction in any medium, provided the original work is properly cited.

The ergodic capacity of fading channels modeled with a κ-μ shadowed distribution is investigated to derive closed-form expressions. The κ-μ shadowed distribution is of particular interest because it contains, as special cases, other classical ones like one-side Gaussian, Rayleigh, Rician, Nakagami-m, κ-μ, and Rician shadowed distributions. The paper discusses the physical meaning of the distribution parameter variations and also their impact on the channel capacity. These results can be used to study the behavior of different channels like the ones in underwater acoustic communications, land mobile satellite systems, body centric communications, and other wireless communication applications. The analytical closed-form expression results are validated with numerical simulations.

1. Introduction

The propagation of radio waves or acoustic waves, used as data carriers, in realistic scenarios where either the transmitter, receiver, or surrounding objects are moving is quite complex. The amplitude and phase instantaneous values of the incident waves exhibit rapid variations according to the interaction patterns with the environment. This interaction produces phenomena like reflection, diffraction, and scattering of the waves on the object surfaces [1]. All this makes the problem of modeling the communication channel behavior almost unmanageable with a deterministic approach. An alternative strategy is to formulate mathematical models that reach a reasonable similarity to the expected signal at the receiver from a statistical approach. Such models try to reproduce the received signal according to different time scales. On the one hand, at a large time scale, there is a path loss modeling that estimates the mean signal strength, which is notably influenced by the transmission distance. On the other hand, there is a fading modeling, at a shorter scale, to represent the rapid fluctuations around the mean due essentially to multipath propagation. Even for this fading, two levels of approximation are usual: a long-term fading due to the influence of macroscopic movements in the environment (associated with a channel time-varying behavior) that is slower than a short-term fading, which is caused by variations in the superposition of the different wave components associated with the transmitted signal, even in a quasistatic environment [2, 3]. There exist many statistical fading models and the κ-μ distribution has been used in some of them to represent the received signal level in a flexible way [4–10].

The present work focused on the short-term, narrowband, fading experienced in multipath propagation scenarios with a line-of-sight condition. Besides the multipath fading, shadowing of the dominant components is also investigated. There are two kinds of models that consider shadowing: in the first one, shadowing is assumed to change the whole signal power (composed of the dominant components and the scattered waves) [11–14]. In the second type of models, the shadowing is considered to affect only the power of the dominant components, like the Rician shadowed model [15]. This latter model was initially employed to fit experimental data from land mobile satellite channels and lately has also been applied to actual underwater acoustic communications (UAC) channels [16].

The present work is based on the *κ-μ shadowed distribution model*, first proposed in [17], which belongs to the second

type of shadowing models and achieves a better fit to UAC channels measurements.

The paper is organized as follows: first, the system model is addressed in Section 2, explaining its physical interpretation and providing some fundamental statistics. In Section 3, the mathematical analysis of the ergodic capacity of the channel for the assumed model is presented, whereas, in Section 4, numerical simulations that support the analytical results are discussed. Finally, some conclusions are given in the last section.

2. System Model

The purpose of this section is to define the framework of the problem and to help the reader to follow the remainder of the paper. To this end, a brief summary of the physical model underneath the κ-μ shadowed distribution is given and the main statistical functions of this distribution are reviewed.

2.1. Physical Model. In the physical model for the κ-μ shadowed distribution [17], the received power W can be expressed in terms of the in-phase and quadrature components of the fading signal by

$$W = \sum_{i=1}^{n} \left(X_i + \xi p_i\right)^2 + \left(Y_i + \xi q_i\right)^2, \tag{1}$$

where n is a natural number, X_i and Y_i are mutually independent Gaussian processes (with $E[X_i] = E[Y_i] = 0$, $E[X_i^2] = E[Y_i^2] = \sigma^2$), and p_i and q_i are real numbers. Each term of the sum represents a multipath cluster and hence n is the number of clusters. The random variable $X_i + jY_i$ models the scattered components of the ith cluster, which is a circularly symmetric complex Gaussian since the number of components is considered large enough so that the central-limit theorem applies. In each cluster, the total power of the scattered components is $2\sigma^2$, while the dominant component of the ith cluster is given by the complex random variable $\xi p_i + j\xi q_i$, whose power is $p_i^2 + q_i^2$ as ξ is a power-normalized random variable.

The following are the main parameters to formulate the κ-μ shadowed distribution.

(i) m–parameter: all the dominant components exhibit a common shadowing fluctuation that is represented by the random amplitude ξ, that is, a Nakagami-m random variable with shaping parameter m and $E[\xi^2] = 1$.

(ii) μ-parameter: the natural number of clusters n can be replaced in (1) by the nonnegative real extension μ, which leads to a more general and flexible distribution.

(iii) κ-parameter: the ratio between the power of the dominant components and the power of the scattered waves is represented by κ that is defined as $\kappa = (\sum_{i=1}^{\mu} p_i^2 + q_i^2)/(2\sigma^2\mu)$, when μ is a natural number.

Assume $\gamma \sim \mathcal{S}_{\kappa\mu}(\overline{\gamma}; \kappa, \mu, m)$ is a κ-μ shadowed random variable with mean $\overline{\gamma}$ and real nonnegative shaping parameters κ, μ, and m. γ represents the instantaneous signal to noise ratio at the receiver and models the fading channel. It can be defined as $\gamma \triangleq \overline{\gamma} W/\overline{W}$, where $\overline{\gamma} \triangleq E[\gamma]$ and $\overline{W} = E[W] = 2\sigma^2\mu + \sum_{i=1}^{\mu} p_i^2 + q_i^2$ (for a natural μ).

2.2. Fundamental Statistics. In this part, the most important statistical functions corresponding to the κ-μ shadowed distribution are presented (see details in [17]).

The probability density function (PDF) of γ is given by

$$f_\gamma(\gamma) = \frac{\mu^\mu m^m (1+\kappa)^\mu}{\Gamma(\mu)\,\overline{\gamma}(\mu\kappa + m)^m} \left(\frac{\gamma}{\overline{\gamma}}\right)^{\mu-1} \times e^{-\mu(1+\kappa)\gamma/\overline{\gamma}}\, {}_1F_1\left(m, \mu; \frac{\mu^2\kappa(1+\kappa)}{\mu\kappa + m}\frac{\gamma}{\overline{\gamma}}\right), \tag{2}$$

where ${}_1F_1(\cdot)$ is the confluent hypergeometric function defined in [19].

The associated cumulative density function (CDF) of γ is given by

$$F_\gamma(\gamma) = \frac{\mu^{\mu-1} m^m (1+\kappa)^\mu}{\Gamma(\mu)(\mu\kappa + m)^m} \left(\frac{1}{\overline{\gamma}}\right)^\mu \gamma^\mu \times \Phi_2\left(\mu - m, m; \mu + 1; -\frac{\mu(1+\kappa)\gamma}{\overline{\gamma}}, -\frac{\mu(1+\kappa)}{\overline{\gamma}}\frac{m\gamma}{\mu\kappa + m}\right), \tag{3}$$

where $\Phi_2(\cdot)$ is the bivariate confluent hypergeometric function defined in [19].

The moment generating function (MGF) of γ is given by

$$\mathcal{M}_\gamma(s) \triangleq E\left[e^{\gamma s}\right] = \frac{(-\mu)^\mu m^m (1+\kappa)^\mu}{\overline{\gamma}^\mu(\mu\kappa + m)^m} \times \frac{\left(s - (\mu(1+\kappa)/\overline{\gamma})\right)^{m-\mu}}{\left(s - (\mu(1+\kappa)/\overline{\gamma})(m/(\mu\kappa + m))\right)^m}. \tag{4}$$

3. Ergodic Capacity Analysis

For the physical model under consideration, the ergodic capacity of the channel (in bit/s/Hz) can be calculated [3] from

$$C = \int_0^\infty \log_2(1+\gamma)\, f_\gamma(\gamma)\, d\gamma, \tag{5}$$

which, after substituting (2), leads to

$$C = \int_0^\infty \log_2(1+\gamma)\, \frac{\mu^\mu m^m (1+\kappa)^\mu}{\Gamma(\mu)\,\overline{\gamma}(\mu\kappa+m)^m} \left(\frac{\gamma}{\overline{\gamma}}\right)^{\mu-1} \times e^{-\mu(1+\kappa)\gamma/\overline{\gamma}}\, {}_1F_1\left(m, \mu; \frac{\mu^2\kappa(1+\kappa)}{\mu\kappa+m}\frac{\gamma}{\overline{\gamma}}\right) d\gamma. \tag{6}$$

In order to find the analytical solution to this equation, the Meijer G-function is going to be introduced. This is a very general function, intended to include many of the known special functions as particular cases, which is represented by a Mellin-Barnes type of contour integral (see 9.3 in [19]). In order to be consistent with (10), the variable of integration in the definition shown in [19] has been changed to $-s$, as follows:

$$G_{p_0,q_0}^{m_0,n_0}\left(\begin{matrix} a_1, a_2, \ldots, a_{n_0}, a_{n_0+1}, \ldots, a_{p_0} \\ b_1, b_2, \ldots, b_{m_0}, b_{m_0+1}, \ldots, b_{q_0}\end{matrix}\,\middle|\, z\right) = G_{p_0,q_0}^{m_0,n_0}\left(\begin{matrix}\mathbf{a_{p_0}} \\ \mathbf{b_{q_0}}\end{matrix}\,\middle|\, z\right) = \frac{1}{2\pi i}\int_L \Psi(s)\, z^{-s} ds, \tag{7}$$

where

$$\Psi(s) = \frac{\prod_{j=1}^{m_0}\Gamma(b_j+s)\prod_{k=1}^{n_0}\Gamma(1-a_k-s)}{\prod_{k=n_0+1}^{p_0}\Gamma(a_k+s)\prod_{j=m_0+1}^{q_0}\Gamma(1-b_j-s)}, \tag{8}$$

$0 \le m_0 \le q_0$, $0 \le n_0 \le p_0$, and the poles of $\Gamma(b_j+s)$ must not coincide with the poles of $\Gamma(1-a_k-s)$ (with $j = 1, \ldots, m_0$ and $k = 1, \ldots, n_0$). L is a suitable closed contour in the complex s-plane which can be chosen among three types of integration paths.

Three special functions can be found in (6): the logarithm, the exponential, and the confluent hypergeometric function. They can be expressed in terms of their Meijer G-identities and then the ergodic capacity can be evaluated using the integration theorem for Meijer G-functions [20] to obtain

$$\int_0^\infty t^{\alpha-1} G_{p_1,q_1}^{m_1,n_1}\left(\begin{matrix}\mathbf{a_{1p_1}} \\ \mathbf{b_{1q_1}}\end{matrix}\,\middle|\, zt\right) G_{p_2,q_2}^{m_2,n_2}\left(\begin{matrix}\mathbf{a_{2p_2}} \\ \mathbf{b_{2q_2}}\end{matrix}\,\middle|\, xt\right) \times G_{p_3,q_3}^{m_3,n_3}\left(\begin{matrix}\mathbf{a_{3p_3}} \\ \mathbf{b_{3q_3}}\end{matrix}\,\middle|\, yt\right) dt = z^{-\alpha} G_{q_1,p_1:p_2,q_2:p_3,q_3}^{n_1,m_1:m_2,n_2:m_3,n_3}\left(\begin{matrix}1-\alpha-\mathbf{b_{1q_1}} \\ 1-\alpha-\mathbf{a_{1p_1}}\end{matrix}\,\middle|\, \begin{matrix}\mathbf{a_{2p_2}} \\ \mathbf{b_{2q_2}}\end{matrix}\,\middle|\, \begin{matrix}\mathbf{a_{3p_3}} \\ \mathbf{b_{3q_3}}\end{matrix}\,\middle|\, \frac{x}{z}, \frac{y}{z}\right). \tag{9}$$

Hence, the solution for (9) is a Meijer G-function of two variables (also denoted [18] as extended generalized bivariate Meijer G-function (EGBMGF)), which is defined as (see II.13 in [21])

$$G_{p_1,q_1:p_2,q_2:p_3,q_3}^{m_1,n_1:m_2,n_2:m_3,n_3}\left(\begin{matrix}\mathbf{a_{1p_1}} \\ \mathbf{b_{1q_1}}\end{matrix}\,\middle|\, \begin{matrix}\mathbf{a_{2p_2}} \\ \mathbf{b_{2q_2}}\end{matrix}\,\middle|\, \begin{matrix}\mathbf{a_{3p_3}} \\ \mathbf{b_{3q_3}}\end{matrix}\,\middle|\, \frac{x}{z}, \frac{y}{z}\right) = \frac{1}{(2\pi i)^2}\int_{L_2}\int_{L_1} \Psi_1(s+t)\,\Psi_2(s)\,\Psi_3(t)\, x^{-s} y^{-t} ds dt, \tag{10}$$

where

$$\Psi_k(\tau) = \frac{\prod_{j=1}^{m_k}\Gamma(b_{kj}+\tau)\prod_{j=1}^{n_k}\Gamma(1-a_{kj}-\tau)}{\prod_{j=n_k+1}^{p_k}\Gamma(a_{kj}+\tau)\prod_{j=m_k+1}^{q_k}\Gamma(1-b_{kj}-\tau)}, \quad k = 1, 2, 3. \tag{11}$$

The contour L_1, in the s-plane, runs from $f_1 - i\infty$ to $f_1 + i\infty$ and separates the poles of $\Gamma(1-a_{1j}-s)$ $(j = 1, \ldots, n_1)$, $\Gamma(1-a_{2j}-s)$ $(j = 1, \ldots, n_2)$ from the poles of $\Gamma(b_{1j}+s)$ $(j = 1, \ldots, m_1)$, $\Gamma(b_{2j}+s)$ $(j = 1, \ldots, m_2)$, when $t \in L_2$. The contour L_2, in the t-plane, runs from $f_2 - i\infty$ to $f_2 + i\infty$ and separates the poles of $\Gamma(1-a_{1j}-s)$ $(j = 1, \ldots, n_1)$, $\Gamma(1-a_{3j}-s)$ $(j = 1, \ldots, n_3)$ from the poles of $\Gamma(b_{1j}+s)$ $(j = 1, \ldots, m_1)$, $\Gamma(b_{3j}+s)$ $(j = 1, \ldots, m_3)$, when $s \in L_1$.

According to the values of the parameters μ and m, the solutions for the ergodic capacity lead to different close-form expressions.

3.1. General Case: $(m-\mu) \notin \mathbb{Z}_0^+$. The parameters in the κ-μ shadowed model can take any arbitrary values; however $(m-\mu)$ cannot be a positive integer.

The Meijer G-identities corresponding to each of the special functions in (6) are [20]

$$\ln(1+x) = G_{2,2}^{1,2}\left(\begin{matrix}1,1\\1,0\end{matrix}\,\middle|\, x\right), \quad e^{-cx} = G_{0,1}^{1,0}\left(\begin{matrix}-\\0\end{matrix}\,\middle|\, cx\right), \quad {}_pF_q\left(\begin{matrix}a_p\\b_q\end{matrix}\,\middle|\, x\right) = \frac{\Gamma(b_q)}{\Gamma(a_p)} G_{p,q+1}^{1,p}\left(\begin{matrix}1-a_p\\0, 1-b_q\end{matrix}\,\middle|\, -x\right). \tag{12}$$

The double integral in (10) must satisfy the convergence theorems (see II.13 in [21]). In particular, the property ${}_1F_1(b-a, b; x) = e^x\, {}_1F_1(a, b; -x)$ must be applied to the confluent hypergeometric function so that the argument in the corresponding G-function is positive and the integral converges.

After some algebraic manipulations, the desired closed-form expression for the ergodic capacity is given by

$$C = \left(\frac{m}{\mu\kappa+m}\right)^{m-\mu} \frac{1}{\Gamma(\mu-m)\log(2)} \times G_{1,0:2,2:1,2}^{0,1:1,2:1,1}\left(\begin{matrix}1-\mu\\-\end{matrix}\,\middle|\, \begin{matrix}1,1\\1,0\end{matrix}\,\middle|\, \begin{matrix}1+m-\mu\\0,1-\mu\end{matrix}\,\middle|\, \frac{\overline{\gamma}(\mu\kappa+m)}{m(1+\kappa)\mu}, \frac{\mu\kappa}{m}\right). \tag{13}$$

The above expression is valid for any set of parameters in the κ-μ shadowed model, except for particular relationships between μ and m that correspond to singularities of the gamma function. For these cases, $(m-\mu) \in \mathbb{Z}_0^+$, a different approach to determine the PDF of γ must be followed. This is done in the next section to obtain a new expression for the ergodic capacity.

3.2. Particular Case: $(m-\mu) \in \mathbb{Z}_0^+$. When $(m-\mu)$ is a positive integer, the singularities in (13) are solved by getting the PDF from the MGF of the κ-μ shadowed fading model. For this purpose, the inverse Laplace transform can be employed: $f_\gamma(\gamma) = \mathscr{L}^{-1}[\mathscr{M}_\gamma(-s); \gamma]$.

It is observed in (4) that the exponent of the s function in the numerator of $\mathscr{M}_\gamma(s)$ is a natural number, so the following expression (see 5.4(4) in [22]) can be used to calculate the inverse Laplace transform:

$$\mathscr{L}^{-1}\left[\Gamma(\nu+1)(s-\lambda)^n(s-\varepsilon)^{-\nu-1}\right] = n!t^{\nu-n}e^{\varepsilon t}L_n^{\nu-n}(-(\varepsilon-\lambda)t), \tag{14}$$

where L is the generalized Laguerre polynomial. Hence, the PDF is given by

$$f_\gamma(\gamma) = \frac{\mu^\mu m^m (1+\kappa)^\mu (m-\mu)!}{\Gamma(m)\overline{\gamma}(\mu\kappa+m)^m}\left(\frac{\gamma}{\overline{\gamma}}\right)^{\mu-1} \times e^{-(\mu(1+\kappa)/\overline{\gamma})(m/(\mu\kappa+m))\gamma} L_{m-\mu}^{\mu-1}\left(\frac{\mu^2\kappa(1+\kappa)}{\mu\kappa+m}\frac{\gamma}{\overline{\gamma}}\right). \tag{15}$$

Since $\mu - 1$ may be a real number and not a natural one, the expression for the generalized Laguerre polynomial must be written as (see 8.97 in [19]) $L_n^\alpha(x) = (\alpha+1)_n/n!\,{}_1F_1(-n, \alpha+1; x)$. Taking into account that ${}_1F_1(a,b;x) = \sum_{i=0}^{\infty}(a)_i/(b)_i x^i/i!$ and after some algebraic manipulations, the ergodic capacity yields

$$C = \left(\frac{m}{\mu\kappa+m}\right)^{m-\mu}\frac{(\mu)_{m-\mu}}{\Gamma(m)\log(2)} \times \sum_{i=0}^{m-\mu}\left[\frac{(-(m-\mu))_i}{(\mu)_i i!}\left(-\frac{\mu\kappa}{m}\right)^i \times G_{3,2}^{1,3}\left(\begin{matrix}1,1,1-(\mu+i)\\1,0\end{matrix}\middle|\frac{\overline{\gamma}(\mu\kappa+m)}{m(1+\kappa)\mu}\right)\right]. \tag{16}$$

For this particular case, the ergodic capacity depends on the sum of weighted Meijer G-functions, which is a simpler expression than the one presented for the general case. It can be proved that when m tends to infinity, (16) matches (6) in [5], which is the average channel capacity of the κ-μ model, after taking into account the following properties:

$$G_{p_0,q_0}^{m_0,n_0}\left(\frac{1}{z}\middle|\begin{matrix}a_1\cdots a_{p_0}\\b_1\cdots b_{q_0}\end{matrix}\right) = G_{q_0,p_0}^{n_0,m_0}\left(z\middle|\begin{matrix}1-b_1\cdots 1-b_{q_0}\\1-a_1\cdots 1-a_{p_0}\end{matrix}\right),$$
$$(a)_p = a(a+1)\cdots(a+p-1) = \frac{\Gamma(a+p)}{\Gamma(a)}. \tag{17}$$

By setting $m = \mu$, the MGF expression boils down to

$$\mathscr{M}_\gamma(s) = \frac{(-m)^m}{\overline{\gamma}^m}\frac{1}{\left(s-\frac{m}{\overline{\gamma}}\right)^m}, \tag{18}$$

and the PDF is directly $f_\gamma(\gamma) = (m^m/(\overline{\gamma}^m\Gamma(m)))\gamma^{m-1}e^{-(m/\overline{\gamma})\gamma}$ and, by means of (5), the ergodic capacity is

$$C = \frac{1}{\log(2)\Gamma(m)}G_{3,2}^{1,3}\left(\begin{matrix}1,1,1-m\\1,0\end{matrix}\middle|\frac{\overline{\gamma}}{m}\right). \tag{19}$$

4. Numerical Results

This section presents numerical simulations to validate the proposed expressions of the ergodic capacity of a κ-μ shadowed fading channel.

For the particular cases $m = \mu$ and $(m-\mu) \in \mathbb{Z}^+$, the Meijer G-function can be evaluated by conventional mathematical packages. However, the Meijer G-function of two variables is not readily available. In the present work, the implementation presented in [18] is followed. The EGBMGF has been extended to any values of m_1 and n_1 in (10) and situations where the contours for the integrals cannot be a straight line parallel to the imaginary axis of the corresponding complex plane. See Appendix for a complete MATHEMATICA implementation of the function that has been used to obtain the numerical results for the ergodic capacity in the general case.

To check the analytical expressions, numerical simulations have been carried out by generating random numbers according to the physical model and the corresponding classical distributions. However, the physical model cannot be used directly when μ is not a natural number. In that situation, a sampled version of the CDF in (3) has been calculated for the selected set of physical parameter values. Afterwards, random numbers have been generated with a uniform distribution and then mapped into a κ-μ shadowed distribution by using the inverse CDF method.

In Figure 1, the ergodic capacity for three different sets of parameters of the fading model is drawn. The parameters have been selected to showcase the three types of expressions obtained for the ergodic capacity (13), (16), and (19). In all cases the simulations and the corresponding analytical results show perfect agreement.

Figures 2–4 highlight the influence of the parameters on the channel capacity, according to the physical model. As mentioned before, the m-parameter represents the level of fluctuation due to shadowing in the dominant component and the κ-parameter indicates the ratio between the dominant components and the scattered waves (and models the fading channel). For large κ values, more power is present in the dominant component with respect to the scattered waves, while, for large m, the power of the dominant component is more stable and therefore there is less shadowing. In Figures 2–4, the sensitivity of the ergodic capacity on the m-parameter is shown at different values of κ (hence different dominant components importance). For the remainder of the paper, the parameter μ has been set to 3, which corresponds to a situation where the scattered waves arrive in the receiver organized in three clusters.

In Figure 2, there is a strong dominant component ($\kappa = 5$) and the influence of m on the ergodic capacity is very significant. This dependency on m increases with γ (the average received signal to noise ratio). For signal to noise ratios above

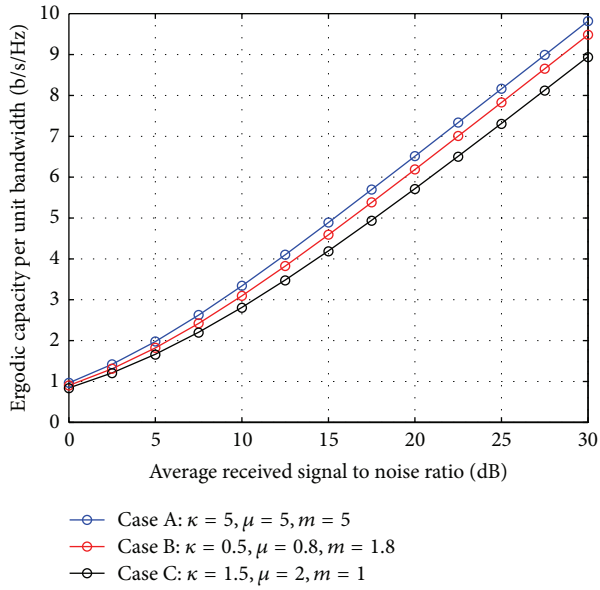

FIGURE 1: Representation of mean capacity values for different kinds of analytical solutions. The marks correspond to results obtained by numerical simulation.

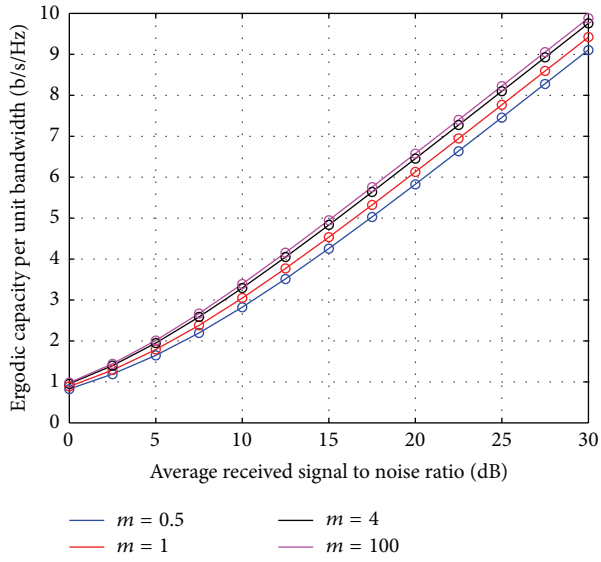

FIGURE 2: Influence of shadowing m-parameter on the mean capacity values when the dominant component is more powerful than the scattered waves ($\kappa = 5$). The value of μ-parameter is set to 3 in all curves. The marks correspond to results obtained by numerical simulation.

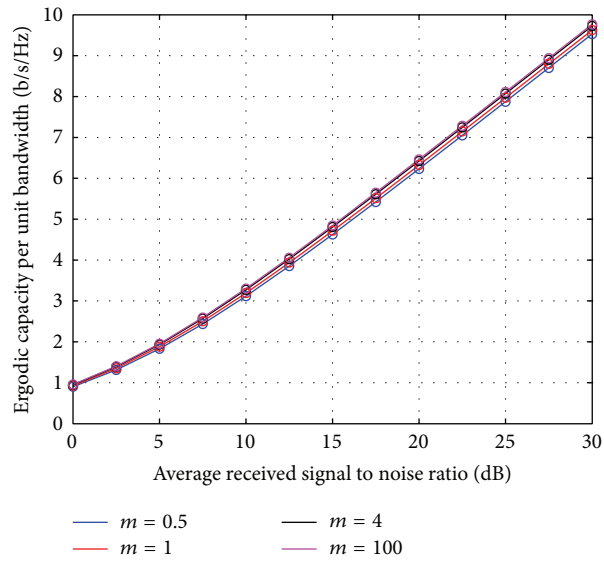

FIGURE 3: Influence of shadowing m-parameter on the mean capacity values when the dominant component has the same power as the scattered waves ($\kappa = 1$). The value of μ-parameter is set to 3 in all curves. The marks correspond to results obtained by numerical simulation.

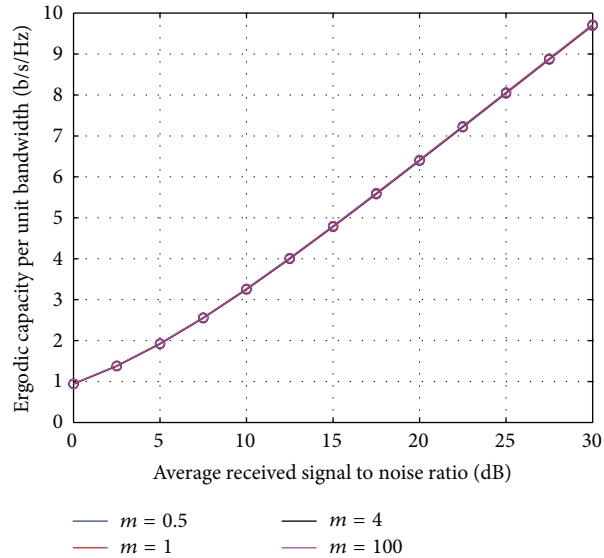

FIGURE 4: Influence of shadowing m-parameter on the mean capacity values when the dominant component is less powerful than the scattered waves ($\kappa = 0.2$). The value of μ-parameter is set to 3 in all curves. The marks correspond to results obtained by numerical simulation.

15–20 dB, the ergodic capacity exhibits a quasilinear behavior, with a constant difference between the minimum capacity (at $m = 0.5$) and maximum (at $m = 100$) of approximately 0.8 bit/s/Hz.

In Figure 3, the power of the dominant component is the same as the scattered waves ($\kappa = 1$) and hence m has a lower influence and there is less than 0.25 bit/s/Hz difference between the capacities at lowest and highest value of m.

Finally, in Figure 4, the dominant component is very weak compared to the scattered components ($\kappa = 0.2$) and the impact of m on the ergodic capacity is negligible.

Table 1 summarizes the ergodic capacity and its dependency on both κ and m parameters. It can be seen that, under a weak shadowing condition (large m), the ergodic capacity increases with κ, while, under a strong shadowing

```
Clear All;
S[{a1st_, b1st_}, {a2s_, b2s_}, {a3t_, b3t_}, μS_, mS_, {zs_, zt_}]:= Module[{},
(*Function Φ1(s + t)*)
Past = Function[u, Product[Gamma[1 − a1st[[1, n]] − u], {n, 1, Length[a1st[[1]]]}]];
Qast = Function[u, Product[Gamma[a1st[[2, n]] + u], {n, 1, Length[a1st[[2]]]}]];
Pbst = Function[u, Product[Gamma[b1st[[1, n]] + u], {n, 1, Length[b1st[[1]]]}]];
Qbst = Function[u, Product[Gamma[1 − b1st[[2, n]] − u], {n, 1, Length[b1st[[2]]]}]];
Mst = Function[u, Past[u] ∗ Pbst[u]/(Qast[u] Qbst[u])];
(*Function Φ2(s)*)
Pas = Function[u, Product[Gamma[1 − a2s[[1, n]] − u], {n, 1, Length[a2s[[1]]]}]];
Qas = Function[u, Product[Gamma[a2s[[2, n]] + u], {n, 1, Length[a2s[[2]]]}]];
Pbs = Function[u, Product[Gamma[b2s[[1, n]] + u], {n, 1, Length[b2s[[1]]]}]];
Qbs = Function[u, Product[Gamma[1 − b2s[[2, n]] − u], {n, 1, Length[b2s[[2]]]}]];
Ms = Function[u, Pas[u] ∗ Pbs[u]/(Qas[u] Qbs[u])];
(*Function Φ3(t)*)
Pat = Function[u, Product[Gamma[1 − a3t[[1, n]] − u], {n, 1, Length[a3t[[1]]]}]];
Qat = Function[u, Product[Gamma[a3t[[2, n]] + u], {n, 1, Length[a3t[[2]]]}]];
Pbt = Function[u, Product[Gamma[b3t[[1, n]] + u], {n, 1, Length[b3t[[1]]]}]];
Qbt = Function[u, Product[Gamma[1 − b3t[[2, n]] − u], {n, 1, Length[b3t[[2]]]}]];
Mt = Function[u, Pat[u] ∗ Pbt[u]/(Qat[u] Qbt[u])];
MT = Function[u, v, Mst[u + v] ∗ Ms[u] ∗ Mt[v]];
(*Countour limiters*)
Zs = zs; (*x*)
Zt = zt; (*y*)
W = 50;
Wp = 10; (*When it is necessary to apply integration by parts. Only for t variable*)
Rs = −1/4;
If[(μS − mS) > 0,
    Rt = (μS − mS)/2;
    (*Final Evaluation*)
    Print["Numerical Integration:"];
    value = 1/(2πI)^2 NIntegrate[MT[s, t] Zs^−s Zt^−t, {s, Rs − I ∗ W, Rs + I ∗ W}, {t, Rt − I ∗ W, Rt + I ∗ W}],
    PosPoleT = Ceiling[Abs[μS − mS]] + (μS − mS);
    NegPoleT = Floor[Abs[μS − mS]] + (μS − mS);
    Rt1 = PosPoleT/2;
    Rt2 = NegPoleT/2;
     (*Final Evaluation*)
    Print["Numerical Integration by parts:"];
    valIni = 1/(2πI)^2 NIntegrate[MT[s, t] Zs^−s Zt^−t, {s, Rs − I ∗ W, Rs + I ∗ W}, {t, Rt1 − I ∗ W, Rt1 − I ∗ Wp}];
    nIter = Abs[Floor[μS − mS]];
    val1T = Sum[1/(2πI)^2 NIntegrate[MT[s, t] Zs^−s Zt^−t, {s, Rs − I ∗ W, Rs + I ∗ W}, {t, (Rt1 − n + 1) − I ∗ Wp,
          (Rt1 − n + 1) + I ∗ Wp}], {n, 1, nIter}];
    val2T = Sum[1/(2πI)^2 NIntegrate[MT[s, t] Zs^−s Zt^−t, {s, Rs − I ∗ W, Rs + I ∗ W}, {t, (Rt1 − n + 1) + I ∗ Wp,
          (Rt2 − n + 1) + I ∗ Wp}], {n, 1, nIter}];
    val3T = Sum[1/(2πI)^2 NIntegrate[MT[s, t] Zs^−s Zt^−t, {s, Rs − I ∗ W, Rs + I ∗ W}, {t, (Rt2 − n + 1) + I ∗ Wp,
          (Rt2 − n + 1) − I ∗ Wp}], {n, 1, nIter}];
    val4T = Sum[1/(2πI)^2 NIntegrate[MT[s, t] Zs^−s Zt^−t, {s, Rs − I ∗ W, Rs + I ∗ W}, {t, (Rt2 − n + 1) − I ∗ Wp,
          (Rt1 − n) − I ∗ Wp}], {n, 1, nIter}];
    valFin = 1/(2πI)^2 NIntegrate[MT[s, t] Zs^−s Zt^−t, {s, Rs − I ∗ W, Rs + I ∗ W}, {t, (Rt1 − nIter) − I ∗ Wp,
          (Rt1 − nIter) + I ∗ W}];
    value = valIni + valFin + val1T + val2T + val3T + val4T];
    (*Returning back the value*)
    Return[value];
];
(*End of MEGBMGF*)
```

Algorithm 1: Implementation of the bivariate Meijer G-function in Mathematica software (*modification of the EGBMGF [18] to conform the κ-μshadowed model*).

Table 1: Ergodic capacity (in bit/s/Hz) for extreme values of m (μ = 3 and $\overline{\gamma}$ = 30 dB).

	$m = 0.5$	$m = 100$
$\kappa = 5$	9.109	9.885
$\kappa = 1$	9.530	9.770
$\kappa = 0.2$	9.692	9.720

condition (low m), the ergodic capacity decreases with κ as the contribution of the scattered waves is advantageous.

5. Conclusion

In the paper, an exact closed-form expression is presented for the ergodic capacity of communications channels that exhibit a fading according to the κ-μ shadowed distribution. These communication channels can be found in systems where a line-of-sight component experiences shadowing, for example, in land mobile satellite systems, underwater acoustic communications, or body centric communications. The derived analytical expressions have been validated against numerical simulations for different capacity curves. The influence of parameters on the shadowing level has been also investigated. The results contained in this work can be used for future evaluation of channels communication performance on different applications.

Appendix

See Algorithm 1.

Conflict of Interests

The authors declare that there is no conflict of interests regarding the publication of this paper.

Acknowledgments

This work has been supported by FEDER and the Spanish and Andalusian Governments, under Projects TEC2011-25473 and P11-TIC-8238, respectively.

References

[1] T. S. Rappaport, *Wireless Communications. Principles and Practice*, Prentice Hall, Englewood Cliffs, NJ, USA, 1996.

[2] W. R. Braun and U. Dersch, "A physical mobile radio channel model," *IEEE Transactions on Vehicular Technology*, vol. 40, no. 2, pp. 472–482, 1991.

[3] A. Goldsmith, *Wireless Communications*, Cambridge University Press, 2005.

[4] M. D. Yacoub, "The $\kappa - \mu$ and the $\eta - \mu$ distribution," *IEEE Antennas and Propagation Magazine*, vol. 49, pp. 68–81, 2007.

[5] D. B. da Costa and M. D. Yacoub, "Average channel capacity for generalized fading scenarios," *IEEE Communications Letters*, vol. 11, no. 12, pp. 949–951, 2007.

[6] X. Wang and N. C. Beaulieu, "Switching rates of two-branch selection diversity in $\kappa - \mu$ and $\alpha - \mu$ distributed fadings," *IEEE Transactions on Wireless Communications*, vol. 8, no. 4, pp. 1667–1671, 2009.

[7] R. Cogliatti, R. A. A. de Souza, and M. D. Yacoub, "Practical, highly efficient algorithm for generating $\kappa - -\mu$ and $\eta - -\mu$ variates and a near-100% efficient algorithm for generating $\alpha - -\mu$ variates," *IEEE Communications Letters*, vol. 16, no. 11, pp. 1768–1771, 2012.

[8] K. P. Peppas, "Sum of nonidentical squared $\kappa - \mu$ Variates and applications in the performance analysis of diversity receivers," *IEEE Transactions on Vehicular Technology*, vol. 61, no. 1, pp. 413–419, 2012.

[9] P. Sofotasios, E. Rebeiz, L. Zhang et al., "Energy detection based spectrum sensing over $\kappa - \mu$ and $\kappa - \mu$ extreme fading channels," *IEEE Transactions on Vehicular Technology*, vol. 62, no. 3, pp. 1031–1040, 2013.

[10] S. L. Cotton, "A statistical model for shadowed body-centric communications channels: theory and validation," *IEEE Transactions on Antennas and Propagation*, vol. 62, no. 3, pp. 1416–1424, 2014.

[11] I. Trigui, A. Laourine, S. Affes, and A. Stéphenne, "Performance analysis of mobile radio systems over composite fading/shadowing channels with co-located interference," *IEEE Transactions on Wireless Communications*, vol. 8, no. 7, pp. 3448–3453, 2009.

[12] J. Zhang, M. Matthaiou, Z. Tan, and H. Wang, "Performance analysis of digital communication systems over composite $\eta - -\mu$/gamma fading channels," *IEEE Transactions on Vehicular Technology*, vol. 61, no. 7, pp. 3114–3124, 2012.

[13] S. R. Panic, D. M. Stefanović, I. M. Petrović, M. Č. Stefanović, J. A. Anastasov, and D. S. Krstić, "Second-order statistics of selection macro-diversity system operating over Gamma shadowed $\kappa - -\mu$ fading channels," *EURASIP Journal on Wireless Communications and Networking*, vol. 2011, article 151, 2011.

[14] P. C. Sofotasios and S. Freear, "On the κ-μ/gamma composite distribution: a generalized multipath/shadowing fading model," in *Proceedings of the IEEE International Microwave and Optoelectronics Conference (IMOC' 11)*, Natal, Brazil, October 2011.

[15] A. Abdi, W. C. Lau, M. Alouini, and M. Kaveh, "A new simple model for land mobile satellite channels: First-and second-order statistics," *IEEE Transactions on Wireless Communications*, vol. 2, no. 3, pp. 519–528, 2003.

[16] F. Ruiz-Vega, M. C. Clemente, J. F. Paris, and P. Otero, "Rician shadowed statistical characterization of shallow water acoustic channels for wireless communications," in *Proceedings of the Underwater Communications Conference*, Sestri, Italy, September 2012.

[17] J. F. Paris, "Statistical characterization of $\kappa - -\mu$ shadowed fading channels," *IEEE Transactions on Vehicular Technology*, vol. 63, no. 2, pp. 518–526, 2014.

[18] I. S. Ansari, S. Al-Ahmadi, F. Yilmaz, M. S. Alouini, and H. Yanikomeroglu, "A new formula for the BER of binary modulations with dual-branch selection over generalized-composite fading channels," *IEEE Trans. on Communications*, vol. 59, no. 10, pp. 2654–2658, 2011.

[19] I. S. Gradshteyn and I. M. Ryzhik, *Table of Integrals, Series, and Products*, Academic Press, 7th edition, 2007.

[20] Wolfram Research, MeijerG, http://functions.wolfram.com/HypergeometricFunctions/MeijerG/.

[21] T. H. Nguyen and S. B. Yakubovich, *The Double Mellin-Barnes Type Integrals and Their Applications to Convolution Theory*, World Scientific, 1992.

[22] A. Erdelyi, *Tables of Integral Transforms I*, McGraw Hill, New York, NY, USA, 1954.

Hindawi Publishing Corporation
International Journal of Antennas and Propagation
Volume 2014, Article ID 318421, 5 pages
http://dx.doi.org/10.1155/2014/318421

Research Article

Capacity Estimation of the Very Short-Range Electromagnetic Underwater Channel Based on Measurements

Jesús López-Fernández, Unai Fernández-Plazaola, and Jose F. Paris

Communications Engineering Department, Malaga University, Campus Teatinos, 29071 Malaga, Spain

Correspondence should be addressed to Jesús López-Fernández; jlf@ic.uma.es

Received 9 May 2014; Revised 11 July 2014; Accepted 13 July 2014; Published 22 July 2014

Academic Editor: Paschalis Sofotasios

Copyright © 2014 Jesús López-Fernández et al. This is an open access article distributed under the Creative Commons Attribution License, which permits unrestricted use, distribution, and reproduction in any medium, provided the original work is properly cited.

The significant attenuation experienced by electromagnetic waves in sea water is the main reason why acoustic waves are generally preferred in underwater communication. Nevertheless, acoustic waves have various drawbacks. For example, they are negatively affected by factors such as mechanical noise, slow propagation speed, and, particularly, low bandwidth, which leads to digital links at a lower bit rate. However, in short-range links, these problems can be overcome by reconsidering the use of electric current communications. For instance, data collected by remote-control vehicles in offshore oil and gas and renewable energy plants can be transmitted at distances of even 1 m or less. This study uses previous frequency response measurements taken in deep water to explore the capacity of a short-range electromagnetic underwater channel. Because of water movement, the nonstatic position of the vehicle when the transmission occurs means that the channel is regarded as randomly time-variant. A statistical model is proposed and the ergodic capacity is calculated for a 7 MHz bandwidth channel at distances ranging from 0.5 m to 5 m as well as for different values of transmitter power. The results of this study reflect capacity values of tens of kbps at distances of approximately 5 m to several Mbps at distances of less than 1.5 m.

1. Introduction

Nowadays real-time monitoring of marine environment and supervision of undersea equipment health of oil and gas companies are demanding wireless underwater digital links with growing digital speed. Three technologies have been considered for this purpose over the years: acoustic, optical, and electromagnetic. Acoustic waves experiment low attenuation in sea water and, hence, long distance links (up to 20 km) can be achieved but the allowable bandwidth is very limited (leading to a maximum digital speed of around 40 kbps [1]). A higher bandwidth can be obtained with radio frequency electromagnetic waves at the cost of a much higher attenuation and, hence, shorter links. Optical technologies are being considered due to their extremely high bandwidth. However, the need for line of sight and precise alignment between transmitter and receiver as well as their susceptibility to turbidity and marine fouling imposes a critical constraint on their underwater application. In [2] an up-to-date overview of these technologies is presented.

Underwater wireless links have conventionally been achieved using acoustic waves. This is the unique option for long range links (>100 m). With the advent of remotely operated vehicles (ROV) data can be collected from sensors at very small distances (<1 m) (see Figure 1). In this new scenario, the use of electromagnetic waves can be readdressed as it may greatly exceed the ≈40 kbps achieved (in the most favorable case) by acoustic means.

An excellent overview of the use of electromagnetic waves for underwater communications from the beginning of the last century to present day is found in [3]. However, the information about data rates attained through an electromagnetic underwater channel is very scarce in the literature.

In [2] data rates over 8 kbps are predicted for ranges under 10 m using a binary phase shift keying (BPSK) modulation scheme. Experimental measurements carried out both in [1] and later in [4] report data rates up to 1 Mbps at ranges shorter than 1 m. Moreover, Wireless For Subsea (WFS) company [5] delivers a current line of products offering data rates from 100 bps (<30 m) to 1 Mbps (<1 m).

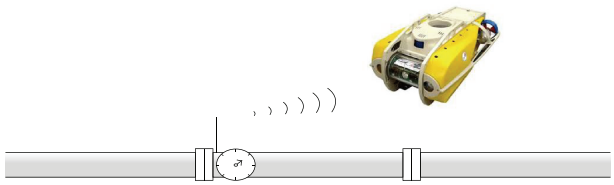

Figure 1: Contactless pressure data collection from subsea gas pipe by a remotely operated vehicle.

In this paper the electromagnetic underwater channel capacity is explored for the case of very short-range (<5 m), deep sea communication. The starting point for this work is [6] where the authors explore the characteristics of this type of channel by conducting a set of experiments focused on obtaining a model for the frequency response.

This paper is organized as follows. In Section 2 a model for frequency response of the channel is described for a separation between transmitter and receiver of 0.1 m. Based on the electric field radiated by a linear dipole antenna the frequency response model is extrapolated to an arbitrary range in Section 3. Section 4 explores the capacity of the channel assuming a statistical model that accounts for the random fluctuation of the receiver due to water movement. Finally, conclusions are extracted in Section 5.

2. Channel Frequency Response

In [6] magnitude and phase delay of the underwater channel transfer function were measured employing OFDM probe signals with 128 carriers, total bandwidth 6.25 MHz, lower band edge 100 kHz, and QPSK modulation. Both transmitter and receiver units were equipped with linear dipole antennas. The experiment in the ocean was carried out at a depth of 5 m (boundary free) and at $r_0 = 0.1$ m separation between transmitter and receiver.

The collected data were then used to fit different frequency response models corresponding to different approximations of the electromagnetic field propagation in a conducting homogeneous medium.

Three models for the frequency response were considered. The first one corresponds to a far field approximation of the waves in a highly conducting media resulting in an exponential dependence with the square root of the frequency, $|H_{r_0}(f)| = A_1 e^{-\alpha_1 \sqrt{f}}$. In the second one the conductivity is assumed to be moderate yielding the model $|H_{r_0}(f)| = A_2 e^{-\alpha_2 f}$. In the last two expressions A_1, A_2, α_1, and α_2 are the fitting parameters, and r_0 is the distance between transmitter and receiver. Finally, in the third model the far field approximation is not considered. This yields a rational-polynomial model formulated as

$$\left|H_{r_0}(f)\right| = \frac{p_1 f^2 + p_2 f + p_3}{q_1 f^2 + q_2 f + q_3} e^{-\alpha f}, \tag{1}$$

where p_1, p_2, p_3, q_1, q_2, q_3, and α are the fitting parameters. Best results were obtained with this rational-polynomial model. The values of the fitting parameters under a least-square criterium are listed in Table 1.

Table 1: Frequency response fitting parameters.

p_1	p_2	p_3	q_1	q_2	q_3	α
$3.4e-5$	$1.2e-4$	$1.5e-5$	0.4	0.22	0.16	0.39

See that expression (1) models the magnitude of the frequency response. This is because for calculating the capacity of a channel only the magnitude of the frequency response is relevant and no attention needs to be paid to the phase response, as indicated by the coming expression (7) in the next section.

3. Frequency Response Extrapolation

Once the frequency response of the channel $H_{r_0}(f)$ is known for a certain distance r_0 between transmitter and receiver, our goal is to extrapolate this result and obtain the frequency response $H_r(f)$ at different arbitrary distance r. To do so, a propagation model must be first recalled.

In a homogeneous conducting medium, the main component of the electric field radiated by a linear dipole antenna at a certain distance r is given by [7]

$$E = j\eta \frac{kI_0 l \sin(\theta)}{4\pi r} \left(1 + \frac{1}{jkr} - \frac{1}{(kr)^2}\right) e^{-jkr} \widehat{\theta}, \tag{2}$$

where I_0 and l are the antenna current and length, respectively, and θ is the polar angle of the observation point assuming that the dipole is aligned with the z-axis. The characteristic impedance of the medium η is given by

$$\eta = \sqrt{\frac{\mu}{\epsilon}\left(1 - j\frac{\sigma}{\omega\epsilon}\right)^{-1}}, \tag{3}$$

where ω is the angular frequency, ϵ, μ, and σ are the permittivity, permeability, and conductivity of sea water, respectively, and k is the propagation constant whose expression is

$$k = \omega\sqrt{\mu\epsilon\left(1 - j\frac{\sigma}{\omega\epsilon}\right)}. \tag{4}$$

The measured channel consists of a path of homogeneous medium between two points separated by a certain distance r_0. If those two points separate a different distance $r = r_0 + \Delta r$ then the new channel is the series connection of two channels. The new frequency response can be estimated as

$$H_r(f) = H_{r_0}(f) \cdot H_{\Delta r}(f) = H_{r_0}(f) \cdot \frac{E_{r_0+\Delta r}(f)}{E_{r_0}(f)}, \tag{5}$$

where $E_r(f)$ is the electric field in (2) at a distance r and frequency f. Explicit dependence on distance and frequency of the electric field has been included in the notation for convenience. Subtituting (2) in (5) yields

$$H_r(f) = H_{r_0}(f) \cdot \frac{r_0\left(1 + (1/jkr) - \left(1/(kr)^2\right)\right)}{r\left(1 + (1/jkr_0) - \left(1/(kr_0)^2\right)\right)} e^{-jk(r-r_0)}. \tag{6}$$

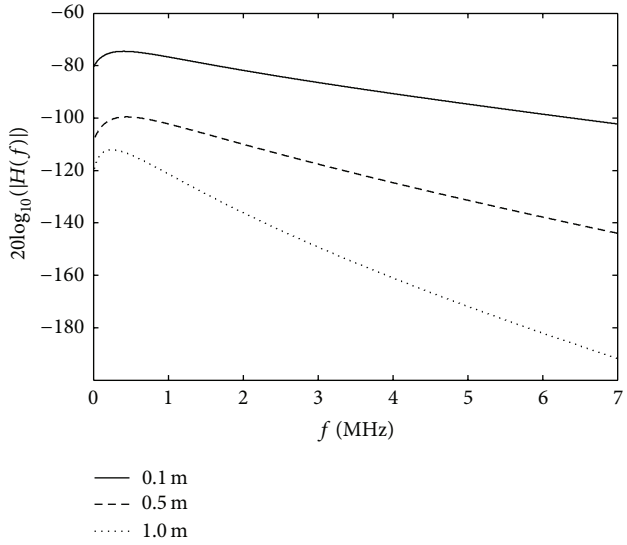

Figure 2: Frequency response of the channel for reference distance $r_0 = 0.1$ m and for extrapolated distances $r = 0.5$ m and $r = 1.0$ m.

With expression (6) the channel frequency response can be extrapolated to any distance r. Figure 2 depicts the frequency response of the underwater channel with the parameters shown in Table 2 for $r_0 = 0.1$ m, $r = 0.5$ m, and $r = 1.0$ m.

As expected, the channel magnitude shows a strong attenuation varying from 75 dB to 100 dB in the given frequency range for the shortest distance. This attenuation increases significantly with the separation between transmitter and receiver. This increase is more evident in the higher end of the frequency band.

4. Channel Capacity

Once the frequency response is available, the capacity of the channel C_r for a given separation between transmitter and receiver r can be easily determined assuming the noise is additive white and gaussian (AWG) and using the well-known Shannon's expression

$$C_r = \int_0^B \log_2 \left(1 + \frac{S_x(f)\left|H_r(f)\right|^2}{N_0}\right) df, \tag{7}$$

where $S_x(f)$ and N_0 are the power spectrum density of the transmitted signal and the noise, respectively, and B is the channel bandwidth. Given a total available power P_x constraint, the water pouring algorithm can be used to find the $S_x(f)$ that maximizes (7) with

$$P_x = \int_{-\infty}^{\infty} S_x(f)\, df. \tag{8}$$

An important issue must however be considered before solving (7). In the communication system under study the transmitter is assumed to be attached to a subsea infrastructure while the receiver is on board of a ROV. This means that the length of the link is not constant over the transmission period but randomly fluctuates due to the water movement. Suppose that the nominal distance between transmitter and receiver is D meters. According to Figure 3, the transmitter is at coordinates $(0, 0, 0)$ and the receiver is at $(D, 0, 0)$. The fluctuations can be accounted for by introducing three normal *i.i.d.* zero-mean normal random variables x', y', and z' with standard deviation σ_{xyz} so that the new position of the receiver is now at coordinates $(D + x', y', z')$. The distance from transmitter to receiver changes therefore from a constant D to a random variable r given by

Table 2: Channel parameters.

Parameter	Description	Value
σ	Sea water conductivity	4.3 S/m
ϵ	Sea water relative permittivity	85
μ	Sea water permeability	$4\pi \cdot 10^{-7}$ H/m
N_0	Noise power spectral density	−177 dBm/Hz

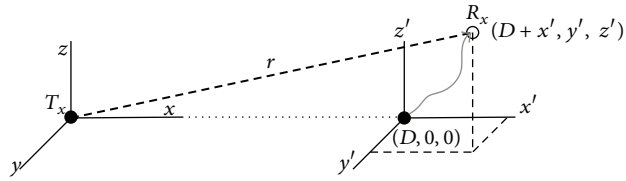

Figure 3: Coordinate system for transmitter and receiver location.

$$r = \sqrt{(D + x')^2 + y'^2 + z'^2}. \tag{9}$$

Moreover, the random fluctuation of the receiver will also cause a random misalignment of the transmitter and receiver dipole antennas lowering the frequency response gain and the capacity. The misalignment angle can be modeled by a normal random variable ψ with standard deviation σ_ψ. This introduces a factor $\cos(\psi)$ in the frequency response of the channel in (5) and (6).

In this new scenario a measure of the channel capacity is given by the ergodic capacity C_{erg} defined in [8] as the average of the instantaneous capacity given in (7). Assuming independence between r and ψ the expression for C_{erg} is

$$C_{\text{erg}} = E[C_r] = \iint_{-\infty}^{\infty} C_r\, p_R(r)\, p_\psi(\psi)\, d\psi\, dr, \tag{10}$$

where $p_R(r)$ is the probability density function of the distance r defined in (9) and $p_\psi(\psi)$ is the probability density function of the misalignment angle ψ.

Substituting (7) into (10) yields

$$C_{\text{erg}} = E\left[\int_0^B \log_2 \left(1 + \frac{S_x(f)\left|H_r(f)\right|^2}{N_0}\right) df\right]. \tag{11}$$

The inner integral in (11) is solved numerically and the expectation is solved by simulation. Results have been obtained in two different scenarios regarding the movement of the sea water: calm water and troubled water. In each one,

Table 3: Simulation parameters.

Parameter	Description	Value
σ_{xyz}	Standard deviation of x', y', and z'	0.05 m (calm water) 0.25 m (calm water)
σ_ψ	Standard deviation of ψ	$\pi/20$ rad (calm water) $\pi/5$ rad (troubled water)
B	Bandwidth	7 MHz
P_x	Total available power	1 mW, 5 mW, and 10 mW

the values of both σ_{xyz} and σ_ψ are different. Low values will correspond to calm water and high values to troubled water. The values of the parameters used in the simulation are listed in Table 3. Results are shown in Figure 4 where the ergodic capacity as a function of the distance is plotted for three different values of transmitter power P_x and for two sets of values of σ_{xyz} and σ_ψ corresponding to calm and troubled water.

Solid and dashed lines correspond to calm and troubled water, respectively. As can be seen there is a general reduction in the capacity when going from calm to troubled water. The relative reduction is quite uniform over the length of the path. In average terms a drop of around 20% is experimented in longer distances (>3 m) and 15% for shorter distances. This is true for the three values of P_x.

Regarding the behavior of the capacity with distance, a strong dependence is observed. Values range from tens of kbps at distances between 5 m and 3 m, growing to hundreds of kpbs between 3 m and 1.5 m, and reaching several Mbps in shorter distances. See that capacity values in the order of 10 Mbps and higher are obtained for distances of 0.5 m and shorter. According to Figure 4, at distances less than ≈3 m the capacity exceeds the maximum data rates achieved by conventional acoustic links (40 kbps). It is in this short-range scenario where the electromagnetic alternative finds its new potential, as stated earlier in this paper. Finally, notice that moderate available power P_x values have been used in the calculations. An increase of these values (as suggested by some commercial units now on the market [5]) would remarkably improve the results.

5. Conclusion and Future Work

The electromagnetic underwater channel capacity has been estimated for the case of very short-range (<5 m), deep sea communication. A known model for the frequency response has been extrapolated to any channel range and a statistical model has been introduced for the channel to account for the random fluctuation of the receiver location and antenna misalignment. Under these circumstances the ergodic capacity has been calculated with a realistic set of parameters. Results show capacity values ranging from tens of kbps to several Mbps for distances from 5 m to 0.5 m. Special attention must be paid to the shorter distances (<1 m) where most of the new applications are developing. Capacity values up to 10 Mbps set a new horizon for future underwater electromagnetic communication systems.

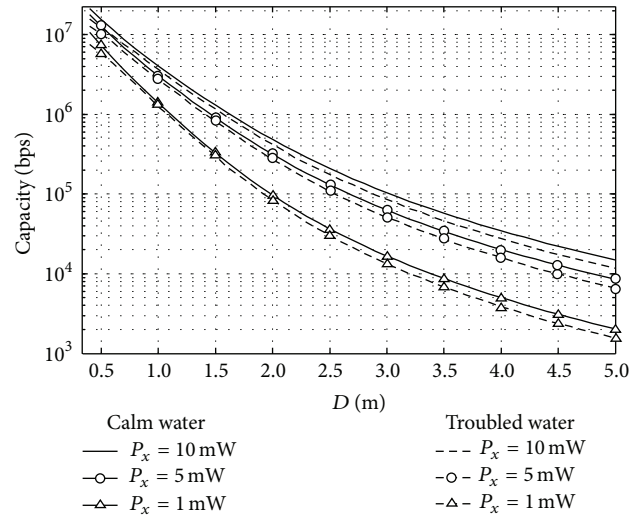

Figure 4: Ergodic capacity as a function of distance D for different values of P_x and for two scenarios: calm and troubled water.

The authors are working towards the experimental validation of the results. A measurement equipment is being set up to be eventually loaded on a small boat. Frequency response measurements at separations other than 0.1 m between transmitter and receiver will be made to validate the extrapolation model presented in this work.

Conflict of Interests

The authors declare that there is no conflict of interests regarding the publication of this paper.

Acknowledgments

This work has been partially supported by FEDER and the Spanish and Andalusian Governments, under projects TEC2011-25473 and P11-TIC-8238, respectively. This work has also been partially supported by the project SUMERGI + DOS which is funded by the Centro para el Desarrollo Tecnológico Industrial (CDTI) and cofunded by FEDER through the FEDER-INNTERCONECTA research program.

References

[1] J. Joe and S. H. Toh, "Digital underwater communication using electric current method," in *OCEANS 2007—Europe*, pp. 1–4, June 2007.

[2] X. Che, I. Wells, G. Dickers, P. Kear, and X. Gong, "Re-evaluation of RF electromagnetic communication in underwater sensor networks," *IEEE Communications Magazine*, vol. 48, no. 12, pp. 143–151, 2010.

[3] J. Li and M. Toulgoat, "EM channel characteristics and their impact on MAC layer performance in underwater surveillance networks," *Wireless Communications and Mobile Computing*, 2014.

[4] Z. Wu, J. Xu, and B. Li, "A high-speed digital underwater communication solution using electric current method," in

Proceedings of the 2nd International Conference on Future Computer and Communication (ICFCC '10), pp. V2-14–V2-16, Wuhan, China, May 2010.

[5] Wireless For Subsea (WFS), *Subsea Wireless Instrumentation and Control Solutions*, 2014, http://www.wfs-tech.com/.

[6] A. Zoksimovski, D. Sexton, M. Stojanovic, and C. Rappaport, "Underwater electromagnetic communications using conduction—channel characterization," in *Proceedings of the 7th ACM International Conference on Underwater Networks and Systems (WUWNet '12)*, Los Angeles, Calif, USA, November 2012.

[7] C. A. Balanis, *Antenna Theory, Analysis and Design*, chapter 4, John Wiley & Sons, New York, NY, USA, 1999.

[8] A. Goldsmith, *Wireless Communications*, chapter 4, Cambridge University Press, 2005.

Hindawi Publishing Corporation
International Journal of Antennas and Propagation
Volume 2014, Article ID 650236, 12 pages
http://dx.doi.org/10.1155/2014/650236

Research Article

Characterization of Path-Loss Disparity in Virtual Multiple-Input-Single-Output Links

Haejoon Jung and Mary Ann Weitnauer

Department of Electrical and Computer Engineering, Georgia Institute of Technology, Atlanta, GA 30332, USA

Correspondence should be addressed to Haejoon Jung; h.j.jung@ieee.org

Received 7 March 2014; Revised 21 June 2014; Accepted 22 June 2014; Published 21 July 2014

Academic Editor: Theodoros Tsiftsis

Copyright © 2014 H. Jung and M. A. Weitnauer. This is an open access article distributed under the Creative Commons Attribution License, which permits unrestricted use, distribution, and reproduction in any medium, provided the original work is properly cited.

Cooperative transmission (CT) is an effective technique to achieve spatial diversity in fading environments, where spatially separated wireless nodes collaborate to form a virtual antenna array or virtual multiple-input-multiple-output (VMISO) link. Many authors model the path loss of the VMISO link as though the elements in the virtual antenna array are colocated, even though they are spread out. In this paper, we show that the spreading causes a signal-to-noise-ratio (SNR) penalty of up to 3 dB. Moreover, in the high SNR regime, we show that the performance degradation caused by the path-loss disparity can be characterized equivalently by log-normal distribution. We use these two observations to propose a new CT link model, expressed in closed form as an outage probability based on the log-normal shadowing model. The quality of the model is evaluated by a statistical test based on Kolmogorov-Smirnov method.

1. Introduction

For small wireless nodes with limited power, where collocated antennas (a real antenna array) cannot be deployed, CT is an alternative way to achieve spatial diversity in fading channels [1, 2]. CT provides an SNR advantage through array and diversity gains by creating a VMISO link that connects a transmitting cluster (multiple nodes) with a single receiver node. Based on the SNR advantage of CT, various higher layer protocols have been proposed, in which the VMISO links provide gains at higher layers such as throughput improvement, energy saving, energy balancing, and range extension [3–16].

In multihop ad hoc networks, the CT-based protocols are divided into two (decentralized and centralized architectures) depending on how the cooperative clusters are activated and supported [17]. In the decentralized architecture such as [3–8], the cluster is activated randomly in a distributed manner, where all the nodes in a cluster have an equal role. On the other hand, in the centralized cluster architecture, which has a cluster head in each cluster, the cluster head recruits its cooperators and triggers the group transmission to the cluster head in the next cluster [12–16]. Because the member nodes follow their cluster heads' decision and the cluster size can be readily controlled, a cluster can work as a single node. Therefore, the centralized cluster architecture is highly compatible with the conventional non-CT or single-input-single-output- (SISO-) based systems.

In network layer research using CT, the nodes in the centralized cooperative cluster are often assumed to be colocated [12–15]; in this model, the disparate path losses caused by the different distances between the transmitting nodes in a cluster to the receiver node are ignored. The authors in [18] realized through simulation of some specific topologies that there can be a significant error (i.e., SNR penalty) incurred for making the colocated assumption.

Motivated by this fact, in this paper, we focus on the error in the colocated assumption, for the centralized cluster architecture with finite node degree. To be specific, we analyze the impact of path-loss disparity, which is ignored in the colocated approximation. When relays are randomly located around a cluster head, their disparate path losses cause variation in the statistics of received SNR or power at the receiver of the VMISO link compared to the colocated (or real) MISO link. Even though the centralized CT is highly compatible with the classical SISO-based system, this SNR variation

ignored in the colocated assumption limits accurate design and evaluation of high-layer protocols based on CT. For this reason, we quantify the error of the colocated assumption in the presence of path-loss disparity by comparing the required SNRs to achieve a certain outage probability.

Beaulieu and Hu [19] derived a closed form expression for the outage probability at the destination for the case of the decode-and-forward (DF) relays, where the location of the relays is assumed to be known. The paper [19] has an intermediate result, where the number of relays that successfully decode is assumed to be known, while the final result in [19] allows for the opportunistic case, in which the number of relays that successfully decode is not known a priori. However, this final expression in [19] is long, complicated, and numerically sensitive [20]. Moreover, the SNR penalty for the colocated assumption is not considered in [19], nor are random locations of nodes taken into account.

In this paper, we allow the node locations to be random and analyze two-hop DF cooperative networks with multiple relays. Cho et al. [21] compared outage performances of random and best relay selection schemes assuming random relay locations, but they only assumed single-relay amplify-and-forward (AF) system. Wang et al. [22] also analyzed outage probabilities with the single-relay DF two-hop network, where the relay is selected by different criteria. Zhai et al. [23] proposed a cooperative automatic repeat request (ARQ) scheme, in which randomly located relays try to retransmit in response to a negative acknowledgement (NACK) from the destination. However, if more than one relay accesses the channel simultaneously, collision occurs and the retransmission is unsuccessful. Aalo et al. in [24, 25] analyzed outage and average bit error rate (ABER) of multihop AF relay networks with randomly located nodes. However, it only assumed a single-relay node for each hop in the interference-limited scenario focusing on signal-to-interference ratio (SIR) instead of SNR.

On the other hand, Wang et al. [26] derived the outage rates for both single- and multirelay scenarios with a two-hop DF network. The authors assumed transmit power control for different nodes and maximum ratio transmission (MRT) [27], which is not practical because channel state information (CSI) should be known at both the transmitters (i.e., source and relays) and receiver (i.e., destination). Moreover, for some types of networks such as sensor networks, constraints on node (e.g., transmit power, processor, and memory) may preclude optimal power control. Also, the presence of multiple time and frequency offsets in CT may make channel estimation very challenging [28], especially when a large number of nodes do CT as in [3]. For the same reason, in this type of network, distributed beamforming schemes in [29, 30], which require CSI at the transmitters, are also difficult to implement in practice.

Therefore, we assume equal transmit power for any transmitting nodes with cooperative DF relaying, which does not require CSI at the transmitters. Moreover, while [26] provides an approximate outage rate, which is complex to interpret, we capture the impact of the random relay locations in an intuitive form. To be specific, for the known number of successfully decoding relays, we show that the random locations of nodes produce a random received power that, when averaged over multipath fading, has a log-normal distribution as in shadowing, when averaged over multipath fading. We also treat the opportunistic case and derive the outage performance for the case when the number of relays that successfully decode is not known a priori by assuming that the first-hop errors are independent and identically distributed (i.i.d.). The conference version of this paper [31] presents that a SNR penalty of up to 3 dB should be included, when making colocated assumption to achieve a certain target outage probability. This paper extends the analysis in [31] with a single approximate outage probability $\widetilde{P}_{\text{out}}$ based on the log-normal approximation, which is more accurate than the upper and lower bounds in [31]. Moreover, the log-normal distribution model of the path-loss disparity, which is the key contribution of this paper, is analyzed in more detail by the statistical normality test based on the Kolmogorov-Smirnov method. In other words, we evaluate the statistical validity of the log-normal model with different system parameters.

The organization of the paper is as follows. In Section 2, the system models including network topology, channel, and outage are presented. The following three sections correspond to three stages for the outage capacity approximation. In Section 3, first-hop error is approximated to decouple the first and second-hop errors. Then, the log-normal distribution to model the path-loss disparity in the second hop is presented in Section 4. Also, the equivalent log-normal model is evaluated by the cumulative distribution function (CDF) comparison and the statistical normality test. Section 5 is the final stage to derive the outage approximation in a closed form, in which first and second moments of channel gain parameter λ are derived under the random relay locations. Section 6 provides the simulation results that show the error of the colocated assumption and the accuracy of the proposed approximate outage capacity $\widetilde{P}_{\text{out}}$.

2. System Model

We consider a VMISO communication in each hop consisting of two phases as shown in Figure 1, where the source, which is indicated by the left black dot at the center of the dotted lined circle, first transmits a packet to the destination (the right black dot) in Phase 1. After that, the multiple relays (the white-filled circles) around the source decode and then forward using orthogonal channels to the destination in Phase 2 [19]. We note that, instead of orthogonal transmission, space-time block codes (STBCs) can be used, in which case the analysis in this paper is still applicable with a slight modification. This cluster architecture is referred to as the centralized cluster [17], where each cluster has a cluster head that recruits its cooperating relays and triggers the group transmission.

2.1. Network Topology. We consider a static VMISO network as shown in Figure 2, where the source node is located at the origin with a distance d_0 to the destination. Also, there are N number of cooperating relays around the source, which are

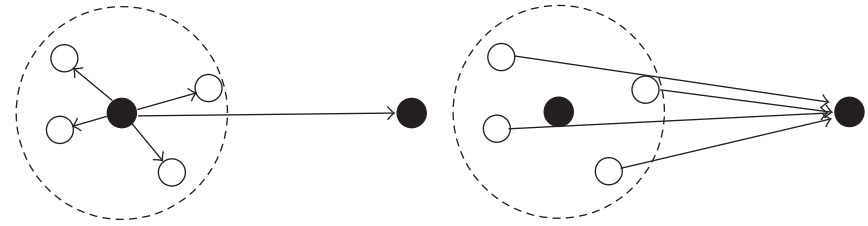

Figure 1: Two-hop cooperative transmission scenario.

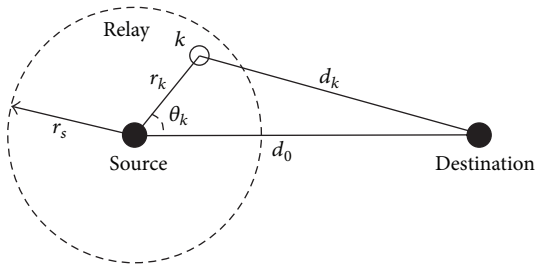

Figure 2: Network topology model.

located in the dotted lined circle with a radius r_s centered at the source node. r_s can be regarded as the SISO range, over which the source collects its cooperators. As in [12–14], we assume the "*CT range extension case,*" where $1.5 \leq d_0/r_s \leq 4$, which was demonstrated in [32]. We note that maximum range extension happens when radios do not decrease their transmit powers when cooperating and they transmit using either orthogonal channels or space-time block coding, so the link benefits from diversity gain [20]. The colocated VMISO model in [12–14] assumes that the links between the source and the relays are error-free, which is another factor that causes the error of the colocated assumption.

We assume that N relays are independently and identically distributed in the circle with the radius r_s following the uniform distribution. As shown in Figure 2, relay k represented by the white-filled circle exists at a distance of r_k from the source with an angle θ_k with respect to the line connecting the source and destination. Also, relay k is d_k away from the destination, which determines the path loss between the relay and the destination. It follows that the polar coordinates (r_k, θ_k) of relay k have the probability distribution functions (PDFs):

$$f_{r_k}(r_k) = \frac{2r_k}{r_s^2}, \tag{1}$$

$$f_{\theta_k}(\theta_k) = \frac{1}{2\pi}, \tag{2}$$

where $0 < r_k \leq r_s$ and $0 \leq \theta_k \leq 2\pi$, respectively.

2.2. Channel Model. We assume mutually independent Rayleigh fading for any links between two nodes (the source, relays, and destination). The node indices of the source and destination are zero and $N + 1$, and the relay index k satisfies $1 \leq k \leq N$. The complex channel gains are denoted by $h_{0:k}$ (from the source to relay k), $h_{0:N+1}$ (from the source to the destination), and $h_{k:N+1}$ (from relay k to the destination). Hence, $\Omega_{i:j} = |h_{i:j}|^2$ follows the exponential distribution with a parameter $\lambda_{i:j}$ that is determined by the locations of nodes i and j. Therefore, when the node locations are given, the cumulative distribution function (CDF) of Ω_k given $\lambda_{i:j}$ is expressed as

$$F_{\Omega_{i:j}|\lambda_{i:j}}(x) = 1 - e^{-\lambda_{i:j}x}, \tag{3}$$

where the conditional mean and variance are $\mathbb{E}\{\Omega_{i:j} \mid \lambda_{i:j}\} = 1/\lambda_{i:j}$ and $\mathbb{VAR}\{\Omega_{i:j} \mid \lambda_{i:j}\} = 1/\lambda_{i:j}^2$, respectively. If the path-loss exponent is α, then $\lambda_{0:k} = r_k^\alpha$ for the source-relay link and $\lambda_{k:N+1} = d_k^\alpha$ for the relay-destination link.

2.3. Outage Model. In this section, we first consider the outage probability for a deterministic network topology (i.e., the relay locations are given), the closed form of which is provided in [19]. Next, we consider the random spatial distribution of the relays to capture how random path-loss disparities impact outage probability.

Assuming the same transmission powers for the source and N relays, the conditional mutual information between the source and relay k given that $\lambda_{0:k} = r_k^\alpha$ is

$$\mathbf{I}_{0:k}(\mathtt{SNR} \mid \lambda_{0:k}) = \frac{1}{N+1}\log_2(1 + \mathtt{SNR} \cdot \Omega_{0:k}), \tag{4}$$

where $\mathtt{SNR}$ is the transmit SNR of each node [19]. Also, the normalization factor $1/(N + 1)$ is for orthogonal DF transmissions of the source and relays, where the destination achieves diversity gain. Therefore, for a certain transmission rate $\mathtt{R}$ (bit/Hz/sec), the probability that relay k fails to decode the received signal from the source is given by

$$p_k = F_{\Omega_{0:k}|\lambda_{0:k}}(g(\mathtt{SNR}, \mathtt{R})) = 1 - e^{-\lambda_{0:k} \cdot g(\mathtt{SNR}, \mathtt{R})}, \tag{5}$$

where $F_{\Omega_{0:k}|\lambda_{0:k}}(x)$ is the conditional CDF of $\Omega_{0:k}$, given $\lambda_{0:k} = r_k^\alpha$, and $g(t, \mathtt{R}) = (2^{(N+1)\mathtt{R}} - 1)/t$.

Suppose that, for a given network topology, $\mathcal{S}$ is a particular set of M relays that successfully decode the source transmission, where $0 \leq M \leq N$. Therefore, the conditional

mutual information of the VMISO link, conditioned on $\mathcal{S}$, is given by

$$\mathbf{I}(\mathtt{SNR} \mid \mathcal{S}) = \frac{1}{N+1}\log_2\left(1 + \mathtt{SNR}\cdot\Omega_{0:N+1} + \sum_{k\in\mathcal{S}} \mathtt{SNR}\cdot\Omega_{k:N+1}\right). \tag{6}$$

Thus, the outage probability of the VMISO communication for a given network topology indicated by two parameter vectors $\overline{\mathbf{\Lambda}}_s = [\lambda_{0:1}, \lambda_{0:2}, \ldots, \lambda_{0:N}]^T$ and $\overline{\mathbf{\Lambda}}_d = [\lambda_{1:N+1}, \lambda_{2:N+1}, \ldots, \lambda_{N:N+1}]^T$ that satisfy $\lambda_{0:k} = r_k^\alpha$ and $\lambda_{k:N+1} = d_k^\alpha$, with $1 \le k \le N$ is expressed as

$$P_{\text{out}|\overline{\mathbf{\Lambda}}_s,\overline{\mathbf{\Lambda}}_d}(\mathtt{SNR}, \mathtt{R}) = \sum_{\mathcal{S}} \Pr[\mathbf{I} < \mathtt{R} \mid \mathcal{S}] \cdot \Pr[\mathcal{S}], \tag{7}$$

where $\Pr[\mathcal{S}] = (\prod_{k\notin\mathcal{S}} p_k)\cdot(\prod_{k\in\mathcal{S}}(1-p_k))$. This equation is the same as in [19] except that we suppose $\Pr[\mathcal{S}]$ is the probability conditioned on the certain network topology (i.e., $\overline{\mathbf{\Lambda}}_s$ and $\overline{\mathbf{\Lambda}}_d$). Considering the randomness of the relay locations, the outage rate averaged over the random network topology has N^2-fold integral as

$$P_{\text{out}}(\mathtt{SNR}, \mathtt{R}) = \int\cdots\int P_{\text{out}|\overline{\mathbf{\Lambda}}_s,\overline{\mathbf{\Lambda}}_d}(\mathtt{SNR}, \mathtt{R}) \times \prod_{k=1}^{N}\left[f_{\lambda_{0:k},\lambda_{k:N+1}}(\lambda_{0:k}, \lambda_{k:N+1}) \times d\lambda_{0:k} d\lambda_{k:N+1}\right], \tag{8}$$

where $f_{\lambda_{0:k},\lambda_{k:N+1}}(x_1, x_2)$ is the joint PDF of $\lambda_{0:k}$ and $\lambda_{k:N+1}$, which can be obtained by the variable transformation from $f_{r_k}(r_k)$ and $f_{\theta_k}(\theta_k)$.

3. First-Hop Error Approximation

It is difficult to obtain the closed form expression of the outage probability under the random relay locations in (8), because the first hop (between the source and the relays) and second hop (between the relays and the destination) depend on each other by the random relay locations. Therefore, to obtain a single estimate of the outage probability with random relay locations, we first approximate the first-hop error rates of the N relays by independent Bernoulli trials. Then, assuming that M out of N relays successfully decode the first-hop transmission from the source, we derive the second-hop outage probability for a given (deterministic) relay topology.

3.1. Bernoulli Trial Approximation of First-Hop Error. The first-hop outage rate of relay k in (5) satisfies that $0 \le p_k \le p_{\max} = 1 - e^{-r_s^\alpha \cdot g(\mathtt{SNR},\mathtt{R})}$, because $0 < r_k \le r_s$. To decouple the outage rates between the first (source-relays) and second (relays-destination) hops, we approximate the first-hop error rates of the N relays by independent Bernoulli trials with the same probability p. If all N relays have the same constant first-hop error rate of p, where $0 \le p \le p_{\max}$, $P_{\text{out}|\overline{\mathbf{\Lambda}}_s,\overline{\mathbf{\Lambda}}_d}$ in Section 2.3, which does not depend on $\overline{\mathbf{\Lambda}}_s$ anymore, is simplified as

$$P_{\text{out}|\overline{\mathbf{\Lambda}}_d}(\mathtt{SNR}, \mathtt{R}) = \sum_{M=0}^{N}\binom{N}{M} p^{N-M}(1-p)^M \Pr\left[\sum_{k=0}^{M}\Omega_{k:N+1} < g(\mathtt{SNR}, \mathtt{R})\right]. \tag{9}$$

Also, if $Y = \sum_{k=0}^{M}\Omega_{k:N+1}$, then $\Pr[\sum_{k=0}^{M}\Omega_{k:N+1} < g(\mathtt{SNR},\mathtt{R})] = F_{Y|M,\overline{\mathbf{\Lambda}}_{d(1:M)}}(g(\mathtt{SNR},\mathtt{R}))$ that is the conditional CDF of Y for given M and a truncated vector with M elements out of N, $\overline{\mathbf{\Lambda}}_{d(1:M)} = [\lambda_{1:N+1}, \ldots, \lambda_{M:N+1}]^T$. Therefore, the final outage in (8) is approximated by N-fold integral by

$$\widetilde{P}_{\text{out}}(\mathtt{SNR}, \mathtt{R}) = \sum_{M=0}^{N}\binom{N}{M} p^{N-M}(1-p)^M \times \int\cdots\int F_{Y|M,\overline{\mathbf{\Lambda}}_{d(1:M)}}(g(\mathtt{SNR}, \mathtt{R})) \times f_{\lambda_{1:N+1}}(\lambda_{1:N+1})\cdots f_{\lambda_{N:N+1}} \times (\lambda_{N:N+1})\, d\lambda_{1:N+1}\cdots d\lambda_{N:N+1}. \tag{10}$$

The upper and lower bounds of outage capacity in [31] are obtained using $p = p_{\max}$ and $p = 0$, respectively. Alternatively (i.e., new in this paper), to obtain a single estimate of the outage rate with higher accuracy than the two bounds, we will use the average first-hop outage rate $p = \mathbb{E}\{p_k\}$, which is derived by (1) and (5) as

$$p = \mathbb{E}\{p_k\} = \int_0^{r_s}\left(1 - e^{-(g(\mathtt{SNR},\mathtt{R})/x^\alpha)}\right)\cdot\frac{2x}{r_s^2}dx = 1 + \frac{2}{\alpha}\cdot P_\varepsilon\left(1 - \frac{-2}{\alpha}, g(\mathtt{SNR}, \mathtt{R})\cdot r_s^\alpha\right), \tag{11}$$

where $P_\varepsilon(n, z)$ is nth order exponential integral [33], which is given by

$$P_\varepsilon(n, z) = \int_1^\infty \frac{\exp(-zt)}{t^n}dt. \tag{12}$$

We note that this exponential function can be easily calculated by popular numerical tools such as MATLAB, MATHEMATICA, and MAPLE [34].

3.2. Second-Hop Error and Path-Loss Disparity. In this section, we look at the second-hop outage rate $P_{\text{out}|\overline{\mathbf{\Lambda}}_d}(\mathtt{SNR}, \mathtt{R})$ for a given relay topology, assuming the number of active relays participating in the second-hop transmission is M. As a general case with path-loss disparities, when $\lambda_{k:N+1} \ne \lambda_{j:N+1}$ for $k \ne j$, $F_{Y|M,\overline{\mathbf{\Lambda}}_{d(1:M)}}(y)$ in (10) follows the hypoexponential distribution as

$$F_{Y|M,\overline{\mathbf{\Lambda}}_{d(1:M)}}(y) = 1 - \sum_{k=0}^{M} A_k \exp(-\lambda_k y), \tag{13}$$

where $A_k = \prod_{k\ne j}(\lambda_j/(\lambda_j - \lambda_k))$ and $\sum_{i=0}^{M} A_k = 1$ [20].

On the other hand, when $\lambda_{0:N+1} = \lambda_{1:N+1} = \cdots = \lambda_{M:N+1} = \lambda$, which corresponds to the colocated antenna array with M elements, $F_{Y|M,\overline{\Lambda}_{d(1:M)}}(y)$ is the CDF of the gamma distribution as

$$F_{Y|M,\lambda}(y) = 1 - \sum_{k=0}^{M} \frac{\exp(-\lambda y) \cdot (\lambda y)^k}{k!}. \tag{14}$$

Therefore, as shown in the equation, $F_{Y|M,\overline{\Lambda}_{d(1:M)}}(y)$ can be simplified into $F_{Y|M,\lambda}(y)$ with the single condition variable λ instead of the condition vector $\overline{\Lambda}_{d(1:M)}$. Also, the outage probability in (10) can be expressed with a single integral as

$$\begin{aligned}\widetilde{P}_{\text{out}}(\mathtt{SNR}, \mathtt{R}) &= \sum_{M=0}^{N} \binom{N}{M} p^{N-M}(1-p)^M \\ &\times \int F_{Y|M,\lambda}(g(\mathtt{SNR}, \mathtt{R}))\, f_{\lambda|M}(\lambda)\, d\lambda.\end{aligned} \tag{15}$$

We note that, for the colocated assumption, $P_{\text{out}} = F_{Y|M=N,\lambda=d_0^\alpha}(g(\mathtt{SNR}, \mathtt{R}))$ without any integral, because all the links have the same distances of d_0 to the destination. Compared to (10), the outage equation in (15) is much simpler, because there is only one integral. Also, the conditional CDF $F_{Y|M,\overline{\Lambda}_{d(1:M)}}(y)$ in (13) is numerically sensitive to compute [20]. Therefore, ultimately to capture the impact of path-loss disparity, we use an approximation to project the vector $\overline{\Lambda}_{d(1:M)} = [\lambda_{1:N+1}, \ldots, \lambda_{M:N+1}]^T$ into a single variable λ assuming high SNR, while keeping the influence of the random relay locations on the outage rate, in the following section.

4. Path-Loss Disparity Modeling by Log-Normal Distribution

In this section, assuming high SNR, we will first approximate the hypoexponential distribution in (13) using the gamma distribution in (14), because the hypoexponential distribution is long, complicated, and numerically sensitive [20]. Also, the approximation into the gamma distribution enables us to characterize the path-loss disparity as the log-normal distribution, which means the impact of the path-loss disparity on the outage rate can be captured by the equivalent log-normal shadowing. Therefore, the final outage rate formula derived in this section is the same as the outage capacity in the conventional composite channel with Rayleigh multipath fading and log-normal shadowing. This log-normal approximation is validated by the illustrative CDF comparison and the statistical normality test using the Kolmogorov-Smirnov (KS) method.

4.1. Gamma Approximation of $F_{Y|M,\overline{\Lambda}_{d(1:M)}}(y)$ into $F_{Y|M,\lambda}(y)$. Many studies on CT focus on the asymptotic performance by the limit of $\mathtt{SNR} \to \infty$ [20]. In [20], the author proposes a simple but accurate way to calculate outage performance of CT with dissimilar (deterministic) path losses, where the outage probability based on hypoexponential distribution in (13) can be approximated by the outage probability computation using gamma distribution in (14) with a negligible error. This enables us to use the traditional notion of the performance analysis based on the real multiple-antenna array system to the VMISO link. The key result in this approximation in [20] is

$$\lambda \approx \left(\prod_{k=0}^{M} \lambda_{k:N+1} \right)^{1/(M+1)}. \tag{16}$$

In other words, in this gamma approximation, the single parameter λ is equal to the geometric mean of the distinct $\lambda_{k:N+1}$ for $k = 0, 1, \ldots, M$. Please see the appendix for the proof, which is relatively simpler than [20].

4.2. Approximation of $f_{\lambda|M}(x)$ by Log-Normal Distribution. To calculate the outage rate with the random relay locations in (15) with the gamma approximation, we need to obtain the conditional PDF of λ for given M. In dB, (16) is expressed as

$$10\log_{10}\lambda \approx \frac{10}{M+1} \sum_{k=0}^{M} \log_{10}\lambda_{k:N+1}, \tag{17}$$

where $\lambda_{0:N+1} = d_0^\alpha$ is deterministic, while $\lambda_{1:N+1}, \ldots, \lambda_{M:N+1}$ are i.i.d. random variables, when d_0, r_s, and α are given.

Because (17) is the sum of i.i.d variables, we model $10\log_{10}\lambda$ as a Gaussian distribution. In other words, λ is approximated by log-normal distribution, which becomes more accurate, as M increases by the Central Limit Theorem (CLT) [35]. The log-normal approximation is also convenient, because it enables us to use the conventional composite channel model (Rayleigh multipath fading and log-normal shadowing). By the log-normal approximation, we have the PDF $f_{\lambda|M}(x)$ as below:

$$f_{\lambda|M}(x) \approx \frac{1}{x\xi\sqrt{2\pi\sigma}} \exp\left[-\frac{(10\log_{10}x - \mu)^2}{2\sigma^2} \right], \tag{18}$$

where $0 < x < \infty$, $\xi = \ln 10/10$. Also, because $\lambda_{k:N+1} = d_k^\alpha$,

$$\begin{aligned}\mu &= \mathbb{E}\{\lambda_{(\text{dB})} \mid M\} = \frac{10\alpha}{M+1}\left(\log_{10}d_0 + M\mathbb{E}\{\log_{10}d_k\}\right), \\ \sigma^2 &= \mathbb{VAR}\{\lambda_{(\text{dB})} \mid M\} = \frac{100\alpha^2 M}{(M+1)^2}\mathbb{VAR}\{\log_{10}d_k\},\end{aligned} \tag{19}$$

where $\mathbb{E}\{\log_{10}d_k\}$ and $\mathbb{VAR}\{\log_{10}d_k\}$ are derived in Section 5, which presents the distribution of d_k.

Using this log-normal approximation, the influence of the random relay locations can be characterized by the log-normal approximation of the PDF of λ, which means that the random separations have the same effect as *log-normal shadowing* on the outage. Based on this approximation,

the outage probability $\widetilde{P}_{\text{out}}$ in (15) can be simplified in a summation form using the Gauss-Hermite method [36]:

$$\widetilde{P}_{\text{out}}(\mathtt{SNR}, \mathtt{R}) \approx \sum_{M=0}^{N} \binom{N}{M} \frac{p^{N-M}(1-p)^{M}}{\sqrt{\pi}} \left[\sum_{i=1}^{m} W_i \cdot G\left(10^{(\sqrt{2}\sigma r_i + \mu)/10}\right) \right], \tag{20}$$

where $G(x) = F_{Y|M,\lambda=x}(g(\mathtt{SNR}, \mathtt{R}))$, W_i are weight factors, r_i are the roots of the Hermite polynomial, and m is the order of the Hermite polynomial. We test this log-normal approximation in the following section.

4.3. Log-Normal Approximation Test. In this section, we test the quality of the log-normal approximation in (18) with different system parameters. First, we compare empirical CDF of $\lambda_{\text{dB}} = 10\log_{10}\lambda$ in (17) and its normal CDF fit by matching their mean and variance.

(1) CDF Comparison Example. Figure 3 shows three CDFs of λ in dB, $F_{\lambda_{(\text{dB})}|M}(x)$, when $\alpha = 4$ and $r_s = 1$. The results in the three subfigures are achieved with different distances from the source to destination d_0 and the number of active relays M. To be specific, Figures 3(a), 3(b), and 3(c) correspond to $(d_0, M) = (3, 4)$, $(3, 1)$, and $(1.5, 4)$, respectively. In each figure, the red solid curve indicates the real empirical CDF $F_{\lambda_{(\text{dB})}|M}(x)$ with 10^4 samples, while the black dotted line with the "o"-markers represents the normal fit of $\lambda_{(\text{dB})}$ (i.e., the log-normal fit of λ).

In Figure 3(a) obtained with $(d_0, M) = (3, 4)$, the two CDF curves are almost identical, which means the log-normal approximation in (18) is highly accurate. On the other hand, when the number of active relays M decreases to one as in Figure 3(b), the normal fit shows a significantly greater error from the empirical CDF compared to Figure 3(a). Also, with $d_0 = 1.5$ and $M = 4$, Figure 3(c) shows a smaller error of the normal fit compared to Figure 3(b). On the other hand, compared to Figure 3(a) with $d_0 = 3$ and $M = 4$, the error of the normal fit in Figure 3(c) is greater. Thus, comparing the three figures, we can conclude that the quality of the log-normal approximation in (18) becomes more accurate, as M and d_0 increase. We note that the quality of the log-normal approximation does not depend on α, because $10\log_{10}\lambda_{k:N+1} = 10\alpha\log_{10}d_{k:N+1}$, where α is a product term.

However, the outage probability is determined by the tail property of the channel distribution, and the log-normal approximation has a longer tail than the original conditional PDF $f_{\lambda|M}(x)$, especially when M is small. Therefore, this outage rate based on the log-normal approximation is higher than (15), which is used to derive the upper bound of the outage rate in the following section.

(2) Statistical Normality Test: Kolmogorov-Smirnov. In this section, we use a well-known statistical normality test: the KS tests [37] at significance level 5%. The KS method is widely used to assess a null hypothesis that distribution of the data is normal in various applications [38–40]. We note that the KS test tends to be more sensitive near the center of the distribution than at the tails. However, [41] shows that the KS method is as powerful as other tests (e.g., Shapiro-Wilk, Anderson-Darling, and Lilliefors), when the number of samples is large enough (more than or equal to 1,000 samples).

Table 1: KS test P value results ($r_s = 1$, $\alpha = 4$).

d_0	M			
	1	2	4	8
1.5	4.777×10^{-6}	1.221×10^{-2}	0.1479	0.3566
2.0	1.257×10^{-4}	7.352×10^{-2}	0.3230	0.5228
2.5	6.162×10^{-4}	0.1539	0.4360	0.6088
3.0	1.531×10^{-3}	0.2279	0.5055	0.6558
3.5	2.593×10^{-3}	0.2855	0.5577	0.6858
4.0	3.763×10^{-3}	0.3265	0.5964	0.7012

We perform the KS test using 2,000 samples with different d_0 and M, when $r_s = 1$ and $\alpha = 4$. Table 1 shows the P values averaged over 10^6 iterative tests. The six rows correspond to d_0 from 1.5 to 4.0 with the same (0.5) interval, while the four columns represent $M = 1$, 2, 4, and 8, respectively. In the table, the P value increases, as d_0 and M increase.

Figure 4 shows the corresponding probability of passing test, which is averaged over 10^6 KS tests, with the significance level of 5%. As in Table 1, we use $\alpha = 4$ and $r_s = 1$. In the figure, the horizontal axis indicates the distance between the source and destination $1.5 \geq d_0 \geq 4$. On the other hand, the vertical axis indicates test-passing probability, which means the probability that P value is greater than the 5% significance level over 10^6 iterative KS tests. Also, the blue solid line, the red dashed line, and the black dotted line represent $M = 2$, 4, and 8, respectively. This figure shows the same trends as in Table 1 with respect to d_0 and M; it becomes more likely to pass the test, as d_0 and M increase. In other words, the log-normal approximation in (18) becomes a better fit, as d_0 and M increase. Moreover, when $d_0 \geq 2$ and $M \geq 4$, the probability of passing is greater than 90%, which means the log-normal fit is good.

5. Distance to Destination under Random Relay Locations

To derive the approximated outage probability in the previous section, the disparate path losses, which depend on the distances to destination d_k, need to be calculated. In particular, to obtain the complete outage rate in (20), $\mathbb{E}\{\log_{10}d_k\}$ and $\mathbb{VAR}\{\log_{10}d_k\}$ should be obtained for μ and σ^2. In this section, we first derive the PDF of d_k, $f_{d_k}(x)$, which characterizes the distance from relay k to the destination. However, because it is difficult to obtain closed form solutions of $\mathbb{E}\{\log_{10}d_k\}$ and $\mathbb{VAR}\{\log_{10}d_k\}$, therefore, as the final stage to derive an approximate outage rate in the presence of the path-loss disparity caused by the random relay locations, we approximate $f_{d_k}(x)$ and derive the corresponding μ and σ^2 in closed forms.

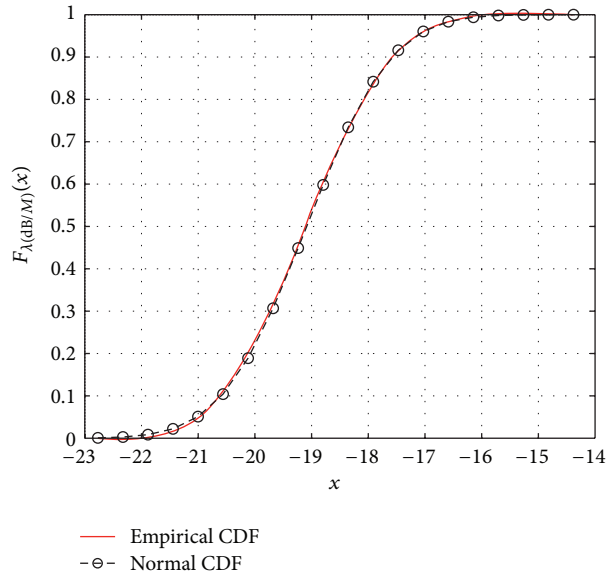

(a) $d_0 = 3$ and $M = 4$

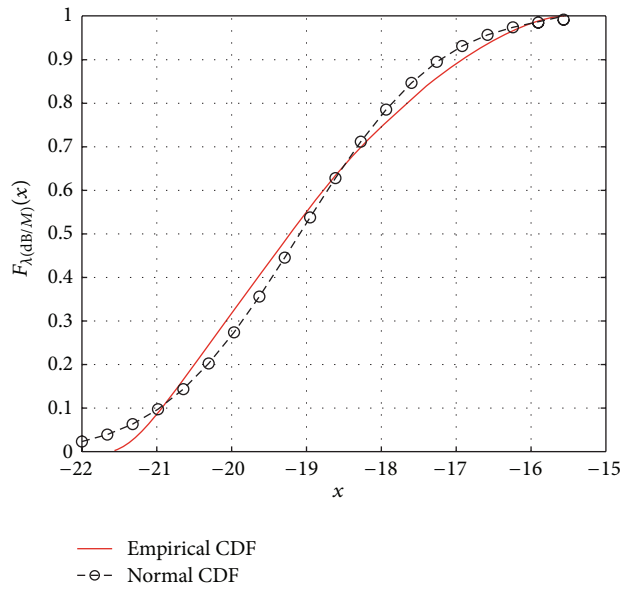

(b) $d_0 = 3$ and $M = 1$

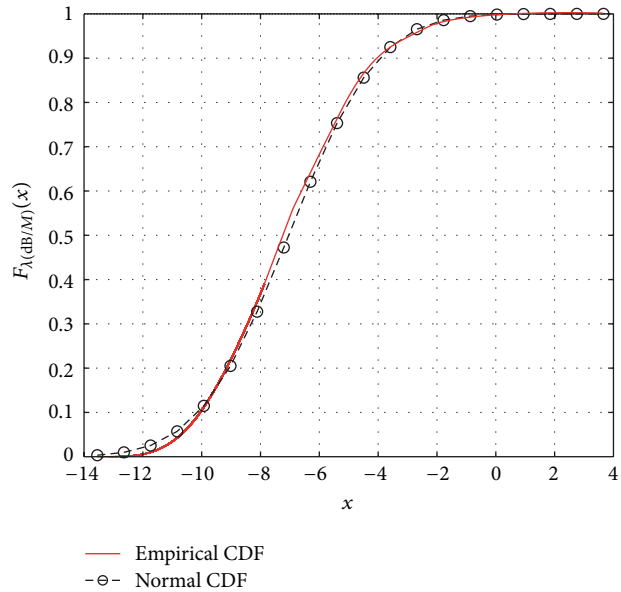

(c) $d_0 = 1.5$ and $M = 4$

FIGURE 3: Normal CDFs compared with the empirical CDFs, $F_{\lambda_{(\mathrm{dB})}|M}(x)$, when $\alpha = 4$ and $r_s = 1$.

5.1. Original Probability Distributions of d_k. Figure 5 illustrates the variable assignments, which are used to derive the PDF of d_k, where a relay node is randomly located inside the left circle centered at the origin O, where the source exists. Also, the destination node is at the distance d_0 from the origin on the x-axis, and the relay node is d_k away from the destination. The locations A, B, B', and C indicate some important intersection points that will be used in the derivation of the probability distribution. Using the illustration, the CDF of d_k can be the ratio of the area of the shaded region (S) to the total area of the left circle, which is given by

$$F_{d_k}(x) = \frac{S}{\pi r_s^2}, \tag{21}$$

where $d_0 - r_s \le x \le d_0 + r_s$, and the area S can be expressed as

$$S = \theta_k r_s^2 + \phi_k x^2 - r_s d_0 \sin\theta_k, \tag{22}$$

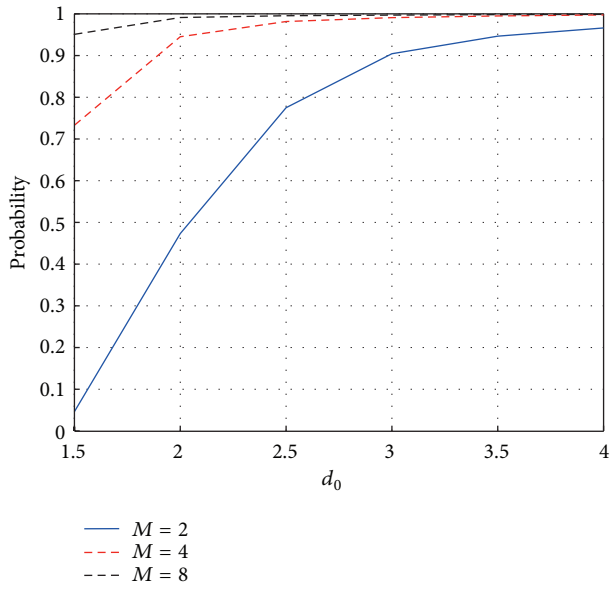

Figure 4: Probability of passing tests with $r_s = 1$ and $\alpha = 4$.

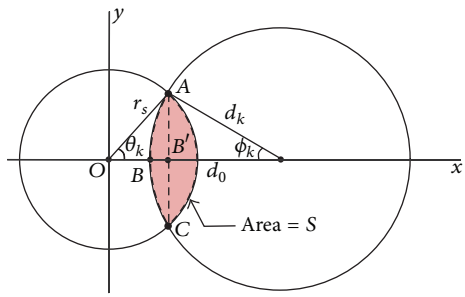

Figure 5: Illustration for derivation of PDF of d_k.

where $\theta_k = \arccos((r_s^2 + d_0^2 - x^2)/2r_s d_0)$, $\phi_k = \arccos((x^2 + d_0^2 - r_s^2)/2xd_0)$. Hence, the PDF of d_k is given by

$$
\begin{aligned}
f_{d_k}(x) &= \frac{1}{\pi r_s^2}\frac{\partial S}{\partial x} \\
&= \frac{x}{\pi r_s^2}\left(\frac{r_s/d_0}{\sqrt{1-\left(\left(d_0^2-x^2+r_s^2\right)^2/4d_0^2r_s^2\right)}}\right. \\
&\quad - \frac{\left((x/d_0)-\left(\left(d_0^2+x^2-r_s^2\right)/2d_0x\right)\right)}{\sqrt{1-\left(\left(d_0^2+x^2-r_s^2\right)^2/4d_0^2x^2\right)}} \\
&\quad - \frac{\left(d_0^2-x^2+r_s^2\right)/2d_0r_s}{\sqrt{1-\left(\left(d_0^2-x^2+r_s^2\right)^2/4d_0^2r_s^2\right)}} \\
&\quad \left. + 2\arccos\left(\frac{d_0^2+x^2-r_s^2}{2d_0x}\right)\right),
\end{aligned}
\tag{23}
$$

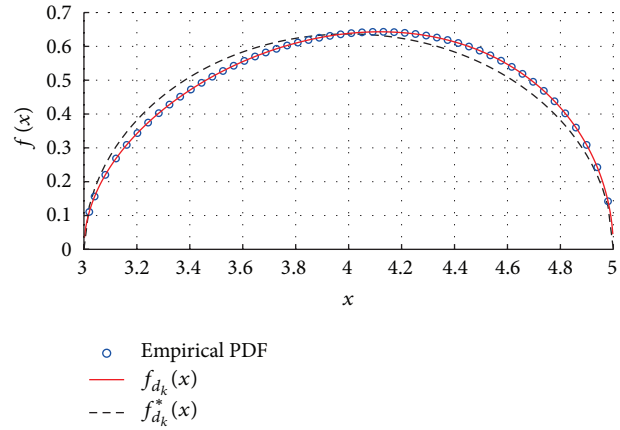

Figure 6: PDF of d_k and its approximations, when $r_s = 1$ and $d_0 = 4$.

where $\partial S/\partial d_k$ is the length of the arc $\overline{ABC}$ in Figure 5. However, this original PDF of d_k does not give the closed form expressions of its mean and variance.

5.2. Approximation of $f_{d_k}(x)$. For the lack of the closed form expressions of the two statistics, we propose an approximated PDF of d_k by using the chord $\overline{AB'C}$, which is indicated by the dotted straight line in Figure 5, instead of the arc $\overline{ABC}$. When d_0 is large enough compared to r_s in Figure 2 (i.e., the arc $\overline{ABC}$ and chord $\overline{AB'C}$ are almost the same), the original PDF of d_k, $f_{d_k}(x)$ can be simplified into

$$
f^*_{d_k}(x) = \frac{2}{\pi r_s^2}\sqrt{r_s^2-(d_0-x)^2}, \tag{24}
$$

where $d_0 - r_s \le x \le d_0 + r_s$.

As an example, in Figure 6, when $d_0 = 4$ and $r_s = 1$, the empirical PDF, obtained with 5×10^6 random samples, is indicated by the blue "o"-markers. Also, the original PDF $f_{d_k}(x)$ is represented by the black solid line, where $f^*_{d_k}(x)$ is indicated by the black dotted line. As shown in the figure, the empirical PDF is identical to $f_{d_k}(x)$ in (23), which verifies its derivation. Moreover, $f^*_{d_k}(x) \approx f_{d_k}(x)$ in the domain $d_0 - r_s \le x \le d_0 + r_s$, which confirms the validity of $f^*_{d_k}(x)$.

Moreover, this approximated PDF $f^*_{d_k}(x)$ has the mean and variance in closed forms as $\mathbb{E}\{d_k\} = d_0$ and $\mathbb{VAR}\{d_k\} = r_s^2/4$. Therefore, by the Taylor expansion, $\mathbb{E}\{\log_{10} d_k\} \approx \log_{10} d_0$ and $\mathbb{VAR}\{\log_{10} d_k\} \approx r_s^2/4(d_0 \ln 10)^2$. Therefore, we can obtain μ and σ^2 as

$$
\begin{aligned}
\mu &= 10\alpha \log_{10} d_0, \\
\sigma^2 &= \frac{25M}{(M+1)^2}\left(\frac{\alpha r_s}{d_0 \ln 10}\right)^2.
\end{aligned}
\tag{25}
$$

By plugging these two parameters with the average first-hop probability $p = \mathbb{E}\{p\}$ in (11) into (20), the outage rate $\tilde{P}_{\text{out}}$ in (20), which is approximated form of the real P_{out} in (8), can be obtained.

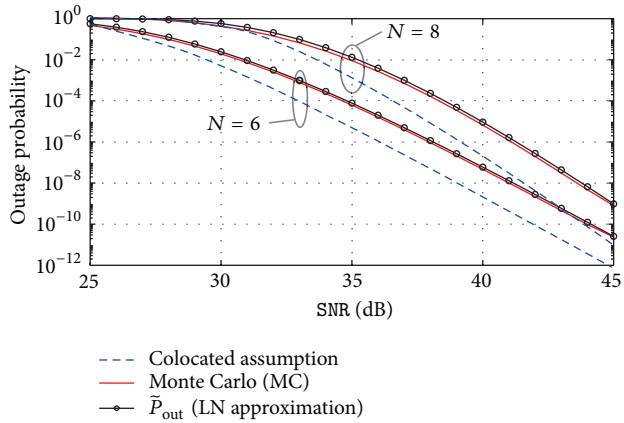

FIGURE 7: Outage curves, when $\mathtt{R} = 1$, $d_0 = 2$, $r_s = 1$, $\alpha = 4$, and $N = 6, 8$.

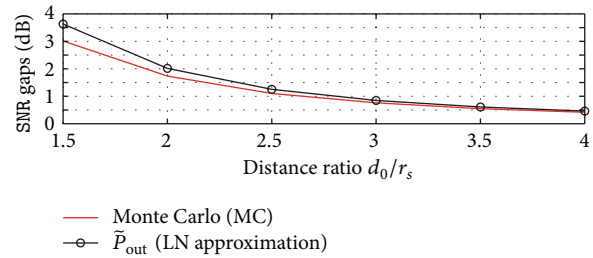

FIGURE 8: SNR gaps versus d_0/r_s, when $r_s = 1$, $\alpha = 4$, and $N = 6$.

6. Simulation Results

In this section, we first compare the outage probability curves of three cases: the real outage obtained by Monte Carlo simulation, the colocated assumption outage, and the proposed estimate based on the three-stage approximations in the previous sections. Then, we measure the error of the colocated assumption by calculating an SNR gap to achieve a certain outage rate 10^{-6}. Also, the SNR gap caused by the path-loss disparity is compared with the SNR gap calculated by the proposed outage rate approximation $\widetilde{P}_{\text{out}}$ in (20) by the log-normal distribution.

6.1. Outage Probability. Figure 7 shows the outage simulation results with $\mathtt{R} = 1$, $d_0 = 2$, $r_s = 1$, and $\alpha = 4$. In the figures, the horizontal axis is SNR in dB, while the vertical axis indicates the outage probability. There are two groups of the curves: the group having the higher outage rates with the steeper slopes corresponds to $N = 8$, while the lower group corresponds to $N = 6$. We note that the heights of the $N = 8$ group are greater than the other group with $N = 6$ because we assume orthogonal channel transmissions of the relays. If space-time block codes are used, the outage curves of the two groups are parallel, with a translation distance corresponding to the code rate, which can be readily calculated.

The blue dashed lines represent the outage rates based on the colocated assumption that ignores the path-loss disparity and first-hop errors. Also, the red solid curves are the true outage probabilities obtained by the Monte Carlo simulation (MC), while the solid line with the "o"-markers indicates the proposed outage approximation $\widetilde{P}_{\text{out}}$ by log-normal (LN) approximation.

Therefore, the gaps between the blue dashed lines and the red solid lines are the errors caused by the colocated assumption. For example, when the target outage rate is 10^{-6}, the errors are about 1.75 and 1.8 dB for $N = 6$ and 8, respectively. In other words, to achieve the outage probability of 10^{-6} considering the relay separations and the source-relay link errors, more transmission power (e.g., 1.75 and 1.8 dB for $N = 6$ and 8, resp.) is required than is indicated by the colocated assumption.

Moreover, in the both groups, the real outage curves obtained by Monte Carlo simulation are very close to $\widetilde{P}_{\text{out}}$ in the high SNR regime (when the outage is less than 10^{-4}), which implies the proposed approximation $\widetilde{P}_{\text{out}}$ has good accuracy. Therefore, the SNR penalty of the colocated assumption (i.e., the error in terms of SNR to achieve the target outage rate) can be estimated by $\widetilde{P}_{\text{out}}$ that characterizes the impact of the path-loss disparity by the equivalent log-normal shadowing model, following the conventional notion of the composite channel.

6.2. SNR Penalty Depending on System Parameters. In this section, we look at the error of the colocated assumption in terms of the SNR penalty or gap to achieve the outage probability of 10^{-6} depending on three system parameters: the distance ratio d_0/r_s, the path-loss exponent α, and the number of relays N. In the simulation results shown in Figures 8, 9, and 10, there are two SNR gaps to the colocated assumption: the real error based on MC (the red solid lines) and the estimated errors by $\widetilde{P}_{\text{out}}$ with the log-normal (LN) approximation (the black curve with the "o"-markers, resp.). In the three figures, the real error is much closer to the error based on $\widetilde{P}_{\text{out}}$, compared to the upper and lower bounds in the conference paper version of this paper [31].

Figure 8 shows the SNR penalty in dB indicated by the y-axis for the different distance ratio d_0/r_s represented by the x-axis, when $r_s = 1$, $\alpha = 4$, and $N = 6$. The two SNR gaps decrease as d_0/r_s increases, because the impact of the path-loss disparity becomes negligible for high d_0/r_s, which is also noticed by that the two variances σ^2 and σ_l^2 of the equivalent log-normal shadowing model are decreasing functions of d_0/r_s. Also, the first-hop error ignored in the colocated assumption is relatively much smaller than the second-hop error, when d_0/r_s is large. However, considering that $d_0/r_s = 1.5$ and 2 are the CT range extension ratios widely assumed in the VMISO-based protocol studies, the corresponding SNR gaps are large enough to degrade the protocols designed and operated with the colocated assumption. Moreover, if comparing the two SNR gap curves, the proposed approximation $\widetilde{P}_{\text{out}}$ curve grows closer to the MC curve as d_0/r_s increases, because the quality of the log-normal approximation becomes more accurate as shown in Section 4.3.

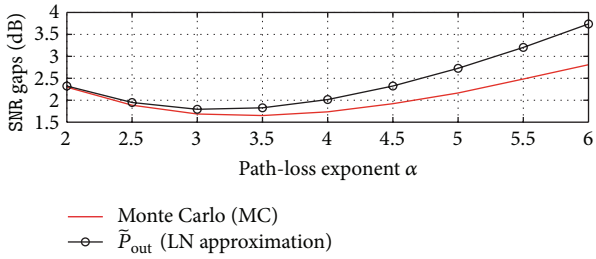

FIGURE 9: SNR gaps versus α, when $r_s = 1$, $d_0 = 2$, and $N = 6$.

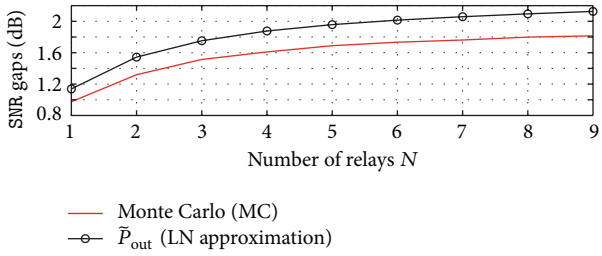

FIGURE 10: SNR gaps versus N, when $r_s = 1$, $d_0 = 2$, and $\alpha = 4$.

Figure 9 displays the impact of the path-loss exponent α on the SNR penalty, when $r_s = 1$, $d_0 = 2$, and $N = 6$. The two SNR gaps based on the MC and the LN approximation ($\widetilde{P}_{\text{out}}$) have the convex curves that have the minimum heights at around $\alpha = 3.5$. The height decreases in the two curves for $2 \leq \alpha \leq 3.5$ are because the first-hop error relative to the second-hop error increases as α decreases for a fixed d_0/r_s, which means that the first-hop error cannot be ignored in this range. On the other hand, when $3.5 \leq \alpha \leq 6$, both curves increase, as α increases, because the path-loss disparity within the VMISO cluster becomes significant (σ^2 and σ_l^2 are increasing functions of α). Also, the height difference between the two curves increases as α increases. By testing first-hop error-free case $M = N$, we conclude that it is because the first-hop error, which is approximated by i.i.d. Bernoulli trials in Section 3.1, is overestimated. In other words, when α is large, the first-hop error relative to the second-hop error in the real outage (MC) is much smaller than the Bernoulli approximation, since $d_{0,k}^{\alpha} \ll d_{k,N+1}^{\alpha}$.

The last figure, Figure 10, shows the impact of the number of relays on the SNR gap, when $r_s = 1$, $d_0 = 2$, and $\alpha = 4$. As shown in the figure, the SNR gap increases as N increases, because the path-loss disparity ignored in colocated approximation increases. Moreover, the height difference between the MC and the LN approximation is caused by the log-normal approximation error with the small $d_0/r_s = 2$ as discussed in Section 4.3. As shown in Figure 8, for $d_0/r_s > 2$, the gap between the two curves is smaller.

7. Conclusion

Motivated by the limited accuracy of the colocated assumption, which ignores the path-loss disparity in VMISO link, we analyze the impact of the path-loss disparity on the outage probability. Simulation results show that the SNR penalty (i.e., error) up to 3 dB should be considered, when the physically separated relays are assumed to be colocated. We investigate how the error changes depending on the system parameters such as d_0/r_s, α, and N. Moreover, by the asymptotic analysis ($\mathtt{SNR} \to \infty$) of the outage capacity, we show that the performance loss by the path-loss disparity has the same model as log-normal shadowing. The proposed outage approximation $\widetilde{P}_{\text{out}}$ is accurate enough to estimate the SNR gap (or the error of the colocated assumption) caused by the first-hop error and the path-loss disparity. Therefore, higher-layer protocol design and analysis with large-scale CT networks can be facilitated by the proposed approximation.

Appendix

Based on the asymptotic outage behavior in the high SNR regime, we propose the *limit matching* method that extracts the single parameter λ by matching the limiting conditional outage rates of two distributions (13) and (14) as follows. First, when $\mathtt{SNR} \to \infty$, the conditional CDF $F_{Y|M,\overline{\mathbf{\Lambda}}_{d(1:M)}}(y)$ in (13) satisfies that

$$\lim_{\mathtt{SNR}\to\infty} \frac{F_{Y|M,\overline{\mathbf{\Lambda}}_{d(1:M)}}\left(g\left(\mathtt{SNR},\mathtt{R}\right)\right)}{\left(g(\mathtt{SNR},\mathtt{R})\right)^{M+1}} = \frac{\prod_{k=0}^{M}\lambda_k}{(M+1)!}. \tag{A.1}$$

On the other hand, the limiting $F_{Y|M,\lambda}(y)$ for the gamma distribution in (14) is given by

$$\lim_{\mathtt{SNR}\to\infty} \frac{F_{Y|M,\lambda}\left(g\left(\mathtt{SNR},\mathtt{R}\right)\right)}{\left(g(\mathtt{SNR},\mathtt{R})\right)^{M+1}} = \frac{\lambda^{M+1}}{(M+1)!}. \tag{A.2}$$

Thus, if we match two limits (A.1) and (A.2), then we have

$$\frac{\prod_{k=0}^{M}\lambda_k}{(M+1)!} \approx \frac{\lambda^{M+1}}{(M+1)!}, \tag{A.3}$$

which gives the projection equation in (16).

Disclosure

The material in this paper is presented in part at the International Conference on Communications (ICC), June 2013, Budapest, Hungary.

Conflict of Interests

The authors declare that there is no conflict of interests regarding the publication of this paper.

Acknowledgment

The authors gratefully acknowledge partial support for this research from the National Science Foundation, Grant no. CNS-1017984.

References

[1] A. Sendonaris, E. Erkip, and B. Aazhang, "User cooperation diversity-part I: system description," *IEEE Transactions on Communications*, vol. 51, no. 11, pp. 1927–1938, 2003.

[2] J. N. Laneman, D. N. C. Tse, and G. Wornell, "Cooperative diversity in wireless networks: efficient protocols and outage behavior," *IEEE Transactions on Information Theory*, vol. 50, no. 12, pp. 3062–3080, 2004.

[3] A. Scaglione and Y.-W. Hong, "Opportunistic large arrays: cooperative transmission in wireless multihop ad hoc networks to reach far distances," *IEEE Transactions on Signal Processing*, vol. 51, no. 8, pp. 2082–2092, 2003.

[4] B. Sirkeci-Mergen, A. Scaglione, and G. Mergen, "Asymptotic analysis of multistage cooperative broadcast in wireless networks," *IEEE Transactions on Information Theory*, vol. 52, no. 6, pp. 2531–2550, 2006.

[5] L. V. Thanayankizil, A. Kailas, and M. A. Ingram, "Routing protocols for wireless sensor networks that have an opportunistic large array (OLA) physical layer," *Ad-Hoc and Sensor Wireless Networks*, vol. 8, no. 1-2, pp. 79–117, 2009.

[6] A. Kailas and M. A. Ingram, "Alternating opportunistic large arrays in broadcasting for network lifetime extension," *IEEE Transactions on Wireless Communications*, vol. 8, no. 6, pp. 2831–2835, 2009.

[7] H. Jung and M. A. Weitnauer, "Multi-packet interference in opportunistic large array broadcasts over disk networks," *IEEE Transactions on Wireless Communications*, vol. 12, no. 11, pp. 5631–5645, 2013.

[8] H. Jung and M. Weitnauer, "Multi-packet opportunistic large array transmission on strip-shaped cooperative routes or networks," *IEEE Transactions on Wireless Communications*, vol. 13, no. 1, pp. 144–158, 2014.

[9] T. R. Halford, K. M. Chugg, and A. Polydoros, "Barrage relay networks: System and protocol design," in *Proceedings of the IEEE 21st International Symposium on Personal Indoor and Mobile Radio Communications (PIMRC '10)*, pp. 1133–1138, September 2010.

[10] Z. Zhou, S. Zhou, S. Cui, and J. Cui, "Energy-efficient cooperative communication in a clustered wireless sensor network," *IEEE Transactions on Vehicular Technology*, vol. 57, no. 6, pp. 3618–3628, 2008.

[11] G. Jakllari, S. V. Krishnamurthy, M. Faloutsos, and P. V. Krishnamurthy, "On broadcasting with cooperative diversity in multi-hop wireless networks," *IEEE Journal on Selected Areas in Communications*, vol. 25, no. 2, pp. 484–496, 2007.

[12] G. Jakllari, S. V. Krishnamurthy, M. Faloutsos, P. V. Krishnamurthy, and O. Ercetin, "A cross-layer framework for exploiting virtual MISO links in mobile ad hoc networks," *IEEE Transactions on Mobile Computing*, vol. 6, no. 6, pp. 579–594, 2007.

[13] S. Lakshmanan and R. Sivakumar, "Diversity routing for multihop wireless networks with cooperative transmissions," in *Proceedings of the 6th Annual IEEE Communications Society Conference on Sensor, Mesh and Ad Hoc Communications and Networks (SECON '09)*, pp. 1–9, June 2009.

[14] J. W. Jung and M. A. Ingram, "Residual-energy-activated cooperative transmission (REACT) to avoid the energy hole," in *Proceedings of the IEEE International Conference on Communications Workshops (ICC '10)*, May 2010.

[15] J. Lin and M. A. Ingram, "SCT-MAC: a scheduling duty cycle MAC protocol for cooperative wireless sensor network," in *Proceedings of the IEEE International Conference on Communications (ICC '12)*, pp. 345–349, IEEE, Ottawa, Canada, June 2012.

[16] A. Aksu and O. Ercetin, "Reliable multi-hop routing with cooperative transmissions in energy-constrained networks," *IEEE Transactions on Wireless Communications*, vol. 7, no. 8, pp. 2861–2865, 2008.

[17] A. Scaglione, D. L. Goeckel, and J. N. Laneman, "Cooperative communications in mobile ad hoc networks," *IEEE Signal Processing Magazine*, vol. 23, no. 5, pp. 18–29, 2006.

[18] B. Bash, D. Goeckel, and D. Towsley, "Clustering in cooperative networks," in *Proceedings of the IEEE INFOCOM*, pp. 486–490, April 2011.

[19] N. C. Beaulieu and J. Hu, "A closed-form expression for the outage probability of decode-and-forward relaying in dissimilar Rayleigh fading channels," *IEEE Communications Letters*, vol. 10, no. 12, pp. 813–815, 2006.

[20] J. N. Laneman, "Limiting analysis of outage probabilities for diversity schemes in fading channels," in *Proceedings of the IEEE Global Telecommunications Conference (GLOBECOM '03)*, pp. 1242–1246, December 2003.

[21] S. Cho, W. Choi, and K. Huang, "QoS provisioning relay selection in random relay networks," *IEEE Transactions on Vehicular Technology*, vol. 60, no. 6, pp. 2680–2689, 2011.

[22] H. Wang, S. Ma, and T. Ng, "On performance of cooperative communication systems with spatial random relays," *IEEE Transactions on Communications*, vol. 59, no. 4, pp. 1190–1199, 2011.

[23] C. Zhai, W. Zhang, and G. Mao, "Uncoordinated cooperative communications with spatially random relays," *IEEE Transactions on Wireless Communications*, vol. 11, no. 9, pp. 3126–3135, 2012.

[24] V. Aalo, G. Efthymoglou, T. Soithong, M. Alwakeel, and S. Alwakeel, "Performance analysis of multi-hop amplify-and-forward relaying systems in rayleigh fading channels with a poisson interference field," *IEEE Transactions on Wireless Communications*, vol. 13, no. 1, pp. 24–35, 2014.

[25] V. Aalo, K. Peppas, G. Efthymoglou, M. Alwakeel, and S. Alwakeel, "Serial amplify-and-forward relay transmission systems in nakagami-m fading channels with a poisson interference field," *IEEE Transactions on Vehicular Technology*, no. 99, p. 1, 2013.

[26] H. Wang, S. Ma, T. Ng, and H. V. Poor, "A general analytical approach for opportunistic cooperative systems with spatially random relays," *IEEE Transactions on Wireless Communications*, vol. 10, no. 12, pp. 4122–4129, 2011.

[27] T. K. Y. Lo, "Maximum ratio transmission," *Proceedings of the IEEE International Conference on Communications (ICC '99)*, vol. 2, pp. 1310–1314, 1999.

[28] M.-K. Oh, X. Ma, G. Giannakis, and D.-J. Park, "Cooperative synchronization and channel estimation in wireless sensor networks," in *Proceedings of the Conference Record of the 37th Asilomar Conference on Signals, Systems and Computers (ASILOMAR '03)*, vol. 1, pp. 238–242, November 2003.

[29] G. Barriac, R. Mudumbai, and U. Madhow, "Distributed beamforming for information transfer in sensor networks," in *Proceedings of the 3rd International Symposium on Information Processing in Sensor Networks (IPSN '04)*, pp. 81–88, April 2004.

[30] R. Mudumbai, G. Barriac, and U. Madhow, "On the feasibility of distributed beamforming in wireless networks," *IEEE Transactions on Wireless Communications*, vol. 6, no. 5, pp. 1754–1763, 2007.

[31] H. Jung and M. A. Weitnauer, "SNR penalty from the path-loss disparity in virtual multiple-input-single-output (VMISO) link," in *Proceedings of the IEEE International Conference on Communications (ICC '13)*, pp. 5350–5354, June 2013.

[32] H. Jung, Y. J. Chang, and M. A. Ingram, "Experimental range extension of concurrent cooperative transmission in indoor environments at 2.4 GHz," in *Proceedings of the 2010 IEEE Military Communications Conference (MILCOM '10)*, pp. 148–153, November 2010.

[33] M. Abramowitz and I. Stegun, *Handbook of Mathematical Functions with Formulas, Graphs, and Mathematical Tables*, vol. 55, Dover, 1964.

[34] W. Choi and J. G. Andrews, "Downlink performance and capacity of distributed antenna systems in a multicell environment," *IEEE Transactions on Wireless Communications*, vol. 6, no. 1, pp. 69–73, 2007.

[35] S. M. Ross, *Introduction to Probability Models*, 2000.

[36] M. Abramowitz and I. A. Stegun, *Handbook of Mathematical Functions 10th Printing with Corrections*, Dover, New York, NY, USA, 1972.

[37] R. B. D'Agostino and M. A. Stephens, *Goodness-of-Fit Techniques*, vol. 68 of *Statistics: Textbooks and Monographs*, CRC Press, New York, NY, USA, 1986.

[38] E. Reusens, W. Joseph, B. Latré et al., "Characterization of on-body communication channel and energy efficient topology design for wireless body area networks," *IEEE Transactions on Information Technology in Biomedicine*, vol. 13, no. 6, pp. 933–945, 2009.

[39] M. L. Sichitiu and V. Ramadurai, "Localization of wireless sensor networks with a mobile beacon," in *Proceedings of the IEEE International Conference on Mobile Ad-Hoc and Sensor Systems*, pp. 174–183, October 2004.

[40] M. Heidari, F. Akgul, and K. Pahlavan, "Identification of the absence of direct path in indoor localization systems," in *Proceedings of the IEEE 18th International Symposium on Personal, Indoor and Mobile Radio Communications (PIMRC '07)*, pp. 1–6, Athens, Greece, September 2007.

[41] N. M. Razali and Y. B. Wah, "Power comparisons of shapiro-wilk, kolmogorov-smirnov, lilliefors and anderson-darling tests," *Journal of Statistical Modeling and Analytics*, vol. 2, no. 1, pp. 21–33, 2011.

Hindawi Publishing Corporation
International Journal of Antennas and Propagation
Volume 2014, Article ID 258308, 5 pages
http://dx.doi.org/10.1155/2014/258308

Review Article

Advances in the Statistical Characterization of Fading: From 2005 to Present

José F. Paris

Departamento Ingeniería de Comunicaciones, Universidad de Málaga, 29071 Málaga, Spain

Correspondence should be addressed to José F. Paris; paris@ic.uma.es

Received 9 May 2014; Accepted 23 June 2014; Published 10 July 2014

Academic Editor: Paschalis Sofotasios

Copyright © 2014 José F. Paris. This is an open access article distributed under the Creative Commons Attribution License, which permits unrestricted use, distribution, and reproduction in any medium, provided the original work is properly cited.

This review paper presents some of the most significant advances in statistical characterization of wireless communication fading. We will focus on the fundamental statistical characterizations of the fading distributions in terms of the probability density function (PDF), the cumulative density function (CDF), and the moment generating function (MGF). The period from 2005 to present will be considered in order to complement the information which can be found in the specialized literature like Simon and Alouini's book on digital communications over fading channels. We present both the advances on classical fading models and a brief summary of some selected new fading models. Some open problems in the field will be also stated.

1. Introduction

Fading is an important peculiarity of wireless communication channels. Statistical characterization of fading is a key aspect for the analysis and simulation of wireless communication systems. In the last years, there has been a huge amount of research work on statistical characterization of wireless communication fading. The most comprehensive account of this research topic is Simon and Alouini's book on digital communications over fading channels [1]. This book presents the statistical characterization of the most popular fading models by 2005.

In this review paper, in order to complement the information available in [1], a selection of the new results on fading statistics in the period from 2005 to present will be considered. Only single-input single-output (SISO) flat fading channels are considered; for an introduction to multiple-input multiple-output (MIMO) fading channels the reader should consider [2, 3]. We will focus on the fundamental statistical characterizations of the fading distributions in terms of the probability density function (PDF), the cumulative density function (CDF), and the moment generating function (MGF). We will also pay special attention to the exact closed-form results concerning the PDF, CDF, and MGF of the fading distributions. The advances on classical fading models and some results on new fading models will be presented. Along the paper, some open problems on fading statistics will be stated.

The remainder of this paper is organized as follows. In Section 2 the precise mathematical definitions of the fundamental statistics are provided. The advances concerning the classical fading distributions are presented in Section 3 and some selected results on new fading models are presented in Section 4. Finally, some conclusions are given in Section 5.

2. Statistical Preliminaries

Let us denote R which is the envelope of the fading channel. In this review paper we will focus on the fundamental statistics of the instantaneous signal-to-noise ratio (SNR) γ. Let $E[\cdot]$ be the expectation operator. The instantaneous SNR can be expressed in terms of the channel envelope R and the average SNR $\overline{\gamma} \triangleq E[\gamma]$:

$$\gamma = \frac{R^2}{E\left[R^2\right]}\overline{\gamma}. \tag{1}$$

The CDF of the instantaneous SNR γ can be obtained from the PDF $f_\gamma(\gamma)$ as follows:

$$F_\gamma\left(\gamma\right) = \int_0^\gamma f_\gamma\left(\xi\right) d\xi, \tag{2}$$

while the MGF is computed as

$$\mathcal{M}_{\gamma}(s) = E\left[e^{s\gamma}\right] = \int_{0}^{\infty} f_{\gamma}(\xi)\, e^{s\xi} d\xi. \tag{3}$$

Note that the definition of the MGF given in (3) differs from the unilateral Laplace transform definition in the sign of the variable s.

From a pure statistical point of view, the three characterizations of the instantaneous SNR γ (the PDF, the CDF, and the MGF) are equivalent; however, from the point of view of the performance analysis of fading channels, the MGF and the CDF play an important role in the computation of key performance metrics such as error probability, outage probability, or outage capacity [1].

3. Advances on Classical Fading Models

In this section we will consider as classical fading models the following: Rayleigh, Nakagami-q (Hoyt), Nakagami-n (Rice), Nakagami-m, Weibull, Beckmann, Lognormal, K, and Rician shadowed. All these fading models are well described in [1].

The PDF, CDF, and MGF of the Rayleigh, Nakagami-m, Nakagami-n (Rice), and Weibull distributions are expressed in closed-form, and the corresponding expressions are found in [1].

Only the PDF and MGF of the Nakagami-q (Hoyt) distribution are given in [1]. A closed-form expression for its CDF was derived in 2009 [4, 5]:

$$\begin{aligned} F_{\gamma}(\gamma) &= Q\left(u(q)\sqrt{\frac{\gamma}{\overline{\gamma}}}, v(q)\sqrt{\frac{\gamma}{\overline{\gamma}}}\right) \\ &\quad - Q\left(v(q)\sqrt{\frac{\gamma}{\overline{\gamma}}}, u(q)\sqrt{\frac{\gamma}{\overline{\gamma}}}\right), \quad \gamma \geq 0, \end{aligned} \tag{4}$$

where $\overline{\gamma} \triangleq E[\gamma]$, q is the Hoyt shape parameter, $u(q) \doteq (\sqrt{1-q^4}/2q)\sqrt{(1+q)/(1-q)}$, $v(q) \doteq (\sqrt{1-q^4}/2q)\sqrt{(1-q)/(1+q)}$, and $Q(\cdot)$ is the Marcum Q function [1].

Interestingly, the Beckmann fading distribution includes the Rayleigh, Nakagami-q (Hoyt), Nakagami-n (Rice), and Nakagami-m distributions as particular cases by a suitable combination of its parameters. Its MGF is expressed in elementary terms [1], but closed-form expressions for both its PDF and its CDF in terms of classical or well-studied special functions are challenging open problems.

Beyond channel modeling, the Lognormal distribution is widely used; its PDF and CDF are easily expressed in closed-form; however, no closed-form expression is known for its MGF. A recent paper on this particular problem which derives an approximate expression is [6].

The PDF and MGF of the K distribution are expressed in closed-form in [1]. Its CDF was derived in closed-form in 2006 [7]:

$$\begin{aligned} F_{\gamma}(\gamma) &= \pi \csc(\pi(\nu-1)) \\ &\quad \times \left[\frac{(\nu\gamma/\overline{\gamma})\ {}_1F_2\left(1; 2-\nu, 2; \nu\left(\gamma/\overline{\gamma}\right)\right)}{\Gamma(\nu)\,\Gamma(2-\nu)}\right. \\ &\quad \left. - \frac{(\nu\gamma/\overline{\gamma})^{\nu}\ {}_1F_2\left(\nu; \nu, 1+\nu; \nu\left(\gamma/\overline{\gamma}\right)\right)}{\Gamma(\nu)\,\Gamma(1+\nu)}\right], \end{aligned} \tag{5}$$

where $\overline{\gamma} \triangleq E[\gamma]$, ν is the distribution shaping parameter, $\Gamma(\cdot)$ is the gamma function, and ${}_pF_q(\cdot)$ is the generalized hypergeometric function [8].

As in the previous model, the PDF and MGF of the Rician shadowed distribution are expressed in closed-form in [1]. Its CDF was derived in closed-form in 2010 [9]:

$$\begin{aligned} F_{\gamma}(\gamma) &= \frac{m^m (1+K)}{(m+K)^m} \frac{\gamma}{\overline{\gamma}} \\ &\quad \times \Phi_2\left(1-m, m; 2; -\frac{1+K}{\overline{\gamma}}\gamma, -\frac{1+K}{\overline{\gamma}}\frac{m\gamma}{K+m}\right), \end{aligned} \tag{6}$$

where $\overline{\gamma} \triangleq E[\gamma]$, K is the classical Rice parameter, m is the parameter corresponding to the line-of-sight (LOS) fluctuations, and $\Phi_2(\cdot)$ is the bivariate confluent hypergeometric function [8].

4. New Fading Models

In this section the author has selected five new fading models which are not listed in [1]. The models presented in this section do not exhaust the list of new fading models recently proposed and not included in [1].

4.1. The η-μ Fading Model. This model was first proposed by Yacoub in 2000 [10] and later enhanced in [11]. From a physical point of view, this model corresponds to a non-line-of-sight (NLOS) scenario where different clusters of multipath waves can propagate simultaneously. The PDF of the η-μ distribution in format 1 (see [11] for the details) is given by

$$\begin{aligned} f_{\gamma}(\gamma) &= \frac{2\sqrt{\pi}\mu^{\mu+1/2}h^{\mu}}{\overline{\gamma}\Gamma(\mu)H^{\mu-1/2}}\left(\frac{\gamma}{\overline{\gamma}}\right)^{\mu-1/2} \\ &\quad \times \exp\left(-\frac{2\mu h\gamma}{\overline{\gamma}}\right) I_{\mu-1/2}\left(\frac{2\mu H\gamma}{\overline{\gamma}}\right), \\ h &\triangleq \frac{2+\eta^{-1}+\eta}{4}, \\ H &\triangleq \frac{\eta^{-1}-\eta}{4}, \end{aligned} \tag{7}$$

where $\overline{\gamma} \triangleq E[\gamma]$, $I_p(\cdot)$ is the modified Bessel function of the first kind [8], η is a positive real number representing

the scattered-wave power ratio between the in-phase and quadrature components of each cluster of multipath, and μ is a positive real number representing the effective number of propagation clusters. This model contains the Rayleigh, Nakagami-q (Hoyt), and Nakagami-m models as particular cases by a suitable combination of the parameters η and μ. In [11] a physical model was given for the η-μ model when μ is a natural number; this model is useful for simulation of η-μ random variables since these can be expressed in terms of Gaussian random variables. The MGF corresponding to the PDF given in (7) was expressed in elementary terms in 2008 [12]:

$$\mathscr{M}_{\gamma}(s) = \left(\frac{4\mu^2 h}{\left(2(h-H)\mu + s\overline{\gamma}\right)\left(2(h+H)\mu + s\overline{\gamma}\right)} \right)^{\mu}. \quad (8)$$

In 2010, an exact closed-form expression for the CDF of the η-μ distribution was derived in terms of the bivariate confluent function [13]:

$$F_{\gamma}(\gamma) = \frac{\left(1-(H/h)^2\right)^{\mu}}{\Gamma(1+2\mu)} \left(\frac{2h\mu\gamma}{\overline{\gamma}}\right)^{2\mu} \times \Phi_2\left(\mu, \mu; 1+2\mu; -\left(1+\frac{H}{h}\right)\frac{2h\mu\gamma}{\overline{\gamma}}, -\left(1-\frac{H}{h}\right)\frac{2h\mu\gamma}{\overline{\gamma}}\right). \quad (9)$$

Expressions (7), (8), and (9) complete the fundamental characterization of the η-μ fading model by closed-form expressions.

4.2. The κ-μ Fading Model. This model was also proposed by Yacoub in 2000 [14] and later enhanced in [11]. From a physical point of view, this model corresponds to a line-of-sight (LOS) scenario where different clusters of multipath waves can propagate simultaneously. The PDF of the κ-μ distribution is given by

$$f_{\gamma}(\gamma) = \frac{\mu(1+\kappa)^{(\mu+1)/2}}{\kappa^{(\mu-1)/2}\overline{\gamma}\exp(\mu\kappa)} \left(\frac{\gamma}{\overline{\gamma}}\right)^{(\mu-1)/2} \times \exp\left(-\frac{\mu(1+\kappa)\gamma}{\overline{\gamma}}\right) I_{\mu-1}\left(2\mu\sqrt{\frac{\kappa(1+\kappa)\gamma}{\overline{\gamma}}}\right), \quad (10)$$

where $\overline{\gamma} \triangleq E[\gamma]$, κ is a real positive number representing the power ratio between dominant and scattered-wave components, and μ is a positive real number representing the effective number of propagation clusters. This model contains the Rayleigh, Nakagami-n (Rice), and Nakagami-m models as particular cases by a suitable combination of the parameters κ and μ. In [11] a physical model was also given for the κ-μ model when μ is a natural number; this model is useful for simulation of κ-μ random variables since these can be expressed in terms of Gaussian random variables. The CDF of the κ-μ distribution was directly given in [11] in terms of the generalized Marcum Q function [1]:

$$F_{\gamma}(\gamma) = 1 - Q_{\mu}\left(\sqrt{2\kappa\mu}, \sqrt{2(1+\kappa)\mu\frac{\gamma}{\overline{\gamma}}}\right), \quad (11)$$

while the MGF was expressed in exact closed-form in 2008 [12]:

$$\mathscr{M}_{\gamma}(s) = \left(\frac{\mu(1+\kappa)}{\mu(1+\kappa)+s\overline{\gamma}}\right)^{\mu} \exp\left(\frac{\mu^2\kappa(1+\kappa)}{\mu(1+\kappa)+s\overline{\gamma}} - \mu\kappa\right). \quad (12)$$

Therefore, expressions (10), (11), and (12) provide a complete set of alternative characterizations for the κ-μ fading model.

4.3. The α-μ Fading Model. Again, this model was proposed by Yacoub in 2002 [15] and improved in 2007 [16]. From a physical point of view, this model is appropriate to consider nonlinear propagation phenomena. In fact, the α-μ distribution is a rewritten form of the Stacy (generalized gamma) distribution. Defining $\Omega_{\alpha} = E[R^{\alpha}]$, the PDF of $\gamma = (R^2/\Omega_2)\,\overline{\gamma}$ in this model is given by

$$f_{\gamma}(\gamma) = \frac{\alpha\mu^{\mu}\gamma^{(\alpha\mu/2)-1}}{2\Gamma(\mu)\widetilde{\gamma}^{\alpha\mu/2}} \exp\left(-\mu\left(\frac{\gamma}{\widetilde{\gamma}}\right)^{\alpha/2}\right), \quad (13)$$

where $\overline{\gamma} \triangleq E[\gamma]$ and $\widetilde{\gamma} \triangleq (\Omega_{\alpha}^{2/\alpha}/\Omega_2)\overline{\gamma}$; otherwise, α and μ are shaping parameters. The CDF of the α-μ fading model is expressed as

$$F_{\gamma}(\gamma) = \frac{\Gamma\left(\mu, \mu(\gamma/\overline{\gamma})^{\alpha/2}\right)}{\Gamma(\mu)}, \quad (14)$$

where $\Gamma(\cdot,\cdot)$ is the incomplete gamma function [8]. The MGF of this distribution was derived in exact closed-form in 2009 (see [17]) by the Meijer G function [8]:

$$\mathscr{M}_{\gamma}(s) = \frac{\alpha\mu^{\mu}}{2\Gamma(\mu)\widetilde{\gamma}^{\alpha\mu/2}} \frac{k^{1/2}l^{(\alpha\mu-1)/2}}{(2\pi)^{(l+k-2)/2}s^{\alpha\mu/2}} \times G_{l,k}^{k,l}\left(\left(\frac{\mu}{\widetilde{\gamma}^{\alpha/2}}\right)^{k}\frac{l^l}{s^l k^k} \mid \frac{i(l, 1-\alpha\mu/2)}{i(k,0)}\right), \quad (15)$$

where $i(n,\xi) = \xi/n, (\xi+1)/n, \ldots, (\xi+n-1)/n$ and $\alpha/2 = l/k$ such that $\gcd(l,k) = 1$ (great common divisor) in order to include noninteger values of α. As happens with the two previous models, the PDF, CDF, and MGF of the α-μ distribution are known in exact closed-form by expressions (13), (14), and (15).

4.4. The $\mathscr{G}$ Fading Model. The $\mathscr{G}$ distribution was first proposed by Frery et al. [18], in the context of synthetic aperture radar (SAR) image modeling. In 2008 Laourine et al. proposed the application of this model to wireless fading channels [19]. The $\mathscr{G}$ distribution can be seen as a composite

Nakagami-m-inverse Gaussian distribution. The PDF of the $\mathcal{G}$ distribution is expressed in closed-form as [19]

$$f_\gamma(\gamma) = A\frac{\gamma^{m-1}}{\left(\sqrt{\alpha+\beta\gamma}\right)^{m+1/2}}K_{m+1/2}\left(b\sqrt{\alpha+\beta\gamma}\right),$$
$$A \triangleq \frac{(\lambda\overline{\gamma})^{(1+2m)/4}}{\Gamma(m)}\sqrt{\frac{2\lambda}{\pi\theta}}\exp\left(\frac{\lambda}{\theta}\right)\left(\frac{m}{\overline{\gamma}}\right)^m, \quad (16)$$
$$b \triangleq \frac{1}{\theta}\sqrt{\frac{\lambda}{\overline{\gamma}}},$$
$$\alpha \triangleq \lambda\overline{\gamma}, \qquad \beta \triangleq 2m\theta,$$

where $\overline{\gamma} \triangleq E[\gamma]$, $K_p(\cdot)$ is the modified Bessel function of the second kind [8], the parameter m comes from the underlying Nakagami-m distribution, and the parameters λ and θ correspond to the parameters of the underlying inverse Gaussian distribution. The CDF was also derived in [19]:

$$F_\gamma(\gamma) = 1 - A\Gamma(m) \times \sum_{k=1}^{m}\frac{2^k\gamma^{m-k}}{(\beta b)^k(m-k)!}\frac{K_{m-k+1/2}\left(b\sqrt{\alpha+\beta\gamma}\right)}{\left(\sqrt{\alpha+\beta\gamma}\right)^{m-k+1/2}}, \quad (17)$$

where m is restricted to be a natural number. Otherwise, the MGF is given by [19]

$$\mathcal{M}_\gamma(s) = 1 + m\sum_{k=1}^{m-1}\frac{(-1)^{k+1}C_{m-1}^k}{(k+1)!} \times \sum_{p=0}^{k}C_k^p\left(2\sqrt{\frac{\alpha s}{\beta}}\right)^{k+1-p}\Gamma(k+p+1) \times H_{-(k+p+1)}\left(\frac{b}{2}\sqrt{\frac{\beta}{s}}+\sqrt{\frac{s\alpha}{\beta}}\right), \quad (18)$$

where C_p^k is the binomial coefficient and $H_p(\cdot)$ is the Hermite function [8]. To the best knowledge of the author, finding exact closed-form expressions for the CDF and MGF of the $\mathcal{G}$ distribution, for arbitrary values of m, is an open problem.

4.5. The κ-μ Shadowed Fading Model. This model has been proposed by the author in 2014 [20]. It is a generalization of both the Rician shadowed model and the κ-μ model. The PDF of the κ-μ shadowed distribution is given by

$$f_\gamma(\gamma) = \frac{\mu^\mu m^m(1+\kappa)^\mu}{\Gamma(\mu)(m+\mu\kappa)^m\overline{\gamma}}\left(\frac{\gamma}{\overline{\gamma}}\right)^{\mu-1} \times e^{-\mu(1+\kappa)\gamma/\overline{\gamma}}{}_1F_1\left(m,\mu;\frac{\mu^2\kappa(1+\kappa)}{\mu\kappa+m}\frac{\gamma}{\overline{\gamma}}\right), \quad (19)$$

where $\overline{\gamma} \triangleq E[\gamma]$, ${}_1F_1(\cdot)$ is the confluent hypergeometric function [8], κ is a real positive number representing the power ratio between dominant and scattered-wave components, μ is a positive real number representing the effective number of propagation clusters, and m is a parameter associated with the LOS fluctuation. This model contains the Rician shadowed when $\mu = 1$ and the κ-μ when $m \to \infty$. In [20] a physical model was also given for the κ-μ shadowed model when μ is a natural number; this model is useful for simulation of κ-μ shadowed random variables since these can be expressed in terms of Gaussian and gamma random variables.

The shaping parameters of this distribution have a clear influence on the amount of fading (AoF) of γ [1]. In absence of LOS fluctuation ($m \to \infty$) the AoF is due to multipath and depends on κ and μ as follows [11]:

$$\mathrm{AoF}[\gamma] = \frac{V[\gamma]}{E[\gamma]^2} = \frac{1}{\mu}\frac{1+2\kappa}{(1+\kappa)^2}, \quad (20)$$

where $V[\cdot]$ is the variance operator. Note that the AoF in (20) is inversely proportional to μ. Otherwise, the AoF of the LOS component is inversely proportional to m.

The CDF of the κ-μ shadowed distribution was also given in [20] in terms of the bivariate confluent hypergeometric function:

$$F_\gamma(\gamma) = \frac{\mu^{\mu-1}m^m(1+\kappa)^\mu}{\Gamma(\mu)(m+\mu\kappa)^m}\left(\frac{\gamma}{\overline{\gamma}}\right)^\mu \times \Phi_2\left(\mu-m,m;\mu+1;-\frac{\mu(1+\kappa)}{\overline{\gamma}}\gamma, -\frac{\mu(1+\kappa)}{\overline{\gamma}}\frac{m\gamma}{\mu\kappa+m}\right), \quad (21)$$

while the MGF is expressed as [20]

$$\mathcal{M}_\gamma(s) = \frac{(-\mu)^\mu m^m(1+\kappa)^\mu}{\overline{\gamma}^\mu(m+\mu\kappa)^m} \times \frac{\left(s-\mu(1+\kappa)/\overline{\gamma}\right)^{m-\mu}}{\left(s-(\mu(1+\kappa)/\overline{\gamma})\right)\left(m/(\mu\kappa+m)\right)^m}. \quad (22)$$

Therefore, expressions (19), (21), and (22) provide a complete set of alternative characterizations for the κ-μ shadowed fading model.

5. Conclusions

This review paper presents some important results concerning fading statistics from 2005 to present. The new results on the most relevant classical fading distributions have been described. A selection of novel proposals for fading distributions is also included. A summary of relevant features of these novel distributions is shown in Table 1. Several open problems concerning the fading distributions have been also stated.

Conflict of Interests

The author declares that there is no conflict of interests regarding the publication of this paper.

Table 1: Relevant statistical information on the novel fading distributions.

Fading distribution	
η-μ	The PDF, CDF, and MGF are expressed in closed-form (see [11–13]). It does include the one-sided Gaussian, Hoyt, Rayleigh, and Nakagami-m distributions as particular cases. Specifically, it does *not* include the Rician, Weibull, and Lognormal distributions.
κ-μ	The PDF, CDF, and MGF are expressed in closed-form (see [11, 12]). It does include the one-sided Gaussian, Rayleigh, Rician, and Nakagami-m distributions as particular cases. Specifically, it does *not* include the Hoyt, Weibull, and Lognormal distributions.
α-μ	The PDF, CDF, and MGF are expressed in closed-form (see [16, 17]). It does include the one-sided Gaussian, Rayleigh, Nakagami-m, exponential, gamma, and Weibull distributions as particular cases. Specifically, it does *not* include the Hoyt, Rician, and Lognormal distributions.
G	The PDF is expressed in closed-form (see [19]). The CDF and MGF are expressed in closed-form only when the parameter m is a natural number (see [19]). It does include the one-sided Gaussian, Rayleigh, Nakagami-m, and inverse Gaussian distributions as particular cases. Specifically, it does *not* include the Hoyt, Rician, Weibull, and Lognormal distributions.
κ-μ shadowed	The PDF, CDF, and MGF are expressed in closed-form (see [20]). It does include the one-sided Gaussian, Rayleigh, Nakagami-m, Rician, Rician shadowed, and κ-μ distributions as particular cases. Specifically, it does *not* include the Hoyt, Weibull, and Lognormal distributions.

Acknowledgments

This work is partially supported by the Spanish Government and FEDER under Project TEC2011-25473.

References

[1] M. K. Simon and M-S. Alouini, *Digital Communications over Fading Channels*, John Wiley & Sons, 2nd edition, 2005.

[2] I. E. Telatar, "Capacity of multiantenna Gaussian channels," *European Transactions on Telecommunications*, vol. 10, no. 6, 1999.

[3] M. Kang and M. Alouini, "Capacity of MIMO Rician channels," *IEEE Transactions on Wireless Communications*, vol. 5, no. 1, pp. 112–122, 2006.

[4] J. F. Paris, "Nakagami-q (Hoyt) distribution function with applications," *Electronics Letters*, vol. 45, no. 4, pp. 210–211, 2009.

[5] J. F. Paris, "Nakagami-q (Hoyt) distribution function with applications," *Electronics Letters*, vol. 45, no. 8, pp. 210–211, 2009.

[6] S. Asmussen, J. L. Jensen, and L. Rojas-Nandayapa, "On the Laplace transform of the Lognormal distribution," Thiele Centre, 2013, http://math.au.dk/publs?publid=994.

[7] P. S. Bithas, N. C. Sagias, P. T. Mathiopoulos, G. K. Karagiannidis, and A. A. Rontogiannis, "On the performance analysis of digital communications over Generalized-K fading channels," *IEEE Communications Letters*, vol. 10, no. 5, pp. 353–355, 2006.

[8] I. S. Gradshteyn and I. M. Ryzhik, *Table of Integrals, Series and Products*, Academic Press, 7th edition, 2007.

[9] J. F. Paris, "Closed-form expressions for Rician shadowed cumulative distribution function," *Electronics Letters*, vol. 46, no. 13, pp. 952–953, 2010.

[10] M. D. Yacoub, "The η-μ distribution: a general fading distribution," in *Proceedings of the 52nd IEEE Vehicular Technology Conference*, vol. 2, pp. 872–877, Boston, Mass, USA, September 2000.

[11] M. D. Yacoub, "The κ-μ distribution and the η-μ distribution," *IEEE Antennas and Propagation Magazine*, vol. 49, no. 1, pp. 68–81, 2007.

[12] N. Y. Ermolova, "Moment generating functions of the generalized η-μ and κ-μ distributions and their applications to performance evaluations of communication systems," *IEEE Communications Letters*, vol. 12, no. 7, pp. 502–504, 2008.

[13] D. Morales-Jiménez and J.F. Paris, "Outage probability analysis for $\eta-\mu$ fading channels," *IEEE Communications Letters*, vol. 14, no. 6, pp. 521–523, 2010.

[14] M. D. Yacoub, "The κ-μ distribution: a general fading distribution," in *IEEE VTS 54th Vehicular Technology Conference VTC Fall*, vol. 3, pp. 1427–1431, Atlantic City, NJ, USA, October 2001.

[15] M. D. Yacoub, "The α-μ distribution: a general fading distribution," in *Proceedings of the 13th IEEE International Symposium on Personal, Indoor and Mobile Radio Communications (PIMRC '02)*, vol. 2, p. 629633, 2002.

[16] M. D. Yacoub, "The α-μ distribution: a physical fading model for the Stacy distribution," *IEEE Transactions on Vehicular Technology*, vol. 56, no. 1, pp. 27–34, 2007.

[17] A. M. Magableh and M. M. Matalgah, "Moment generating function of the generalized α-μ distribution with applications," *IEEE Communications Letters*, vol. 13, no. 6, pp. 411–413, 2009.

[18] A. C. Frery, H. Müller, C. D. C. F. Yanasse, and S. J. S. Sant'Anna, "A model for extremely heterogeneous clutter," *IEEE Transactions on Geoscience and Remote Sensing*, vol. 35, no. 3, pp. 648–659, 1997.

[19] A. Laourine, M.-S. Alouini, S. Affes, and A. Stéphenne, "On the performance analysis of composite multipath/shadowing channels using the G-distribution," in *Proceedings of the IEEE International Conference on Communications (ICC '08)*, pp. 1333–1338, Beijing, China, May 2008.

[20] J. F. Paris, "Statistical characterization of $\kappa-\mu$ shadowed fading," *IEEE Transactions on Vehicular Technology*, vol. 63, no. 2, pp. 518–526, 2014.

Hindawi Publishing Corporation
International Journal of Antennas and Propagation
Volume 2014, Article ID 461713, 13 pages
http://dx.doi.org/10.1155/2014/461713

Research Article

Relay Selection and Subcarrier-Pair Based Energy-Efficient Resource Allocation for Multirelay Cooperative OFDMA Networks

Wanming Hao,[1] Shouyi Yang,[1] and Wanliang Hao[2]

[1] *School of Information Engineering, Zhengzhou University, Zhengzhou 450001, China*
[2] *College of Navigation and Aerospace Engineering, Information Engineering University, Zhengzhou 450001, China*

Correspondence should be addressed to Wanming Hao; wmhao@hotmail.com

Received 8 May 2014; Revised 13 June 2014; Accepted 13 June 2014; Published 10 July 2014

Academic Editor: Theodoros Tsiftsis

Copyright © 2014 Wanming Hao et al. This is an open access article distributed under the Creative Commons Attribution License, which permits unrestricted use, distribution, and reproduction in any medium, provided the original work is properly cited.

Energy-efficient resource allocation is investigated for a relay-based multiuser cooperation orthogonal frequency division multiple access (OFDMA) uplink system with amplify-and-forward (AF) protocol for all relays. The objective is to maximize the total energy efficiency (EE) of the uplink system with consideration of some practical limitations, such as the individual power constraint for the users and relays and the quality of service (QoS) for every user. We formulate an energy-efficient resource allocation problem that seeks joint optimization of subcarrier pairing, relay selection, subcarrier assignment, and power allocation. Unlike previous optimization throughput models, we transform the considered EE problem in fractional form into an equivalent optimal problem in subtractive form, which is solved by using dual decomposition and subgradient methods. To reduce computation costs, we propose two low-complexity suboptimal schemes. Numerical studies are conducted to evaluate the EE of the proposed algorithms.

1. Introduction

Transmit diversity generally requires more than one antenna at the transmitter and receiver. However, many wireless devices are limited to single antenna because of size or hardware complexity. Cooperation communication is a promising solution to address this problem in various wireless systems, such as ad hoc and cellular networks [1, 2]. In contrast to traditional point-to-point or point-to-multipoint wireless communication, cooperation communication allows different users or nodes in a wireless system to share resources and create collaboration through distributed transmission; every piece of user's information is sent not only by itself but also by the collaborating users or nodes [3]. Therefore, cooperative communication formulates a new form of space diversity to combat the negative effect of severe fading [4]. Cooperative communication can improve the overall system performance by improving the spectrum efficiency, extending the coverage area, and prolonging the network lifetime. Orthogonal frequency division multiple access (OFDMA) or multiuser orthogonal frequency division multiplexing (MU-OFDM) is the preferred multiple access scheme for high-speed wireless multiuser communication networks because of its high spectrum efficiency and resistance to multipath fading [5]. Moreover, several users' signals are simultaneously transmitted over different subcarriers on each OFDM symbol to avoid interference between users. Thus, to improve system performance, studying optimal resource allocation in relay-assisted OFDMA communication system is important.

Relaying protocols have three main types, namely, amplify-and-forward (AF), decode-and-forward (DF), and compress-and-forward (CF). In AF, the signal received by relay is amplified and retransmitted to the destination. The noise is also amplified at the relay. This protocol is simple and of low cost. In DF, the relay attempts to decode the received signal. If successful, DF reencodes the information and retransmits the signal. CF attempts to generate an estimate for the received signal. Hoping the estimated value provides some assistance in decoding the original codeword at the destination. Given the limited available space, we only study

the energy-efficient resource allocation with AF protocol. The other relaying protocols will be studied in future works.

Compared with previous studies on single-carrier relay networks or multicarrier noncooperation networks, more technical challenges exist in the study of multicarrier cooperation networks. We not only consider the relaying protocols (AF, DF, and CF) but also solve the problems about relay selection and power allocation between users and relays in relaying networks. Several results have been reported recently about relaying networks [6–14]. The optimal power allocation and subcarrier pairing under AF and DF relay links have been studied, and the optimality of ordered subcarrier pairing (OSP) for these two protocols without diversity under total power constraint has been proved [6]. However, multiple relays usually exist in a practical system; thus, subcarrier-to-relay assignment must be considered [8]. The authors in [9] attempted to solve subcarrier-to-relay assignment and subcarrier pairing problems in multirelay OFDM system with a single user. Individual and total power constraints were all considered, but multiple users were not studied. In [10], the authors studied optimal relay selection, power allocation, and subcarrier assignment scheme under total power constraint. However, individual power constraint and subcarrier pairing were not considered. Optimal power and time allocation under a long-term total power constraint in OFDM-based linear multihop relay networks with DF protocol were considered in [11, 12]. In [13], the authors considered that a subcarrier may carry a signal for different services. They also proposed maximizing the weighted sum rate by joint optimal subcarrier pairing and power allocation under total and individual power constraints for the source and relay. Cross-layer scheduling for the downlink of AF relay-assisted OFDMA networks under imperfect channel-state information at the transmitter in slow fading was introduced in [14]. The authors optimized the rate, power, and subcarrier allocation to maximize the system goodput.

We have discussed only the throughput maximum problem in resource allocation for relay-assisted cooperative OFDMA systems. However, explosively growing data traffic and the requirement for ubiquitous access have triggered the escalation of energy, which results in increased greenhouse gas emission [15]. Therefore, energy efficiency (EE) has become an important problem in later development. Besides, mobile terminals cannot connect to an external charger; EE (bits/Hz/Joule) may be a better performance metric than system throughput (bits/s/Hz) in evaluating the performance of wireless communication systems [16–18]. A number of studies on energy-efficient resource allocation have been reported [19–24]. Power adaptation for maximizing the EE in downlink and uplink OFDMA cellular networks was studied in [19]. For downlink transmission, the total EE was maximized; for the uplink case, the minimum individual EE was maximized. In [20], the fundamental tradeoff between EE and spectral efficiency (SE) in downlink OFDMA systems was studied. In [21], the authors transformed the considered EE problem in fractional form into an equivalent optimal problem in subtractive form. They also studied the resource allocation for energy-efficient communication in multicell OFDMA downlink networks. References [22, 23] used the Dinkelbach method to solve the EE maximum problem in OFDM systems and found the optimal resource allocation. The literature in [24] used the resembled solution in [17] to deal with the energy-efficient resource allocation problem in a multiuser OFDMA system. Users' quality-of-service (QoS) requirements were also considered.

For relaying networks, limited study about EE exists. The authors in [25] formulated EE optimization problem by joint subcarrier assignment, bit, and power allocation. However, they provided only near-optimal and suboptimal resource schemes to maximize the overall EE and did not find the global optimum. Power constraints for sources and relay were also not considered. The power allocation to maximize EE for a two-hop AF relay link under QoS requirement has also been investigated [26]; single user and relay have been studied, but the subcarrier pairing problem has not been considered.

Considerable research exists about the optimal resource allocation mechanisms in relaying networks, including power allocation, subcarrier pairing, and relay selection; see, for example, [6–14]. However, these problems have only been studied in the case of throughput maximization (supposing throughput as objective function). Optimal resource allocation mechanisms will be changed when we consider the system EE (supposing EE as objective function). Hence, we must provide a new optimal resource allocation mechanism to meet the requirements of systems. In this paper, we address the energy-efficient resource allocation in AF-based cooperative two-hop multirelay uplink OFDMA system. Considering an actual situation, individual power constraint for the users and relays is applied. QoS for every user should be considered. Then, the subcarrier pairing, relay selection, subcarrier assignment, and power allocation problem are formulated as a joint optimization problem with the objective of maximizing the uplink system total EE. Given integer assignment variables, the optimal EE problem falls within the scope of combinatorial programming, which is NP-hard. Thus, we transform the EE problem in fractional form into an equivalent optimal problem in subtractive form, which is solved by using dual decomposition and subgradient methods. We also propose two suboptimal algorithms to trade off performance and complexity.

The remainder of this paper is organized as follows. Section 2 introduces the system model and formulates the optimization EE problem. Section 3 presents the optimal resource allocation algorithm. Section 4 shows suboptimal algorithms with low complexity. Section 5 demonstrates simulation results to verify the performance of the proposed algorithms. Section 6 concludes the paper.

2. System Model and Problem Formulation

We consider a multirelay-assisted cooperation OFDMA system, as shown in Figure 1. K users ($1 \leq k \leq K$) and N relays ($1 \leq n \leq N$) are assumed. The relays are shared by all users. The total number of the subcarriers used is M ($1 \leq m \leq M$) in the single cell system. Broadband channel is assumed to be frequency-selective Rayleigh fading. All

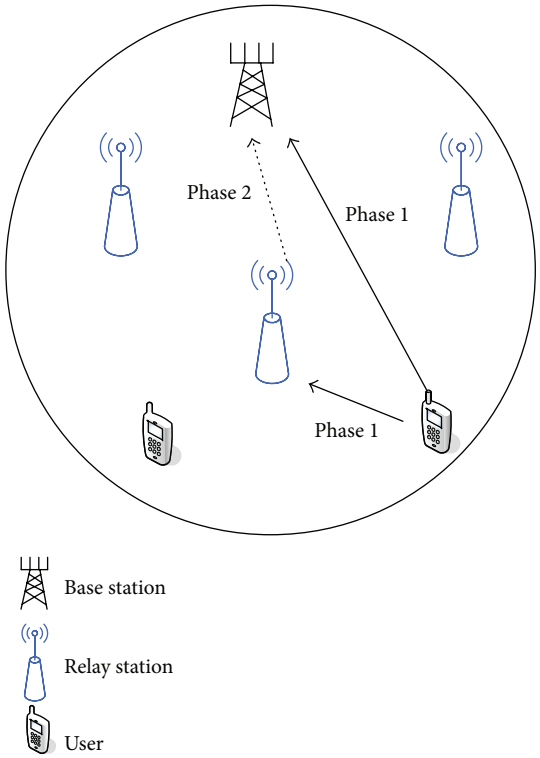

Figure 1: System model.

channel-state information is assumed to be perfectly known. Each relay node operates in a time-division half-duplex mode with AF protocol. Therefore, two phases are needed for the communication between the user and base station. In the first phase, the user transmits the signal to the base station, which is overheard by the selected relay as well. In the second phase, the selected relay forwards the received signal to the base station using AF cooperation protocol. n is supposed to receive the signal from user k on subcarrier m in the first phase, and the signal is then forwarded on subcarrier m' in the second phase; the subcarrier m may not be the same as m', and they are thus called a subcarrier pair (m, m') [9].

The noise variances of the source-to-relay (SR) links, relay-to-destination (RD) links, and source-to-destination (SD) links are denoted by $\sigma_{k,n}^2$, $\sigma_{n,D}^2$, and $\sigma_{k,D}^2$, respectively. The channel coefficients of $S \rightarrow R$ and $S \rightarrow D$ links on the subcarrier m in the first phase are denoted by $h_{k,n}^m$ and $h_{k,D}^m$, respectively, and that of the $R \rightarrow D$ links on the subcarrier m' in the second phase is denoted by $h_{n,D}^{m'}$. The efficient channel gain of the three links on the subcarrier m or m' for user k and relay n can be denoted by $\alpha_{k,n}^m = |h_{k,n}^m|^2/\sigma_{k,n}^2$, $\alpha_{k,D}^m = |h_{k,D}^m|^2/\sigma_{k,D}^2$, and $\alpha_{n,D}^{m'} = |h_{n,D}^{m'}|^2/\sigma_{n,D}^2$, respectively. The channel variances of $S \rightarrow R$, $S \rightarrow D$, and $R \rightarrow D$ links are denoted by $\delta_{k,n}^2$, $\delta_{k,D}^2$, and $\delta_{n,D}^2$, respectively.

In this relaying system, the base station controls all users and relays. The resource allocation information, including subcarrier pairing, relay selection, subcarrier assignment, and power allocation, is sent to users and relays by the base station via downlink control channel.

The achievable rate for the kth user in the subcarrier pair (m, m') when the nth relay is selected is given by

$$r_{k,n}^{m,m'} = \frac{1}{2}\log_2\left(1 + p_{S,k}^m \alpha_{k,D}^m + \frac{p_{S,k}^m \alpha_{k,n}^m p_{R,n}^{m'} \alpha_{n,D}^{m'}}{1 + p_{S,k}^m \alpha_{k,n}^m + p_{R,n}^{m'} \alpha_{n,D}^{m'}}\right), \tag{1}$$

where $p_{S,k}^m$ is the transmit power of the kth user in the mth subcarrier and $p_{R,n}^{m'}$ is the transmit power of the nth relay in the m'th subcarrier. The factor 1/2 is due to the two-phase transmission.

$r_{k,n}^{m,m'}$ is not jointly concave in $p_{S,k}^m$ and $p_{R,n}^{m'}$. To make the problem tractable, we adopt the following approximation:

$$r_{k,n}^{m,m'} \approx \frac{1}{2}\log_2\left(1 + p_{S,k}^m \alpha_{k,D}^m + \frac{p_{S,k}^m \alpha_{k,n}^m p_{R,n}^{m'} \alpha_{n,D}^{m'}}{p_{S,k}^m \alpha_{k,n}^m + p_{R,n}^{m'} \alpha_{n,D}^{m'}}\right). \tag{2}$$

The above approximation is jointly concave in $p_{S,k}^m$ and $p_{R,n}^{m'}$, as proved in Appendix A. This approximation is based on the assumption that the signal is amplified and forwarded by the relay under a high signal-to-ratio (SNR) condition. Such approximation has been used in the literatures [7, 9, 27]. However, in a low-SNR regime, [27] proved that the resource allocation almost reaches the true optimal capacity by optimizing the rate (2).

Our objective is to maximize the uplink system total EE subject to a set of constraints. The relay selection and subcarrier assignment constraints are as follows:

$$\sum_{k=1}^{K}\sum_{n=1}^{N}\rho_{k,n}^{m,m'} = 1, \qquad \rho_{k,n}^{m,m'} \in \{0,1\}, \ \forall m, m', \tag{3}$$

where $\rho_{k,n}^{m,m'} = 1$ indicates that user n uses relay k as a relay in the subcarrier pair (m, m'); otherwise, $\rho_{k,n}^{m,m'} = 0$.

$\gamma_{m,m'}$ denotes the indicator for subcarrier pairing. When $\gamma_{m,m'} = 1$, subcarrier m in the first phase is paired with subcarrier m' in the second phase; otherwise, $\gamma_{m,m'} = 0$. Given that each subcarrier in the first phase can be paired with only one subcarrier in the second phase, the binary variables $\{\gamma_{m,m'}\}$ must satisfy the following equation:

$$\sum_{m=1}^{M}\gamma_{m,m'} = 1, \quad \sum_{m'=1}^{M}\gamma_{m,m'} = 1, \quad \forall m, m'. \tag{4}$$

The individual power constraint of the users and relays can be expressed as follows:

$$\begin{aligned} &\text{User power constraint: } \sum_{m=1}^{M} p_{S,k}^m \le P_{S,k}, \quad \forall k, \\ &\text{Relay power constraint: } \sum_{m'=1}^{M} p_{R,n}^{m'} \le P_{R,n}, \quad \forall n. \end{aligned} \tag{5}$$

Aside from transmit power, the energy consumption also includes circuit energy consumption [28] and overall power

consumption. The power consumptions of user n and relay k are modeled as follows:

$$\begin{aligned} \text{user power consumption: } P_{S,k}^{\text{total}} &= \xi \sum_{m=1}^{M} p_{S,k}^{m} + P_{C,S}^{k}, \\ \text{relay power consumption: } P_{R,n}^{\text{total}} &= \xi \sum_{m'=1}^{M} p_{R,n}^{m'} + P_{C,R}^{n}, \end{aligned} \tag{6}$$

where ξ is the reciprocal of drain efficiency of power amplifier. We assume that the reciprocal is the same for all the users and relays.

The optimization EE problem can be formulated as

$$\begin{aligned} \max \text{EE} = &\left(\sum_{k=1}^{K} w_k \sum_{n=1}^{N} \sum_{m=1}^{M} \sum_{m'=1}^{M} \rho_{k,n}^{m,m'} \gamma_{m,m'} r_{k,n}^{m,m'} \right) \\ &\times \left(\xi \sum_{k=1}^{K} \sum_{n=1}^{N} \sum_{m=1}^{M} \sum_{m'=1}^{M} \rho_{k,n}^{m,m'} \gamma_{m,m'} \left(p_{S,k}^{m} + p_{R,n}^{m'} \right) \right. \\ &\left. + \sum_{k=1}^{K} P_{C,S}^{k} + \sum_{n=1}^{N} P_{C,R}^{n} \right)^{-1}, \end{aligned} \tag{7}$$

which is subject to

$$\rho_{k,n}^{m,m'} \in \{0,1\}, \quad \forall k,n,m,m', \tag{8}$$

$$\sum_{k=1}^{K} \sum_{n=1}^{N} \rho_{k,n}^{m,m'} = 1, \quad \forall m,m', \tag{9}$$

$$\gamma_{m,m'} \in \{0,1\}, \quad \forall m,m', \tag{10}$$

$$\sum_{m=1}^{M} \gamma_{m,m'} = 1, \quad \sum_{m'=1}^{M} \gamma_{m,m'} = 1, \quad \forall m,m', \tag{11}$$

$$\sum_{m=1}^{M} p_{S,k}^{m} \le P_{S,k}, \quad \forall k, \tag{12}$$

$$\sum_{m'=1}^{M} p_{R,n}^{m'} \le P_{S,n}, \quad \forall n, \tag{13}$$

$$R_{S,k} \ge Q_{S,k}, \quad \forall k, \tag{14}$$

$$p_{S,k}^{m} \ge 0, \quad p_{R,n}^{m'} \ge 0, \quad \forall k,n,m,m', \tag{15}$$

where constraint (14) denotes the minimum QoS requirements for the users and $R_{S,k} = \sum_{n=1}^{N} \sum_{m=1}^{M} \sum_{m'=1}^{M} r_{k,n}^{m,m'}$. The predetermined weights, w_k, can provide a certain level of priority and/or fairness among users.

3. Optimal Resource Allocation

The integer assignment variables $\rho_{k,n}^{m,m'}$ and $\gamma_{m,m'}$ above EE problem are generally NP-hard for optimal solution. If we consider all possibilities of subcarrier pairings and subcarrier-pair-to-user and relay assignments, then the complexity is high with large K, N, and M. The fraction further complicates the problem. Hence, we apply an effective method to solve this challenging problem.

3.1. Equivalence Transformation of the Optimization Problem. For the fraction objective function in (7), we first rewrite problems (7)–(15) in the following compact form:

$$\underset{\boldsymbol{\rho},\boldsymbol{\gamma},\mathbf{p}\in\boldsymbol{\pi}}{\text{maximize}} \frac{R(\boldsymbol{\rho},\boldsymbol{\gamma},\mathbf{p})}{P(\boldsymbol{\rho},\boldsymbol{\gamma},\mathbf{p})}, \tag{16}$$

where $\boldsymbol{\rho} = \{\rho_{k,n}^{m,m'}\}$, $\boldsymbol{\gamma} = \{\gamma_{m,m'}\}$, and $\mathbf{p} = \{p_{S,k}^{m}, p_{R,n}^{m'}\}$. $\boldsymbol{\pi}$ denotes the feasible domain defined by (8)–(15). $R(\boldsymbol{\rho},\boldsymbol{\gamma},\mathbf{p})$ and $P(\boldsymbol{\rho},\boldsymbol{\gamma},\mathbf{p})$ are the numerator and denominator in (7), respectively. Problem (16) is a nonlinear fractional problem. According to [29], we transform the considered EE problem in fractional form into an equivalent optimal problem in subtractive form. We then define the following parameter problem:

$$F(q) \triangleq \underset{\boldsymbol{\rho},\boldsymbol{\gamma},\mathbf{p}\in\boldsymbol{\pi}}{\text{maximize}} \{R(\boldsymbol{\rho},\boldsymbol{\gamma},\mathbf{p}) - qP(\boldsymbol{\rho},\boldsymbol{\gamma},\mathbf{p})\}, \tag{17}$$

where $q \in \mathbb{R}$ is treated as a parameter. We have the following theorems, all of which are proved in Appendix B.

Theorem 1. *$F(q)$ is strictly monotonically decreasing for q.*

Theorem 2. *$F(q) = 0$ has a unique solution.*

Theorem 3. *Consider*

$$\begin{aligned} q_0 &= \frac{R(\boldsymbol{\rho}_0,\boldsymbol{\gamma}_0,\mathbf{p}_0)}{P(\boldsymbol{\rho}_0,\boldsymbol{\gamma}_0,\mathbf{p}_0)} = \max_{\boldsymbol{\rho},\boldsymbol{\gamma},\mathbf{p}\in\boldsymbol{\pi}} \frac{R(\boldsymbol{\rho},\boldsymbol{\gamma},\mathbf{p})}{P(\boldsymbol{\rho},\boldsymbol{\gamma},\mathbf{p})} \quad \textit{only if} \\ F(q_0) &= F(q_0,(\boldsymbol{\rho}_0,\boldsymbol{\gamma}_0,\mathbf{p}_0)) \\ &= \max_{\boldsymbol{\rho},\boldsymbol{\gamma},\mathbf{p}\in\boldsymbol{\pi}} \{R(\boldsymbol{\rho},\boldsymbol{\gamma},\mathbf{p}) - q_0(\boldsymbol{\rho},\boldsymbol{\gamma},\mathbf{p})\} = 0. \end{aligned} \tag{18}$$

Based on the above theorems, we can use binary search method to find $F(q) = 0$ and the optimal solution for the primal problem. Therefore, the difficulty is to solve $T(q)$ for a given q. The optimization problem is

$$\max_{\boldsymbol{\rho},\boldsymbol{\gamma},\mathbf{p}\in\boldsymbol{\pi}} R(\boldsymbol{\rho},\boldsymbol{\gamma},\mathbf{p}) - q(\boldsymbol{\rho},\boldsymbol{\gamma},\mathbf{p}). \tag{19}$$

Obtaining the joint optimal $\boldsymbol{\rho}^*$, $\boldsymbol{\gamma}^*$, and $\mathbf{p}^*$ for (19) requires solving a mixed integer programming problem. Therefore, finding the optimal solution for problem (19) requires searching through all possible users, relays, and subcarrier allocation, which is a complex task when the system is large. The literature in [30] showed that the duality gap of a nonconvex resource allocation problem that satisfies the time-sharing condition is nearly zero with a large number of subcarriers in a multicarrier system. Thus, we solve this problem by using the Lagrange dual method.

3.2. Dual Problem. The Lagrange dual function of problem (19) can be written as

$$g(\boldsymbol{\lambda}, \boldsymbol{\mu}, \boldsymbol{\upsilon}) = \max_{\{\boldsymbol{\rho}, \boldsymbol{\gamma}\} \in \Omega} L(\boldsymbol{\rho}, \boldsymbol{\gamma}, \mathbf{p}, \boldsymbol{\lambda}, \boldsymbol{\mu}, \boldsymbol{\upsilon}), \tag{20}$$

$$\begin{aligned} &L(\boldsymbol{\rho}, \boldsymbol{\gamma}, \mathbf{p}, \boldsymbol{\lambda}, \boldsymbol{\mu}, \boldsymbol{\upsilon}) \\ &= \sum_{k=1}^{K} \sum_{n=1}^{N} \sum_{m=1}^{M} \sum_{m'=1}^{M} \frac{w_k}{2} \rho_{k,n}^{m,m'} \gamma_{m,m'} \\ &\qquad \times \log_2 \left(1 + p_{S,k}^{m} \alpha_{k,D}^{m} + \frac{p_{S,k}^{m} \alpha_{k,n}^{m} p_{R,n}^{m'} \alpha_{n,D}^{m'}}{p_{S,k}^{m} \alpha_{k,n}^{m} + p_{R,n}^{m'} \alpha_{n,D}^{m'}} \right) \\ &- q \left(\xi \sum_{k=1}^{K} \sum_{n=1}^{N} \sum_{m=1}^{M} \sum_{m'=1}^{M} \rho_{k,n}^{m,m'} \gamma_{m,m'} \left(p_{S,k}^{m} + p_{R,n}^{m'} \right) \right. \\ &\qquad \left. + \sum_{k=1}^{K} P_{C,S}^{k} + \sum_{n=1}^{N} P_{C,R}^{n} \right) + \sum_{k=1}^{k} \lambda_k \left(P_{S,k} - \sum_{m=1}^{M} p_{S,k}^{m} \right) \\ &+ \sum_{n=1}^{N} \mu_n \left(P_{S,n} - \sum_{m'=1}^{M} p_{R,n}^{m'} \right) + \sum_{k=1}^{k} \upsilon_k \left(R_{S,k} - Q_{S,k} \right), \end{aligned} \tag{21}$$

where Lagrange is given in (21).

In (20), $\boldsymbol{\lambda} = (\lambda_1, \lambda_2, \ldots, \lambda_K) \geq 0$, $\boldsymbol{\mu} = (\mu_1, \mu_2, \ldots, \mu_N) \geq 0$, and $\boldsymbol{\upsilon} = (\upsilon_1, \upsilon_2, \ldots, \upsilon_K) \geq 0$ are the vectors of the dual variables associated with the individual power constraint for the users, individual power constraint for the relays, and individual rate constraint for the users, respectively. Hence, the dual optimization problem is given by

$$\begin{aligned} &\min \quad g(\boldsymbol{\lambda}, \boldsymbol{\mu}, \boldsymbol{\upsilon}), \\ &\text{s.t.} \quad \boldsymbol{\lambda}, \boldsymbol{\mu}, \boldsymbol{\upsilon} \geq 0. \end{aligned} \tag{22}$$

The literature in [31] proved that a dual function is always convex. Therefore, subgradient-based methods can be used to minimize $g(\boldsymbol{\lambda}, \boldsymbol{\mu}, \boldsymbol{\upsilon})$ with guaranteed convergence. Dual variables can be updated in parallel as follows:

$$\begin{aligned} \lambda_k(d+1) &= \left[\lambda_k(d) + o(d) \left(\sum_{m=1}^{M} p_{S,k}^{m} - P_{S,k} \right) \right]^{+} \\ \mu_n(d+1) &= \left[\mu_n(d) + \theta(d) \left(\sum_{m'=1}^{M} p_{R,n}^{m'} - P_{S,n} \right) \right]^{+} \\ \upsilon_k(d+1) &= \left[\upsilon_k(d) + \vartheta(d) \left(Q_{S,k} - R_{S,k} \right) \right]^{+}. \end{aligned} \tag{23}$$

$o(d)$, $\theta(d)$, and $\vartheta(d)$ are used as the step size, and d is the iteration index. To guarantee optimal dual variable convergence, the step size is chosen following the diminishing step size policy [32].

3.3. Optimizing Primal Variables with Given Dual Variables. Computing the dual function $g(\boldsymbol{\lambda}, \boldsymbol{\mu}, \boldsymbol{\upsilon})$ involves determining the optimal $\boldsymbol{\rho}$, $\boldsymbol{\gamma}$, and $\mathbf{p}$ at given dual points $\boldsymbol{\lambda}$, $\boldsymbol{\mu}$, and $\boldsymbol{\upsilon}$. Therefore, we present the detailed solution procedure in three phases.

3.3.1. Finding the Optimal $\mathbf{p}$ *for Fixed* $\boldsymbol{\rho}$ *and* $\boldsymbol{\gamma}$. For the fixed $\boldsymbol{\rho}$ and $\boldsymbol{\gamma}$, we rewrite (20) as

$$\begin{aligned} g(\boldsymbol{\lambda}, \boldsymbol{\mu}, \boldsymbol{\upsilon}) = \max_{\{\boldsymbol{\rho}, \boldsymbol{\gamma}\} \in \Omega} &\sum_{k=1}^{K} \sum_{n=1}^{N} \sum_{m=1}^{M} \sum_{m'=1}^{M} L_{k,n}^{m,m'} + \sum_{k=1}^{k} \lambda_k P_{S,k} \\ &+ \sum_{n=1}^{N} \mu_n P_{S,n} + q \left(\sum_{k=1}^{K} P_{C,S}^{k} + \sum_{n=1}^{N} P_{C,R}^{n} \right) - \sum_{k=1}^{k} \upsilon_k Q_{S,k}, \end{aligned} \tag{24}$$

where

$$\begin{aligned} L_{k,n}^{m,m'} \triangleq\ & \frac{w_k}{2} (1 + \upsilon_k) \\ & \times \log_2 \left(1 + p_{S,k}^{m} \alpha_{k,D}^{m} + \frac{p_{S,k}^{m} \alpha_{k,n}^{m} p_{R,n}^{m'} \alpha_{n,D}^{m'}}{p_{S,k}^{m} \alpha_{k,n}^{m} + p_{R,n}^{m'} \alpha_{n,D}^{m'}} \right) \\ & - (q\xi + \lambda_k) p_{S,k}^{m} - (q\xi + \mu_n) p_{R,n}^{m'}. \end{aligned} \tag{25}$$

A detailed derivation is given in Appendix C.

According to the Lagrange dual decomposition method, the optimal power allocation can be determined by solving the following problem:

$$\begin{aligned} &\max L_{k,n}^{m,m'} \\ &p_{S,k}^{m} \geq 0, \quad p_{R,n}^{m'} \geq 0, \quad \forall k, n, m, m'. \end{aligned} \tag{26}$$

Appendix A indicates that $L_{k,n}^{m,m'}$ is a joint concave function of $(p_{S,k}^{m}, p_{R,n}^{m'})$. Applying the Karush-Kuhn-Tucker (KKT) conditions [28], we can obtain the following optimal power allocation:

$$p_{S,k}^{m} = \begin{cases} b_{k,n}^{m,m'} p_{R,n}^{m'}, & \text{if } p_{R,n}^{m'} > 0 \\ \left(\dfrac{w_k(1+\upsilon_k)}{2\ln 2(q\xi+\lambda_k)} - \dfrac{1}{\alpha_{k,D}^{m}} \right)^{+} & \text{if } p_{R,n}^{m'} = 0, \end{cases} \tag{27}$$

$$p_{R,n}^{m'} = \begin{cases} \left(\dfrac{w_k(1+\upsilon_k)}{2\ln 2} \left(\alpha_{k,n}^{m} \alpha_{n,D}^{m'\,2} + \left(\alpha_{k,D}^{m} - \left(2\left(q\xi+\lambda_k\right)\ln 2\right) / \left(w_k\left(1+\upsilon_k\right)\right) \right) \right. \right. \\ \qquad \left. \times \left(\alpha_{k,n}^{m} b_{k,n}^{m,m'} + \alpha_{n,D}^{m'\,2} \right)^{2} \right) \\ \quad \times \left(b_{k,n}^{m,m'} \left(q\xi+\lambda_k\right) \left(\alpha_{k,n}^{m} b_{k,n}^{m,m'} + \alpha_{n,D}^{m'} \right) \right. \\ \qquad \left. \left. \times \left(\alpha_{k,D}^{m} \alpha_{k,n}^{m} b_{k,n}^{m,m'} + \alpha_{n,D}^{m'} \alpha_{k,D}^{m} + \alpha_{k,n}^{m} \alpha_{n,D}^{m'} \right) \right)^{-1} \right)^{+} & \text{if } \alpha_{n,D}^{m'}\left(q\xi+\lambda_k\right) > \alpha_{k,D}^{m}\left(q\xi+\mu_n\right) \\ 0 & \text{if } \alpha_{n,D}^{m'}\left(q\xi+\lambda_k\right) \le \alpha_{k,D}^{m}\left(q\xi+\mu_n\right). \end{cases} \tag{28}$$

$$b_{k,n}^{m,m'} = \frac{\alpha_{n,D}^{m'} \left(\sqrt{\left(q\xi+\mu_n\right)\left(\alpha_{k,n}^{m}\alpha_{n,D}^{m'}\left(q\xi+\lambda_k\right) - \alpha_{k,n}^{m}\alpha_{k,D}^{m}\left(q\xi+\mu_n\right) + \alpha_{n,D}^{m'}\alpha_{k,D}^{m}\left(q\xi+\lambda_k\right)\right)} + \alpha_{k,D}^{m}\left(q\xi+\mu_n\right) \right)}{\alpha_{k,n}^{m}\left[\alpha_{n,D}^{m'}\left(q\xi+\lambda_k\right) - \alpha_{k,D}^{m}\left(q\xi+\mu_n\right)\right]}. \tag{29}$$

And $p_{R,n}^{m'}$ is given in (28).

A detailed derivation is given in Appendix D.

3.3.2. Finding the Optimal $\boldsymbol{\rho}$ for Fixed $\boldsymbol{\gamma}$. Substituting the optimal power allocation expressions (27) and (28) into (20), we can obtain an alternative expression of the dual without power variables as

$$\begin{aligned} g(\boldsymbol{\lambda},\boldsymbol{\mu},\boldsymbol{\upsilon}) = \max_{\{\boldsymbol{\rho},\boldsymbol{\gamma}\}\in\boldsymbol{\Omega}} & \sum_{k=1}^{K}\sum_{n=1}^{N}\sum_{m=1}^{M}\sum_{m'=1}^{M} \rho_{k,n}^{m,m'} \gamma_{m,m'} H_{k,n}^{m,m'}(\boldsymbol{\lambda},\boldsymbol{\mu},\boldsymbol{\upsilon}) \\ & + \sum_{k=1}^{k}\lambda_k P_{S,k} + \sum_{n=1}^{N}\mu_n P_{S,n} \\ & + q\left(\sum_{k=1}^{K} P_{C,S}^{k} + \sum_{n=1}^{N} P_{C,R}^{n} \right) - \sum_{k=1}^{k}\upsilon_k Q_{S,k}, \end{aligned} \tag{30}$$

where the function $H_{k,n}^{m,m'}(\boldsymbol{\lambda},\boldsymbol{\mu},\boldsymbol{\upsilon})$ can be defined as follows:

$$H_{k,n}^{m,m'} = w_k\left(1+\upsilon_k\right) r_{k,n}^{m,m'} - \left(q\xi+\lambda_k\right) p_{S,k}^{m} - \left(q\xi+\mu_n\right) p_{R,n}^{m'}. \tag{31}$$

Therefore, the function $H_{k,n}^{m,m'}(\boldsymbol{\lambda},\boldsymbol{\mu},\boldsymbol{\upsilon})$ is the optimal criterion for relay and user selection. We can interpret this criterion by using an economic form. The first term can be viewed as the rate obtained by selecting subcarrier pairing (m, m') by user k and relay n, such as our gross income in the business. The second term is the cost for the user's power consumption. The third term is the cost for the relay's power consumption. $H_{k,n}^{m,m'}(\boldsymbol{\lambda},\boldsymbol{\mu},\boldsymbol{\upsilon})$ then represents our net profit. We should find the optimal k and n to maximize the profit. $K \times N$ profit matrix exists for every subcarrier pairing (m, m'). We should find a maximum value in this matrix; thus, the sum of profit could be large. The optimal relay selection and subcarrier allocation should therefore be the maximum value in (31) and is given by

$$\rho_{k,n}^{m,m'} = \begin{cases} 1, & (k^*, n^*) = \arg\max_{k,n} H_{k,n}^{m,m'} \\ 0, & \text{otherwise.} \end{cases} \tag{32}$$

In the operation, the optimal power allocation can first be computed by using (28) and (29). These power values can then be substituted into (31) to compute $H_{k,n}^{m,m'}$. Finally, we need to find a maximum value in $K \times N$ profit matrix, and the user and relay pair will be determined.

3.3.3. Finding the Optimal $\boldsymbol{\gamma}$ for Fixed $\boldsymbol{\rho}$. After finding the optimal $\boldsymbol{\rho}$, we can obtain the corresponding dual function by substituting (32) into (20) as follows:

$$\begin{aligned} g(\boldsymbol{\lambda},\boldsymbol{\mu},\boldsymbol{\upsilon}) = \max_{\boldsymbol{\gamma}\in\boldsymbol{\Omega}} & \sum_{m=1}^{M}\sum_{m'=1}^{M} \gamma_{m,m'} H_{m,m'}(\boldsymbol{\lambda},\boldsymbol{\mu},\boldsymbol{\upsilon}) + \sum_{k=1}^{k}\lambda_k P_{S,k} \\ & + \sum_{n=1}^{N}\mu_n P_{S,n} + q\left(\sum_{k=1}^{K} P_{C,S}^{k} + \sum_{n=1}^{N} P_{C,R}^{n} \right) - \sum_{k=1}^{k}\upsilon_k Q_{S,k}. \end{aligned} \tag{33}$$

(1) **Initialize** $q_{\min} = 0$, $q_{\max} >> 0$ with $F(q_{\min}) > 0$ and $F(q_{\max}) < 0$, ε.
(2) (i)**Update** $q_{\text{middle}} \leftarrow (q_{\min} + q_{\max})/2$;
(ii) **Initialization**: λ_k, μ_n, and ν_k;
(a) Obtain the optimal power via (27) and (28);
(b) Obtain (m, m') via (35);
(c) Obtain (n, k) for given (m, m') via (32);
(d) Update the dual variables λ_k, μ_n, and ν_k via (23);
(e) Repeat (a) $\rightarrow$ (d) until convergence;
(3) If $F(q_{\text{middle}}) > 0$, $q_{\min} \leftarrow q_{\text{middle}}$; otherwise, $q_{\max} \leftarrow q_{\text{middle}}$;
(4) **Repeat** *Steps 2* and *3* until $\left|F(q_{\text{middle}})\right| < \varepsilon$.

Algorithm 1: Bisection-based energy-efficient resource allocation algorithm.

We can then find the optimal subcarrier pairing $\boldsymbol{\gamma}$. To this end, we launch the first term in (33) and define $M \times M$ profit matrix as follows:

$$\begin{bmatrix} \gamma_{1,1}H_{1,1} & \gamma_{1,2}H_{1,2} & \cdots & \gamma_{1,M}H_{1,M} \\ \gamma_{2,1}H_{2,1} & \gamma_{2,2}H_{2,2} & \cdots & \gamma_{2,M}H_{2,M} \\ \vdots & \vdots & \ddots & \vdots \\ \gamma_{M,1}H_{M,1} & \gamma_{M,2}H_{M,2} & \cdots & \gamma_{M,M}H_{M,M} \end{bmatrix}. \quad (34)$$

We need to select one element in each row and each column in matrix (34) for the sum of profit to be large. Clearly, the problem is a standard linear assignment and can be solved by using the Hungarian method [33]. $\Psi(m)$ is defined as the subcarrier index in the second phase optimally paired with subcarrier m in the first phase. The optimal subcarrier pairing can be expressed as

$$\gamma_{m,m'} = \begin{cases} 1, & m' = \psi(m) \\ 0, & \text{otherwise.} \end{cases} \quad (35)$$

We have obtained the optimal variables $\boldsymbol{\rho}$, $\boldsymbol{\gamma}$, and $\mathbf{p}$ for given dual variables $\boldsymbol{\lambda}$, $\boldsymbol{\mu}$, and $\boldsymbol{\nu}$. We can subsequently obtain the joint optimization problem by updating the dual variables.

$T(q)$ is obtained according to the preceding analysis for a given q. However, we should find the optimal q to satisfy $T(q) = 0$. $q = 0$, which yields $T(q) > 0$ and $T(q) < 0$ with $q \rightarrow \infty$. Thus, we can use binary search method to find the optimal q, as stated in Algorithm 1.

4. Suboptimal Schemes

We analyze the complexity of the proposed optimal scheme. For every subcarrier pair, the number of computations needed to perform relay selection is KN. Therefore, the complexity at relay selection for all the subcarrier pair is $O(MKN)$. The complexity of the Hungarian method is $O(M^3)$. The complexity of the subgradient method is polynomial in the number of dual variables. Considering the individual power constraint for the users and relays and the individual rate constraint for the users, the number of the dual variables is $(2K + N)$. Therefore, the overall complexity is $O(|2K + N|^2 M^4 KN \cdot \log_2(1/\varepsilon))$. ε is the accuracy required for the binary search. In this section, we only propose two schemes for the subcarrier pairing.

4.1. Suboptimal Scheme 1: Order Subcarrier Pairing. Similar to the literature in [6], OSP denotes the best $S \rightarrow R$ subcarrier in the first phase with the best $R \rightarrow D$ subcarrier in the secondary phase, pairing the next best $S \rightarrow R$ subcarrier in the first phase with the next best $R \rightarrow D$ subcarrier in the secondary phase until all the subcarriers are paired. The complexity is $O(2M^2)$ for OSP. When the number of subcarriers is small, the advantage of using OSP is not obvious. By contrast, the advantage is obvious when the number of subcarriers is large.

4.2. Suboptimal Scheme 2: Fixed Subcarrier Pairing. To reduce the complexity of the subcarrier pairing, we let the subcarrier pairing be prefixed, rather than seeking the optimal subcarrier pairing. Similar to the previous suboptimal scheme [33], the subcarrier pairing can be arranged as

$$\psi(m) = m, \quad \forall m. \quad (36)$$

Thus, the source and relay use the same subcarrier to transmit and forward a signal in different phases, respectively. We do not need to make the subcarrier pair.

In the two suboptimal schemes, we only reduce the complexity for subcarrier pairing. The dual variables still need to be updated to compute $H_{k,n}^{m,m'}$.

5. Simulation Results

In this section, simulation results are presented to demonstrate the performance of the three proposed schemes. In the simulation, we consider quasistatic frequency-selective Rayleigh fading channels with a six-tap equal-gain, equal-space delay profile. The delay interval between adjacent taps is equal to the inverse of the OFDM system bandwidth. We consider $M = 48$ subcarriers. The bandwidth of each subcarrier is 15 kHz. Without loss of generality, we assume that all the noise terms are complex Gaussian random variables with zero mean and variance with 1. To produce large channel fading between users and destination, we assume that the channel variance of $S \rightarrow D$ link is -8 dB. Two users have the same minimum rate requirement of 0.5 bps/Hz. For each user and relay, the maximum transmit power and the circuit power are 1 W and 0.2 W, respectively. For simplicity, we assume that the drain efficiency of power amplifier is 0.35.

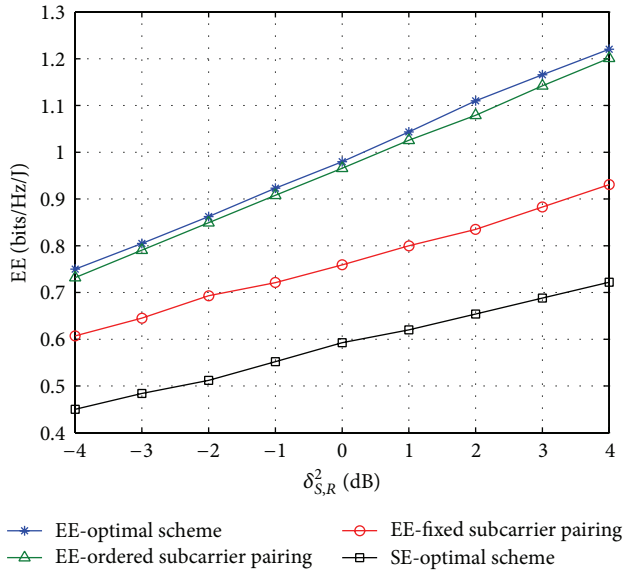

FIGURE 2: Energy efficiency versus channel variance of $S \rightarrow R$ link with $N = 2$ relays, and $w_1 = w_2 = 1$.

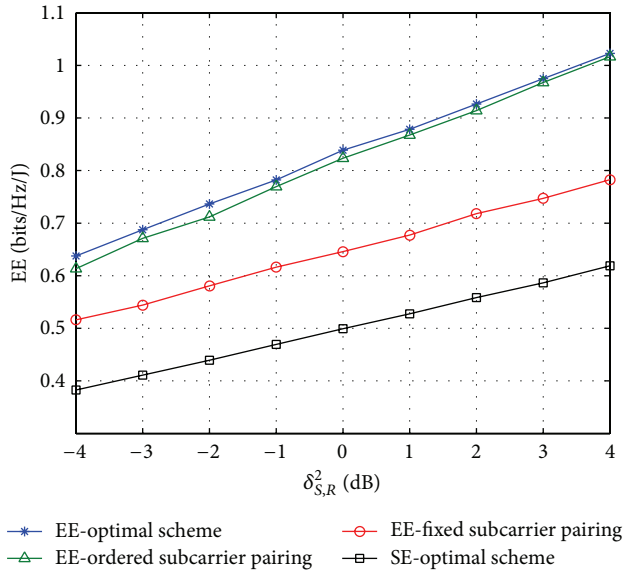

FIGURE 3: Energy efficiency versus channel variance of $S \rightarrow R$ link with $N = 2$ relays, and $w_1 = 1$, $w_2 = 2$.

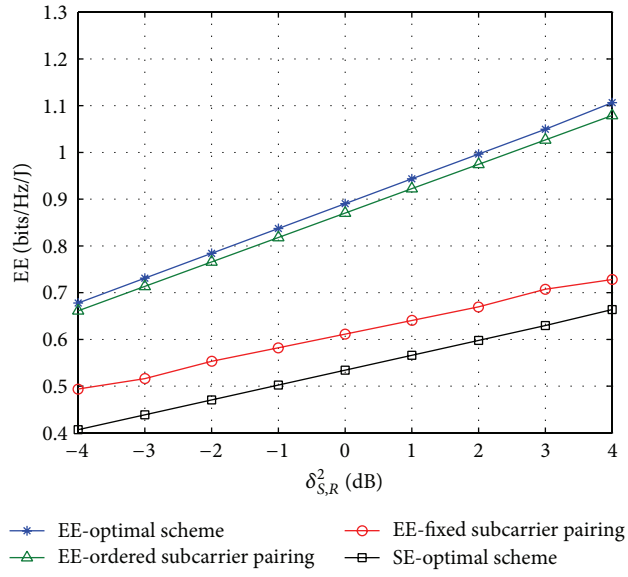

FIGURE 4: Energy efficiency versus channel variance of $S \rightarrow R$ link with $N = 12$ relays, and $w_1 = w_2 = 1$.

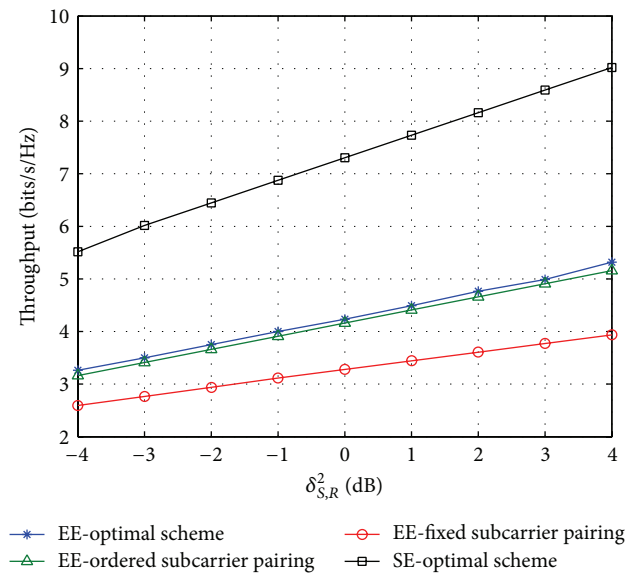

FIGURE 5: Throughput versus channel variance of $S \rightarrow R$ link with $N = 2$ relays, and $w_1 = 1$, $w_2 = 1$.

EE of the energy-efficient design that optimizes EE and the spectral-efficient design that maximizes the weight sum rate with the same constraints is evaluated in Figures 2 and 3. For any k and n, we assume that the value of $\delta^2_{k,n}$ is the same and define it as $\delta^2_{S,R}$. We set $\delta^2_{n,D} = 0$ dB for any n. Accordingly, the energy-efficient design significantly improves EE compared with the spectral-efficient design. The suboptimal scheme-based OSP is close to the optimal scheme, and its performance reached 97% or more of the optimal performance. EE performance of the suboptimal scheme-based fixed subcarrier paring is worse compared with the other two schemes. However, this scheme does not need subcarrier pairing, and its computation complexity is lower. Figure 3 shows that EE will decrease when considering the user's priority, namely, the weight factors.

For comparison with EE performance under different number of relays, we also plot EE with 12 relays with equal weight factor for all the users in Figure 4. EE in Figure 4 is lower than that in Figure 2 for a given $\delta^2_{S,R}$. The literature in [8] indicated that, as the number of relays increases, the average throughput increases. When considering EE, this relationship may be changed, as presented in Figures 2 and 4. Aside from the power consumption of signals, additional circuit energy consumption for the users and relays must be considered.

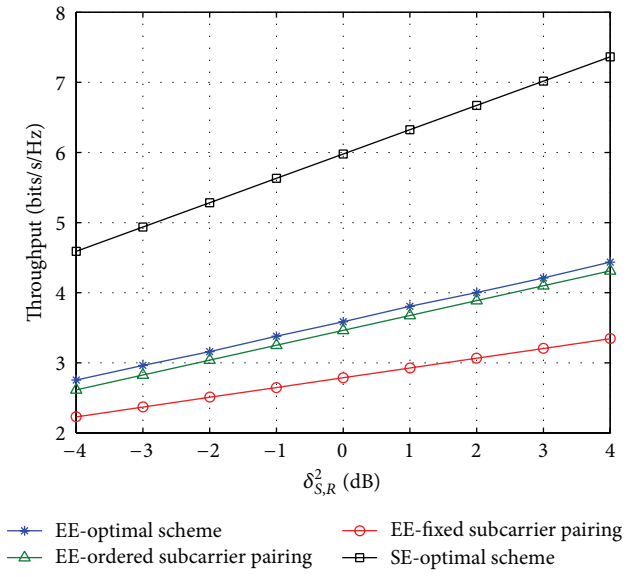

FIGURE 6: Throughput versus channel variance of $S \rightarrow R$ link with $N = 2$ relays, and $w_1 = 1$, $w_2 = 2$.

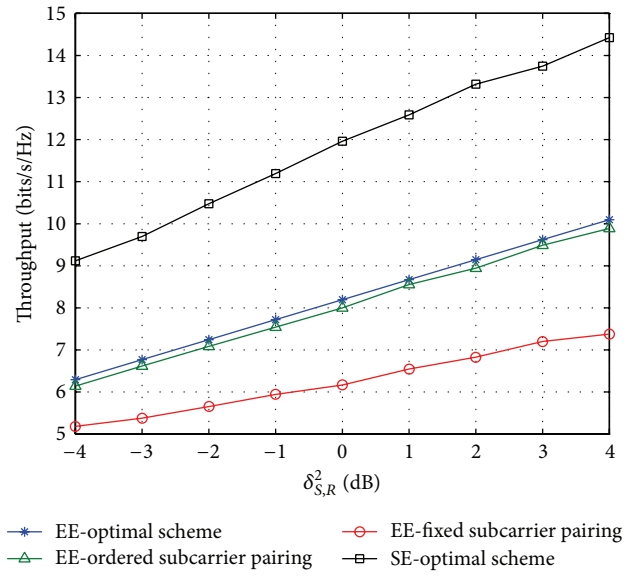

FIGURE 7: Throughput versus channel variance of $S \rightarrow R$ link with $N = 12$ relays, and $w_1 = w_2 = 1$.

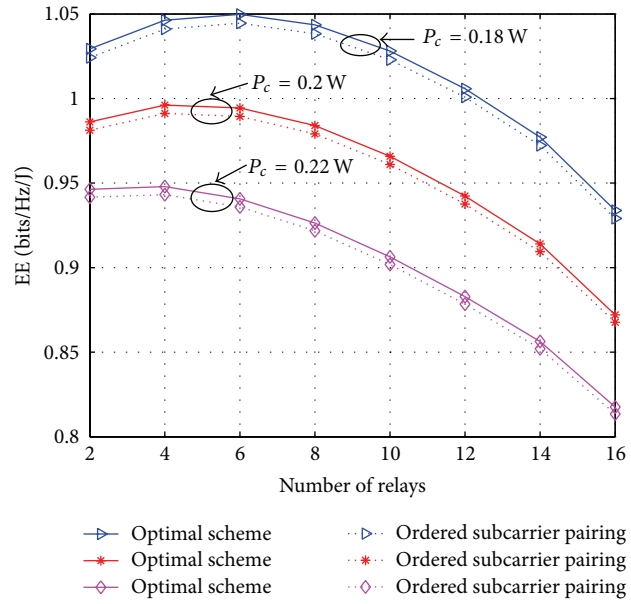

FIGURE 8: Energy efficiency versus different numbers of relays with $w_1 = w_2 = 1$.

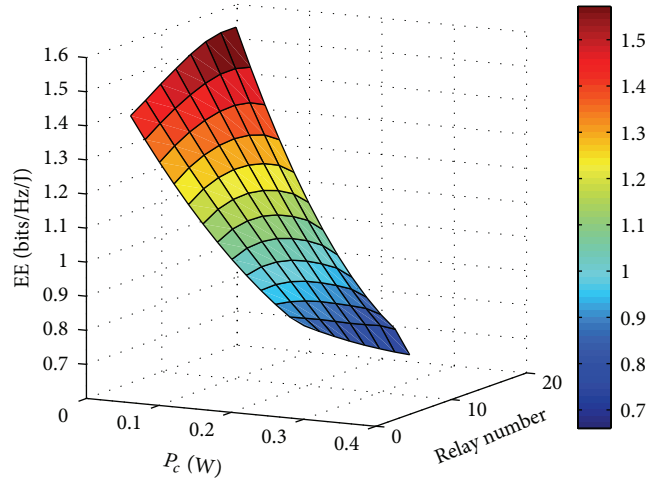

FIGURE 9: Energy efficiency versus different numbers of relays and circuit energy consumption with $w_1 = w_2 = 1$.

Such additional circuit energy consumption will increase with the number of relays. We consider the throughput per unit power rather than the throughput. Therefore, EE will decrease when the energy consumption is greater than its contribution in rate. This phenomenon will occur especially when the number of relays is large.

Figures 5, 6, and 7 plot the throughput corresponding to the EE in Figures 2, 3, and 4, respectively. From them, the throughput of the spectral-efficient design is, as expected, more than that of the energy-efficient design. Combining Figures 2 and 5, Figures 3 and 6, and Figures 4 and 7, we can get that the maximum EE and the maximum throughput are not necessarily simultaneously achieved. Due to the limited space, we will investigate the tradeoff relationship in detail in our future work.

Figure 8 illustrates EE versus different numbers of relays under the proposed optimal scheme and suboptimal scheme-based OSP. $\delta^2_{k,n}$ and $\delta^2_{n,D}$ are set to zero. Figure 8 indicates that, as the relay number increases, EE first increases and then decreases. For different circuit energy consumption, the relay number also differs when EE reaches the maximum. For example, for $P_c = 0.18$ W, EE reaches the maximum when the number of relays is 6. However, for $P_c = 0.2$ W, the best relay number is 4. With the decreased circuit energy consumption, the best relay number increases. To express the relationship clearly, we plot EE versus different relay

numbers and circuit energy consumption with the optimal scheme only in Figure 9. The figure illustrates that the change of EE with the relay number differs under different circuit energy consumption. For example, when the circuit energy consumption is low, EE increases with the relay number. However, with increasing circuit energy consumption, EE first increases and then decreases. When the circuit energy consumption is high, EE monotone decreases. Therefore, high circuit energy consumption is unfavorable to EE when the number of relays is large.

6. Conclusion

In this paper, we formulate an energy-efficient resource allocation problem for a cooperative multirelay OFDMA uplink system with AF protocol. This paper determines the joint optimization of subcarrier pairing, relay assignment, subcarrier assignment, and power allocation with the objective of maximizing EE. Individual power constraint for every user and relay is applied. To solve the complex fraction problem, we transform the considered EE problem in fractional form into an equivalent optimal problem in subtractive form. However, the mixed integer programming problem is NP-hard. We utilize the dual method to solve the problem efficiently. To reduce the complexity of the problem, we propose two low-complexity schemes for subcarrier pairing. The simulation results show greater EE improvement of the energy-efficient design than that of the spectral-efficient design, and the performance of the proposed suboptimal algorithm OSP-based is close to that of the optimal algorithm. EE differs under different relay numbers and is also affected by circuit energy consumption. In future work, we will study the fundamental tradeoff between EE and SE in cooperative communication.

Appendices

A. Proof of Convex Function

We define the function as

$$f(x,y) = \log\left(1 + x + \frac{xy}{x+y}\right), \quad x, y > 0. \tag{A.1}$$

The Hessian of $f(x, y)$ can be written as

$$\nabla^2 f(x,y) = \begin{bmatrix} \dfrac{\partial^2 f}{\partial x^2} & \dfrac{\partial^2 f}{\partial y \partial x} \\ \dfrac{\partial^2 f}{\partial x \partial y} & \dfrac{\partial^2 f}{\partial y^2} \end{bmatrix}, \tag{A.2}$$

where

$$\frac{\partial^2 f}{\partial x^2} = \frac{-(x+y)^4 - y^2\left[3(x+y)^2 + 2x + 2y + x^2 + 2xy\right]}{(x+y)^2(x+y+x^2+2xy)^2}, \tag{A.3}$$

$$\frac{\partial^2 f}{\partial y \partial x} = -\frac{-x^2\left[(x+y)^2 + y^2\right] + 2x^2 y(1 + x + y + 2y)}{(x+y)^2(x+y+x^2+2xy)^2}, \tag{A.4}$$

$$\frac{\partial^2 f}{\partial x \partial y} = -\frac{-x^2\left[(x+y)^2 + y^2\right] + 2x^2 y(1 + x + y + 2y)}{(x+y)^2(x+y+x^2+2xy)^2}, \tag{A.5}$$

$$\frac{\partial^2 f}{\partial y^2} = \frac{-x^2\left[3x^2 + 2x + 2y + 4xy\right]}{(x+y)^2(x+y+x^2+2xy)^2}, \tag{A.6}$$

$$\begin{aligned} &\begin{bmatrix} a & b \end{bmatrix} \nabla^2 f(x,y) \begin{bmatrix} a & b \end{bmatrix}^T \\ &= \Big(-\left[a(x+y)^2 + bx^2\right]^2 - \left(ay^2 + bx^2\right)^2 - 2(x + y + 2xy) \\ &\qquad \times (ay - bx)^2 - \left(2axy - bx^2\right)^2 - 2a^2 y^3 (y + 2x) \Big) \\ &\quad \times \left((x+y)^2\left(x + y + x^2 + 2xy\right)^2\right)^{-1} \le 0. \end{aligned} \tag{A.7}$$

For any a and b, (A.7) means that the Hessian of $f(x, y)$ is negative semidefinite, and $f(x, y)$ is jointly concave on x and y [23]. Using affine mapping operation, $f(\alpha x, \beta y)$ remains the concavity on x and y, where α and β are constant values.

B. Proof of Theorems 1–3

Proof of Theorem 1. We assume that $q_1 > q_2$ and $F(q_1) = R(\boldsymbol{\rho}_1, \boldsymbol{\gamma}_1, \mathbf{p}_1) - q_1(\boldsymbol{\rho}_1, \boldsymbol{\gamma}_1, \mathbf{p}_1)$. Consider

$$\begin{aligned} F(q_1) &= \max_{\boldsymbol{\rho},\boldsymbol{\gamma},\mathbf{p}\in\boldsymbol{\pi}} \{R(\boldsymbol{\rho},\boldsymbol{\gamma},\mathbf{p}) - q_1(\boldsymbol{\rho},\boldsymbol{\gamma},\mathbf{p})\} \\ &= R(\boldsymbol{\rho}_1,\boldsymbol{\gamma}_1,\mathbf{p}_1) - q_1(\boldsymbol{\rho}_1,\boldsymbol{\gamma}_1,\mathbf{p}_1) \\ &< R(\boldsymbol{\rho}_1,\boldsymbol{\gamma}_1,\mathbf{p}_1) - q_2(\boldsymbol{\rho}_1,\boldsymbol{\gamma}_1,\mathbf{p}_1) \\ &\le \max_{\boldsymbol{\rho},\boldsymbol{\gamma},\mathbf{p}\in\boldsymbol{\pi}} \{R(\boldsymbol{\rho},\boldsymbol{\gamma},\mathbf{p}) - q_2(\boldsymbol{\rho},\boldsymbol{\gamma},\mathbf{p})\} = F(q_2). \end{aligned} \tag{B.1}$$

□

Proof of Theorem 2. Considering the integer variables $\rho_{k,n}^{m,m'}$ and $\gamma_{m,m'}$, the feasible domain of $(\boldsymbol{\rho}, \boldsymbol{\gamma})$ is a discrete and finite set that consists of all possible subcarrier allocations. Therefore, $F(q)$ is generally a continuous but nondifferentiable function for q. Given that $\lim_{q\to-\infty} F(q) = +\infty$ and $\lim_{q\to\infty} F(q) = -\infty$, as well as considering Theorem 1, we can obtain Theorem 2. □

Proof of Theorem 3. We define problem 1 as follows:

$$q_0 = \frac{R(\boldsymbol{\rho}_0, \boldsymbol{\gamma}_0, \mathbf{p}_0)}{P(\boldsymbol{\rho}_0, \boldsymbol{\gamma}_0, \mathbf{p}_0)} = \max_{\boldsymbol{\rho},\boldsymbol{\gamma},\mathbf{p}\in\boldsymbol{\pi}} \frac{R(\boldsymbol{\rho}, \boldsymbol{\gamma}, \mathbf{p})}{P(\boldsymbol{\rho}, \boldsymbol{\gamma}, \mathbf{p})}. \tag{B.2}$$

Problem 2 is expressed as follows:

$$\begin{aligned} F(q_0) &= F(q_0, (\boldsymbol{\rho}_0, \boldsymbol{\gamma}_0, \mathbf{p}_0)) \\ &= \max_{\boldsymbol{\rho},\boldsymbol{\gamma},\mathbf{p}\in\boldsymbol{\pi}} \{R(\boldsymbol{\rho}, \boldsymbol{\gamma}, \mathbf{p}) - q_0(\boldsymbol{\rho}, \boldsymbol{\gamma}, \mathbf{p})\} = 0. \end{aligned} \tag{B.3}$$

(a) If we have known

$$\begin{aligned} q_0 &= \frac{R(\boldsymbol{\rho}_0, \boldsymbol{\gamma}_0, \mathbf{p}_0)}{P(\boldsymbol{\rho}_0, \boldsymbol{\gamma}_0, \mathbf{p}_0)} \\ &= \max_{\boldsymbol{\rho},\boldsymbol{\gamma},\mathbf{p}\in\boldsymbol{\pi}} \frac{R(\boldsymbol{\rho}, \boldsymbol{\gamma}, \mathbf{p})}{P(\boldsymbol{\rho}, \boldsymbol{\gamma}, \mathbf{p})} \geq \frac{R(\boldsymbol{\rho}, \boldsymbol{\gamma}, \mathbf{p})}{P(\boldsymbol{\rho}, \boldsymbol{\gamma}, \mathbf{p})}, \end{aligned} \tag{B.4}$$

we can obtain

$$R(\boldsymbol{\rho}, \boldsymbol{\gamma}, \mathbf{p}) - q_0 P(\boldsymbol{\rho}, \boldsymbol{\gamma}, \mathbf{p}) \leq 0 \tag{B.5a}$$

$$R(\boldsymbol{\rho}_0, \boldsymbol{\gamma}_0, \mathbf{p}_0) - q_0 P(\boldsymbol{\rho}_0, \boldsymbol{\gamma}_0, \mathbf{p}_0) = 0. \tag{B.5b}$$

According to (B.5a), we have $F(q_0) = \max_{\boldsymbol{\rho},\boldsymbol{\gamma},\mathbf{p}\in\boldsymbol{\pi}}\{R(\boldsymbol{\rho}, \boldsymbol{\gamma}, \mathbf{p}) - q_0 P(\boldsymbol{\rho}, \boldsymbol{\gamma}, \mathbf{p})\} = 0$. Equation (B.5b) indicates that the maximum is $(\boldsymbol{\rho}_0, \boldsymbol{\gamma}_0, \mathbf{p}_0)$. Thus, the first part of the proof is finished.

(b) If we know

$$\begin{aligned} F(q_0) &= F(q_0, (\boldsymbol{\rho}_0, \boldsymbol{\gamma}_0, \mathbf{p}_0)) \\ &= \max_{\boldsymbol{\rho},\boldsymbol{\gamma},\mathbf{p}\in\boldsymbol{\pi}} \{R(\boldsymbol{\rho}, \boldsymbol{\gamma}, \mathbf{p}) - q_0(\boldsymbol{\rho}, \boldsymbol{\gamma}, \mathbf{p})\} = 0, \end{aligned} \tag{B.6}$$

then we can have

$$\begin{aligned} &R(\boldsymbol{\rho}, \boldsymbol{\gamma}, \mathbf{p}) - q_0 P(\boldsymbol{\rho}, \boldsymbol{\gamma}, \mathbf{p}) \\ &\quad \leq R(\boldsymbol{\rho}_0, \boldsymbol{\gamma}_0, \mathbf{p}_0) - q_0 P(\boldsymbol{\rho}_0, \boldsymbol{\gamma}_0, \mathbf{p}_0) = 0. \end{aligned} \tag{B.7}$$

Hence,

$$R(\boldsymbol{\rho}, \boldsymbol{\gamma}, \mathbf{p}) - q_0 P(\boldsymbol{\rho}, \boldsymbol{\gamma}, \mathbf{p}) \leq 0 \tag{B.8a}$$

$$R(\boldsymbol{\rho}_0, \boldsymbol{\gamma}_0, \mathbf{p}_0) - q_0 P(\boldsymbol{\rho}_0, \boldsymbol{\gamma}_0, \mathbf{p}_0) = 0. \tag{B.8b}$$

Using (B.8a), we have $q_0 \geq R(\boldsymbol{\rho}, \boldsymbol{\gamma}, \mathbf{p})/P(\boldsymbol{\rho}, \boldsymbol{\gamma}, \mathbf{p})$. Thus, q_0 is the maximum of problem 1. With (B.8b), we have $q_0 = R(\boldsymbol{\rho}_0, \boldsymbol{\gamma}_0, \mathbf{p}_0)/P(\boldsymbol{\rho}_0, \boldsymbol{\gamma}_0, \mathbf{p}_0)$. Therefore, $(\boldsymbol{\rho}_0, \boldsymbol{\gamma}_0, \mathbf{p}_0)$ is a solution vector of problem 1. □

C. Derivation of (24)

We present the detailed derivation about (24) in (C.1) as follows:

$$\begin{aligned} &g(\boldsymbol{\lambda}, \boldsymbol{\mu}, \boldsymbol{\upsilon}) \\ &\triangleq \max_{\{\boldsymbol{\rho},\boldsymbol{\gamma}\}\in\boldsymbol{\Omega}} L(\boldsymbol{\rho}, \boldsymbol{\gamma}, \mathbf{p}, \boldsymbol{\lambda}, \boldsymbol{\mu}, \boldsymbol{\upsilon}) \\ &= \max_{\{\boldsymbol{\rho},\boldsymbol{\gamma}\}\in\boldsymbol{\Omega}} \sum_{k=1}^{K}\sum_{n=1}^{N}\sum_{m=1}^{M}\sum_{m'=1}^{M} w_k r_{k,n}^{m,m'} \\ &\quad - q\left(\xi\sum_{k=1}^{K}\sum_{n=1}^{N}\sum_{m=1}^{M}\sum_{m'=1}^{M}\left(p_{S,k}^{m} + p_{R,n}^{m'}\right) + \sum_{k=1}^{K} P_{C,S}^{k} + \sum_{n=1}^{N} P_{C,R}^{n}\right) \\ &\quad + \sum_{k=1}^{k}\lambda_k\left(P_{S,k} - \sum_{m=1}^{M} p_{S,k}^{m}\right) \\ &\quad + \sum_{n=1}^{N}\mu_n\left(P_{S,n} - \sum_{m'=1}^{M} p_{R,n}^{m'}\right) + \sum_{k=1}^{k}\upsilon_k\left(R_{S,k} - Q_{S,k}\right) \\ &= \max_{\{\boldsymbol{\rho},\boldsymbol{\gamma}\}\in\boldsymbol{\Omega}} \sum_{k=1}^{K}\sum_{n=1}^{N}\sum_{m=1}^{M}\sum_{m'=1}^{M} w_k r_{k,n}^{m,m'} + \sum_{k=1}^{k}\upsilon_k R_{S,k} \\ &\quad - q\xi\sum_{k=1}^{K}\sum_{n=1}^{N}\sum_{m=1}^{M}\sum_{m'}^{M} p_{S,k}^{m} - \sum_{k=1}^{k}\lambda_k\sum_{m=1}^{M} p_{S,k}^{m} - q\xi\sum_{k=1}^{K}\sum_{n=1}^{N}\sum_{m=1}^{M}\sum_{m'=1}^{M} p_{R,n}^{m'} \\ &\quad - \sum_{n=1}^{N}\mu_n P_{S,n} + \sum_{k=1}^{k}\lambda_k P_{S,k} + \sum_{n=1}^{N}\mu_n P_{S,n} \\ &\quad + q\left(\sum_{k=1}^{K} P_{C,S}^{k} + \sum_{n=1}^{N} P_{C,R}^{n}\right) - \sum_{k=1}^{k}\upsilon_k Q_{S,k} \\ &= \max_{\{\boldsymbol{\rho},\boldsymbol{\gamma}\}\in\boldsymbol{\Omega}} \sum_{k=1}^{K}\sum_{n=1}^{N}\sum_{m=1}^{M}\sum_{m'=1}^{M}\left(w_k(1+\upsilon_k) r_{k,n}^{m,m'} - (q\xi + \lambda_k) p_{S,k}^{m}\right. \\ &\qquad \left. - (q\xi + \mu_n) p_{R,n}^{m'}\right) \\ &\quad + \sum_{k=1}^{k}\lambda_k P_{S,k} + \sum_{n=1}^{N}\mu_n P_{S,n} + q\left(\sum_{k=1}^{K} P_{C,S}^{k} + \sum_{n=1}^{N} P_{C,R}^{n}\right) - \sum_{k=1}^{k}\upsilon_k Q_{S,k}. \end{aligned} \tag{C.1}$$

D. Solving Process of (26)

We can obtain the partial derivative of L below.

For simplicity, variables $p_{S,k}^{m}$, $p_{R,n}^{m'}$, $\alpha_{k,D}^{m}$, $\alpha_{k,n}^{m}$, and $\alpha_{n,D}^{m'}$ are replaced by P_1, P_2, α_1, α_2, and α_3, respectively. Consider

$$\frac{\partial L}{\partial p_1} = \frac{w(1+v)}{2\ln 2} \cdot \frac{1}{a} \cdot \frac{\alpha_3 (p_1\alpha_1 + p_2\alpha_2)^2 + p_2^2\alpha_1\alpha_2^2}{p_1\alpha_1 + p_2\alpha_2} - (q\xi + \lambda) \tag{D.1}$$

$$\begin{aligned} \frac{\partial L}{\partial p_2} &= \frac{w(1+v)}{2\ln 2} \cdot \frac{1}{a} \cdot \frac{p_1^2\alpha_1^2\alpha_2}{p_1\alpha_1 + p_2\alpha_2} - (q\xi + \mu) \\ a &= p_1\alpha_1 + p_2\alpha_2 \\ &\quad + p_1 (p_1\alpha_1\alpha_3 + p_2\alpha_2\alpha_3 + p_2\alpha_1\alpha_2). \end{aligned} \tag{D.2}$$

When P_1 and P_2 are positive, (D.1) and (D.2) will be zero. Thus, we can have

$$\begin{aligned} &(q\xi + \mu)\left[\alpha_3 (p_1\alpha_1 + p_2\alpha_2)^2 + {p_2}^2\alpha_1\alpha_2^2\right] \\ &\quad = (q\xi + \lambda)\left(p_1^2\alpha_1^2\alpha_2\right). \end{aligned} \tag{D.3}$$

Equation (D.3) can be simplified as follows:

$$p_1 = bp_2, \tag{D.4}$$

where

$$\begin{aligned} b = &\left(\alpha_2 \left(((q\xi + \mu)(\alpha_1\alpha_2 (q\xi + \lambda) - \alpha_1\alpha_3 (q\xi + \mu) \right.\right. \\ &\left.\left. + \alpha_2\alpha_3 (q\xi + \lambda)))^{1/2} + \alpha_3 (q\xi + \mu)\right)\right) \\ &\times (\alpha_1 [\alpha_2 (q\xi + \lambda) - \alpha_3 (q\xi + \mu)])^{-1}. \end{aligned} \tag{D.5}$$

The factor b must be greater than zero. We therefore have $\alpha_2(q\xi + \lambda) > \alpha_3(q\xi + \mu)$. Substituting (D.4) into (D.1), we obtain

$$\begin{aligned} p_2 = &\frac{w(1+v)}{2\ln 2} \\ &\times \left(\alpha_1\alpha_2^2 + \left(\alpha_3 - \frac{2(q\xi + \lambda)\ln 2}{w(1+v)}\right)\left(\alpha_1 b + \alpha_2^2\right)^2\right) \\ &\times (b(q\xi + \lambda)(\alpha_1 b + \alpha_2)(\alpha_3\alpha_1 b + \alpha_2\alpha_3 + \alpha_1\alpha_2))^{-1}. \end{aligned} \tag{D.6}$$

If $p_2 < 0$, then P_2 should be set to zero.

When $\alpha_2(q\xi + \lambda) \le \alpha_3(q\xi + \mu)$, $p_2 = 0$. For these cases, the optimal power allocation in the first phase can be expressed as follows:

$$p_1 = \left(\frac{w(1+v)}{2\ln 2(q+\lambda)} - \frac{1}{\alpha_3}\right)^{+}. \tag{D.7}$$

Thus, (27) and (28) are proved.

Conflict of Interests

The authors declare that there is no conflict of interests regarding the publication of this paper.

Acknowledgment

This study is funded by the National Natural Science Foundation of China (Grant no. 61271421).

References

[1] A. Nosratinia, T. E. Hunter, and A. Hedayat, "Cooperative communication in wireless networks," *IEEE Communications Magazine*, vol. 42, no. 10, pp. 74–80, 2004.

[2] Ö. Oyman, J. N. Laneman, and S. Sandhu, "Multihop relaying for broadband wireless mesh networks: from theory to practice," *IEEE Communications Magazine*, vol. 45, no. 11, pp. 116–122, 2007.

[3] W. Su, A. K. Sadek, and K. J. Ray Liu, "Cooperative communication protocols in wireless networks: performance analysis and optimum power allocation," *Wireless Personal Communications*, vol. 44, no. 2, pp. 181–217, 2008.

[4] J. N. Laneman, D. N. C. Tse, and G. W. Wornell, "Cooperative diversity in wireless networks: efficient protocols and outage behavior," *IEEE Transactions on Information Theory*, vol. 50, no. 12, pp. 3062–3080, 2004.

[5] D. W. K. Ng, E. S. Lo, and R. Schober, "Energy-efficient resource allocation in multi-cell OFDMA systems with limited backhaul capacity," in *Proceedings of the IEEE Wireless Communications and Networking Conference (WCNC '12)*, Paris, France, 2012.

[6] Y. Li, W. Wang, J. Kong, and M. Peng, "Subcarrier pairing for amplify-and-forward and decode-and-forward OFDM relay links," *IEEE Communications Letters*, vol. 13, no. 4, pp. 209–211, 2009.

[7] Y. Li, W. Wang, J. Kong, W. Hong, X. Zhang, and M. Peng, "Power allocation and subcarrier pairing in OFDM-based relaying networks," in *Proceedings of the IEEE International Conference on Communications (ICC '08)*, pp. 2602–2606, May 2008.

[8] M. Kaneko, K. Hayashi, P. Popovski, K. Ikeda, H. Sakai, and R. Prasad, "Amplify-and-forward cooperative diversity schemes for Multi-Carrier systems," *IEEE Transactions on Wireless Communications*, vol. 7, no. 5, pp. 1845–1850, 2008.

[9] W. Dang, M. Tao, H. Mu, and J. Huang, "Subcarrier-pair based resource allocation for cooperative multi-relay OFDM systems," *IEEE Transactions on Wireless Communications*, vol. 9, no. 5, pp. 1640–1649, 2010.

[10] M. S. Alam, J. W. Mark, and X. S. Shen, "Relay selection and resource allocation for multi-user cooperative OFDMA networks," *IEEE Transactions on Wireless Communications*, vol. 12, no. 5, pp. 2193–2205, 2013.

[11] X. Zhang, W. Jiao, and M. Tao, "End-to-end resource allocation in OFDM based linear multi-hop networks," in *Proceedings of the 27th IEEE Communications Society Conference on Computer Communications (INFOCOM '08)*, Phoenix, Ariz, USA, April 2008.

[12] X. Zhang, M. Tao, W. Jiao, and C. S. Ng, "End-to-end outage minimization in OFDM based linear relay networks," *IEEE Transactions on Communications*, vol. 57, no. 10, pp. 3034–3044, 2009.

[13] C. N. Hsu, H. J. Su, and P. H. Lin, "Joint subcarrier pairing and power allocation for OFDM transmission with decode-and-forward relaying," *IEEE Transactions on Signal Processing*, vol. 59, no. 1, pp. 399–414, 2011.

[14] D. W. K. Ng and R. Schober, "Cross-layer scheduling for OFDMA amplify-and-forward relay networks," *IEEE Transactions on Vehicular Technology*, vol. 59, no. 3, pp. 1443–1458, 2010.

[15] Y. Chen, S. Zhang, S. Xu, and G. Y. Li, "Fundamental trade-offs on green wireless networks," *IEEE Communications Magazine*, vol. 49, no. 6, pp. 30–37, 2011.

[16] T. Chen, H. Kim, and Y. Yang, "Energy efficiency metrics for green wireless communications," in *Proceedings of the International Conference on Wireless Communications and Signal Processing (WCSP '10)*, pp. 1–6, October 2010.

[17] C. Han, T. Harrold, S. Armour et al., "Green radio: radio techniques to enable energy-efficient wireless networks," *IEEE Communications Magazine*, vol. 49, no. 6, pp. 46–54, 2011.

[18] H. Bogucka and A. Conti, "Degrees of freedom for energy savings in practical adaptive wireless systems," *IEEE Communications Magazine*, vol. 49, no. 6, pp. 38–45, 2011.

[19] C. Xiong, G. Y. Li, S. Zhang, Y. Chen, and S. Xu, "Energy-efficient resource allocation in OFDMA networks," in *Proceedings of the 54th Annual IEEE Global Telecommunications Conference (GLOBECOM '11)*, pp. 1–5, Houston, Tex, USA, December 2011.

[20] C. Xiong, G. Y. Li, S. Zhang, Y. Chen, and S. Xu, "Energy- and spectral-efficiency tradeoff in downlink OFDMA networks," *IEEE Transactions on Wireless Communications*, vol. 10, no. 11, pp. 3874–3886, 2011.

[21] D. W. K. Ng, E. S. Lo, and R. Schober, "Energy-efficient resource allocation in multi-cell OFDMA systems with limited backhaul capacity," *IEEE Transactions on Wireless Communications*, vol. 11, no. 10, pp. 3618–3631, 2012.

[22] D. W. K. Ng, E. S. Lo, and R. Schober, "Wireless information and power transfer: energy efficiency optimization in OFDMA systems," *IEEE Transactions on Wireless Communications*, vol. 12, no. 12, pp. 6352–6370, 2013.

[23] R. S. Prabhu and B. Daneshrad, "An energy-efficient water-filling algorithm for OFDM systems," in *Proceedings of the IEEE International Conference on Communications (ICC '10)*, May 2010.

[24] X. Xiao, X. Tao, and J. Lu, "QoS-aware energy-efficient radio resource scheduling in multi-user OFDMA systems," *IEEE Communications Letters*, vol. 17, no. 1, pp. 75–78, 2013.

[25] J. Zhang, Y. Jiang, and X. Li, "Energy-efficient resource allocation in multiuser relay-based OFDMA networks," *Concurrency and Computation: Practice and Experience*, vol. 25, no. 9, pp. 1113–1125, 2013.

[26] H. Yu, H. Qin, Y. Z. Li, Y. Zhao, and J. Wang, "Energy-efficient power allocation for non-regenerative OFDM relay links," *Science China Information Sciences*, vol. 56, no. 2, pp. 185–192, 2013.

[27] J. Tang and X. Zhang, "Cross-layer resource allocation over wireless relay networks for quality of service provisioning," *IEEE Journal on Selected Areas in Communications*, vol. 25, no. 4, pp. 645–655, 2007.

[28] S. Cui, A. J. Goldsmith, and A. Bahai, "Energy-constrained modulation optimization," *IEEE Transactions on Wireless Communications*, vol. 4, no. 5, pp. 2349–2360, 2005.

[29] W. Dinkelbach, "On nonlinear fractional programming," *Management Science*, vol. 13, no. 7, pp. 492–498, 1967.

[30] W. Yu and R. Lui, "Dual methods for nonconvex spectrum optimization of multicarrier systems," *IEEE Transactions on Communications*, vol. 54, no. 7, pp. 1310–1322, 2006.

[31] S. Boyd and L. Vandenberghe, *Convex Optimization*, Cambridge University Press, Cambridge, UK, 2004.

[32] S. Boyd, L. Xiao, and A. Mutapcic, "Subgradient methods," lecture Notes EE392o, Stanford University, Stanford, Calif, USA, 2004.

[33] H. W. Kuhn, "The Hungarian method for the assignment problem," *Naval Research Logistics Quarterly*, vol. 2, pp. 83–97, 1955.

Hindawi Publishing Corporation
International Journal of Antennas and Propagation
Volume 2014, Article ID 798015, 9 pages
http://dx.doi.org/10.1155/2014/798015

Research Article

An Analytical Study of the Impact of Arbitrary Receive Antenna Correlation in TAS/MRC

Juan P. Peña-Martín and Juan M. Romero-Jerez

Department of Electronic Technology, E.T.S.I. of Telecommunication, University of Malaga, 29071 Malaga, Spain

Correspondence should be addressed to Juan P. Peña-Martín; jppena@uma.es

Received 13 March 2014; Accepted 29 May 2014; Published 16 June 2014

Academic Editor: Theodoros Tsiftsis

Copyright © 2014 J. P. Peña-Martín and J. M. Romero-Jerez. This is an open access article distributed under the Creative Commons Attribution License, which permits unrestricted use, distribution, and reproduction in any medium, provided the original work is properly cited.

Novel closed-form expressions are derived for the performance analysis of a multiple-input multiple-output (MIMO) system in Rayleigh fading using transmit antenna selection (TAS) at the transmitter and maximal ratio combining (MRC) at the receiver. Receive antennas are assumed to be arbitrarily correlated, as no restriction is imposed on the correlation matrix. General exact and asymptotic expressions to evaluate the bit error rate (BER) of different modulation schemes are presented for uncoded transmission, and a closed-form expression is presented for the channel capacity. It is demonstrated that channel capacity may improve due to correlation at the receive antennas if the transmit array size is large enough as a result of a higher signal variability and the antenna selection performed at the transmitter. Monte Carlo simulations have been carried out to validate the analysis, showing an excellent agreement with the theoretical results.

1. Introduction

Multiple-input multiple-output (MIMO) systems use multiple antennas at both the transmit and receive ends to improve the performance of wireless links. Among the different possible MIMO schemes, TAS/MRC, employing transmit antenna selection at the transmitter and maximal ratio combining at the receiver, has been proposed as a means to provide full diversity gain and reduce implementation complexity [1].

Several works have analyzed the performance of TAS/MRC systems in different fading conditions in the last decade; however, most previous works assume uncorrelated antennas at both the transmit and receive ends [1–5]. In practice, space correlation among antennas may occur, which can be significant in portable terminals due to space limitations. Few works have studied the performance of TAS/MRC systems in correlated fading. An error rate analysis for a semicorrelated scenario, assuming receive antenna correlation, was presented in [6] for Rayleigh fading; however, the analysis was simplified by assuming that all the eigenvalues of the correlation matrix are different, which may not be realistic in practice. In [7], the outage probability was evaluated for Nakagami fading, which includes Rayleigh fading as a special case, and the same system model was used in [8] to obtain an exact expression for the bit error rate (BER) of binary phase-shift keying (BPSK), but again considering that all eigenvalues are distinct. A TAS/MRC system with arbitrarily correlated receive antennas is considered in [9], but the analysis is approximated by considering that the sum of gamma variates with arbitrary parameters is a gamma variate. The error made with this approximation was extensively studied in [10], under the assumptions of constant or circular correlation, where it was shown that the approximated pdf tends to deviate in the lower tail from the exact pdf, and this lower tail is critical for error rate calculations. Lee's spatiotemporal model was considered in TAS/MRC in [11], but only a uniform linear receive antenna array is studied. The analysis of ergodic capacity in TAS/MRC systems seems to have received less attention. Recently, ergodic capacity was studied in [12] for TAS/MRC in the context of spectrum sharing systems. However, the study was restricted to uncorrelated antennas.

In this work, we study a TAS/MRC system in semicorrelated Rayleigh fading channels where transmit antennas are assumed to be independent and receive antennas are considered to be arbitrarily correlated. No restriction is

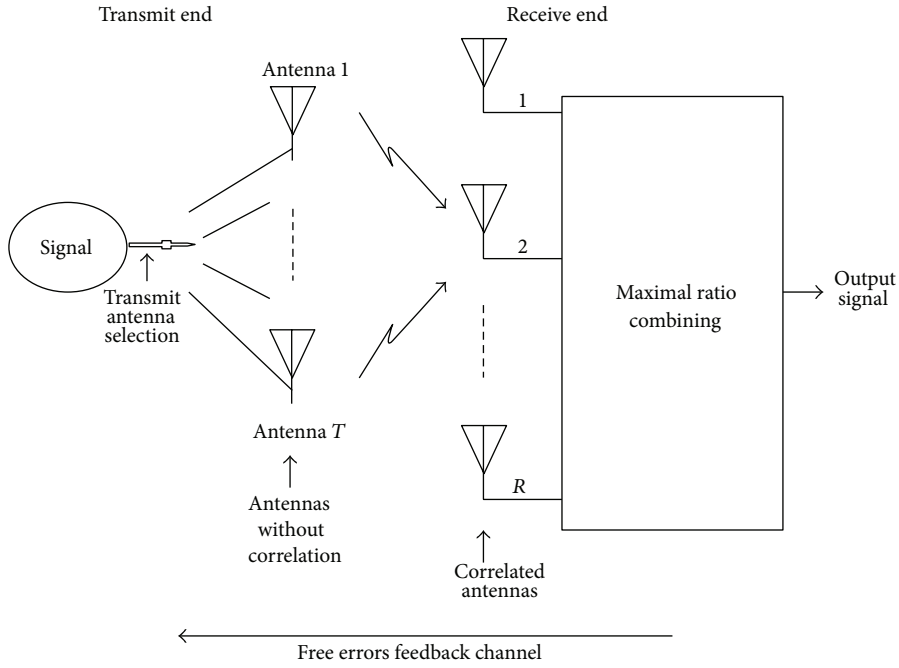

Figure 1: Simplified system model.

imposed on the correlation matrix of the receive array, as arbitrary correlation is considered between any pair of receive antennas, thereby allowing the multiplicity of the receive correlation matrix eigenvalues to be arbitrary. We derive closed-form expressions for the pdf and CDF of the signal-to-noise ratio (SNR) as well as for the BER of different modulation schemes for uncoded transmission. In order to provide insight into the impact of the different system parameters on performance, a simple and compact asymptotic expression of the BER for the high SNR regime is also derived and it is shown that correlation results in an increased BER for high values of the SNR. We also develop an expression for the ergodic capacity and, by studying the derivative of capacity with respect to correlation, we demonstrate that the presence of correlation may increase channel capacity if the number of transmit antennas is high enough. This beneficial impact of correlation on capacity has also been observed in multiuser MIMO schemes (see [13] and references therein) where the user with the best channel gain is selected for transmission. However, results in multiuser MIMO are usually based on bounds or, as in [13], asymptotic analysis on the number of users. On the other hand, our analysis yields closed-form expressions for any number of transmit antennas, which allow calculating the number of the required transmit antennas for the correlation to be beneficial, which will be a function of the number of receive antennas. Monte Carlo simulations have been carried out to validate our analysis, showing an excellent agreement with the theoretical results.

2. System Model and Output SNR Statistics

Let us consider a wireless system with T transmit and R receive antennas where the signal at every receive antenna is corrupted by additive white Gaussian noise (AWGN). At the receive end, MRC is used, whereas at the transmit end the antenna that maximizes the instantaneous SNR after combining is selected for transmission. A simple diagram of the system model is shown in Figure 1. We assume independent and identically distributed (i.i.d.) slowly varying (with respect to the symbol duration) flat Rayleigh fading between any pair of transmit and receive antennas. Thus, the instantaneous SNR at receive antenna i due to the signal transmitted from transmit antenna j, denoted as β_{ij}, follows an exponential distribution with probability density function (pdf):

$$f_{\beta_{ij}}(x) = \left(\frac{1}{\Omega}\right)\exp\left(\frac{-x}{\Omega}\right); \quad x \geq 0; \quad i = 1, \ldots, R; \quad j = 1, \ldots, T, \tag{1}$$

where Ω is the average SNR per branch.

For MRC combining, it is known that, when the transmit antenna j is selected for transmission, the instantaneous output SNR per symbol is $\beta_j = \sum_{i=1}^{R} \beta_{ij}$. As the receive antennas are assumed to be arbitrarily correlated, the pdf of β_j can be obtained from its moment generating function (MGF), which is given by [14]

$$\Psi_{\beta_j}(s) = \prod_{i=1}^{J}(1 - s\lambda_i)^{-n_i}, \tag{2}$$

where $\{\lambda_i\}_{i=1}^{J}$ are the distinct eigenvalues of the matrix $\mathbf{A} = \Omega\mathbf{M}_x$, $\mathbf{M}_x$ is a full rank signal correlation matrix of the receive array, J is the number of distinct eigenvalues, and eigenvalue λ_i is assumed to have multiplicity n_i. The elements of the SNR

correlation matrix are denoted by ρ_{ik}, which are related to the elements of $\mathbf{M}_x$ by [15]

$$\mathbf{M}_x(i,k) = (\rho_{ik})^{1/2}; \quad i,k = 1,\ldots,R. \tag{3}$$

Using partial fraction expansion, (2) can be written more conveniently as

$$\Psi_{\beta_j}(s) = \sum_{i=1}^{J}\sum_{k=1}^{n_i} \frac{A_{ik}}{(1-s\lambda_i)^{n_i-k+1}}, \tag{4}$$

where the coefficients A_{ik} can be written in closed form as

$$A_{ik} = (-1)^{k-1} \cdot \sum_{\tau(i,k-1,J-1)} \prod_{\substack{m=1 \\ m\neq i}}^{J} \binom{n_m+q_m-1}{n_m-1} \frac{\lambda_m^{q_m}\lambda_i^{n_m}}{(\lambda_i-\lambda_m)^{n_m+q_m}}, \tag{5}$$

and $\tau(i,k-1,J-1)$ is the set of $(J-1)$-tuples such that

$$\left\{ (q_1,\ldots,q_{i-1},q_{i+1},\ldots,q_J) : q_k \in \mathbb{N}, \sum_{\substack{m=1 \\ m\neq i}}^{J} q_m = k-1 \right\}. \tag{6}$$

From (4), by the inverse Laplace transform, the pdf of β_j can be calculated as

$$f_{\beta_j}(x) = \sum_{i=1}^{J}\sum_{k=1}^{n_i} \frac{A_{ik}x^{n_i-k}}{(n_i-k)!\lambda_i^{n_i-k+1}} e^{-x/\lambda_i}, \tag{7}$$

and its cumulative distribution function (CDF) is obtained by integrating (7), yielding

$$F_{\beta_j}(x) = \sum_{i=1}^{J}\sum_{k=1}^{n_i} A_{ik}\left(1 - e^{-x/\lambda_i}\sum_{r=0}^{n_i-k}\frac{1}{r!}\left(\frac{x}{\lambda_i}\right)^r\right). \tag{8}$$

The unconditional instantaneous output SNR per symbol will be $\beta = \max_j\{\beta_j\}$, and its CDF can be calculated, assuming statistical independence among transmit antennas, as $F_\beta(x) = \prod_{j=1}^{T} F_{\beta_j}(x)$. Then,

$$F_\beta(x) = \left(\sum_{i=1}^{J}\sum_{k=1}^{n_i} A_{ik}\left(1 - e^{-x/\lambda_i}\sum_{r=0}^{n_i-k}\frac{1}{r!}\left(\frac{x}{\lambda_i}\right)^r\right)\right)^T, \tag{9}$$

which, for subsequent manipulation, can be rewritten more conveniently, using the binomial expansion theorem, as a finite summation as

$$F_\beta(x) = \sum_{j=0}^{T}\binom{T}{j} a^{T-j}(-1)^j b^j(x) = a^T + \sum_{j=1}^{T}\binom{T}{j} a^{T-j}(-1)^j b^j(x), \tag{10}$$

where $a = \sum_{i=1}^{J}\sum_{k=1}^{n_i} A_{ik}$ and where we have defined the function

$$b(x) = \sum_{i=1}^{J}\sum_{k=1}^{n_i} A_{ik}\exp\left(\frac{-x}{\lambda_i}\right)\sum_{r=0}^{n_i-k}\frac{x^r}{\lambda_i^r r!}. \tag{11}$$

Using the multinomial theorem [16], the jth power of function $b(x)$ can be written as

$$b^j(x) = \sum_{\tau_j}\binom{j}{n_{1,1,0},\ldots,n_{i,k,r},\ldots,n_{J,n_i,0}} c_{\tau_j} e^{-xd_{\tau_j}} x^{g_{\tau_j}}, \tag{12}$$

where $\binom{j}{q_1,\ldots,q_m} = j!/(q_1!\cdots q_m!)$ is the multinomial coefficient and τ_j is the set of tuples

$$\left\{ \left(n_{1,1,0},\ldots,n_{i,k,r},\ldots,n_{J,n_i,0}\right) : n_{i,k,r} \in \mathbb{N}; \; 1 \le i \le J, 1 \le k \le n_i, 0 \le r \le n_i - k; \sum_{i,k,r} n_{i,k,r} = j \right\} \tag{13}$$

and where we have defined the following coefficients:

$$c_{\tau_j} = \prod_{i,k,r}\left(\frac{A_{ik}}{r!\lambda_i^r}\right)^{n_{i,k,r}}, \quad d_{\tau_j} = \sum_i \frac{1}{\lambda_i}\sum_k\sum_r n_{i,k,r}, \quad g_{\tau_j} = \sum_i\sum_k\sum_r r n_{i,k,r}. \tag{14}$$

For the sake of compactness, in the following we will write $\binom{j}{n_{1,1,0},\ldots,n_{i,k,r},\ldots,n_{J,n_i,0}} = \binom{j}{\tau_j}$. Note that $g_{\tau_j} \in \mathbb{Z}^+$ and $d_{\tau_j} \in \mathbb{R}^+$ because $j \ge 1$.

The pdf of the output SNR can therefore be written in compact form by differentiating (10), yielding

$$f_\beta(x) = \sum_{j=1}^{T}\binom{T}{j} a^{T-j}(-1)^j \cdot \sum_{\tau_j}\binom{j}{\tau_j} c_{\tau_j} e^{-xd_{\tau_j}}\left(g_{\tau_j}x^{g_{\tau_j-1}} - d_{\tau_j}x^{g_{\tau_j}}\right). \tag{15}$$

3. Bit Error Probability

The average BER depends on the fading distribution and the modulation technique and can be obtained by averaging the conditional error probability (CEP), that is, the error rate under AWGN, over the output SNR. Alternatively, the average error rate can be expressed in terms of the CDF of the output SNR as

$$\overline{P_e} = \int_0^\infty P_e(x) f_\beta(x)\,dx = -\int_0^\infty P_e'(x) F_\beta(x)\,dx, \tag{16}$$

where $P_e'(x)$ is the first order derivative of the CEP.

For the sake of compactness, in order to compute the BER of the considered modulations, we will use the following expression for the CEP [17, equation (8.100)]:

$$P_e(x) = \frac{\Gamma(\eta, \alpha x)}{2\Gamma(\eta)}, \tag{17}$$

where $\Gamma(a, x) = \int_x^\infty z^{a-1} e^{-z} dz$ is the complementary incomplete gamma function and $\Gamma(a) = \Gamma(a, 0)$ is the gamma function. The values of the constants in (17) are $(\alpha, \eta) = (1, 0.5)$ for BPSK, $(\alpha, \eta) = (0.5, 0.5)$ for BFSK, $(\alpha, \eta) = (1, 1)$ for DBPSK, and $(\alpha, \eta) = (0.5, 1)$ for NCBFSK. Moreover, introducing an additional multiplicative constant and considering the relation between the complementary incomplete gamma function and the Gaussian Q-function, it is possible to use (17) to obtain a good approximation of the symbol error rates for several M-ary modulation schemes [18, Table 6.1].

Taking the derivative of the CEP, we can write

$$P_e'(x) = \frac{-\alpha^\eta x^{\eta-1} e^{-\alpha x}}{2\Gamma(\eta)}. \tag{18}$$

An exact expression of the average BER for the considered modulations can be obtained by introducing (10) and (18) into (16) and solving the integral. The integration is reduced to a sum of terms that match with the gamma function definition. Therefore, we obtain the average BER as

$$\overline{P_e} = \frac{a^T}{2} + \sum_{j=1}^{T} \binom{T}{j} a^{T-j} (-1)^j \frac{\alpha^\eta}{2\Gamma(\eta)} \cdot \sum_{\tau_j} \binom{j}{\tau_j} c_{\tau_j} \left(d_{\tau_j} + \alpha\right)^{-\eta - g_{\tau_j}} \Gamma\left(\eta + g_{\tau_j}\right). \tag{19}$$

Note the simplicity of (19), which is actually a finite sum of elementary functions.

Although the error rate expression (19) is exact and can be easily computed, it does not provide a straightforward insight into the impact of the different system parameters on performance. In the appendix, we show that an asymptotic, yet accurate, simple expression of the error rate for the high SNR regime, from which the effect of system parameters on performance can be established in a simple way, is given by

$$\overline{P_e} \approx \left(\frac{1}{R! \det(\mathbf{M}_x) \alpha^R}\right)^T \frac{\Gamma(RT + \eta)}{2\Gamma(\eta)} \Omega^{-RT}, \quad \Omega \gg 1. \tag{20}$$

It can be observed in (20) that the average BER decreases inversely with the RT^{th} power of the average SNR per antenna, which indicates that the proposed TAS/MRC scheme achieves full diversity gain. On the other hand, it is straightforward to show that the error rate increases in the high SNR regime as antenna correlation increases. Note that, for example, for two receive antennas with SNR correlation denoted as ρ, we have that $\det(\mathbf{M}_x) = 1 - \rho$.

4. Channel Capacity

4.1. Closed-Form Expression of Channel Capacity. The ergodic capacity of the channel $\langle C \rangle_{\text{erg}}$, also referred to as channel capacity, is given by [18]

$$\frac{\langle C \rangle_{\text{erg}}}{B} = \frac{1}{\ln(2)} \int_0^\infty \ln(1 + x) f_\beta(x) dx, \tag{21}$$

where B is the channel bandwidth, ln() is the natural logarithm, and $f_\beta()$ is the pdf of the output SNR given in (15). In this expression, an optimal channel encoding is implicitly assumed. Introducing (15) into (21) and using [19]

$$\int_0^\infty t^{n-1} \ln(1 + t) e^{-\tau t} dt = \Gamma(n) e^\tau \sum_{k=1}^{n} \frac{\Gamma(-n + k, \tau)}{\tau^k}; \quad \tau > 0; \quad n \in \mathbb{Z}^+, \tag{22}$$

the channel capacity can be calculated as

$$\begin{aligned} \frac{\langle C \rangle_{\text{erg}}}{B} &= \frac{1}{\ln(2)} \sum_{j=1}^{T} \binom{T}{j} a^{T-j} (-1)^j \\ &\cdot \sum_{\tau_j} \binom{j}{\tau_j} c_{\tau_j} \Gamma\left(g_{\tau_j} + 1\right) e^{d_{\tau_j}} \\ &\times \left[-\frac{\Gamma\left(0, d_{\tau_j}\right)}{d_{\tau_j}^{g_{\tau_j}}} + \sum_{k=1}^{g_{\tau_j}} \left(\frac{\Gamma\left(k - g_{\tau_j}, d_{\tau_j}\right)}{d_{\tau_j}^k} - \frac{\Gamma\left(k - g_{\tau_j} - 1, d_{\tau_j}\right)}{d_{\tau_j}^{k-1}} \right) \right]. \end{aligned} \tag{23}$$

4.2. Impact of Receive Antenna Correlation on Capacity. When MRC is performed at the receiver and there is a single transmit antenna, it is known that correlation has a detrimental effect on capacity [20]. In this section, we demonstrate that, when multiple independent antennas are considered at the transmitter performing transmit antenna selection, correlation at the receive antennas may result in an increased capacity.

In order to simplify our analysis, let us consider the case of constant correlation, denoted as ρ, between any pair of receive antennas. For simplicity, we define $\eta = \sqrt{\rho}$, so that any function increasing or decreasing with ρ will have the same behavior with η. For this case, the elements of matrix $\mathbf{A}$ become

$$\begin{aligned} A(i, j) &= \Omega\eta, \quad i \neq j; \\ A(i, j) &= \Omega, \quad i = j; i, \\ &\quad j = 1, 2, \ldots, R, \end{aligned} \tag{24}$$

and only two distinct eigenvalues are obtained [10, equation (12)]:

$$\begin{aligned} \lambda_1 &= \Omega\left(1-\eta\right), \qquad n_1 = R-1; \\ \lambda_2 &= \Omega\left(1+(R-1)\,\eta\right), \qquad n_2 = 1. \end{aligned} \tag{25}$$

Introducing (25) into (5), the coefficients A_{ik} can be written as

$$\begin{aligned} A_{1k} &= -\frac{\left(1-\eta\right)\left(1+(R-1)\eta\right)^{k-1}}{\left(R\eta\right)^{k}}, \\ A_{21} &= \left(\frac{1+(R-1)\eta}{R\eta}\right)^{R-1}. \end{aligned} \tag{26}$$

A general treatment of (23) using (26) would be too long and difficult to manage. However, the simplest case with two receive antennas ($R = 2$) can be easily studied. Then, the different parameters used in this section become

$$\begin{aligned} &\lambda_1 = \Omega\left(1-\eta\right), \qquad n_1 = 1; \\ &\lambda_2 = \Omega\left(1+\eta\right), \qquad n_2 = 1; \\ &A_{11} = \frac{\eta-1}{2\eta}; \\ &A_{21} = \frac{1+\eta}{2\eta}; \\ &a = 1; \\ &\left\{\tau_j\right\} = \left\{\left(n_{1,1,0} = q, n_{2,1,0} = j-q\right) : q \le j, q \in \mathbb{N}\right\}; \\ &\sum_{\tau_j} \Longleftrightarrow \sum_{q=0}^{j}, \\ &\binom{j}{\tau_j} = \binom{j}{q} = \frac{j!}{q!\left(j-q\right)!}; \\ &c_{\tau_j} = c_{jq} = A_{11}^{q} A_{21}^{j-q}; \\ &d_{\tau_j} = d_{jq} = \frac{q}{\lambda_1} + \frac{j-q}{\lambda_2}; \\ &g_{\tau_j} = 0. \end{aligned} \tag{27}$$

Therefore, the capacity expression (23) can be written in this case as

$$\begin{aligned} \frac{\langle C\rangle_{\text{erg}}}{B} &= \frac{1}{\ln(2)} \sum_{j=1}^{T} \binom{T}{j} (-1)^{j-1} \sum_{q=0}^{j} \binom{j}{q} \\ &\cdot c_{jq} e^{d_{jq}} \Gamma\left(0, d_{jq}\right). \end{aligned} \tag{28}$$

In order to study the effect of correlation on capacity, we calculate the derivative of capacity with respect to η. Using [21, equation (6.5.25)], we can obtain

$$\begin{aligned} &\frac{d}{d\eta}\frac{\langle C\rangle_{\text{erg}}}{B} \\ &= \frac{1}{\ln(2)} \sum_{j=1}^{T} \binom{T}{j} (-1)^{j-1} \sum_{q=0}^{j} \binom{j}{q} \\ &\cdot \left\{ \frac{\partial c_{jq}}{\partial \eta} e^{d_{jq}} \Gamma\left(0, d_{jq}\right) \right. \\ &\left. + \frac{\partial d_{jq}}{\partial \eta} c_{jq} \left(e^{d_{jq}} \Gamma\left(0, d_{jq}\right) - \frac{1}{d_{jq}} \right) \right\}, \end{aligned} \tag{29}$$

where

$$\begin{aligned} \frac{\partial c_{jq}}{\partial \eta} &= c_{jq} \left(\frac{q}{\eta-1} + \frac{j-q}{\eta+1} - \frac{j}{\eta} \right), \\ \frac{\partial d_{jq}}{\partial \eta} &= \frac{1}{\Omega} \left(\frac{q}{(1-\eta)^2} - \frac{j-q}{(1+\eta)^2} \right). \end{aligned} \tag{30}$$

To study the monotonicity of capacity, the capacity derivative given in (29) is represented in Figure 2 for different number of transmit antennas as a function of the correlation coefficient for an average SNR per branch of 0 and 20 dB, and, in Figure 3, the capacity derivative is represented as a function of the average SNR per branch for 2 receive antennas. It can be observed that, for only one transmit antenna ($T = 1$), the derivative is always negative, which means that the capacity is monotonically decreasing with correlation; that is, the higher the correlation, the lower the capacity, which is consistent with the results in [14, 20]. Figure 2 also shows that the capacity will be quickly degraded, for $T = 1$, as correlation increases if the average SNR per branch is high. On the other hand, for $T \ge 3$, capacity is monotonically increasing with correlation; that is, the higher the correlation, the higher the capacity. An intuitive explanation of the reason of such behavior can be found in the fact that the higher the correlation the higher the variability of the output signal received from a given transmit antenna. Therefore, as the number of transmit antennas increases, the probability that a transmit antenna with good channel conditions is selected for transmission also increases. Ultimately, if the number of transmit antennas for selection is high enough, this will lead to an increase of capacity.

5. Numerical Results

In this section, numerical results are presented for the BER as well as for the channel capacity of the analyzed TAS/MRC scheme. Monte Carlo simulations have also been carried out showing an excellent agreement with the analytical results.

Figure 4 shows the average BER for BPSK as a function of the average SNR, for a TAS/MRC system with 4 receive antennas, high and low correlations ($\rho = 0.9$ and

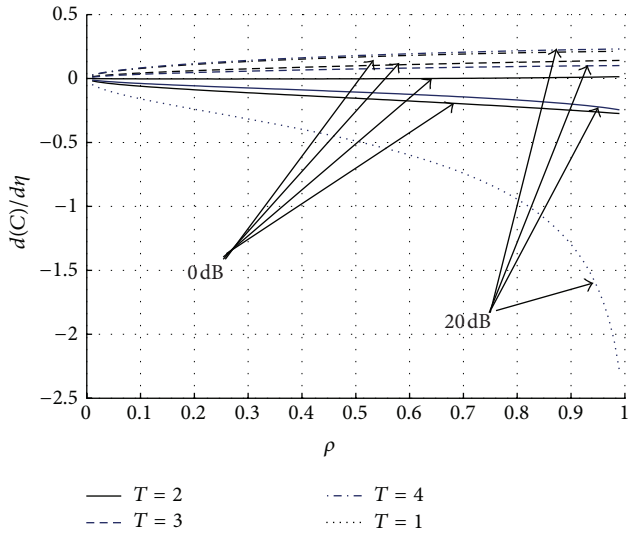

Figure 2: Derivative of ergodic capacity versus correlation coefficient ρ for $R = 2$; $T = 1, 2, 3, 4$. Average SNR per branch is 0 dB and 20 dB.

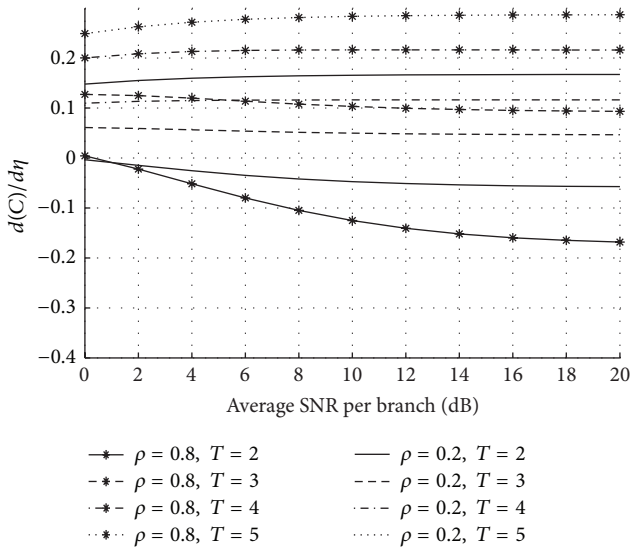

Figure 3: Derivative of ergodic capacity versus average SNR per branch for low correlation ($\rho = 0.2$) and high correlation ($\rho = 0.8$). The considered array sizes are $R = 2$; $T = 2, 3, 4, 5$.

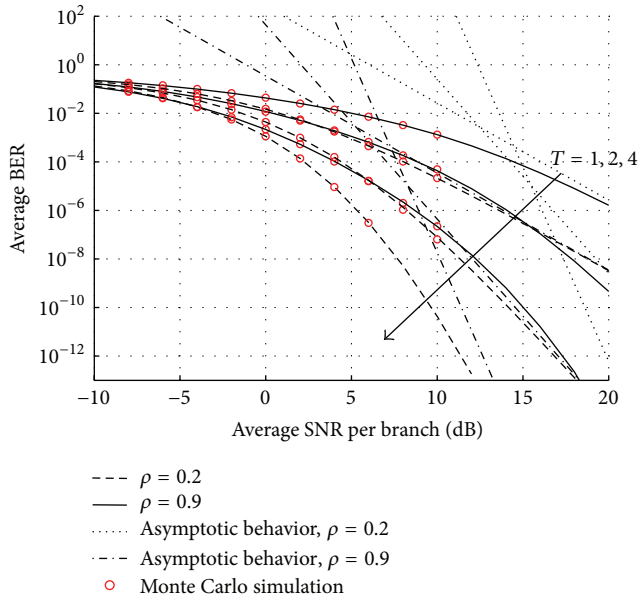

Figure 4: Average BER versus average SNR per receive antenna with BPSK modulation for $T = 1, 2, 4$, $R = 4$ and constant correlation with $\rho = 0.2, 0.9$. Simulation points and asymptotic behavior are also shown.

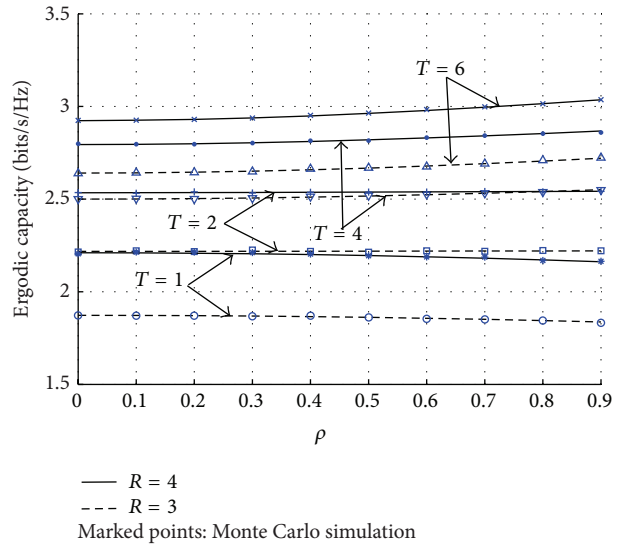

Figure 5: Ergodic capacity versus constant correlation parameter ρ for $R = 3, 4$; $T = 1, 2, 4, 6$. Average SNR per branch is 0 dB.

$\rho = 0.2$, resp.), and different number of transmit antennas. The asymptotic behavior is also shown. In all cases, it can be observed that a lower correlation results in a lower BER, except for very low values of the average SNR.

Figures 5 and 6 show the ergodic capacity for 3 and 4 receive antennas and an average SNR per branch of, respectively, 0 and 20 dB as a function of the correlation coefficient ρ, which is assumed to be the same for any pair of receive antennas. It can be observed that when there is only one transmit antenna, $T = 1$, the channel capacity diminishes as correlation increases, which is consistent with the results in [14, 20]. However, for $T > 2$, highly correlated antennas result in an increased capacity. Note that these results do not contradict the detrimental impact that the correlation has on the BER (except for very low average SNR) in uncoded communications, as channel capacity implicitly assumes an error-free communication link. Figure 7 reveals how the width of the SNR pdf becomes larger when correlation increases for a given transmit antenna (note that the abscissa is represented in dB), which indicates a higher variance. This higher variability for high correlation is responsible for the increased capacity when transmit antenna selection

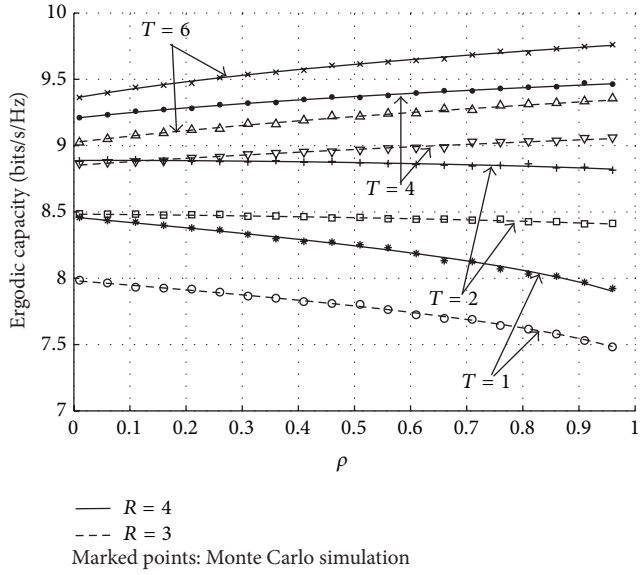

Figure 6: Ergodic capacity versus constant correlation parameter ρ for $R = 3, 4$; $T = 1, 2, 4, 6$. Average SNR per branch is 20 dB.

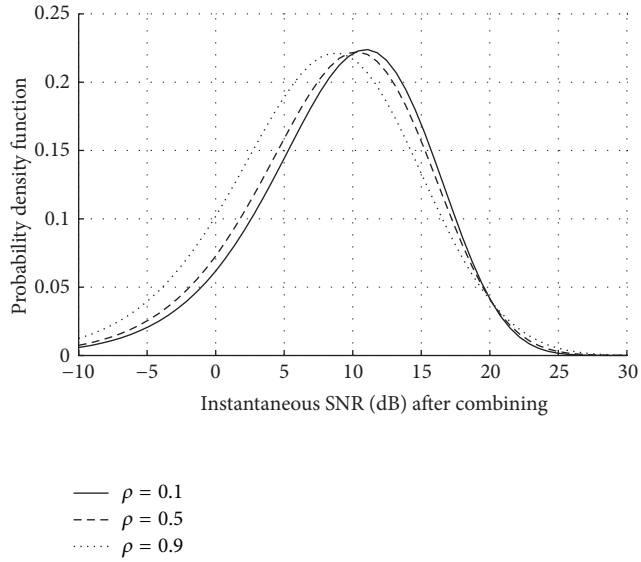

Figure 7: Probability density function of output SNR for a given transmit antenna ($T = 1$) and $R = 4$.

is performed. Note that the probability of having a higher instantaneous SNR after combining increases as correlation increases.

Figure 8 shows the ergodic capacity as a function of the average SNR per branch for different number of transmit and receive antennas considering a constant correlation or linear-array correlation. The linear-array correlation matrix has been built such that $M_x(i, j) = 1$ if $i = j$ and $M_x(i, j) = \eta/|i-j|^2$ if $i \neq j$. Again, an increased capacity with correlation when $T = 6$ can be observed, which is larger if the correlation is constant (as the receive antennas suffer a stronger correlation). For low correlation ($\rho = 0.2$), almost

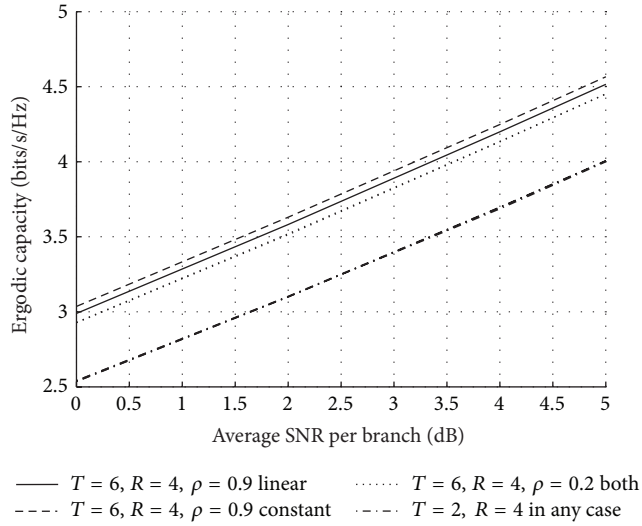

Figure 8: Ergodic capacity versus average SNR per receive antenna; $R = 4$; $T = 2, 6$; $\rho = 0.2, 0.9$; constant or linear receive array correlation. The cases when the curves overlap and cannot be distinguished are indicated in the legend.

no difference can be appreciated between constant and linear array. For $T = 2$, there is no appreciable difference in any of the depicted cases.

6. Conclusion

We have presented novel closed-form expressions for the pdf and CDF of the output SNR of TAS/MRC systems in Rayleigh fading with arbitrarily correlated receive antennas. Additionally, a novel closed-form expression has been derived for the average BER under several modulation techniques, and the corresponding asymptotic expression is also presented. Our results show that antenna correlation has always a detrimental impact on BER except for very low average SNR per receive antenna. We have also studied the impact of correlation on ergodic capacity and we have shown that correlation may have a beneficial impact on ergodic capacity of TAS/MRC systems due to the antenna selection performed at the transmitter, as a higher variability of the output signal increases the probability that a transmit antenna in good fading conditions is selected for transmission. As a consequence, the capacity will increase as receive antenna correlation increases if the number of transmit antennas is high enough.

Appendix

Derivation of (20)

We will follow the framework provided in [22], where it is shown that the asymptotic error performance depends on the behavior of the SNR's pdf at the origin or, equivalently, on the decaying order of its MGF.

First, let us consider that a single transmit antenna j is used. From (2), we can write

$$\lim_{s\to\infty}\left|\Psi_{\beta_j}(s)\right| = \lim_{s\to\infty}\prod_{i=1}^{J}\left|1-s\lambda_i\right|^{-n_i} = \lim_{s\to\infty} b|s|^{-R}, \tag{A.1}$$

where

$$b = \prod_{i=1}^{J}\left(\frac{1}{\lambda_i^{n_i}}\right) = \frac{1}{\det\left(\mathbf{M}_x\right)\Omega^R}. \tag{A.2}$$

The pdf of the random variable β_j near the origin can be approximated by calculating the inverse Laplace transform of (A.1). By noticing that the single-sided Laplace transform of x^n, with n integer, is $n!/s^{n+1}$, we can write

$$f_{\beta_j}(x) \approx \frac{b}{(R-1)!}x^{R-1}, \quad x \rightharpoonup 0^+. \tag{A.3}$$

By integrating (A.3), the CDF of β_j at the origin is obtained as

$$F_{\beta_j}(x) \approx \frac{b}{R!}x^R, \quad x \rightharpoonup 0^+. \tag{A.4}$$

When transmit antenna selection is performed, the CDF of the output SNR at the origin can thus be written as

$$F_{\beta}(x) \approx \left(\frac{b}{R!}\right)^T x^{RT}, \quad x \rightharpoonup 0^+. \tag{A.5}$$

Note that (A.5) is actually the first nonzero term of the Maclaurin series expansion of the CDF of β, that is, the term with the lower exponent in x. The remaining terms become lower as Ω increases. The asymptotic BER can thus be calculated by introducing (18) and (A.5) into (16), yielding, after solving the integral, (20).

Conflict of Interests

The authors declare that there is no conflict of interests regarding the publication of this paper.

Acknowledgments

This work has been supported by European FEDER funds and the Spanish Ministry of Economy and Competitiveness (Grant TEC2009-13763-C02-01).

References

[1] A. F. Molisch and M. Z. Win, "Mimo systems with antenna selection," *IEEE Microwave Magazine*, vol. 5, no. 1, pp. 46–56, 2004.

[2] Z. Chen, J. Yuan, and B. Vucetic, "Analysis of transmit antenna selection/maximal-ratio combining in Rayleigh fading channels," *IEEE Transactions on Vehicular Technology*, vol. 54, no. 4, pp. 1312–1321, 2005.

[3] Z. Chen, Z. Chi, Y. Li, and B. Vucetic, "Error performance of maximal-ratio combining with transmit antenna selection in flat Nakagami-m fading channels," *IEEE Transactions on Wireless Communications*, vol. 8, no. 1, pp. 424–431, 2009.

[4] J. M. Romero-Jerez and A. J. Goldsmith, "Performance of multichannel reception with transmit antenna selection in arbitrarily distributed Nagakami fading channels," *IEEE Transactions on Wireless Communications*, vol. 8, no. 4, pp. 2006–2013, 2009.

[5] J. P. Peña-Martín, J. M. Romero-Jerez, and C. Téllez-Labao, "Performance of TAS/MRC wireless systems under hoyt fading channels," *IEEE Transactions on Wireless Communications*, vol. 12, no. 7, pp. 3350–3359, 2013.

[6] L. Yang, D. Tang, and J. Qin, "Performance of spatially correlated MIMO channel with antenna selection," *Electronics Letters*, vol. 40, no. 20, pp. 1281–1282, 2004.

[7] B.-Y. Wang and W. X. Zheng, "Outage probability of transmitter antenna selection/receiver-MRC over spatially correlated Nakagami-fading channel," in *Proceedings of the 8th International Conference on Signal Processing (ICSP '06)*, November 2006.

[8] B.-Y. Wang and W.-X. Zheng, "BER performance of transmitter antenna selection/receiver-MRC Over arbitrarily correlated fading channels," *IEEE Transactions on Vehicular Technology*, vol. 58, no. 6, pp. 3088–3092, 2009.

[9] B.-Y. Wang, "Accurate BER of transmitter antenna selection/receiver-MRC over arbitrarily correlated nakagami fading channels," in *Proceedings of the IEEE International Conference on Acoustics, Speech and Signal Processing (ICASSP '06)*, pp. IV753–IV756, May 2006.

[10] M.-S. Alouini, A. Abdi, and M. Kaveh, "Sum of gamma variates and performance of wireless communication systems over Nakagami-fading channels," *IEEE Transactions on Vehicular Technology*, vol. 50, no. 6, pp. 1471–1480, 2001.

[11] Y. Liang, "Performance analysis of transmit antenna selection with MRC over correlated fast-fading channels," in *Proceedings of the 4th International Conference on Wireless Communications, Networking and Mobile Computing (WiCOM '08)*, October 2008.

[12] V. Blagojevic and P. Ivanis, "Ergodic capacity for TAS/MRC spectrum sharing cognitive radio," *IEEE Communications Letters*, vol. 16, no. 3, pp. 321–323, 2012.

[13] H. Wang, P. Wang, and L. Ping, "On the capacity gain from antenna correlation in multi-user MIMO systems," in *Proceedings of the IEEE International Conference on Communications (ICC '12)*, pp. 3878–3883, June 2012.

[14] J. P. Peña-Martín, J. M. Romero-Jerez, and J. L. Arellano-Millner, "Capacity analysis of adaptive transmission with MRC in arbitrarily correlated Rayleigh fading," in *Proceedings of the 74th IEEE Vehicular Technology Conference (VTC Fall '11)*, September 2011.

[15] P. Lombardo, G. Fedele, and M. M. Rao, "MRC performance for binary signals in Nakagami fading with general branch correlation," *IEEE Transactions on Communications*, vol. 47, no. 1, pp. 44–52, 1999.

[16] M. R. Spiegel, *Mathematical Handbook of Formulas and Tables*, McGraw-Hill, New York, NY, USA, 1968.

[17] M. K. Simon and M. -S. Alouini, *Digital Communications Over Fading Channels*, Wiley-Interscience, John Wiley & Sons, 2nd edition, 2005.

[18] A. Goldsmith, *Wireless Communications*, Cambridge University, 2005.

[19] M.-S. Alouini and A. J. Goldsmith, "Capacity of Rayleigh fading channels under different adaptive transmission and diversity-combining techniques," *IEEE Transactions on Vehicular Technology*, vol. 48, no. 4, pp. 1165–1181, 1999.

[20] R. K. Mallik, M. Z. Win, J. W. Shao, M.-S. Alouini, and A. J. Goldsmith, "Channel capacity of adaptive transmission with maximal ratio combining in correlated Rayleigh fading," *IEEE Transactions on Wireless Communications*, vol. 3, no. 4, pp. 1124–1133, 2004.

[21] M. Abramowitz and I. A. Stegun, *Handbook of Mathematical Functions with Formulas, Graphs, and Mathematical*, Department of Commerce—N.B.S., 10th edition, 1972.

[22] Z. Wang and G. B. Giannakis, "A simple and general parameterization quantifying performance in fading channels," *IEEE Transactions on Communications*, vol. 51, no. 8, pp. 1389–1398, 2003.

Hindawi Publishing Corporation
International Journal of Antennas and Propagation
Volume 2014, Article ID 619304, 10 pages
http://dx.doi.org/10.1155/2014/619304

Research Article

Practical and Simple Wireless Channel Models for Use in Multipolarized Antenna Systems

KwangHyun Jeon, Xin Su, Bing Hui, and KyungHi Chang

Electronic Engineering Department, Inha University, Incheon 402-751, Republic of Korea

Correspondence should be addressed to KyungHi Chang; khchang@inha.ac.kr

Received 21 February 2014; Accepted 10 May 2014; Published 25 May 2014

Academic Editor: Paschalis Sofotasios

Copyright © 2014 KwangHyun Jeon et al. This is an open access article distributed under the Creative Commons Attribution License, which permits unrestricted use, distribution, and reproduction in any medium, provided the original work is properly cited.

The next-generation wireless systems are expected to support data rates of more than 100 Mbps in outdoor environments. In order to support such large payloads, a polarized antenna may be employed as one of the candidate technologies. Recently, the third generation partnership standards bodies (3GPP/3GPP2) have defined a cross-polarized channel model in SCM-E for MIMO systems; however, this model is quite complex since it considers a great many channel-related parameters. Furthermore, the SCM-E channel model combines the channel coefficients of all the polarization links into one complex output, making it impossible to exploit the MIMO spatial multiplexing or diversity gains in the case of employing polarized antenna at transmitter and receiver side. In this paper, we present practical and simple 2D and 3D multipolarized multipath channel models, which take into account both the cross-polarization discrimination (XPD) and the Rician factor. After verifying the proposed channel models, the BER and PER performances and throughput using the EGC and MRC combining techniques are evaluated in multipolarized antenna systems.

1. Introduction

The next-generation wireless systems are required to possess high voice quality and high data rate services compared to the current cellular mobile radio standards and also provide seamless data service. Recent work has shown that independent spatial channels can be used to greatly enhance capacity under situations subject to scattering, such as urban areas or indoor environments [1–3]. Multiple input multiple output (MIMO) systems have been shown to dramatically increase the capacity of wireless systems and so have drawn an increasing amount of attention in recent years [4]. This capacity gain, however, strongly depends on the transmit (Tx) and receive (Rx) antenna spacing. In practical situations, antennas spacing of several wave lengths is required in order to achieve a significant multiplexing gain. Unfortunately, this large antenna spacing requirement increases both the size and the cost of base stations and makes it quite difficult to render the use of multiple antennas in customer devices. Antenna elements employing multiple polarizations can increase the capacity and often require less space per Tx and Rx channel than spatially separated polarization elements [5–7].

A great deal of research is in progress in regard to spatial MIMO channel models; however, models regarding the polarized antenna channel are still in their early stages. Existing polarized antenna channel models can be divided into two categories: two-dimensional (2D) channel models where all of the scatterers are located in a 2D plane and three-dimensional (3D) channel models where all the scatterers are located in 3D space. One of the well-known 2D polarized antenna channel models is the one defined by the spatial channel model extended (SCM-E) [8], which is quite complex since it considers a great many parameters, such as angle spread, angle of arrival, angle of departure, power azimuth spectrum, lognormal shadowing, delay spread, and path loss. On top of that, there is only a single output of complex channel gain from the SCM-E polarized channel model resulting from the combination of all polarized channel links. When polarized antenna is employed at both Tx and Rx sides,

it is not possible to exploit spatial multiplexing gain or other types of combining gains using the SCM-E polarized antenna channel model since it combines the channel coefficients of all the polarization links into one complex output. In addition, it is not convenient to observe the characteristics of each polarized channel link (e.g., *v*-*h*, *h*-*v*, *h*-*h*, and *v*-*v*; *v* for vertical, *h* for horizontal), such as the cross-polarization discrimination (XPD) values and the contributions from the above four types of polarized links. This is because it obtains only a single complex output resulting from the combination of all polarized links. In this case, it is impossible to exploit spatial multiplexing gain or other types of combining gains since the polarized links become indistinguishable from each other. Here, XPD is defined as the ratio of the copolarized average received power to the cross-polarized average received power; it has an essential role in the polarized antenna channel models in quantifying the separation between two transmission channels that use different polarization orientations. 3D geometry-based statistical modeling of channel depolarization for polarized antenna systems has been proposed by Kwon and Stüber in [9]. However, it is also quite complicated since it also considers many parameters, such as the cylindrical scattering surface radius, the azimuth angle of arrival, the elevation angle of arrival, and the distance between the base station (BS) and mobile station (MS). Furthermore, the double integrals in [9] by assuming an infinite number of scatterers make their channel model too complex to be practically implemented. Another typical 3D polarized MIMO channel based on SCM 2D channel model is given in [10]. The spherical coordinate system is the same as our proposed scatterer structure; however, their 3D channel model is derived from SCM 2D channel model, which can be considered as update of SCM channel model in mathematical perspective. Similar problems as aforementioned about SCM-E channel model still exist in their 3D MIMO channel model.

In our preliminary work [11], we suggested the dual-polarized channel model mainly based on the 2D scattering scenario. In order to complete our research work, in this paper, a practical and simple (PS) wireless channel model for use in multipolarized (i.e., dual-/triple-polarized) antenna systems based on both 2D and 3D scattering scenarios is presented. Our proposed channel model aims at the indoor or dense urban communication environment. Therefore by referring to [2], we assume that the statistical locations of the scatterers are uniformly distributed around the MS. In addition by assuming that the energy contribution of remote scatters is negligible, a finite but sufficient number of scatterers are satisfied to reflect the scattering scenario in the proposed model. The proposed channel model preserves the continuity of time-varying phase response, which is caused by the mobility of the MS. Thus, the practical channel estimation using the training sequence becomes meaningful in the aspect of phase compensation under the proposed channel model.

The remaining parts of this paper are organized as follows. Section 2 introduces the propagation characteristics of polarized antenna systems. Section 3 presents the proposed 2D and 3D polarized channel models. The verification of the proposed polarized antenna channel models through receiver diversity is discussed in Section 4, and conclusions are drawn in Section 5.

2. Propagation Characteristics of Polarized Antenna Systems

This section describes the propagation characteristics of polarized antenna systems. Usually there are multiple scatterers, such as buildings, cars, and trees, uniformly located around the MS in urban environments. The propagation characteristics of polarized antenna systems can be determined through XPD, which quantifies the separation between two transmission channels that use different polarization orientations as

$$\begin{aligned} \text{XPD} &= \frac{\text{Cochannel Rx Power}}{\text{Cross-channel Rx Power}} \\ &= \frac{\text{Rx Power (VV)}}{\text{Rx Power (VH)}} \text{ or } \frac{\text{Rx Power (HH)}}{\text{Rx Power (HV)}}. \end{aligned} \tag{1}$$

The larger the XPD, the smaller the amount of energy coupled between the cross-polarized channels. When a horizontally polarized antenna receives a signal sent from a vertically polarized antenna (and vice versa), the received signal strength is reduced in proportion to the XPD value. XPD values have been found to decrease with an increase in the distance [9]. Usually, the XPD is revealed to have the relation with the antenna properties, distance between the transmitter and receiver, scatterers distributions, and so forth. However, in this paper, we defined XPD as the ratio of the copolarized average received power to the cross-polarized average received power [9], where it is specified only by the power coupled to the polarized channel links. In order to minimize the modeling complexity without loss of accuracy, we directly assign the XPD value according to the measurement results returned by literature references, for example, 5.8 dB in [9].

For polarized channel modeling in macro and micro cell environments, we use the same number of scatterers, six, as laid out in the 1st and 2nd mid rays of the SCM-E urban channel model [8]. Two kinds of channel models are introduced in this paper, based on the channel model components, one of which contains only non-line-of-sight (NLoS) components and the other both line-of-sight (LoS) and NLoS components, that is, the Rayleigh channel model and the Rician channel model, respectively.

2.1. The 2D Scatterer Model. As shown in Figure 1, the MS mobility is taken into consideration in regard to the polarized antenna channel model found in [11]. θ is the phase rotation of the received signal at the MS due to the scatterers, and θ' is the updated phase rotation according to the MS movement, as described by

$$\theta' = \arctan\left(\frac{r\sin\theta}{r\cos\theta + \Delta}\right), \tag{2}$$

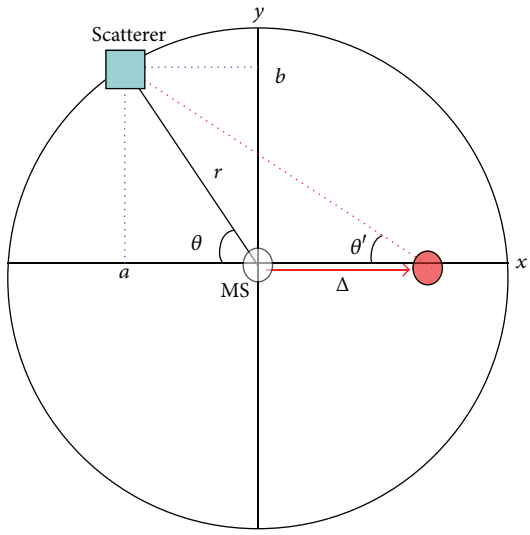

Figure 1: 2D scatterer model.

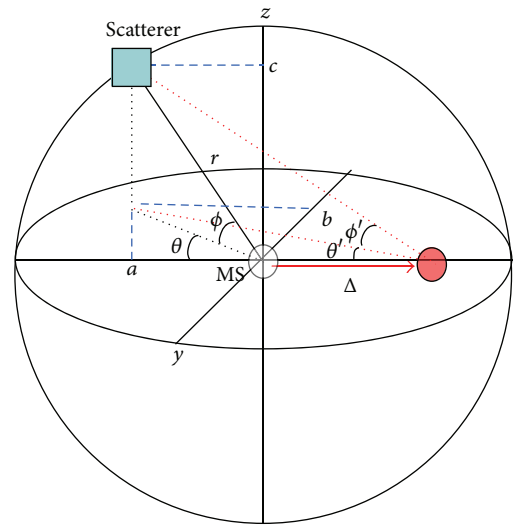

Figure 2: 3D scatterer model.

where r is the radius of the scatterers and Δ is the moving distance of the MS for a 1-packet duration (e.g., 5 us). In this case, Δ is quite a small value compared to the radius r, so we assume that the moving direction of the MS does not change within such a short time duration. This assumption will be explained in more detail when introducing the system parameters described in Section 4. The details of the parameters for the 2D scatterer model are presented in Table 1.

2.2. The 3D Scatterer Model. We extend the 2D scatterer model to the 3D scatterer model by adding a new parameter, ϕ, which is the elevation angle, as shown in Figure 2. Similar to the 2D scatter model, the elevation angle ϕ represents the phase rotation of the received signal projected in the x-z plane (due to the movement of the MS along the x axis); ϕ' is the updated phase rotation projected in the x-z plane according to the MS movement. The azimuth and the elevation angles related to the phase rotations seen above are obtained by using the triangular function as shown in (3) and (4), respectively. The parameters used for the 3D scatterer model are described in Table 2. Consider

$$\theta' = \arctan\left(\frac{b}{a+\Delta}\right) \tag{3}$$

$$\phi' = \arctan\left(\frac{c}{a+\Delta}\right). \tag{4}$$

2.3. The Propagation Characteristics of the Rician Channel. The analytical performance under Rician polarized channel environment was discussed in [12]. The polarization matrix **H** in (5) includes the degree of suppression of the individual co-/cross-polarized components, the cross-correlation, and the cross-coupling of the energy from one polarization state to the other polarization state. Consider

$$\mathbf{H} = \begin{bmatrix} h_{v,v} & h_{v,h} \\ h_{h,v} & h_{h,h} \end{bmatrix}. \tag{5}$$

The elements of polarized channel matrix **H** are, in general, correlated to complex Gaussian random variables.

Table 1: 2D scatterer model parameters.

a	Scatterer signal projected to x-axis ($a = r\cos\theta$)
b	Scatterer signal projected to y-axis ($b = r\sin\theta$)
r	Distance between scatterers and MS
θ	Phase rotation of received signal at MS
θ'	Updated phase rotation according to MS movement
Δ	Moving distance of MS

Table 2: 3D scatterer model parameters.

a	Scatterer signal projected to x-axis ($a = r\cos\theta\cos\phi$)
b	Scatterer signal projected to y-axis ($b = r\cos\theta\sin\phi$)
c	Scatterer signal projected to z-axis ($c = r\sin\theta$)
r	Distance between scatterers and MS
θ	Phase rotation of received signal projected in x-y plan at MS
θ'	Updated phase rotation projected in x-y plan according to MS movement
ϕ	Phase rotation of received signal projected in x-z plan at MS
ϕ'	Updated phase rotation projected in x-z plan according to MS movement
Δ	Moving distance of MS

We decompose the channel matrix into the sum of an average (or fixed, possibly LoS) component and a variable (or scattered) component using

$$\mathbf{H} = \sqrt{\frac{k}{k+1}} \cdot \overline{\mathbf{H}} + \sqrt{\frac{1}{k+1}} \cdot \widetilde{\mathbf{H}}, \tag{6}$$

where k is the Rician factor, $\overline{\mathbf{H}}$ is the LoS component, and $\widetilde{\mathbf{H}}$ is the NLoS component. Here, $\varepsilon\{\mathbf{H}\} = \sqrt{k/(1+k)} \cdot \overline{\mathbf{H}}$ and $\sqrt{1/(1+k)} \cdot \widetilde{\mathbf{H}}$ are the average and variable components of the channel matrix, respectively. The factors $\sqrt{k/(1+k)}$ and $\sqrt{1/(1+k)}$ in (6) are the power normalization factors. The elements of matrix $\widetilde{\mathbf{H}}$ are denoted as $\widetilde{h}_{v,h}$ (v, h: x-pol component). The signal power of the NLoS components is determined using

$$\begin{aligned} \varepsilon\left\{\left|\widetilde{h}_{h,h}\right|^2\right\} &= \varepsilon\left\{\left|\widetilde{h}_{v,v}\right|^2\right\} = 1, \\ \varepsilon\left\{\left|\widetilde{h}_{h,v}\right|^2\right\} &= \varepsilon\left\{\left|\widetilde{h}_{v,h}\right|^2\right\} = \alpha, \end{aligned} \tag{7}$$

where $0 \le \alpha \le 1$ is related to the XPD value for the variable components of the channel. A good discrimination of the orthogonal polarizations has a small XPD value, and vice versa. The elements of matrix $\overline{\mathbf{H}}$, which are denoted as $\overline{h}_{v,h}$, are non-time-varying complex numbers satisfying

$$\left|\overline{h}_{h,h}\right| = \left|\overline{h}_{v,v}\right| = 1, \qquad \left|\overline{h}_{h,v}\right| = \left|\overline{h}_{v,h}\right| = \alpha_f, \tag{8}$$

where $0 \le \alpha_f \le 1$ is directly related to the XPD value for the fixed component of the channel. It is important to note that the presence of a fixed channel component does not always imply LoS conditions. For pure LoS conditions, α_f, unlike α, is solely a function of the antenna's ability to separate the orthogonal polarizations. The XPD values presented in dB and in linear values are related to α as shown by

$$\text{XPD (dB)} = 10\log\left(\frac{1}{\sqrt{\alpha}}\right)^2, \qquad \text{XPD} = \frac{1}{\alpha}. \tag{9}$$

The Rician factor for a fading channel is defined as the ratio of the power in the fixed component to the power in the variable components. Under the definitions of α and α_f made above, the Rician factor for each element of the channel matrix can be expressed as

$$\mathbf{K} = \begin{bmatrix} k_{v,v} & k_{v,h} \\ k_{h,v} & k_{h,h} \end{bmatrix} = \begin{bmatrix} k & \dfrac{\alpha_f}{\alpha}k \\ \dfrac{\alpha_f}{\alpha}k & k \end{bmatrix} \tag{10}$$

$$h_{u,s,n}(t) = \sqrt{\frac{P_n \sigma_{\text{SF}}}{M}} \sum_{m=1}^{M} \left(\begin{bmatrix} \chi_{\text{BS}}^{(v)}(\theta_{n,m,\text{AoD}}) \\ \chi_{\text{BS}}^{(h)}(\theta_{n,m,\text{AoD}}) \end{bmatrix}^T \begin{bmatrix} \exp\left(j\Phi_{n,m}^{(v,v)}\right) & \sqrt{r_{n1}}\exp\left(j\Phi_{n,m}^{(h,v)}\right) \\ \sqrt{r_{n2}}\exp\left(j\Phi_{n,m}^{(v,h)}\right) & \exp\left(j\Phi_{n,m}^{(h,h)}\right) \end{bmatrix} \begin{bmatrix} \chi_{\text{MS}}^{(v)}(\theta_{n,m,\text{AoA}}) \\ \chi_{\text{MS}}^{(h)}(\theta_{n,m,\text{AoA}}) \end{bmatrix} \right.$$

$$\left. \times \exp\left(jkd_s \sin\left(\theta_{n,m,\text{AoD}}\right)\right) \times \exp\left(jkd_u \sin\left(\theta_{n,m,\text{AoA}}\right)\right) \times \exp\left(jk\|v\| \cos\left(\theta_{n,m,\text{AoA}} - \theta_v\right) t\right) \right) \tag{11}$$

$$\mathbf{H}_{\text{2D-Rayleigh}}(t)$$

$$= \sqrt{\frac{P_n}{M}} \sum_{m=1}^{M} \left(\begin{bmatrix} \exp\left(j\arctan\left(\dfrac{r\sin\theta_{n,m}^{(v,v)}}{r\cos\theta_{n,m}^{(v,v)} + (n-1)\Delta}\right)\right) & \sqrt{\alpha_{\text{NLoS}}}\exp\left(j\arctan\left(\dfrac{r\sin\theta_{n,m}^{(v,h)}}{r\cos\theta_{n,m}^{(v,h)} + (n-1)\Delta}\right)\right) \\ \sqrt{\alpha_{\text{NLoS}}}\exp\left(j\arctan\left(\dfrac{r\sin\theta_{n,m}^{(h,v)}}{r\cos\theta_{n,m}^{(h,v)} + (n-1)\Delta}\right)\right) & \exp\left(j\arctan\left(\dfrac{r\sin\theta_{n,m}^{(h,h)}}{r\cos\theta_{n,m}^{(h,h)} + (n-1)\Delta}\right)\right) \end{bmatrix} \right) \tag{12}$$

$$\mathbf{H}_{\text{3D-Rayleigh-Dual}}(t) = \sqrt{\frac{P_n}{M}} \sum_{m=1}^{M} \left(\begin{bmatrix} \cos\left(\theta_{n,m}^{(v,v)}\right) \cdot \exp\left(j\phi'^{(v,v)}_{n,m}\right) & \sqrt{\alpha_{\text{NLoS}}}\cos\left(\theta_{n,m}^{(v,h)}\right) \cdot \exp\left(j\phi'^{(v,h)}_{n,m}\right) \\ \sqrt{\alpha_{\text{NLoS}}}\cos\left(\theta_{n,m}^{(h,v)}\right) \cdot \exp\left(j\phi'^{(h,v)}_{n,m}\right) & \cos\left(\theta_{n,m}^{(h,h)}\right) \cdot \exp\left(j\phi'^{(h,h)}_{n,m}\right) \end{bmatrix} \right) \tag{13}$$

$$\mathbf{H}_{\text{3D-Rayleigh-Triple}}(t) = \sqrt{\frac{P_n}{M}} \sum_{m=1}^{M} \begin{pmatrix} \cos\left(\theta_{n,m}^{(1,1)}\right) \cdot \exp\left(j\phi'^{(1,1)}_{n,m}\right) & \sqrt{\alpha_{\text{NLoS}}} \cos\left(\theta_{n,m}^{(1,2)}\right) \cdot \exp\left(j\phi'^{(1,2)}_{n,m}\right) & \sqrt{\alpha_{\text{NLoS}}} \cos\left(\phi_{n,m}^{(1,3)}\right) \cdot \exp\left(j\theta'^{(1,3)}_{n,m}\right) \\ \sqrt{\alpha_{\text{NLoS}}} \cos\left(\theta_{n,m}^{(1,2)}\right) \cdot \exp\left(j\phi'^{(1,2)}_{n,m}\right) & \cos\left(\theta_{n,m}^{(2,2)}\right) \cdot \exp\left(j\phi'^{(2,2)}_{n,m}\right) & \sqrt{\alpha_{\text{NLoS}}} \sin\left(\phi_{n,m}^{(2,3)}\right) \cdot \exp\left(j\theta'^{(1,3)}_{n,m}\right) \\ \sqrt{\alpha_{\text{NLoS}}} \cos\left(\phi_{n,m}^{(3,1)}\right) \cdot \exp\left(j\theta'^{(3,1)}_{n,m}\right) & \sqrt{\alpha_{\text{NLoS}}} \sin\left(\phi_{n,m}^{(3,2)}\right) \cdot \exp\left(j\theta'^{(3,2)}_{n,m}\right) & \cos\left(\phi_{n,m}^{(3,3)}\right) \cdot \exp\left(j\theta'^{(3,3)}_{n,m}\right) \end{pmatrix}. \tag{14}$$

3. Proposed Practical and Simple Multipolarized Channel Models

The practical and simple (PS) multipolarized channel models are presented in this section; they are categorized into the Rayleigh channel model and the Rician channel model through the consideration of the wireless channel statistical properties. In addition, according to the scatterer environments, they are further classified into a 2D channel model and a 3D channel model.

The PS multipolarized channel models are based on SCM-E channel model given by (11). It is a well-known 2D PMIMO channel model, which obtains only a single complex output resulting from the combination of all the polarized links. In this case, it is impossible to exploit spatial multiplexing gain or other types of combining gains since the polarized links become indistinguishable from each other. Here, P_n is the power of the nth path, σ_{SF} is the lognormal shadow fading, and M is the number of subpaths per path. $\theta_{n,m,\text{AoD}}$ is the AoD for the mth subpath of the nth path, and $\theta_{n,m,\text{AoA}}$ is the AoA for the mth subpath of the nth path. k is the wave number, d_s is the distance in meters between the BS antenna elements and the reference antenna element in the BS antenna array, and d_u is the distance in meters between the MS antenna elements and the reference antenna element in the MS antenna array. The SCM-E channel model defines $\Phi_{n,m}^{(x,y)}$ to be the phase offset of the mth subpath of the nth path between the x component (e.g., either the horizontal h or vertical v) of the BS element and the y component (e.g., either the horizontal h or vertical v) of the MS element as i.i.d. random variables drawn from a uniform 0- to 360-degree distribution. x and y can alternatively represent the copolarized and cross-polarized orientations. $\|v\|$ and θ_v are the magnitude and angle of the MS velocity vector, respectively. $\chi_{\text{BS}}^{(x)}(\theta_{n,m,\text{AoD}})$ and $\chi_{\text{MS}}^{(x)}(\theta_{n,m,\text{AoA}})$ are the BS and MS antenna complex response for the x-pol component, respectively. r_{n1} and r_{n2} are the linear XPD values in the SCM-E model, as described in [8].

The SCM-E channel model is very complex for use in imitating the practical wireless propagation channel since it employs a pseudoray tracing model. Another drawback is that there is only a single output of complex channel gain from the SCM-E polarized channel model for each instant in time, which makes the exploiting of MIMO spatial multiplexing or Rx combining techniques impossible. Moreover, it is not convenient to observe the characteristics of each of the polarized channel links (e.g., v-h, h-v, h-h, and v-v), such as the XPD values and contributions from the above four polarized links. Therefore, we develop new channel models that use a matrix determining the channel complex gain and thereby represent the characteristics of all the polarized channel links, that is, v-h, h-v, h-h, and v-v.

3.1. The PS 2D Dual-Polarized Rayleigh Channel Model. PS 2D dual-polarized Rayleigh channel is modeled as depicted by (12) based on the polarized characteristics of the SCM-E channel model applied to the 2D scatterer environment shown in Figure 1. Comparisons between the proposed channel model and the SCM-E channel model are given through four perspectives below.

Angle between Antenna Branches. $\chi_{\text{BS}}^{(x)}(\theta_{n,m,\text{AoD}})$ and $\chi_{\text{MS}}^{(x)}(\theta_{n,m,\text{AoA}})$ in (11) describe the angle between the x-pol antenna branches in the SCM-E channel model. In our proposed channel model, however, we assume that the v and h branches at Tx (or Rx) are always orthogonal with respect to each other. That is, only the polarized channel characteristics are considered in our channel model. So, the parameters, such as $\chi_{\text{BS}}^{(x)}(\theta_{n,m,\text{AoD}})$ and $\chi_{\text{MS}}^{(x)}(\theta_{n,m,\text{AoA}})$, used to reflect the angle between the v and h branches can be considered additionally when the elliptic polarized antenna is assumed or the slant angel mismatch exists for Tx and Rx polarized antennas.

Fading Channel. In our proposed channel model, as in the SCM-E polarized channel model, $\theta_{n,m}^{(v,h)}$ is the phase offset of the mth subpath of the nth path, which are i.i.d. random variables drawn from a uniform 0- to 360-degree distribution. The phase rotation in the SCM-E channel model is randomly generated in a statistical sense. In order to guarantee a continuously time-varying phase response in our channel model, however, the phase offset is updated according to the MS mobility in place of random generation.

Mobility. $\exp(jk\|v\|\cos(\theta_{n,m,\text{AoA}} - \theta_v)\ t)$ is a variable related to the mobility in the SCM-E channel model. However, the mobility in our proposed model is derived using Δ and θ in the channel matrix seen in (12) in order to generate the time-varying phase response. Because the mobility introduces frequency (phase) offset, by employing the parameters Δ and θ, the Doppler effect can be represented intuitively. That is, the angel θ reflects the direction of mobility, and the displacement of UE within one slot period is represented by Δ. The value of Δ increases as the mobility increases, so the frequency (phase) offset is also increasing.

MIMO. $\exp(jkd_s \sin(\theta_{n,m,\mathrm{AoD}}))$ and $\exp(jkd_u \sin(\theta_{n,m,\mathrm{AoA}}))$ in the SCM-E channel model are variables related to the AoD and AoA of the MIMO polarized antenna system. In this study, we decide to model the SISO polarized channel to be employed in the polarized antenna system for SISO and independent MIMO cases. For the correlated MIMO polarized antenna system, the correlation regarding the SISO polarized antenna needs to be additionally considered. Furthermore, due to the assumption that there is sufficient distance between the BS and MS in our channel models, all the input signals are incident in parallel at the MS, which means that the AoD value becomes 0 in our channel models. However, the AoA angels are considered due to the scatterer environment shown in Figure 1, which contributes to the phase response of the received signal.

Instead of the independent consideration of the channel parameters used in the SCM-E channel model, all the contributions mentioned above are jointly coupled in order to build a complete channel matrix in our proposed polarized channel model, which results in the simple and practical channel model.

Based on these principles, the PS 2D dual-polarized Rayleigh channel is modeled as described in (12). Here, M is the number of subpaths (scatterers), P_n is the power of the nth path, $\theta_{n,m}^{(v,h)}$ is the phase rotation of the received signal at the MS from the mth subpath of the nth path, α_{NLoS} is the linear XPD value for the NLoS components, r is the distance between the scatterers and the MS, and Δ is the moving distance of the MS. $\sqrt{P_n/M}$ is the power normalization factor. When a horizontally polarized antenna receives a signal sent from a vertically polarized antenna (and vice versa), the received signal strength is reduced proportionally to the linear XPD value α_{NLoS}.

3.2. The PS 3D Dual-Polarized Rayleigh Channel Model. The PS 3D dual-polarized Rayleigh channel is modeled as described in (13) based on the polarized characteristics of the SCM-E channel model applied to the 3D scatterer environment shown in Figure 2.

We expand the 2D scatterer model to the 3D scatterer model by adding an elevation angle parameter ϕ which is updated according to the MS mobility using

$$\phi' = \arctan\left(\frac{r\cos\theta_{n,m}\sin\phi_{n,m}}{r\cos\theta_{n,m}\cos\phi_{n,m} + (n-1)\,\Delta}\right). \tag{15}$$

Since a dual-polarized antenna on the x-y plane is employed in the 3D environment, the projection of the reflected signals by the 3D scatterers in the x-y plane is considered as seen in (13). Therefore, the 3D dual-polarized channel model depicts the channel complex gain using a (2×2) matrix. Similar to the 2D channel model, the cross-channel complex gain is attenuated by the linear XPD value α_{NLoS}.

3.3. The PS 3D Triple-Polarized Rayleigh Channel Model. The PS 3D triple-polarized Rayleigh channel is modeled as seen in (14), based on the PS 3D dual-polarized channel model. In addition to the projected signal in the x-y plane due to the dual-polarization, the projected signals in the x-z and y-z planes are considered in order to account for a triple polarization. The updated azimuth angle and elevation angle due to mobility are shown in (16) and (17), respectively. Consider

$$\theta' = \arctan\left(\frac{r\cos\theta_{n,m}\sin\phi_{n,m}}{r\cos\theta_{n,m}\cos\phi_{n,m} + (n-1)\,\Delta}\right), \tag{16}$$

$$\phi' = \arctan\left(\frac{r\sin\theta_{n,m}}{r\cos\theta_{n,m}\cos\phi_{n,m} + (n-1)\,\Delta}\right). \tag{17}$$

This channel model generates a (3×3) matrix for its complex channel output; the complex gain of the cross-channels is attenuated by the linear XPD value α_{NLoS}. Since the XPD values describe the long-term characteristics (primarily mean values), all of the XPD values are assumed to be the same.

3.4. The PS Multipolarized Rician Channel Model. Similar to the Rayleigh channel model described above, the PS dual-polarized Rician channel for both the 2D and 3D cases can be generated by introducing the Rician factor [12] into the Rayleigh channel model for both the LoS component and the NLoS components:

$$\begin{aligned}\mathbf{H}_{\text{Rician-Dual}}(t) &= \begin{bmatrix} \sqrt{\frac{k}{k+1}} & \sqrt{\frac{k'}{k'+1}} \\ \sqrt{\frac{k'}{k'+1}} & \sqrt{\frac{k}{k+1}} \end{bmatrix} \odot \overline{\mathbf{H}}(t) \\ &\quad + \begin{bmatrix} \sqrt{\frac{1}{k+1}} & \sqrt{\frac{1}{k'+1}} \\ \sqrt{\frac{1}{k'+1}} & \sqrt{\frac{1}{k+1}} \end{bmatrix} \odot \mathbf{H}_{\text{Rayleigh-Dual}}(t),\end{aligned} \tag{18}$$

where k is the conventional Rician factor, k' is $(\alpha_{\mathrm{LoS}}/\alpha_{\mathrm{NLoS}})k$, and $\odot$ is the Hadamard product. The LoS component $\overline{\mathbf{H}}(t)$ is given as described by (19), and the NLoS component $\mathbf{H}_{\text{Rayleigh-Dual}}(t)$ is given as described in (12) for the 2D case and in (13) for the 3D case. Consider

$$\overline{\mathbf{H}}(t) = \begin{bmatrix} \overline{h}_{v,v} & \sqrt{\alpha_{\mathrm{LoS}}} \cdot \overline{h}_{v,h} \\ \sqrt{\alpha_{\mathrm{LoS}}} \cdot \overline{h}_{h,v} & \overline{h}_{h,h} \end{bmatrix}. \tag{19}$$

The dual-polarized case is extended into a (3×3) channel matrix for the PS 3D triple-polarized Rician channel model. Similar to the dual-polarized Rician channel model, the PS 3D triple-polarized Rician channel model is determined by the LoS component and NLoS components, as shown in (20).

The LoS component $\overline{\mathbf{H}}(t)$ is determined by (21), and the NLoS component $\mathbf{H}_{\text{3D-Rayleigh-Triple}}(t)$ is as shown in (14):

$$\begin{aligned}\mathbf{H}_{\text{3D-Rician-Triple}}(t) &= \begin{bmatrix} \sqrt{\frac{k}{k+1}} & \sqrt{\frac{k'}{k'+1}} & \sqrt{\frac{k'}{k'+1}} \\ \sqrt{\frac{k'}{k'+1}} & \sqrt{\frac{k}{k+1}} & \sqrt{\frac{k'}{k'+1}} \\ \sqrt{\frac{k'}{k'+1}} & \sqrt{\frac{k'}{k'+1}} & \sqrt{\frac{k}{k+1}} \end{bmatrix} \odot \overline{\mathbf{H}}(t) \\ &+ \begin{bmatrix} \sqrt{\frac{1}{k+1}} & \sqrt{\frac{1}{k'+1}} & \sqrt{\frac{1}{k'+1}} \\ \sqrt{\frac{1}{k'+1}} & \sqrt{\frac{1}{k+1}} & \sqrt{\frac{1}{k'+1}} \\ \sqrt{\frac{1}{k'+1}} & \sqrt{\frac{1}{k'+1}} & \sqrt{\frac{1}{k+1}} \end{bmatrix} \\ &\odot \mathbf{H}_{\text{3D-Rayleigh-Triple}}(t), \end{aligned} \tag{20}$$

$$\overline{\mathbf{H}}(t) = \begin{bmatrix} \overline{h}_{1,1} & \sqrt{\alpha_{\text{LoS}}} \cdot \overline{h}_{1,2} & \sqrt{\alpha_{\text{LoS}}} \cdot \overline{h}_{1,3} \\ \sqrt{\alpha_{\text{LoS}}} \cdot \overline{h}_{2,1} & \overline{h}_{2,2} & \sqrt{\alpha_{\text{LoS}}} \cdot \overline{h}_{2,3} \\ \sqrt{\alpha_{\text{LoS}}} \cdot \overline{h}_{3,1} & \sqrt{\alpha_{\text{LoS}}} \cdot \overline{h}_{3,2} & \overline{h}_{3,3} \end{bmatrix}. \tag{21}$$

3.5. The PS Multipolarized Multipath Channel Model. The PS multipolarized channel models are designed for use in macro and micro cell environments. Therefore, the power delay profile of ITU-R M.1224 Veh. A from [13] is adopted in order to generate multipath channel models, as shown in (22). Consider

$$\mathbf{H}_{\text{multipath}}(t) = \sum_{l=1}^{L} \sqrt{\frac{P_l}{M}} \mathbf{H}_l(t)\, \delta(t - \tau_l), \tag{22}$$

where L is the number of multipaths, P_l is the signal power per path, $\mathbf{H}_l$ is the polarized flat fading channel, and τ_l is the time delay of each path.

4. Performance Gain by the Polarized Antenna System

4.1. The General Parameters of Multipolarized Antenna System. The multipolarized antenna system is designed to be used in macro and micro cell environments; therefore we use 64 scatterers by setting the scatterer radius to 10 m and the MS mobility to 0, 30, and 60 km/h. The carrier frequency is set to 1.8 GHz in order to use the measured XPD values found in [14]. Since the measured XPD values are adopted in the simulations, the depolarization effects due to both channel and the slant angel mismatch of polarized antenna branches are involved, which makes the simulation results more meaningful to reflect the scenario of real word. The Rician factor is chosen to be 9 dB, which is a typical value in urban terrestrial wireless environments. All the parameters are given in Table 3.

The system bandwidth is 20 MHz, resulting in a symbol duration of 0.05 μs. In order to verify the proposed polarized channel model, a simple single-carrier packet structure composed of 100 QPSK symbols is applied to the multipolarized antenna system, wherein 5% of the symbols are used as pilots. When the MS mobility is 60 km/h, the MS moving distance becomes 8.335×10^{-6} m during a 1-packet duration, which is quite a small value compared to the scatterer radius. Therefore, we can assume that the MS moving direction does not appreciably change within a 1-packet duration, as mentioned in Section 2.

4.2. The Verification of PS 3D Triple-Polarized Rayleigh Channel Model. Figure 3 shows the *normalized* fading envelopes of the co-/cross-channel links in the PS 3D triple-polarized Rayleigh channel model, assuming that all of the generated channel links are independent. The solid H_{11} line represents the fading envelope of the cochannel link; the H_{12} and H_{13} dotted lines depict the envelopes of the cross-channel links. The mean value of the fading envelope for cochannel H_{11} is almost 5.8 dB higher than those found for cross-channels H_{12} and H_{13} due to the NLoS XPD value shown in Table 3. Figure 3(a) shows the MS mobility at 0 km/h, wherein the channel envelopes do not change during one-packet duration (100 symbols). Figure 3(b) shows the MS mobility at 60 km/h; the channel envelopes are continuously time-varying due to the MS movement.

Figure 4 shows the phase response of the PS 3D triple-polarized channel model, which is continuously time-varying and changes about 0.002 radians during a 1-packet duration.

Figure 5 shows the power spectrum density (PSD) of the PS 3D triple-polarized channel model. The lines are designated by circles, squares, and triangles, which correspond to the MS mobility PSD at 3 km/h, 30 km/h, and 60 km/h, respectively. The PSD results show that the maximum Doppler spreads are 10, 100, and 200 Hz, respectively, according to mobility.

4.3. The Receiver Diversity Gain under PS 3D Multipolarized Rician Channel. Equal gain combining (EGC) and maximum ratio combining (MRC) are performed at the MS in order to combine the signals of the polarized channel links [15, 16]. The EGC and MRC mathematical representations are given in (23) and (24), respectively, for a dual-polarized antenna. Consider

$$\text{EGC} = \frac{S_{vv} + S_{vh} + S_{hv} + S_{hh}}{h_{vv} + h_{vh} + h_{hv} + h_{hh}}, \tag{23}$$

$$\text{MRC} = \frac{h_{vv}^* \cdot S_{vv} + h_{vh}^* \cdot S_{vh} + h_{hv}^* \cdot S_{hv} + h_{hh}^* \cdot S_{hh}}{|h_{vv}|^2 + |h_{vh}|^2 + |h_{hv}|^2 + |h_{hh}|^2}, \tag{24}$$

where S_{vh} is the Tx signal power, h_{vh} is the channel link, and h_{vh}^* is the conjugate of h_{vh}.

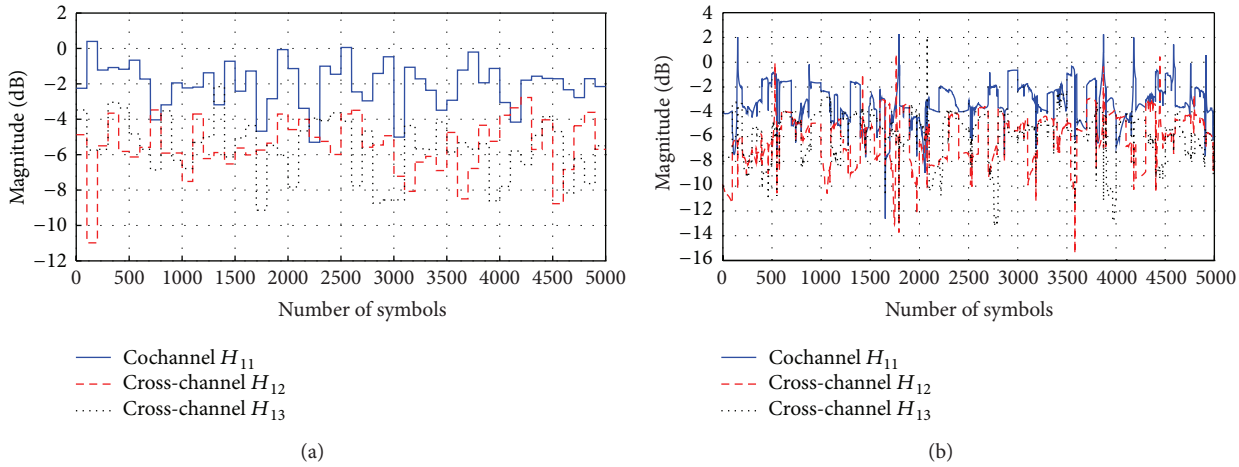

Figure 3: Normalized fading envelope of the PS 3D triple-polarized channel model: (a) MS mobility = 0 km/h and (b) MS mobility = 60 km/h.

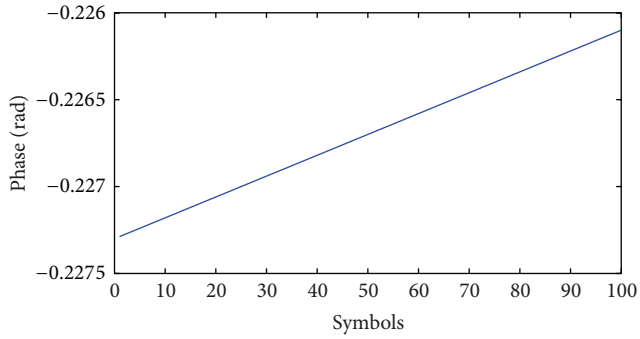

Figure 4: Phase response of the PS 3D triple-polarized channel model.

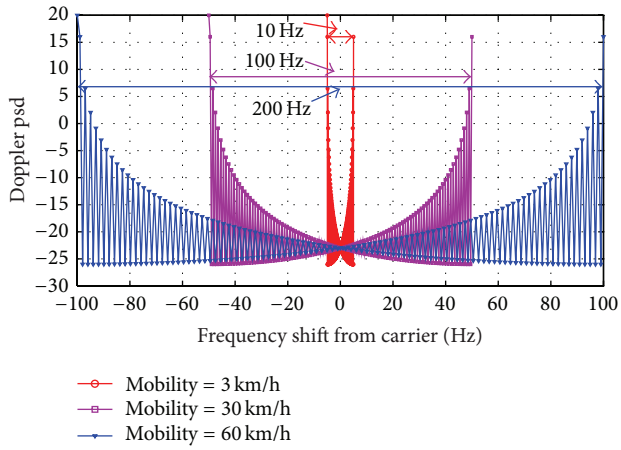

Figure 5: PSD of the PS 3D triple-polarized channel model.

We vary the XPD values in order to verify the proposed PS 3D polarized channel model in the aspect of the Eb/N0 versus bit-error-rate (BER) performance shown in Figure 6. The simulation scenario designated as "Single" shows that only a vertical dipole antenna is placed at the BS and MS.

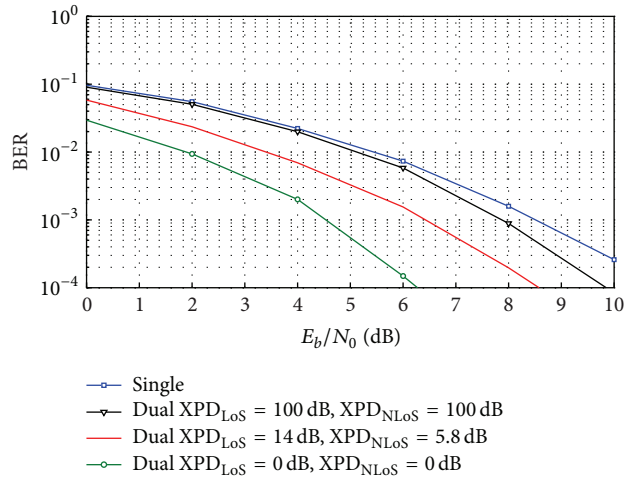

Figure 6: The BER performances for antennas and XPD values under a flat PS 3D fading Rician channel.

Table 3: System parameters.

System parameters	Values
Target cell	Macro, micro
Carrier frequency	1.8 GHz
System BW	20 MHz
Scatterer radius	10 m
Rician factor	9 dB
LoS XPD value	14 dB
NLoS XPD value	5.8 dB
Number of symbols in packet	100 symbols
Modulation	QPSK
Combining techniques	EGC, MRC
Equalizer	1-tap time-domain equalizer

The BER performance in this case is the same as that found for a conventional SISO channel; it is used for a reference curve. The "Dual" simulation scenarios use dual-polarized antennas at the BS and MS to communicate with each other; EGC is employed to combine the signals of v and h links. The XPD values of 100 dB and 0 dB represent the upper and lower bounds of the BER for the dual-polarized antennas. The simulation results with XPD values of 0 dB achieve the best BER performance. In this case, a maximum diversity gain is obtained due to the full contributions from four channel links (v-h, h-v, h-h, and v-v). Conversely, in the case of large 100 dB XPD values, the contributions from the v-h and h-v cross-channel links become very small compared to the v-v and h-h cochannel links due to the large XPD values, resulting in the worst BER performance. When XPD values are XPD_{LoS} = 14 dB and XPD_{NLoS} = 5.8 dB, the simulation results show a 2 dB gain, a 1.5 dB gain, and a 2 dB loss compared to the "1∗1" case and XPD values of 100 dB and 0 dB, respectively, at the target BER of 10^{-3}. In other words, the BER curve in this case is located between the curves for the upper and lower bounds.

Figures 7 and 8 show the BER and packet-error-rate (PER) performances when adopting the aforementioned combining techniques for the 3D multipolarized multipath Rician fading channel. The simulation scenario designated "Single" uses only a vertical dipole antenna at the BS and MS. The simulation scenarios "Dual EGC" and "Dual MRC" mean that a dual-polarized antenna is used at the Tx and Rx sides employing EGC and MRC combining techniques, respectively, and "Triple EGC" and "Triple MRC" both use triple-polarized antennas. As shown in Figures 7 and 8, it is obvious that the systems employing the triple-polarized antennas always show the best performance. The "Triple MRC BER" and "Triple EGC BER" provide 28 dB gain and 6 dB gain, respectively, compared to the "Single BER" at the target BER of 10^{-4}. In addition, the relationship among the PER curves is similar to that found for the BER curves. Multipolarized systems using MRC provide more gain than those using EGC; the increased gain by the MRC with a 1-tap time-domain equalizer comes from the meaningful contribution of the LoS component in the Rician channel. In other words, what the MRC does better is that it is the optimum combining in terms of SNR and weights the strong antenna elements more than the weak. Figure 9 shows the throughput of five different simulation scenarios using the 3D multipolarized multipath Rician fading channel. At Eb/N0 of 12 dB, for example, the "Triple MRC" scenario has a 20 times higher throughput than the "Single" scenario, and more than a 1.3 times higher throughput than the "Dual MRC" scenario.

The proposed channel model in [9] is verified by geometrically deriving the XPD value and then comparing it with the measured results. The verification results given in [9] validate the accuracy of the proposed channel model since the derived XPD values approximate the measured results. However, due to the modeling complexity in [9], it is difficult to be extended to support the cases with triple-polarized system as well as antenna array. In this paper, we verify our proposed channel model by directly specifying the XPD value according to the existing literatures and then

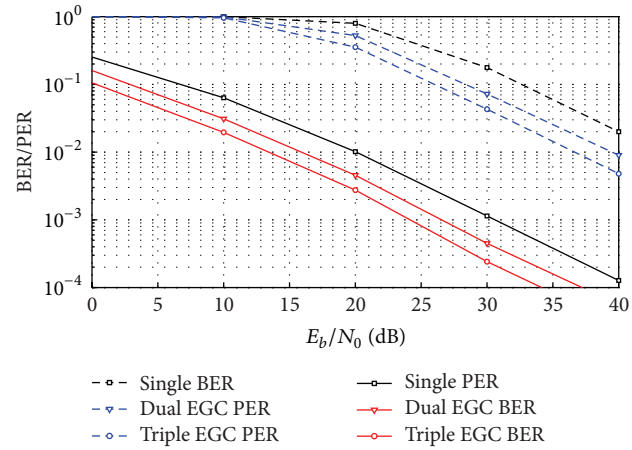

Figure 7: The BER and PER performances using EGC in the PS 3D multipolarized multipath Rician fading channel.

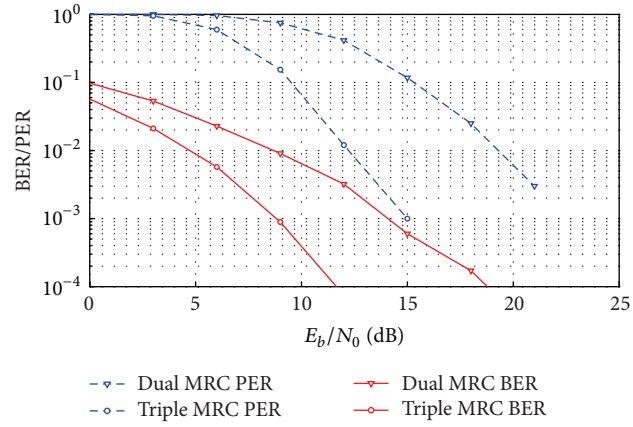

Figure 8: The BER and PER performances using MRC in the PS 3D multipolarized multipath Rician fading channel.

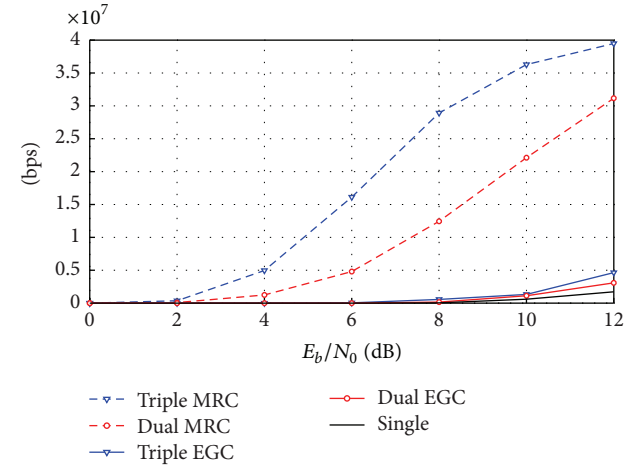

Figure 9: The throughput in the PS 3D multipolarized multipath Rician fading channel.

test the proposed channel via the common diversity schemes. Based on the simulated BER/PER and throughput analysis by the diversity techniques, we also prove that the proposed channel model is accurate and reliable to be implemented for the computer simulation.

5. Conclusions

In this paper, PS 2D and 3D multipolarized multipath fading channel models have been presented based on the polarized characteristic of the SCM-E channel model. In order to verify and evaluate our proposed channel models, the measured XPD values in practical environments are employed. The BER and PER performances and the throughput using EGC and MRC combining techniques for multipolarized antenna systems have been presented. Under the polarized Rician fading channel, the triple-polarized antenna system employing MRC provides 20 times and 1.3 times higher throughput than a single antenna system and a dual-polarized antenna system with MRC, respectively, at an Eb/N0 of 12 dB. In other words, the use of polarized antennas can greatly increase the reliability of wireless links, which can be turned into throughput increase, depending on the discrimination capabilities of the cross-channels of the polarized system. The use of a polarized antenna is also an efficient way to reduce antenna spacing, which helps to decrease both the size and the cost of a BS with a MIMO configuration.

Conflict of Interests

The authors declare that there is no conflict of interests regarding the publication of this paper.

Acknowledgments

This work was supported by Basic Science Research Program through the National Research Foundation of Korea (NRF) funded by the Ministry of Education (2013R1A1A2010287) and the project "Development of marine RF based ad hoc network for ship" from Ministry of Oceans and Fisheries (MOF), Korea. This work was also supported by Inha University Research grant. Part of this work has been published with preliminary form in the proceeding of the International Conference on Information Networking (ICOIN) in February 2012.

References

[1] M. A. Jensen and J. W. Wallace, "A review of antennas and propagation for MIMO wireless communications," *IEEE Transactions on Antennas and Propagation*, vol. 52, no. 11, pp. 2810–2824, 2004.

[2] O. Franek, J. B. Andersen, and G. F. Pedersen, "Diffuse scattering model of indoor wideband propagation," *IEEE Transactions on Antennas and Propagation*, vol. 59, no. 8, pp. 3006–3012, 2011.

[3] R. S. Blum, "Limiting case of a lack of rich scattering environment for MIMO radar diversity," *IEEE Signal Processing Letters*, vol. 16, no. 10, pp. 901–904, 2009.

[4] G. J. Foschini and M. J. Gans, "On limits of wireless communication in a fading environment when using multiple antennas," *Wireless Personal Communications*, vol. 6, no. 3, pp. 311–335, 1998.

[5] M. R. Andrews, P. P. Mitra, and R. Decarvalho, "Tripling the capacity of wireless communications using electromagnetic polarization," *Nature*, vol. 409, no. 6818, pp. 316–318, 2001.

[6] R. G. Vaughan, "Polarization diversity in mobile communications," *IEEE Transactions on Vehicular Technology*, vol. 39, no. 3, pp. 177–186, 1990.

[7] A. S. Y. Poon and D. N. C. Tse, "Degree-of-freedom gain from using polarimetric antenna elements," *IEEE Transactions on Information Theory*, vol. 57, no. 9, pp. 5695–5709, 2011.

[8] 3GPP, Spatial Channel Model for Multiple Input Multiple Output MIMO Simulations, vol. TR25.996, v6.1.0, September 2003.

[9] S.-C. Kwon and G. L. Stüber, "Geometrical theory of channel depolarization," *IEEE Transactions on Vehicular Technology*, vol. 60, no. 8, pp. 3542–3556, 2011.

[10] M. Shafi, M. Zhang, A. L. Moustakas et al., "Polarized MIMO channels in 3-D: models, measurements and mutual information," *IEEE Journal on Selected Areas in Communications*, vol. 24, no. 3, pp. 514–527, 2006.

[11] K. H. Jeon, B. Hui, K. H. Chang, H. S. Park, and Y. O. Park, "SISO polarized flat fading channel modeling for dual-polarized antenna systems," in *Proceedings of the 26th International Conference on Information Networking (ICOIN '12)*, pp. 368–373, February 2012.

[12] R. U. Nabar, H. Bölcskei, V. Erceg, D. Gesbert, and A. J. Paulraj, "Performance of multiantenna signaling techniques in the presence of polarization diversity," *IEEE Transactions on Signal Processing*, vol. 50, no. 10, pp. 2553–2562, 2002.

[13] ITU-R Rec. ITU-R M.1225, *Guidelines for Evaluation of Radio Transmission Technologies for IMT-2000*, 1997.

[14] J. J. A. Lempiäinen and J. K. Laiho-Steffens, "The performance of polarization diversity schemes at a base station in small/micro cells at 1800 MHz," *IEEE Transactions on Vehicular Technology*, vol. 47, no. 3, pp. 1087–1092, 1998.

[15] A. S. Lioumpas, G. K. Karagiannidis, and A. C. Iossifides, "Channel Quality Estimation Index (CQEI): a long-term performance metric for fading channels and an application in EGC receivers," *IEEE Transactions on Wireless Communications*, vol. 6, no. 9, pp. 3315–3323, 2007.

[16] A. Nasri, R. Schober, and M. Uysal, "Enhanced MRC for decode-and-forward cooperative diversity systems," *IEEE Transactions on Wireless Communications*, vol. 11, no. 10, pp. 3418–3423, 2012.